



Advanced Metrology for Characterization of Magnetic Tunnel Junctions

Kjær, Daniel

Publication date:
2015

Document Version
Publisher's PDF, also known as Version of record

[Link back to DTU Orbit](#)

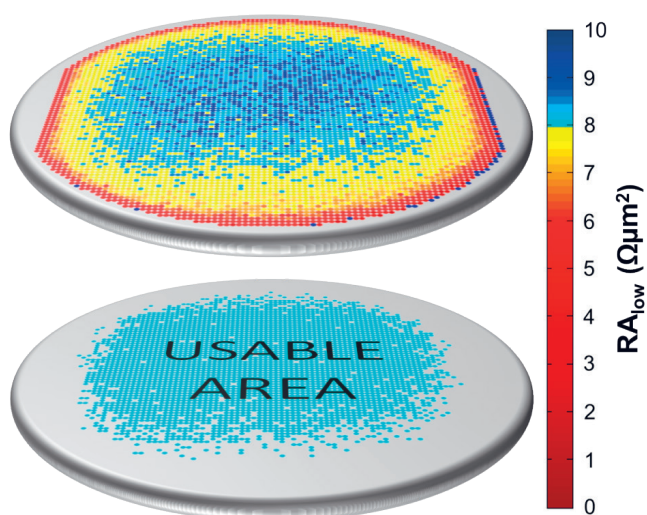
Citation (APA):
Kjær, D. (2015). *Advanced Metrology for Characterization of Magnetic Tunnel Junctions*. DTU Nanotech.

General rights

Copyright and moral rights for the publications made accessible in the public portal are retained by the authors and/or other copyright owners and it is a condition of accessing publications that users recognise and abide by the legal requirements associated with these rights.

- Users may download and print one copy of any publication from the public portal for the purpose of private study or research.
- You may not further distribute the material or use it for any profit-making activity or commercial gain
- You may freely distribute the URL identifying the publication in the public portal

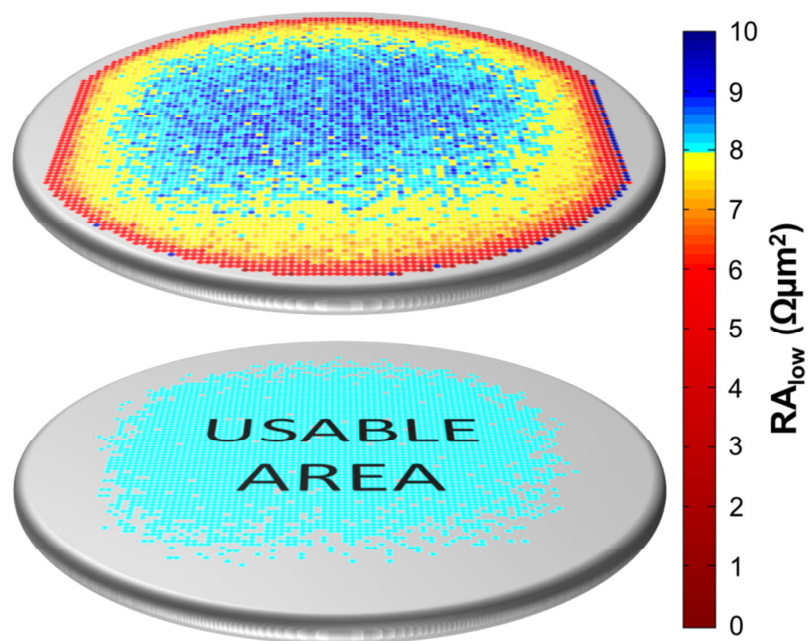
If you believe that this document breaches copyright please contact us providing details, and we will remove access to the work immediately and investigate your claim.



Advanced Metrology for Characterization of Magnetic Tunnel Junctions

Daniel Kjær
PhD Thesis May 2015

Advanced Metrology for Characterization of Magnetic Tunnel Junctions



Daniel Kjær

CAPRES A/S
and
Department of Micro- and Nanotechnology
Technical University of Denmark

Ph.D. Thesis, May 26th 2015

Abstract

For the past 50 years the prediction that turned into what is now known as Moore's Law has held true. It states that the complexity of integrated circuits such as computer processors will double approximately every second year. In order to keep up the industry has been on constant lookout for new solutions to take products to the next node and the field of memory technology is no exception. Over the past decade research and development in a novel, non-volatile memory type known as MRAM has intensified, and commercial MRAM devices are now available. MRAM holds an extremely favorable position as it is believed to have the potential of becoming a truly universal memory solution dominant within all fields of memory application.

A decade ago the company CAPRES A/S introduced the so-called CIPTech, which is a metrology tool utilizing micro four-point probes (M4PPs) and a method known as current in-plane tunneling (CIPT) for characterization of magnetic tunnel junctions (MTJs), which constitutes the key component not only in MRAM but also the read-heads of modern hard disk drives. MTJs are described by their tunnel magnetoresistance (TMR), which is the relative difference of the resistance area products (RA) at two characteristic resistance levels (high and low) of the MTJ device. In the final memory application these resistance states correspond to a digital "1" or "0" stored. During CIPT measurements the tool will alter the state of the MTJ by application of an external magnetic field. With the CIPTech the turn-around time for measurements on magnetic tunnel junctions shortened dramatically from two days to one or two minutes. As one happy user put it, it was like going from a tricycle to a Ferrari in one step, and the tool is now in use in all major memory companies throughout the world.

However, with a measurement time of 1-2 minutes per measurement, the technique is commonly used just for research and development of novel MTJ stacks and not for full wafer analysis, which would otherwise provide valuable information with respect to uniformity, e.g. for tool optimization. The precision of CIPT measurements is limited by electrode position errors, the importance of which increases for decreasing electrode pitch. This is a challenge to the measurement method as such and may become even more so in the future, when the cell size of MRAM is scaled down to increase memory density.

The fundamental goal of this project has been to provide cheaper, faster and more precise metrology for MTJs.

This goal has been achieved in part by the demonstration of a static field CIPT method, which allows us to reduce the measurement time by a factor of 5, by measuring only RA thus excluding TMR. This enhancement is obtained purely by acquiring only half of the data needed for the conventional switching field CIPT measurement and particularly by avoiding magnetic field switching. We observe that the new method measures essentially the same RA values as compared to the conventional strategy. By offering the choice of characterizing either RA_{low} or RA_{high} the static field CIPT method has an added advantage over the conventional switching field CIPT method, which relies on the characterization of both RA values. This allows for an improved matching of the range of available electrode pitches and sample transfer lengths, which may effectively increase the dynamic range of any given micro 12-point probe (M12PP).

Without the requirement for switching magnetic fields during measurements the static field CIPT method has inspired the concept of detached magnet setups for future CIPTech tools. While lowering the complexity of the measurement system a detached magnet setup, e.g. a proposed letterbox magnet, could provide superior dynamic range and field homogeneity as compared to current state of the art solutions.

We have carried out an extensive characterization of electrode position errors and experimentally shown that the dominant sources of error in single configuration micro four-point probe resistance measurements are in-line probe geometry errors and in-line static position errors. These errors were shown to be eliminated very effectively using dual-configuration measurements and position error correction algorithms. The standard deviation of the static in-line position error for measurements with Au coated electrodes on Ru thin film samples was found to be in the range from 3.9 nm to 7.5 nm. The standard deviation of the dynamic in-line position error was shown to be small ~ 3 Å and only detectable in measurements with high measurement current. At lower measurement currents the electrical measurement noise was the dominant error source. No significant ageing effect on position errors (except for a very slight reduction in position error with measurement age) was observed for a probe in the course of 5000 measurements. We have demonstrated how new probe designs may be evaluated and benchmarked against each other using the same strategy.

Based on Monte Carlo simulations we have studied the influence of electrical noise as well as static and dynamic, in-line and off-line electrode position errors on four-point resistance measurements on MTJs. This study points out the van der Pauw position correction strategy based on combined measurement in four-point configuration A and C as being the most effective method to lower the relative standard deviation on the measured resistance. In line with this we find that the same method also provides the broadest dynamic range for the M12PP used in this project.

As a means to further enhance the measurement precision we have proposed the addition of more sub-probes of nominally identical electrode spacing and shown, that for one added sub-probe, the option for which two sub-probes shares two pins, yields the most significant reduction of electrode positional errors. Finally, a radical probe design entirely occupied by equidistant electrodes was proposed.

Resumé

Over en periode på mere end 50 år har prognosen, der blev kendt som Moores Lov, vist sig at holde stik. Den forudsiger i praksis, at antallet af transistorer integreret i en computer processor vil fordobles hvert andet år, og for at holde trit med den udvikling har industrien til stadighed måttet være på udkig efter nye løsninger, der kunne bringe deres produkter videre til den næste teknologinode. Branchen for digital hukommelse har ikke været en undtagelse. I løbet af det seneste årti er forskning og udvikling i en ny hukommelsestype kaldet MRAM intensiveret, og teknologien spås en lys fremtid med potentiale for at kunne blive en universel hukommelsesløsning, der vil komme til at dominere indenfor alle anvendelser af hukommelse.

Firmaet CAPRES A/S introducerede for 10 år siden den såkaldte CIPTech. Det er et måleudstyr, der ved hjælp af mikro-fire-punkts-prober (M4PP) og en metode kendt som current in-plane tunneling (CIPT) anvendes til karakterisering af magnetiske tunnel junctions (MTJs), som udgør en kernekomponent ej blot i MRAM, men også i læsehovederne i moderne harddiskdrev. MTJs kan beskrives ved deres tunnel-magnetoreistans (TMR), hvilket er den relative forskel mellem modstand-areal-produktet (RA) ved to karakteristiske modstandsniveauer (højt og lavt) for MTJ-enheden. I den endelige hukommelsesapplikation vil disse modstandstilstande svare til den digitalt lagrede information "1" eller "0", og under en CIPT-måling vil udstyret ændre tilstanden for en MTJ ved at påtrykke et eksternt magnetfelt. Ved brug af CIPTech'en er turn-around-tiden for målinger på MTJs forkortet dramatisk fra to dage til et eller to minutter. Som en glad bruger udtrykte det, var det som at gå direkte fra en trehjulet cykel til en Ferrari, og udstyret er nu i anvendelse hos alle ledende hukommelsesproducenter verden over.

Med en måletid på blot 1-2 minutter pr. punkt er metoden dog stadig for tidskrævende til, at man kan udnytte dens fulde potentiale til procesoptimering gennem udførelsen af scans med flere hundrede målinger på samme prøve. Målepræcisionen for CIPT udstyret begrænses af positionsfejl for mikroprobens elektroder, hvis indflydelse stiger for faldende elektrodeafstand. Det er en udfordring for målemetoden som sådan, og kan blive det i endnu højere grad i fremtiden, når MRAM-cellens størrelse skaleres ned for at øge hukommelsestætheden.

Målet for dette projekt har været at tilvejebringe løsninger, der resulterer i både hurtigere, billigere og mere præcis karakterisering af (MTJs).

Dette mål er opnået til dels ved demonstration af en statisk-felt CIPT-metode, som giver os mulighed for at reducere måletiden med en faktor 5 ved kun at måle RA og altså udelade TMR. Denne forbedring opnås ved at foretage blot halvdelen af de målinger, der er nødvendige for den konventionelle CIPT-målemetode, og i særdeleshed ved at udgå magnetfeltsskift. Vi observerer, at den nye metode i al væsentlighed måler de samme RA-værdier, som findes med den konventionelle strategi. Statisk-felt CIPT-metoden har, idet den tilbyder valgfrihed i forhold til karakterisering af enten RA_{lav} eller $RA_{høj}$, en ekstra fordel i forhold til standardmetoden, der bygger på karakteriseringen af begge RA-værdier. Dette giver mulighed for en forbedret matchning af tilgængelige mikroprober og den enkelte prøves transferlængde, hvilket effektivt set kan øger det dynamiske område for en given mikro 12-punkts probe (M12PP).

Uden kravet om at skifte magnetfelt under en måling har statisk-felt CIPT-metoden inspireret et koncept med en fritliggende magnetopstilling for fremtidige CIPTech-udstyr. Samtidig med at sænke kompleksiteten af målesystemet vil en fritliggende magnetopstilling, f.eks. den foreslåede ”brevsprække-magnet”, kunne tilbyde dynamikområde og felt homogenitet, som er overlegent i forhold til den nuværende løsning.

Vi har foretaget en omfattende karakterisering af elektrodepositionsfejl og eksperimentelt påvist, at de dominerende fejlkilder i enkelt-konfigurations-modstandsmålinger, foretaget med en M4PP, er in-line probegeometriefejl og in-line, statiske positionsfejl. Det blev vist, at disse fejl effektivt elimineres ved hjælp af dual-konfigurations-målinger og positionsfejls-korrigerende algoritmer. Standardafvigelsen af de statiske, in-line positionsfejl for målinger med Au-elektroder på Ru-tyndfilmsprøver viste sig at være fra 3.9 nm til 7.5 nm. Standardafvigelsen af den dynamiske, in-line positionsfejl blev vist til at være ~ 3 Å, og var kun påviselig i målinger med høj målestrøm. Ved lavere målestrøm var den elektriske støj den dominerende fejlkilde. Ingen signifikant ældningseffekt på positionsfejl blev observeret for en probe i løbet af 5000 målinger (bortset fra en meget lille reduktion i positionsfejl). Vi har vist, hvordan nye probe design kan vurderes og benchmarkes mod hinanden ved hjælp af den samme strategi.

Baseret på Monte Carlo-simuleringer har vi studeret indflydelsen af elektrisk støj samt statiske og dynamiske, in-line og off-line elektrodepositionsfejl på fire-punkts-modstandsmålinger på MTJs. Denne undersøgelse udpeger van-der-Pauw-positions-korrektionsstrategien baseret på kombinationen af modstandsmålinger optaget i fire-punkts-konfigurationerne A og C, som værende den mest effektive metode til at sænke den relative standardafvigelse på den målte modstand. I tråd med dette finder vi, at den samme metode også giver det bredeste dynamikområde for den M12PP, der anvendes i dette projekt.

Som et middel til yderligere forbedring af målepræcisionen har vi foreslået tilføjelsen af flere sub-prober med nominelt identiske elektrodeafstande og vist, at to kombinationen af to sub-prober, der deler to elektroder, giver den største reduktion af elektrodepositionsfejl. Endelig blev et radikalt probedesign, udelukkende besat af ækvidistante elektroder, foreslået.

Preface

This dissertation is submitted in partial fulfillment of the requirements to obtain the PhD degree at the Technical University of Denmark (DTU). The work described in this thesis was carried out at CAPRES A/S and at the Department of Micro- and Nanotechnology (DTU Nanotech) in the period from April 2012 to May 2015. The work was supervised by senior researcher Dirch H. Petersen (DTU Nanotech), professor Ole Hansen (DTU Nanotech) and Peter F. Nielsen (CAPRES A/S). The project is a joint collaboration between DTU Nanotech and CAPRES A/S and has been co-financed by the Innovation Fund Denmark.

I would like to thank my supervisors for obtaining the financial support for this project and for time and effort spent discussing the work, answering questions and solving problems. I thank Dirch H. Petersen and Ole Hansen for their exceptional commitment to theoretical calculations and their invaluable help in writing papers. Numerous other persons have contributed to this project and I wish to thank my colleagues at DTU Nanotech for their interest in my work; Henrik H. Henriksen (DTU Nanotech, now CAPRES A/S) and Frederik W. Østerberg (DTU Nanotech) for inspiring conversations on a daily basis; Lim Sze Ter, Jacob W. Chenchen and Randall Law from the Data Storage Institute (DSI) in Singapore for their help on sample fabrication and hours of qualified discussions; David M. Love, Justin Llandro and Joshua J. Hughes from the University of Cambridge for their effort to extend the use of micro probes in low temperature experiments; Lauge Gammelgaard (CAPRES A/S) for probe fabrication and fruitful discussions on probe design and micro probe applications; Morten Bjørn, Brian L. Lauridsen, Kim J. Schmock and in particular Kristian Nørgaard (CAPRES A/S) for help and assistance with software related challenges; Lise Midjord, Lior Shiv, and Rasmus Hansen (CAPRES A/S) for their effort to supply probes; Mette S. Balslev, Hans Henrik Jankjær, Ane Jensen, Mihalis Kampanis, Chaker Khalfaoui, Rong Lin and Thomas Meelby (CAPRES A/S) for generously sharing their knowledge and experience on micro probe technology. Finally, I would like to thank Christian Markvardsen (CAPRES A/S) for his dedication to innovative thinking and his encouragement and support through stimulating discussions.

Daniel Kjær

Kgs. Lyngby, May 26th 2015

Table of Contents

List of Symbols	11
List of Acronyms	13
1 Introduction.....	15
1.1 Magnetic tunnel junctions	16
1.1.1 Read heads	16
1.1.2 MRAM.....	18
1.2 MTJ metrology	20
1.2.1 CIPT	20
1.3 Motivation	22
1.4 Outline.....	23
2 Theory.....	25
2.1 Four-point resistance (single sheet).....	25
2.1.1 Position errors (single sheet).....	26
2.1.2 Position error correction (single sheet)	29
2.1.3 Electrical noise (single sheet)	31
2.2 CIPT (MTJ)	32
2.2.1 Position errors (MTJ)	36
2.2.2 Position error correction (MTJ)	39
2.2.3 Tunnel barrier conductance.....	41
3 Experimental.....	43
3.1 Micro 12-point probe.....	43
3.2 Experimental setup	44
3.3 Data treatment	47
3.4 Samples	47
4 Static field CIPT method	49
4.1 Sample uniformity	49
4.2 Switching field CIPT vs. static field CIPT.....	54
4.3 Detached magnet concept.....	55
4.4 Summary	56

5	Characterization of position errors and electrical noise	59
5.1	Experimental	59
5.2	Results and discussion.....	60
5.3	Evaluation of alternative probe design.....	66
5.4	Summary	67
6	Enhanced precision for CIPT measurements.....	69
6.1	Experimental	69
6.2	Results and discussion.....	69
6.2.1	Static position errors	70
6.2.2	Dynamic position errors.....	72
6.2.3	Electrical noise	76
6.2.4	Combined errors.....	77
6.2.5	Increased dynamic range.....	79
6.2.6	Measurements and position errors	83
6.2.7	Enhanced measurement precision.....	85
6.3	Equidistant probe design	88
6.4	Summary	89
7	Outlook	91
7.1	CIPT measurements on small test pads	91
7.2	Direct characterization of MTJ devices using a microscopic multi-point probe	93
8	Conclusion	97
	Bibliography	99
	List of papers	107
	Paper I	109
	Paper II	117
	Paper III	127
	Paper IV	135
	Paper V	141

List of Symbols

A, B, C	Four-point configurations A, B and C
A', B', C'	Inverted four-point configurations A', B' and C'
B	Magnetic flux density
d	Tunnel barrier thickness
g	Conductance per area
I_-	Current drain
I_+	Current source
K_0	Modified Bessel function of second kind and order zero
K_1	Modified Bessel function of second kind and order one
k_B	Boltzmann's constant
R	Resistance
RA	Resistance area product
R_{2p}	Two-point resistance
R_b	Sheet resistance of MTJ bottom electrode
$R_{ }$	Parallel resistance of MTJ top and bottom layers
R_p	Pseudo four-point resistance
R_S	Sheet resistance
R_t	Sheet resistance of MTJ top electrode
R_u	First order position corrected four-point resistance (BC-configurations)
R_v	First order position corrected four-point resistance (AC-configurations)
R_w	First order position corrected four-point resistance (AB-configurations)
s	Electrode spacing
T	Temperature T Tunneling probability
t	Time
TMR	Tunnel magnetoresistance
V	Voltage
V_n	Electrical noise
w	Width

α	Geometrical coefficient (A-configuration, single sheet)
α^*	Geometrical coefficient (A-configuration, MTJ)
α_ℓ	Area fraction
β	Geometrical coefficient (B-configuration, single sheet)
β^*	Geometrical coefficient (B-configuration, MTJ)
γ_w	Geometric pre-factor for first order position correction (AB-configurations)
γ_v	Geometric pre-factor for first order position correction (AB-configurations)
γ_u	Geometric pre-factor for first order position correction (AB-configurations)
Δf	Frequency bandwidth
ζ	Geometrical coefficient (C-configuration, single sheet)
ζ^*	Geometrical coefficient (C-configuration, MTJ)
λ	Transfer length for MTJ
σ	Standard deviation
σ^{rel}	Relative standard deviation
σ_x	Standard deviation on static, in-line electrode position error
σ_x^{dyn}	Standard deviation on dynamic, in-line electrode position error
σ_y	Standard deviation on static, off-line electrode position error
σ_y^{dyn}	Standard deviation on dynamic, off-line electrode position error
χ	Geometrical coefficient (MTJ)
Φ	Electrostatic potential
Φ_B	Tunnel barrier height

List of Acronyms

AFM	Atomic force microscopy
CAFM	Conductive AFM
dcw	First order approximation method (based on vdp)
DRAM	Dynamic random access memory
FFU	Fan filter unit
GMR	Giant magnetoresistance
HDD	Hard disk drive
IT	Information technology
M12PP	Micro twelve-point probe
M4PP	Micro four-point probe
MC	Monte Carlo (Monte Carlo simulations)
MEMS	Micro-electro-mechanical systems
MRAM	Magnetoresistive random access memory
MTJ	Magnetic tunnel junction
RIE	Reactive ion etch
SRAM	Static random access memory
STT	Spin transfer torque
vdp	van der Pauw method
VSM	Vibrating sample magnetometry

Chapter 1

1 Introduction

In 1965 Gordon E. Moore, co-founder of the Intel Corporation and Fairchild Semiconductor, stated in an article in the Electronics magazine [1], [2] that “*The complexity for minimum component cost has increased at a rate of roughly a factor of two per year. Certainly over the short term this rate can be expected to continue, if not to increase. Over the longer term, the rate of increase is a bit more uncertain, although there is no reason to believe it will not remain nearly constant for at least 10 years.*” This forecast has since become known as Moore’s Law [3] and turned out to hold true for the past five decades (see Fig. 1.1) [4]. Acting as a driver for the semiconductor industry it reflects the advances that have been made within information technology (IT) and shaped society of today for which electronic data processing and data storage is of fundamental importance.

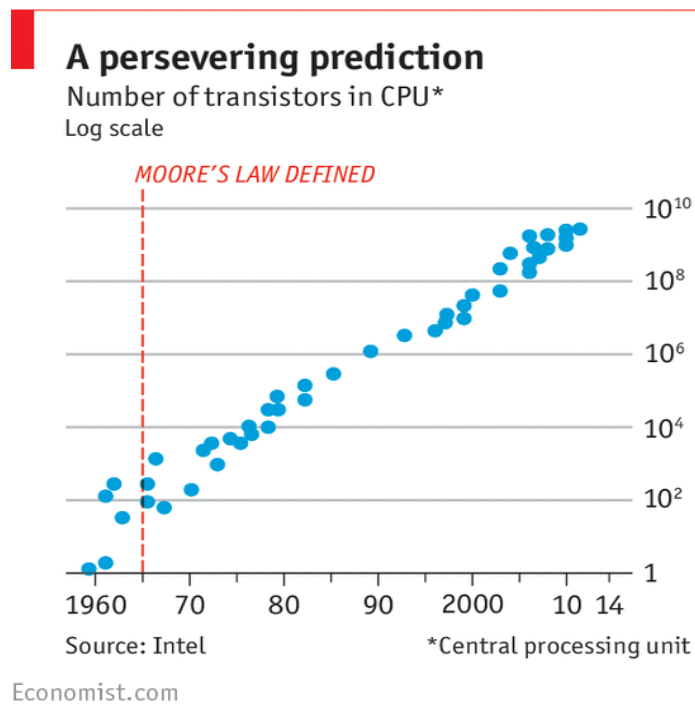


Fig. 1.1: Number of transistors in processors. In line with Moore's Law the number has doubled approximately every two years. Source: [5].

Whether or not the technological development can keep up with Moore’s Law in decades to come may be questioned [6] but it should be safe to assume that the industry will come up with new and more advanced solutions as it strives to meet the challenge. One place to look for solutions would be within the field of spintronics, which covers electronic devices based on spin-dependent electron transport [7]–[9]. One such device, the so-called magnetic tunnel junction (MTJ) [10], [11], can already be found

in modern hard disk drives (HDDs) [12]–[16] and memory units known as magnetoresistive random access memory (MRAM) [12], [17]–[22], and has attracted a lot of attention as a promising candidate also for future main stream memory applications including possible replacement of dynamic and static random access memory (DRAM and SRAM) [12], [17], [23].

1.1 Magnetic tunnel junctions

The basic MTJ (see Fig. 1.2a) is a three layer structure: Two ferromagnetic electrodes are separated by a thin (~1 nm), insulating barrier, typically AlO_x or MgO [12], which is thin enough for electrons to tunnel through, when a bias voltage is applied [24]–[27]. The orientation of the magnetic moment of the two ferromagnetic electrodes surrounding the barrier can be changed by the application of an external magnetic field. Typically one of the electrodes is pinned by an adjacent antiferromagnetic layer, which increases the magnetic field (switching field) required for a shift in magnetic orientation as compared to that of its unpinned counterpart, and thus allows the magnetic moments of the two layers to be either parallel or anti-parallel to each other. The two electrode layers are denoted the fixed layer and the free layer respectively.

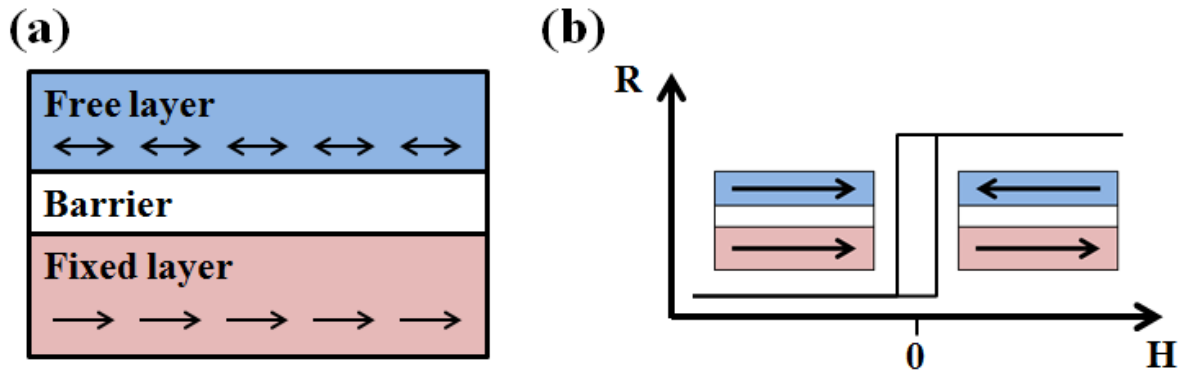


Fig. 1.2: (a) Basic MTJ structure composed of two ferromagnetic layers with free and fixed magnetization separated by an insulating tunnel barrier. (b) Hysteresis loop showing the resistance change as a function of applied magnetic field.

Due to the spin polarizing effect of the ferromagnetic layers the probability of electrons tunneling through the barrier is higher in the parallel state as compared to the anti-parallel state. It follows that the resistance across the barrier is lowest in the parallel state and the observed relative increase in resistance as the magnetic orientation is changed to the anti-parallel state is the tunnel magnetoresistance (TMR) (see Fig. 1.2b). The overall resistance across the MTJ barrier is characterized by the resistance area product (RA) or simply the specific contact resistance. Thus the TMR can be defined as: $\text{TMR} = (\text{RA}_{\text{high}} - \text{RA}_{\text{low}}) / \text{RA}_{\text{low}}$, where RA_{low} and RA_{high} refers to the resistance area product of the MTJ in the parallel and anti-parallel states, respectively [28]. In general the reported RA value of an MTJ is that of the low resistance mode i.e. RA_{low} .

1.1.1 Read heads

In conventional HDDs (see Fig. 1.3) data are stored by controlling the magnetization of magnetic grains distributed in a thin layer on the surface of a spinning disk. A bit of data is represented by a

cluster of magnetic grains with the same magnetization. Write and read heads are placed at the tip of an actuator arm, which provides random access to any location on the rotating disk. Data are read using a magnetic sensor to detect the fringing fields at the transitions between individual bits [8], where changes in the magnetic field lead to changes in the electrical resistance of the sensor.

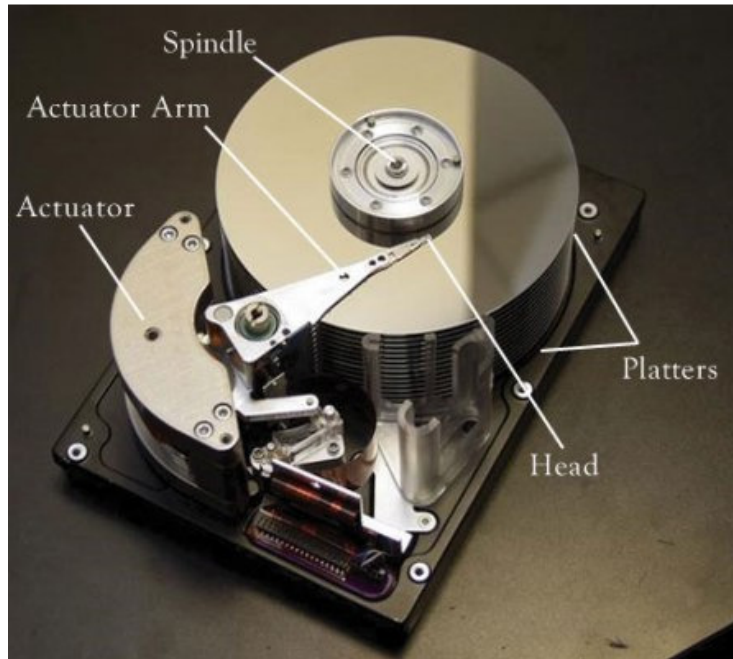


Fig. 1.3: HDD with several disks/platters available for data storage. The read and write heads are located at the tip of the actuator arm. Source: [29].

In earlier versions of HDDs the functionality of the read head was based on a phenomenon known as anisotropic magnetoresistance (AMR) [30], [31]. This is based on a bulk scattering effect, which will alter the resistance of the read head as a function of applied magnetic field (from the magnetic bit) and the direction of the current inside the sensor. The AMR effect is rather weak however, and will only change the resistance by a few percent, which effectively limits the obtainable storage density of this technology [8]. AMR was replaced by sensor elements utilizing giant magnetoresistance (GMR) [32], [33], which is a much stronger effect leading to relative resistance changes up to more than 100% [34]. GMR is caused by spin dependent elastic scattering at the interface between magnetic and non-magnetic metals [35], [36] and depends on the relative magnetization of the magnetic layers [37]. An implementation of GMR, which is particularly suitable for read heads, is the so-called spin valve [38]. This structure is almost identical to the MTJ described above with the important difference being a non-magnetic metal spacer instead of the isolating barrier of the MTJ. Electrons passing through the non-magnetic spacer from one ferromagnetic electrode the other will experience increased scattering if the magnetic moments of the two ferromagnetic layers are anti-parallel [37]. As is the case for MTJs pinning of one of the ferromagnetic layers introduces different switching fields for the two ferromagnetic layers and allows the spin valve to detect lower magnetic fields (smaller magnetic bit) as compared to a regular GMR sensor [38]. Surpassing all predecessors are however the read heads based on MTJs. TMR values of more than 600% have been reported for measurements at room temperature

[39]. It was first introduced in read heads in 2004 by Seagate [12] and has enabled the continued increase of memory density in HDDs over the past decade.

1.1.2 MRAM

Power consumption is one of the main focus points in the development of future memory solutions [40]. In particular for battery powered mobile devices such as phones, tablets and laptops the power consumption is a key parameter. This is one of the reasons why MRAM has attracted much attention: MRAM is a non-volatile memory and thus does not require continuous refreshing (or re-writing) as DRAM or power at all, like SRAM, in order to keep data stored [7], [12], [18], [20], [22], [41]. In MRAM every bit is represented by an individual MTJ, which state “0” or “1” depends on the magnetic configuration being parallel or anti-parallel and therefore data are stored in principle indefinitely also when the power is switched off [17]. This characteristic has lead to reflections on “instant-on” devices, which could be completely powered off and still keep recent data loaded to allow instant availability once the device is turned back on [42].

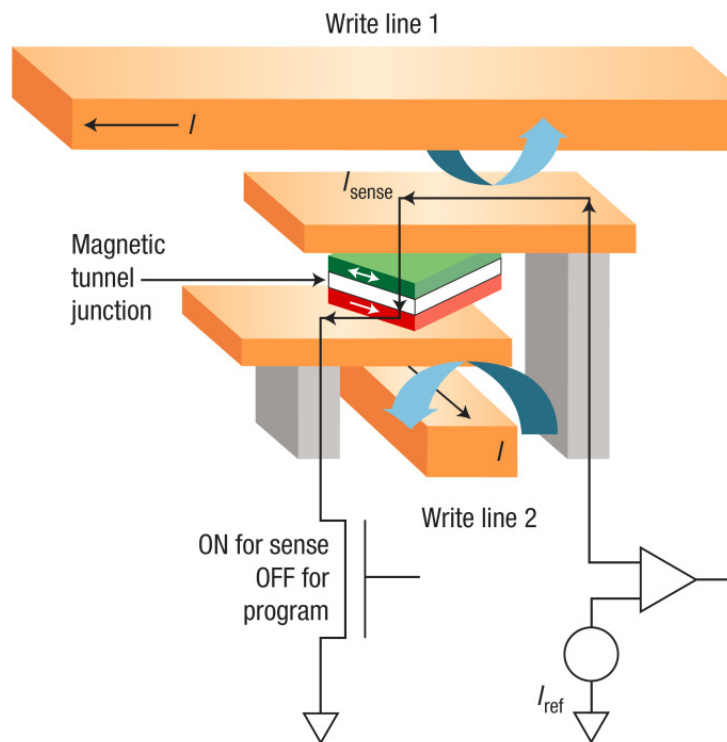


Fig. 1.4: Toggle MRAM cell. Source: [43].

In first generation of commercialized MRAM also known as toggle MRAM [20], [44], [45] the individual memory cells (see Fig. 1.4) are written by the application of an external magnetic field, generated by the current passing in write lines 1 and 2, respectively [18], [20], [22], [31], [43]. The magnetic field generated by a single write pulse in either of the write lines is not strong enough to change the magnetic state of a memory cell but at the intersection of write lines 1 and 2 the combined magnetic fields generated by a sequence of current pulses acts together to set the magnetic state [20],

[44], [45]. In this way only the cell at the intersection is written and other cells in the circuit are left unchanged. A major drawback of toggle MRAM is the relatively high current needed to write a bit, which increases for decreasing cell size and thus reduces scalability [41], [44], [45].

Second generation MRAM (see Fig. 1.5) utilizes a writing principle known as spin transfer torque (STT) [46], [47]. The write current is passed directly through the cell and the spin polarizing effect of the electrodes surrounding the barrier is used to switch the magnetic state of the cell.

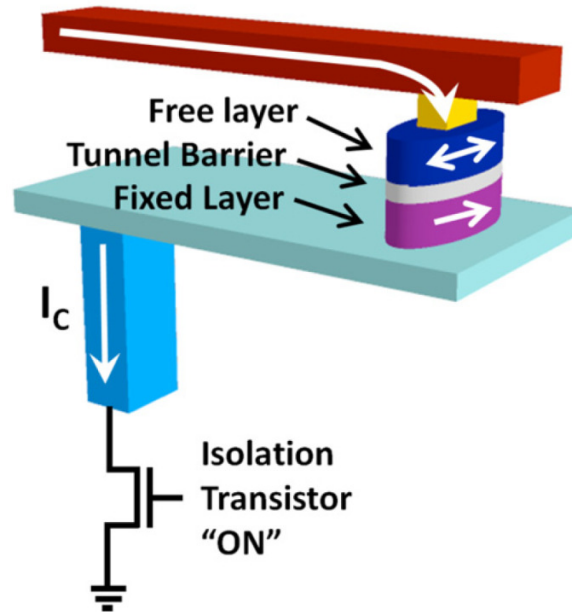


Fig. 1.5: STT MRAM cell. Source: [41].

Fig. 1.6 shows the working principle of spin transfer torque. The transverse component of the spin angular momentum is absorbed and transmitted to the total spin of the layer and thus exerts a torque on the magnetization of the layer. When the current exceeds a threshold the torque will switch the magnetization of the free layer. Depending on the direction of the electron flow parallel or anti-parallel magnetization is favored as the magnetization of the free layer is affected by transmitted or reflected electrons, respectively.

STT MRAM provides excellent scalability due to its simple design and low write power, which decreases for decreasing cell size. Since the spin polarized current is generated only in the cell to be written, while other cells are left undisturbed, high writing speed as well as multibit writing can be achieved.

Due to the many advantages over competing technologies, some of them mentioned here, MRAM is believed to have the potential of becoming a truly universal memory solution dominant within all fields of memory application [12], [17].

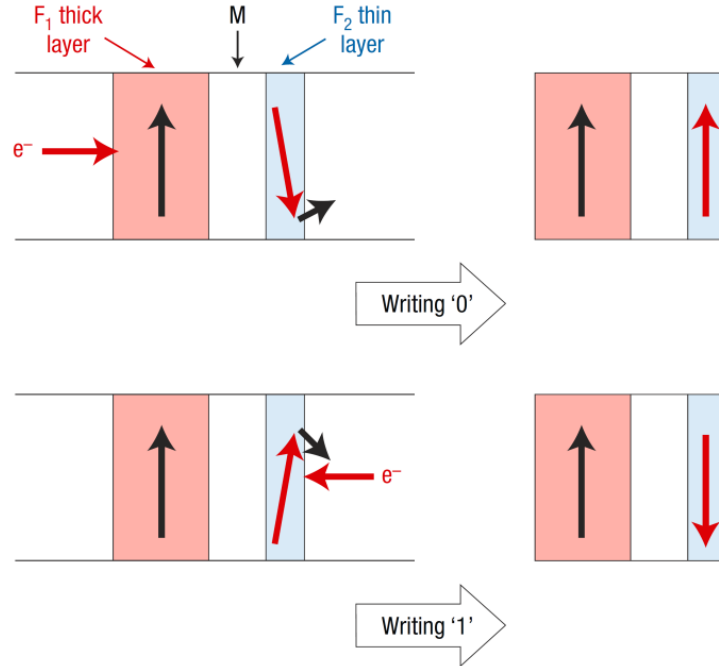


Fig. 1.6: Spin torque transfer. Source: [31].

1.2 MTJ metrology

Metrology is of crucial importance in the development of new materials, devices and fabrication techniques as well as in production optimization and process monitoring. Fabrication of MTJs relies on full-wafer deposition of ultra-thin layers (on the order of nm) of material and subsequent processing, including annealing in an applied magnetic field and device patterning. The ability to successfully develop and fabricate MTJ devices is strongly tied to the understanding and control of these processes and hence a number of metrology techniques must be applied. Among the important metrology for characterization of MTJs we find Kerr magnetometry, vibrating sample magnetometry (VSM), conductive AFM (CAFM) and current in-plane tunneling (CIPT). Each of these measurement techniques provide valuable insight into different properties of the MTJ at blanket film level as well as after patterning has taken place [48].

1.2.1 CIPT

For the past decade CIPT has been the standard method to evaluate RA and TMR of non-patterned MTJ stacks. In this method a series of four-point resistance measurements is carried out on the surface of an MTJ, while the magnetization of the MTJ free layer and pinned layer is controlled by an external magnetic field and thus set to the parallel and anti-parallel state. In a four-point resistance measurement a fixed current is passed between two electrodes while measuring the resulting potential difference over another pair of electrodes. In this way the contact resistances between electrodes and sample can be neglected since practically no current flows through the voltage sensing electrodes. As illustrated in Fig. 1.7 the current flow in the MTJ depends on the electrode spacing and to accurately estimate the

properties of the MTJ, resistance measurements are carried out at varying electrode pitch typically in the range from $1.5\ \mu\text{m}$ to $20\ \mu\text{m}$. Data are then fitted to a theoretical model [28], [49] from which RA_{low} and RA_{high} (and thus TMR) can be extracted.

For small electrode spacing the current will flow primarily in the top-layer of the MTJ since the area available for tunneling is small (scales with electrode spacing) and therefore leads to a high barrier resistance compared to the sheet resistance of the top electrode. At relatively large electrode pitch the barrier resistance is negligible and allows the current to spread out over top and bottom electrodes like the current flow in to two paralleled resistors. No measurements at either of these extremes provide the necessary information on RA . However, at some intermediate electrode spacing the barrier resistance is sufficiently low to allow some current to flow in the bottom electrode, while still contributing significantly to the measured resistance. It is this pitch-dependent behavior of the current flow that forms the basis for the CIPT method. The CIPT measurement technique is enabled by micro fabricated electrodes, the so-called micro four-point probes (M4PP) with up to twelve electrodes included on the same chip (M12PP), thus allowing four-point measurements at varying electrode pitch by combining different subsets of four electrodes (see Fig. 1.8).

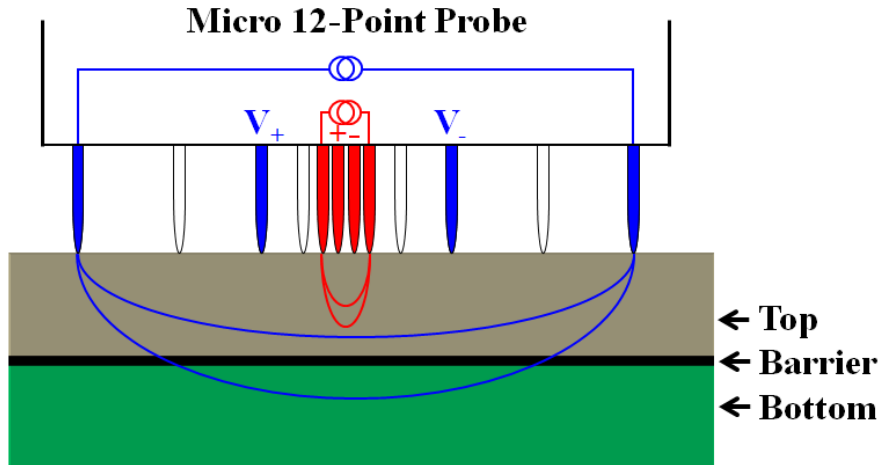


Fig. 1.7: Four-point measurement on an MTJ. At small electrode pitch the current is confined to the top electrode. At larger electrode pitch the current will flow in both electrode layers. By utilizing a micro 12-point probe the electrode spacing may be varied by selecting different subsets of four electrodes.

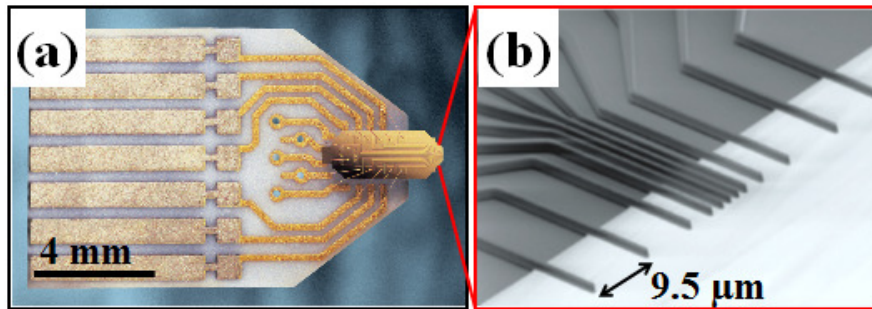


Fig. 1.8: Micro 12-point probe with electrode spacing from $1.5\ \mu\text{m}$ to $18.5\ \mu\text{m}$. (a) Probe chip mounted and wire bonded to a ceramic substrate for interfacing with measurement equipment [50]. (b) Scanning electron micrograph showing the cantilever electrodes.

1.3 Motivation

The CIPT method was commercialized in a metrology tool (see Fig. 1.9) by CAPRES A/S [50] in 2004 and has since been employed as an increasingly important MTJ metrology at leading semiconductor and magnetic storage fabrication facilities and it is today used in industry and research worldwide.



Fig. 1.9: CAPRES CIPTech-M300. Source: [50].

The method reduces the turnaround time in tunnel junction development due to the ability of measuring on non-patterned MTJ stacks. However, with a measurement time of 1-2 minutes per measurement, the technique is commonly used just for research and development of novel MTJ stacks and not for full wafer analysis, which would otherwise provide valuable information with respect to uniformity, e.g. for tool optimization. The precision of CIPT measurements is limited by electrode position errors, which increases for decreasing electrode pitch [51]. This is a challenge to the measurement method as such and may become even more so in the future, when the cell size of MRAM is scaled down to increase memory density. Lower RA values may be pursued in order to reduce the overall cell resistance, and since in general the relevant electrode spacing for CIPT measurements scales with the RA value of the MTJ, measurement precision at small electrode spacing becomes more important. As the industry moves towards volume production of MRAM and starts focusing on thin film homogeneity and other performance related factors, the need for suitable metrology is increasing. In order for the CIPT method to meet the future requirements for MTJ based products, improvements to measurement speed, dynamic range, precision, reliability and cost are all urgent challenges.

The fundamental goal of this project is to provide cheaper, faster and more precise metrology for MTJs.

1.4 Outline

Here follows a brief overview of the content of the thesis:

- Chapter 2 presents the theoretical background for four-point measurements on single sheet thin film samples as well as an introduction to position error correction for this sample type. Hereafter follows a presentation of the CIPT model and description of electrode position errors and position error correction for measurements on MTJs.
- Chapter 3 describes the experimental setup used for the work presented in this thesis. A detailed description of the M12PP is followed by a general introduction to the CIPT measurement equipment and the standard data treatment routines.
- Chapter 4 presents a new CIPT measurement strategy offering reduced measurement time. This chapter also includes a description of an alternative magnet concept, which could reduce the general complexity of the CIPT metrology tool while increasing its dynamic range.
- Chapter 5 presents a study of position errors and electrical noise for measurements on single sheet thin film samples. Preliminary evaluation of an alternative probe design is demonstrated based on the proposed strategy.
- Chapter 6 includes a comparative study of the effectiveness of position error correction algorithms based on Monte Carlo simulations. Actual four-point resistance measurements are compared to simulated results. An alternative probe design strategy is proposed as a means to enhance the CIPT measurement precision and evaluated based on analytical calculations.
- Chapter 7 presents an outlook including a description of a modified CIPT-model developed for measurements on small test pads. A new measurement concept aimed at characterization of individual MTJ devices is also included.
- Chapter 8 presents the conclusions of the thesis.

Chapter 2

2 Theory

In this chapter relevant theory is presented. First the simple case of four-point probe sheet resistance measurements on samples with a thin, electrically conductive, top layer (single sheet sample) is described together with a presentation of the different electrode configurations. Hereafter follows a review of electrode position errors and algorithms designed to reduce the influence these errors. The influence of electrical noise is also described before turning the focus to CIPT measurements on MTJs. The theoretical CIPT model is then presented together with a description of electrode position errors and position error correction for measurements on MTJs. Finally we introduce a simple model for conductance across the tunnel barrier of an MTJ.

This chapter is based on and repeats text and figures from papers I and II.

2.1 Four-point resistance (single sheet)

The purpose of a four-point probe measurement on a thin film is usually to determine the sheet resistance, R_s , of the film. The generic measurement is carried out by passing current, I_{ij} , through two point-like electrode contacts, (i, j) , to the sample and measure the voltage, V_{kl} , across two other point-like electrode contacts, (k, l) . For a uniform thin film sample the expected four-point resistance, $R_{kl,ij}$, is [52]

$$R_{kl,ij} = \frac{V_{kl}}{I_{ij}} = \frac{R_s}{2\pi} \ln \frac{|\mathbf{r}_l - \mathbf{r}_i| |\mathbf{r}_k - \mathbf{r}_j|}{|\mathbf{r}_k - \mathbf{r}_i| |\mathbf{r}_l - \mathbf{r}_j|}, \quad (1)$$

where \mathbf{r}_n is the in-plane position vector for the contacts, $n, m \in [i, j, k, l]$. It follows that the sheet resistance can be calculated from a measured value of $R_{kl,ij}$ by solving Eq. 1 for R_s if the four inter-electrode distances, $|\mathbf{r}_n - \mathbf{r}_m|$, are known accurately. In most practical implementations the electrodes are arranged on a single line, a collinear probe, as illustrated in Fig. 2.1, where the intended distances between neighboring contact points are s_1 , s_2 and s_3 .

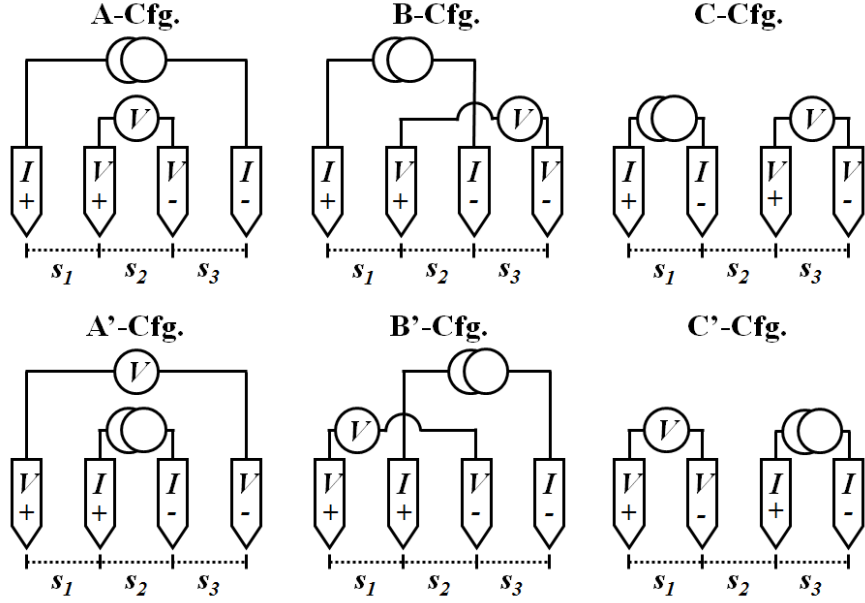


Fig. 2.1: Collinear four-point probes and the independent configurations, A, B and C, and their inverted (dual) versions, A', B' and C'. The distances between neighboring electrodes are denoted s_1 , s_2 and s_3 . Reproduced from paper II.

Four-point probe measurements with the collinear probe can be arranged in several configurations, usually denoted A, B and C and their inverted versions A', B' and C' [53] (see Fig. 2.1). Of the resistances R_A , R_B and R_C , measured in configurations A, B and C, only two are independent since $R_C = R_A - R_B$ [54]. Equivalent dependence applies to resistances measured in the inverted configurations and in the absence of a magnetic field, $R_{A'} = R_A$, $R_{B'} = R_B$ and $R_{C'} = R_C$ due to reciprocity [55], [56]. For the collinear four-point probe the expected measured resistances according to Eq. 1 are

$$R_A = \frac{R_S}{2\pi} \ln \frac{|\mathbf{r}_3 - \mathbf{r}_1| |\mathbf{r}_2 - \mathbf{r}_4|}{|\mathbf{r}_2 - \mathbf{r}_1| |\mathbf{r}_3 - \mathbf{r}_4|} = \frac{R_S}{2\pi} \ln \frac{s_1 + s_2}{s_1} \frac{s_2 + s_3}{s_3} \quad (2)$$

$$R_B = \frac{R_S}{2\pi} \ln \frac{|\mathbf{r}_4 - \mathbf{r}_1| |\mathbf{r}_2 - \mathbf{r}_3|}{|\mathbf{r}_2 - \mathbf{r}_1| |\mathbf{r}_4 - \mathbf{r}_3|} = \frac{R_S}{2\pi} \ln \frac{s_1 + s_2 + s_3}{s_1} \frac{s_2}{s_3} \quad (3)$$

$$R_C = \frac{R_S}{2\pi} \ln \frac{|\mathbf{r}_3 - \mathbf{r}_1| |\mathbf{r}_4 - \mathbf{r}_2|}{|\mathbf{r}_4 - \mathbf{r}_1| |\mathbf{r}_3 - \mathbf{r}_2|} = \frac{R_S}{2\pi} \ln \frac{s_1 + s_2}{s_1 + s_2 + s_3} \frac{s_2 + s_3}{s_2}. \quad (4)$$

2.1.1 Position errors (single sheet)

When the electrode spacings, s_1 , s_2 and s_3 , become small, the actual spacings may differ significantly from their nominal value such that e.g. $|\mathbf{r}_2 - \mathbf{r}_1| \neq s_1$ and then resistances calculated from Eqs. 2 and 3 will be inaccurate due to the electrode spacing error; this is what we define as general position errors (see Fig. 2.2).

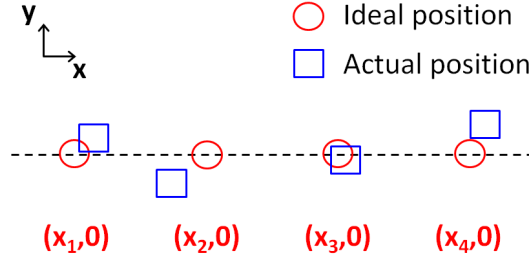


Fig. 2.2: Sketch illustrating position errors for a four-point probe. Due to in-line and off-line position errors the actual positions of the electrodes deviate from their ideal, intended positions $((x_1,0), (x_2,0), (x_3,0)$ and $(x_4,0))$.

These position errors arise for a number of different physical reasons and may have both in-line and off-line components:

Probe geometry errors. The real probe may be fabricated with different electrode spacings than intended.

Static position errors. Each probe-sample engage may result in slightly different contact spacing, e.g. induced by plastic deformation of the electrode tips or due to the surface topology of the sample.

Dynamic position errors. While the probe is engaged on the sample, the contact points may move slightly on the sample surface, e.g. due to vibrations.

As a result of these errors the position, \mathbf{r}_n , of electrode $n \in [1, 2, 3, 4]$ may be displaced from the ideal position, $\mathbf{r}_{n0} = (x_{n0}, 0)$, according to

$$\mathbf{r}_n = (x_{n0} + \Delta x_{n0} + \Delta x_n + \delta x_n, \Delta y_{n0} + \Delta y_n + \delta y_n) = (x_{n0} + \Delta_{nx}, \Delta_{ny}), \quad (5)$$

where the ideal y-position is taken as $y_0 = 0$ without loss of generality; Δx_{n0} and Δy_{n0} are probe geometry errors, Δx_n and Δy_n are static position errors while δx_n and δy_n are dynamic position errors; finally Δ_{nx} and Δ_{ny} are total in-line and off-line errors, respectively. As a result the probe spacing, $|\mathbf{r}_2 - \mathbf{r}_1|$, becomes

$$\begin{aligned} |\mathbf{r}_2 - \mathbf{r}_1| &= \sqrt{(s_1 + \Delta_{2x} - \Delta_{1x})^2 + (\Delta_{2y} - \Delta_{1y})^2} \\ &= s_1 \sqrt{\left(1 + \frac{\Delta_{2x} - \Delta_{1x}}{s_1}\right)^2 + \left(\frac{\Delta_{2y} - \Delta_{1y}}{s_1}\right)^2} \\ &\approx s_1 \left(1 + \frac{\Delta_{2x} - \Delta_{1x}}{s_1} + \frac{1}{2} \left(\frac{\Delta_{2y} - \Delta_{1y}}{s_1}\right)^2\right), \end{aligned} \quad (6)$$

and similar expressions are valid for the other probe spacings involved in the measurements. It follows that in-line position errors affect four-point probe measurements to first order, while the effects of off-line position errors are of second order. Thus, off-line position errors may be neglected for small electrode position errors relative to the electrode spacing.

When the electrical measurement noise on the extracted four-point resistance is smaller than contributions from geometrically induced errors, we may evaluate the extent of these geometrical errors. We assume that all electrodes suffer from normal distributed static in-line position errors with the standard deviation σ_x and dynamic in-line position errors with the standard deviation σ_x^{dyn} . With these assumptions it has been shown [57] that the relative standard deviations, $\sigma_{R_A}^{\text{rel}}$, $\sigma_{R_B}^{\text{rel}}$ and $\sigma_{R_C}^{\text{rel}}$, on R_A , R_B and R_C , respectively, are

$$\sigma_{R_A}^{\text{rel}} = \frac{1}{R_A} \sqrt{\sum_{n=1}^4 \left(\frac{\partial R_A}{\partial x_n} \sigma_x \right)^2} = \alpha \frac{\sigma_x}{\langle s \rangle}, \quad (7)$$

$$\sigma_{R_B}^{\text{rel}} = \frac{1}{R_B} \sqrt{\sum_{n=1}^4 \left(\frac{\partial R_B}{\partial x_n} \sigma_x \right)^2} = \beta \frac{\sigma_x}{\langle s \rangle} \quad (8)$$

and

$$\sigma_{R_C}^{\text{rel}} = \frac{1}{R_C} \sqrt{\sum_{n=1}^4 \left(\frac{\partial R_C}{\partial x_n} \sigma_x \right)^2} = \zeta \frac{\sigma_x}{\langle s \rangle}, \quad (9)$$

where $\langle s \rangle = (s_1 + s_2 + s_3)/3$ is the mean electrode pitch. The geometrical coefficients, α , β and ζ , can be shown to be

$$\alpha = \frac{\frac{s_3 + s_2 + s_1}{3} \sqrt{\left(\frac{1}{s_1} - \frac{1}{s_2 + s_1} \right)^2 + \left(\frac{1}{s_1} + \frac{1}{s_2 + s_3} \right)^2 + \left(\frac{1}{s_2 + s_1} + \frac{1}{s_3} \right)^2 + \left(\frac{1}{s_3 + s_2} - \frac{1}{s_3} \right)^2}}{\ln \left(\frac{s_2 + s_1}{s_1} \frac{s_2 + s_3}{s_3} \right)}, \quad (10)$$

$$\beta = \frac{\frac{s_3 + s_2 + s_1}{3} \sqrt{\left(\frac{1}{s_1} - \frac{1}{s_3 + s_2 + s_1} \right)^2 + \left(\frac{1}{s_1} + \frac{1}{s_2} \right)^2 + \left(\frac{1}{s_2} + \frac{1}{s_3} \right)^2 + \left(\frac{1}{s_3 + s_2 + s_1} - \frac{1}{s_3} \right)^2}}{\ln \left(\frac{s_1 + s_2 + s_3}{s_1} \frac{s_2}{s_3} \right)} \quad (11)$$

and

$$\zeta = \frac{\frac{s_3 + s_2 + s_1}{3} \sqrt{\left(\frac{1}{s_1 + s_2 + s_3} - \frac{1}{s_1 + s_2} \right)^2 + \left(\frac{1}{s_2} - \frac{1}{s_2 + s_3} \right)^2 + \left(\frac{1}{s_2 + s_1} - \frac{1}{s_2} \right)^2 + \left(\frac{-1}{s_1 + s_2 + s_3} + \frac{1}{s_2 + s_3} \right)^2}}{\ln \left(\frac{(s_2 + s_1)}{(s_1 + s_2 + s_3)} \frac{(s_2 + s_3)}{(s_2)} \right)}. \quad (12)$$

In the case of equidistant electrodes ($s_n = s$) the geometrical coefficients become particularly simple

$$\sigma_{R_A}^{\text{rel}} = \frac{\sqrt{5}}{\ln 4} \frac{\sigma_x}{s} \cong 1.61 \times \frac{\sigma_x}{s} \quad (13)$$

$$\sigma_{R_B}^{\text{rel}} = \frac{4\sqrt{5}}{3 \ln 3} \frac{\sigma_x}{s} \cong 2.71 \times \frac{\sigma_x}{s} \quad (14)$$

$$\sigma_{R_C}^{\text{rel}} = \frac{\sqrt{5}}{3 \ln \frac{4}{3}} \frac{\sigma_x}{s} \approx 2.59 \times \frac{\sigma_x}{s}. \quad (15)$$

With these equations, static position errors may be evaluated from repeated measurements of R_A , R_B and R_C , where the probe is retracted from the sample and re-engaged between each recorded four-point measurement. Similarly, we can evaluate the dynamic in-line position errors from the variations of R_A , R_B or R_C during probe-sample engage. This gives similar expressions, i.e. $\sigma_{R_A}^{\text{rel, dyn}} = \alpha \sigma_x^{\text{dyn}} / \langle s \rangle$, $\sigma_{R_B}^{\text{rel, dyn}} = \beta \sigma_x^{\text{dyn}} / \langle s \rangle$ and $\sigma_{R_C}^{\text{rel, dyn}} = \zeta \sigma_x^{\text{dyn}} / \langle s \rangle$.

2.1.2 Position error correction (single sheet)

Rymaszewski has suggested a position correction algorithm [54] which eliminates the influence of in-line position errors for four-point measurements obtained using collinear electrodes. Based on the work by van der Pauw [58], he showed that the sheet resistance, R_s , must be related to R_A and R_B as follows:

$$\exp\left(\frac{2\pi R_A}{R_s}\right) - \exp\left(\frac{2\pi R_B}{R_s}\right) = 1. \quad (16)$$

Similar expressions are valid for R_A and R_C

$$\exp\left(-\frac{2\pi R_A}{R_s}\right) + \exp\left(-\frac{2\pi R_C}{R_s}\right) = 1 \quad (17)$$

or R_B and R_C

$$\exp\left(\frac{2\pi R_C}{R_s}\right) - \exp\left(-\frac{2\pi R_B}{R_s}\right) = 1. \quad (18)$$

From these expressions (without geometric parameters), the sheet resistance can be calculated accurately if the measured resistances are only affected by in-line static position errors and in-line geometry errors. We shall denote this position correction scheme the van der Pauw (vdp) method. However, this correction scheme will not correct for off-line position errors, and it will not correct for dynamic in-line position errors since the two resistance values to be combined (R_A and R_B , R_A and R_C or R_B and R_C) are not measured simultaneously. This can be understood by inserting Eq. 1 in Eqs. 16-18 to get the geometry requirement, which must be fulfilled in order for Eqs. 16-18 to be correct

$$\left(\frac{|\mathbf{r}_3 - \mathbf{r}_1| |\mathbf{r}_2 - \mathbf{r}_4|}{|\mathbf{r}_2 - \mathbf{r}_1| |\mathbf{r}_3 - \mathbf{r}_4|}\right)_A - \left(\frac{|\mathbf{r}_4 - \mathbf{r}_1| |\mathbf{r}_2 - \mathbf{r}_3|}{|\mathbf{r}_2 - \mathbf{r}_1| |\mathbf{r}_4 - \mathbf{r}_3|}\right)_B = 1 \quad (19)$$

$$\left(\frac{|\mathbf{r}_3 - \mathbf{r}_1| |\mathbf{r}_2 - \mathbf{r}_4|}{|\mathbf{r}_2 - \mathbf{r}_1| |\mathbf{r}_3 - \mathbf{r}_4|}\right)_A - \left(\frac{|\mathbf{r}_3 - \mathbf{r}_1| |\mathbf{r}_4 - \mathbf{r}_2|}{|\mathbf{r}_4 - \mathbf{r}_1| |\mathbf{r}_3 - \mathbf{r}_2|}\right)_C = 1 \quad (20)$$

$$\left(\frac{|\mathbf{r}_4 - \mathbf{r}_1| |\mathbf{r}_2 - \mathbf{r}_3|}{|\mathbf{r}_2 - \mathbf{r}_1| |\mathbf{r}_4 - \mathbf{r}_3|}\right)_B - \left(\frac{|\mathbf{r}_3 - \mathbf{r}_1| |\mathbf{r}_4 - \mathbf{r}_2|}{|\mathbf{r}_4 - \mathbf{r}_1| |\mathbf{r}_3 - \mathbf{r}_2|}\right)_C = 1, \quad (21)$$

where subscripts indicate geometry during the respective measurements. The geometry requirement is trivially fulfilled under static conditions if the electrode-sample contacts are in-line. Any off-line component in the geometry will violate this condition as will any dynamic in-line electrode displacement, and thus this scheme cannot correct such errors.

A position correction algorithm [59] proposed by D. C. Worledge uses a linear combination of R_A and R_B , i.e. $R_A - \gamma_w R_B$ where γ_w is a geometric pre-factor, to reduce the influence of position errors. With this method the sheet resistance estimate, R_w , is calculated from

$$R_w = \frac{2\pi(R_A - \gamma_w R_B)}{\ln\left(\frac{s_1 + s_2}{s_1} \frac{s_2 + s_3}{s_3}\right) - \gamma_w \ln\left(\frac{s_1 + s_2 + s_3}{s_1} \frac{s_2}{s_3}\right)} \quad (22)$$

with the geometric pre-factor, γ_w , defined as (the numerical value is valid for equidistant electrodes)

$$\gamma_w = \frac{(s_1 + s_2 + s_3)s_2}{(s_1 + s_2)(s_2 + s_3)} \approx \frac{3}{4}. \quad (23)$$

Note, different symbols were used in the equations than those originally used by D. C. Worledge. Since this method essentially is a first order approximation to the vdp method it is expected to correct the same errors, but only if they are sufficiently small such that higher order terms can be ignored.

Obviously, similar first order correction schemes based on R_A and R_C or R_B and R_C may be used, i.e. using $R_A + \gamma_v R_C$ the sheet resistance estimate, R_v , becomes

$$R_v = \frac{2\pi(R_A + \gamma_v R_C)}{\ln\left(\frac{s_1 + s_2}{s_1} \frac{s_2 + s_3}{s_3}\right) + \gamma_v \ln\left(\frac{s_1 + s_2}{s_1 + s_2 + s_3} \frac{s_2 + s_3}{s_2}\right)}, \quad (24)$$

with the pre-factor, γ_v , defined as (the numerical value is valid for equidistant electrodes)

$$\gamma_v = s_2 \frac{s_1 + s_2 + s_3}{s_1 s_3} \approx 3, \quad (25)$$

and using $R_B + \gamma_u R_C$ the sheet resistance estimate, R_u , becomes

$$R_u = \frac{2\pi(R_B + \gamma_u R_C)}{\ln\left(\frac{s_1 + s_2 + s_3}{s_1} \frac{s_2}{s_3}\right) + \gamma_u \ln\left(\frac{s_1 + s_2}{s_1 + s_2 + s_3} \frac{s_2 + s_3}{s_2}\right)} \quad (26)$$

with the pre-factor, γ_u , obtained from (the numerical value is valid for equidistant electrodes)

$$\gamma_u = \frac{(s_1 + s_2)(s_2 + s_3)}{s_1 s_3} \approx 4. \quad (27)$$

The position correction schemes presented above will eliminate the effect of in-line geometry and static position errors whereas the extracted sheet resistance will still be affected by dynamic in-line position errors. The analysis of the effect of dynamic in-line position errors is most easily carried out for the first order corrections; the results, however, will also be valid for the full vdp corrections if the dynamic in-line position errors are small enough. Since the dynamic position error on say R_A may be assumed to be uncorrelated to the dynamic position errors on R_B and R_C it can be deduced that the

relative standard deviation on the extracted position corrected sheet resistances based on R_A and R_B , R_A and R_C and R_B and R_C are

$$\sigma_{R_w}^{\text{rel, dyn}} = \frac{\sqrt{\alpha^2 + \left(\gamma_w \frac{R_B}{R_A} \beta\right)^2}}{1 - \gamma_w \frac{R_B}{R_A}} \frac{\sigma_x^{\text{dyn}}}{\langle s \rangle} = \frac{\sqrt{10}}{\ln 4 - \frac{3}{4} \ln 3} \frac{\sigma_x^{\text{dyn}}}{s} \approx 5.62 \times \frac{\sigma_x^{\text{dyn}}}{s}, \quad (28)$$

$$\sigma_{R_v}^{\text{rel, dyn}} = \frac{\sqrt{\alpha^2 + \left(\gamma_v \frac{R_C}{R_A} \zeta\right)^2}}{1 + \gamma_v \frac{R_C}{R_A}} \frac{\sigma_x^{\text{dyn}}}{\langle s \rangle} = \frac{\sqrt{10}}{\ln 4 + 3 \ln \frac{4}{3}} \frac{\sigma_x^{\text{dyn}}}{s} \approx 1.41 \times \frac{\sigma_x^{\text{dyn}}}{s} \quad (29)$$

and

$$\sigma_{R_u}^{\text{rel, dyn}} = \frac{\sqrt{\beta^2 + \left(\gamma_u \frac{R_C}{R_B} \zeta\right)^2}}{1 + \gamma_u \frac{R_C}{R_B}} \frac{\sigma_x^{\text{dyn}}}{\langle s \rangle} = \frac{\frac{4}{3} \sqrt{10}}{\ln 3 + 4 \ln \frac{4}{3}} \frac{\sigma_x^{\text{dyn}}}{s} \approx 1.87 \times \frac{\sigma_x^{\text{dyn}}}{s}, \quad (30)$$

where the numerical values are for equidistant electrodes.

2.1.3 Electrical noise (single sheet)

The electronic noise is assumed to be voltage noise with the standard deviation V_n (e.g. $V_n = 65\text{nV}$). It follows that the relative standard deviation on R_A , R_B and R_C due to electronic noise are

$$\sigma_{R_A}^{\text{rel}} = \frac{V_n}{IR_A} = \frac{R_S}{R_A} \frac{V_n}{IR_S} = \frac{2\pi}{\ln \frac{s_1+s_2}{s_1} \frac{s_2+s_3}{s_3}} \frac{V_n}{IR_S} \approx \frac{2\pi}{\ln 4} \frac{V_n}{IR_S}, \quad (31)$$

$$\sigma_{R_B}^{\text{rel}} = \frac{V_n}{IR_B} = \frac{R_S}{R_B} \frac{V_n}{IR_S} = \frac{2\pi}{\ln \frac{s_1+s_2+s_3}{s_1} \frac{s_2}{s_3}} \frac{V_n}{IR_S} \approx \frac{2\pi}{\ln 3} \frac{V_n}{IR_S} \quad (32)$$

and

$$\sigma_{R_C}^{\text{rel}} = \frac{V_n}{IR_C} = \frac{R_S}{R_C} \frac{V_n}{IR_S} = \frac{2\pi}{\ln \frac{s_1+s_2}{s_1+s_2+s_3} \frac{s_2+s_3}{s_2}} \frac{V_n}{IR_S} \approx \frac{2\pi}{\ln \frac{4}{3}} \frac{V_n}{IR_S}, \quad (33)$$

where the simplified expressions are true for equidistant probes ($s_1 = s_2 = s_3$).

Then the standard deviation on the position corrected sheet resistances becomes

$$\sigma_{R_w}^{\text{rel}} = \frac{\sqrt{1 + \gamma_w^2}}{1 - \gamma_w \frac{R_B}{R_A}} \left(\frac{V_n}{IR_A} \right) = \frac{10\pi}{4 \ln 4 - 3 \ln 3} \left(\frac{V_n}{IR_S} \right) \approx 13.97 \times \left(\frac{V_n}{IR_S} \right), \quad (34)$$

$$\sigma_{R_v}^{\text{rel}} = \frac{\sqrt{1 + \gamma_v^2}}{1 + \gamma_v \frac{R_C}{R_A}} \left(\frac{V_n}{IR_A} \right) = \frac{2\sqrt{10}\pi}{\ln 4 + 3 \ln \frac{4}{3}} \left(\frac{V_n}{IR_S} \right) \approx 8.83 \times \left(\frac{V_n}{IR_S} \right) \quad (35)$$

and

$$\sigma_{R_u}^{\text{rel}} = \frac{\sqrt{1 + \gamma_u^2}}{1 + \gamma_u \frac{R_C}{R_B}} \left(\frac{V_n}{IR_B} \right) = \frac{2\sqrt{17}\pi}{\ln 3 + 4 \ln \frac{4}{3}} \left(\frac{V_n}{IR_S} \right) \approx 11.52 \times \left(\frac{V_n}{IR_S} \right), \quad (36)$$

where the simplified expressions are true for equidistant probes ($s_1 = s_2 = s_3$).

As expected the effect of electronic noise decreases with increasing measurement current, it also decreases with increasing sample sheet resistance (assuming that the electronic noise is independent on sample sheet resistance; ultimately $V_n > \sqrt{4k_B T R_{2p} \Delta f}$ where R_{2p} is the two-point probe-sample resistance, Δf the measurement bandwidth, k_B Boltzmann's constant and T the absolute temperature).

The total standard deviation is obtained by adding the noise contributions on a power basis:

$$\sigma_{R_w}^{\text{rel}} = \sqrt{\left(5.62 \times \frac{\sigma_x^{\text{dyn}}}{s}\right)^2 + \left(13.97 \times \frac{V_n}{IR_s}\right)^2}, \quad (37)$$

$$\sigma_{R_v}^{\text{rel}} = \sqrt{\left(1.41 \times \frac{\sigma_x^{\text{dyn}}}{s}\right)^2 + \left(8.83 \times \frac{V_n}{IR_s}\right)^2}, \quad (38)$$

$$\sigma_{R_u}^{\text{rel}} = \sqrt{\left(1.87 \times \frac{\sigma_x^{\text{dyn}}}{s}\right)^2 + \left(11.52 \times \frac{V_n}{IR_s}\right)^2}. \quad (39)$$

Both with respect to electronic noise and in particular dynamic position error the AC correction is favorable, and BC is better than AB, which is the inferior correction scheme with respect to the resulting standard deviation.

2.2 CIPT (MTJ)

For several decades, specific contact resistance measurements have been done using a variety of so-called transmission line methods [60]–[63]. The use of collinear four-point probes for specific contact resistance measurements was pioneered by Severin et al. [64] in 1971 and in 1991 extended in a hitherto unnoticed paper by Vu et al. [49] for the specific case of two parallel coupled sheets of finite conductance. They both solved for the electrical potential distribution on the surface of a two-layer structure with a specific contact resistance at the interface, and showed how the transfer length could be extracted from four-point probe configuration switching [64] and variable electrode pitch [49]. Vu et al. also applied the measurement technique to an Al/RuO₂/Al stack [65]. Essentially the same technique, Current In-Plane Tunneling [28], is now the standard method for evaluating RA and TMR of MTJs.

Fig. 2.3 shows an electrical model describing the current flow in a small sample volume of width dr placed a radial distance, r , away from the current inlet. At some small electrode pitch, s , the current will flow primarily in the top layer, while at some large electrode pitch the barrier resistance will be negligible and the current flow will be limited only by the parallel resistance of the top and bottom layer. The latter is the case for probe pitches $s \gg \lambda$, where $\lambda = [RA/(R_t + R_b)]^{1/2}$ is the transfer length for a given sample [28], [49], [65] and R_t and R_b characterize the sheet resistance of the top and bottom layers, respectively.

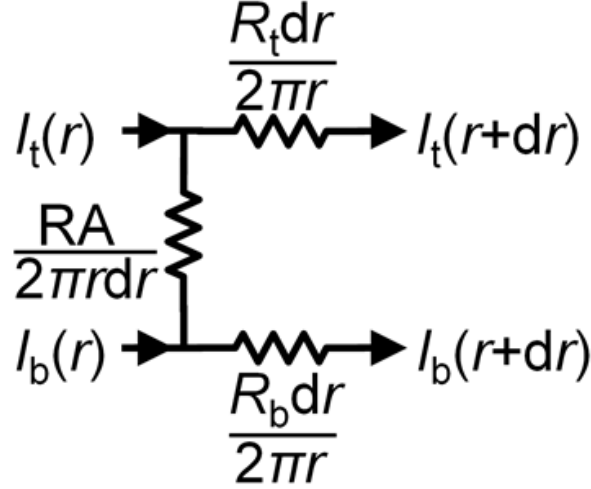


Fig. 2.3: Electrical model describing the current flow in a small sample volume of width dr placed a radial distance, r , away from the current inlet. Reproduced from paper I.

The electrostatic potential of the sample surface a distance, $\mathbf{r}-\mathbf{r}_0$, away from a single current source is given by [49]:

$$\Phi(\mathbf{r}, \mathbf{r}_0) = \frac{IR_t R_b}{2\pi(R_t + R_b)} \left[\frac{R_t}{R_b} K_0 \left(\frac{|\mathbf{r} - \mathbf{r}_0|}{\lambda} \right) - \ln(|\mathbf{r} - \mathbf{r}_0|) \right], \quad (40)$$

where I is the injected current and K_0 is the modified Bessel function of the second kind of order zero. In a four-point probe setup two current electrodes positioned at \mathbf{r}_+ and \mathbf{r}_- can be considered using the superposition principle to evaluate the potential at position \mathbf{r} . The four-point resistance can be defined as $R=V/I$, where V is the voltage difference between the two potential electrodes and I is the current passed between the two current electrodes.

For a standard four-point probe with electrodes at positions \mathbf{r}_1 , \mathbf{r}_2 , \mathbf{r}_3 and \mathbf{r}_4 the measured potential difference can be evaluated as:

$$V_A = \Phi(\mathbf{r}_2, \mathbf{r}_1) - \Phi(\mathbf{r}_2, \mathbf{r}_4) - \Phi(\mathbf{r}_3, \mathbf{r}_1) + \Phi(\mathbf{r}_3, \mathbf{r}_4), \quad (41)$$

$$V_B = \Phi(\mathbf{r}_2, \mathbf{r}_1) - \Phi(\mathbf{r}_2, \mathbf{r}_3) - \Phi(\mathbf{r}_4, \mathbf{r}_1) + \Phi(\mathbf{r}_4, \mathbf{r}_3) \quad (42)$$

and

$$V_C = \Phi(\mathbf{r}_4, \mathbf{r}_1) - \Phi(\mathbf{r}_4, \mathbf{r}_2) - \Phi(\mathbf{r}_3, \mathbf{r}_1) + \Phi(\mathbf{r}_3, \mathbf{r}_2), \quad (43)$$

for A-, B- and C-configurations, respectively [66].

Inserting Eq. 40 into Eqs. 41-43 gives us the following expressions for the four-point resistances, R_A , R_B and R_C , measured with a collinear four-point probe with expected electrode distances s_1 , s_2 and s_3 (see Fig. 2.1):

$$R_A = \frac{R_t R_b}{R_t + R_b} \frac{1}{2\pi} \left(\frac{R_t}{R_b} \left(K_0 \left(\frac{s_1}{\lambda} \right) - K_0 \left(\frac{s_1 + s_2}{\lambda} \right) - K_0 \left(\frac{s_2 + s_3}{\lambda} \right) + K_0 \left(\frac{s_3}{\lambda} \right) \right) + \ln \left(\frac{(s_1 + s_2)(s_2 - s_3)}{s_1 s_3} \right) \right), \quad (44)$$

$$R_B = \frac{R_t R_b}{R_t + R_b} \frac{1}{2\pi} \left(\frac{R_t}{R_b} \left(K_0 \left(\frac{s_1}{\lambda} \right) - K_0 \left(\frac{s_1 + s_2 + s_3}{\lambda} \right) - K_0 \left(\frac{s_2}{\lambda} \right) + K_0 \left(\frac{s_3}{\lambda} \right) \right) + \ln \left(\frac{(s_1 + s_2 + s_3)s_3}{s_1 s_3} \right) \right) \quad (45)$$

and

$$R_C = \frac{R_t R_b}{R_t + R_b} \frac{1}{2\pi} \left(\frac{R_t}{R_b} \left(K_0 \left(\frac{s_1 + s_2 + s_3}{\lambda} \right) - K_0 \left(\frac{s_1 + s_2}{\lambda} \right) - K_0 \left(\frac{s_2 + s_3}{\lambda} \right) + K_0 \left(\frac{s_2}{\lambda} \right) \right) + \ln \left(\frac{(s_1 + s_2)(s_2 + s_3)}{(s_1 + s_2 + s_3)(s_2)} \right) \right). \quad (46)$$

To allow easy comparison on the same scale the measured four-point resistance of an MTJ can be expressed in terms of an apparent, non-physical, sheet resistance, R_s , by combining Eq. 1 and Eqs. 44-46. In Fig. 2.4 the apparent sheet resistance is shown as a function of electrode spacing (normalized to λ), for an equally spaced four-point probe and for A-, B- and C-configurations, respectively. Here $R_t = 10 \text{ } \Omega/\square$ and $R_b = 1 \text{ } \Omega/\square$ has been used and it is seen from the plot that for $s \ll \lambda$ essentially R_t is measured, while for $s \gg \lambda$ the parallel resistance of R_t and R_b , $R_{\parallel} = R_t R_b / (R_t + R_b)$, is measured. This reflects the fact that for probe pitches in either of these extremes ($s \ll \lambda$ or $s \gg \lambda$), measurements on an MTJ sample are essentially identical to measurements on a single sheet sample. Similar plots are presented in Fig. 2.5 and Fig. 2.6 for R_t/R_b -ratios of 1 and 0.1, respectively. Comparing the three plots illustrates the how the current flow, for all values of s/λ , will approach that of a single sheet sample in the extreme cases of $R_t/R_b \rightarrow 0$, for which the current flow would be constricted to the top electrode.

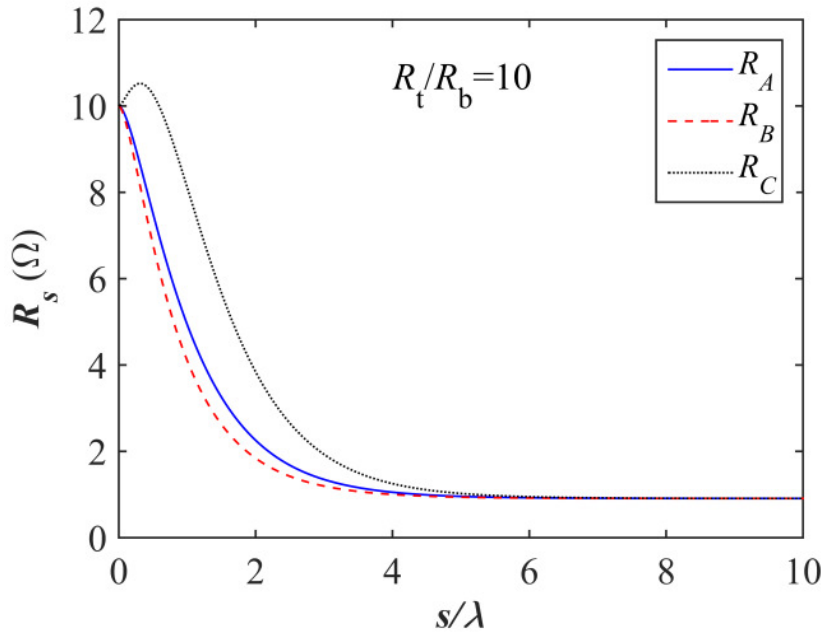


Fig. 2.4: Apparent sheet resistance, R_s , as a function of electrode spacing, s (normalized to λ), for an equally spaced, collinear four-point probe and A-, B- and C-configurations, respectively. $R_t = 10 \text{ } \Omega/\square$ and $R_b = 1 \text{ } \Omega/\square$.

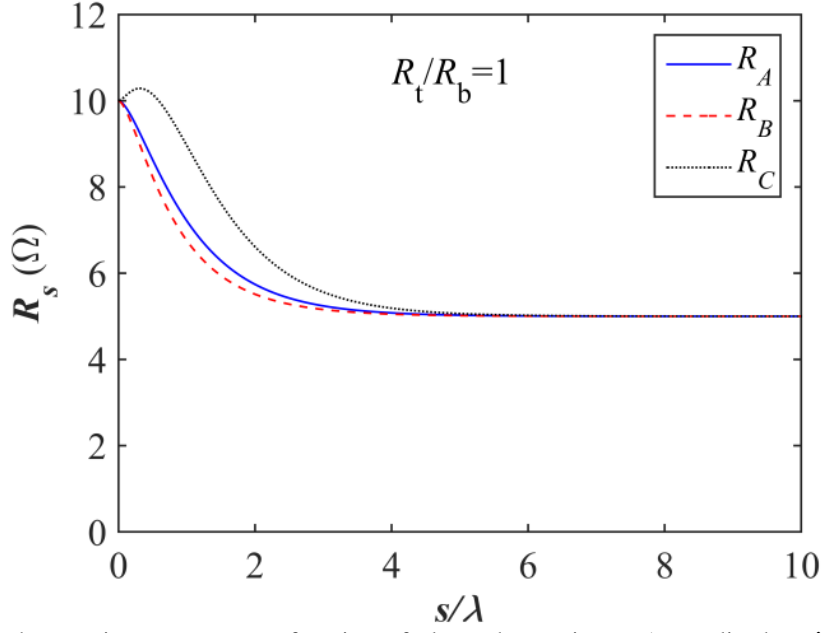


Fig. 2.5: Apparent sheet resistance, R_s , as a function of electrode spacing, s (normalized to λ), for an equally spaced, collinear four-point probe and A-, B- and C-configurations, respectively. $R_t = 10 \text{ } \Omega/\square$ and $R_b = 10 \text{ } \Omega/\square$.

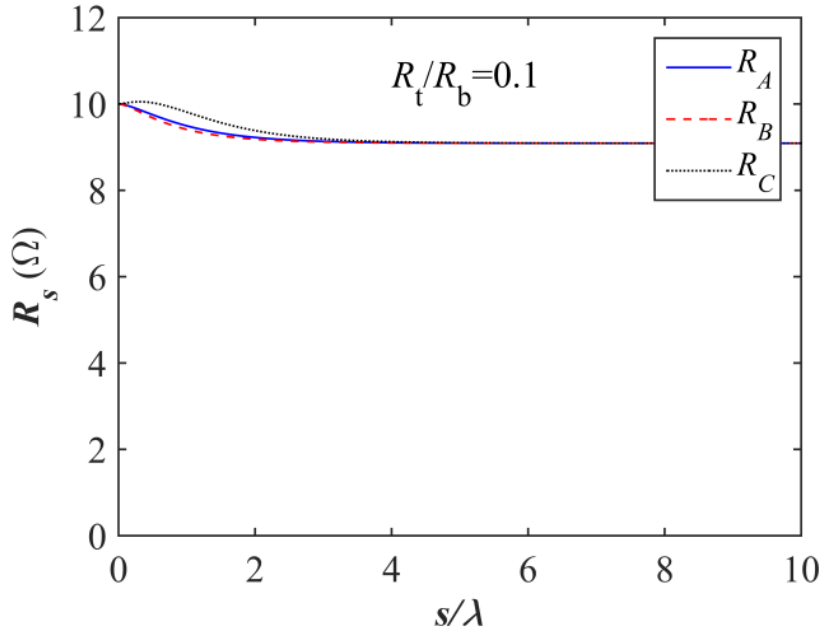


Fig. 2.6: Apparent sheet resistance, R_s , as a function of electrode spacing, s (normalized to λ), for an equally spaced, collinear four-point probe and A-, B- and C-configurations, respectively. $R_t = 10 \text{ } \Omega/\square$ and $R_b = 100 \text{ } \Omega/\square$.

2.2.1 Position errors (MTJ)

The different components of electrode position errors, described above for four-point resistance measurements on single sheet samples, also constitutes a major challenge for measurements on MTJs. The same basic approach will here be used to characterize the influence of position errors on four-point resistance measurements on MTJs. Using the same assumptions as for Eqs. 7-9, the relative standard deviations, $\sigma_{R_A}^{\text{rel}}$, $\sigma_{R_B}^{\text{rel}}$ and $\sigma_{R_C}^{\text{rel}}$, on the measured four-point resistances R_A , R_B and R_C , respectively, are

$$\sigma_{R_A}^{\text{rel}} = \frac{1}{R_A} \sqrt{\sum_{n=1}^4 \left(\frac{\partial R_A}{\partial x_n} \sigma_x \right)^2} = \alpha^* \frac{\sigma_x}{\langle s \rangle}, \quad (47)$$

$$\sigma_{R_B}^{\text{rel}} = \frac{1}{R_B} \sqrt{\sum_{n=1}^4 \left(\frac{\partial R_B}{\partial x_n} \sigma_x \right)^2} = \beta^* \frac{\sigma_x}{\langle s \rangle} \quad (48)$$

and

$$\sigma_{R_C}^{\text{rel}} = \frac{1}{R_C} \sqrt{\sum_{n=1}^4 \left(\frac{\partial R_C}{\partial x_n} \sigma_x \right)^2} = \zeta^* \frac{\sigma_x}{\langle s \rangle}, \quad (49)$$

where $\langle s \rangle = (s_1 + s_2 + s_3)/3$ is the mean electrode pitch. For equidistant electrodes ($s_n = s$) geometrical coefficients, α^* , β^* and ζ^* , can be shown to be

$$\alpha^* = \frac{1}{\sqrt{2}} \frac{\sqrt{\left(\frac{s}{\lambda} (K_1(\frac{s}{\lambda}) - K_1(2\frac{s}{\lambda})) + \frac{1}{2} \frac{R_b}{R_t} \right)^2 + \left(\frac{s}{\lambda} (K_1(\frac{s}{\lambda}) + K_1(2\frac{s}{\lambda})) + \frac{3}{2} \frac{R_b}{R_t} \right)^2}}{K_0(\frac{s}{\lambda}) - K_0(2\frac{s}{\lambda}) + \frac{R_b}{R_t} \ln(2)}, \quad (50)$$

$$\beta^* = \frac{\sqrt{2 \left(\frac{s}{\lambda} K_1(\frac{s}{\lambda}) - \frac{s}{\lambda} K_1(3\frac{s}{\lambda}) + \frac{2}{3} \frac{R_b}{R_t} \right)^2 + 8 \left(\frac{s}{\lambda} K_1(\frac{s}{\lambda}) + \frac{R_b}{R_t} \right)^2}}{K_0(\frac{s}{\lambda}) - K_0(3\frac{s}{\lambda}) + \frac{R_b}{R_t} \ln 3} \quad (51)$$

and

$$\zeta^* = \frac{\sqrt{2 \left(\frac{s}{\lambda} (-K_1(2\frac{s}{\lambda}) + K_1(3\frac{s}{\lambda})) - \frac{1}{6} \frac{R_b}{R_t} \right)^2 + \left(\frac{s}{\lambda} (K_1(\frac{s}{\lambda}) - K_1(2\frac{s}{\lambda})) + \frac{1}{2} \frac{R_b}{R_t} \right)^2}}{K_0(\frac{s}{\lambda}) - 2K_0(2\frac{s}{\lambda}) + K_0(3\frac{s}{\lambda}) + \frac{R_b}{R_t} \ln\left(\frac{4}{3}\right)}. \quad (52)$$

From Eqs. 50-52 it is clear that $\sigma_{R_A}^{\text{rel}}$, $\sigma_{R_B}^{\text{rel}}$ and $\sigma_{R_C}^{\text{rel}}$ not only depend on the electrode positions but also on the sample properties R_A , R_t and R_b . This is illustrated in Fig. 2.7, where the geometrical coefficients α^* , β^* and ζ^* are plotted for $R_t/R_b = 10$ as a function of electrode spacing (normalized to λ). Whereas the geometrical coefficients α , β and ζ , defined for single sheet measurements (see section 2.1.1), describes a constant relation between σ_R^{rel} and σ_x/s , the geometrical coefficients for

MTJs vary as a function of sample properties. However, for $s \ll \lambda$ or $s \gg \lambda$ the values of α^* , β^* and ζ^* approach those of α , β and ζ . For electrode distances in the intermediate range the sensitivity to position errors is higher as compared to four-point resistance measurements on single sheet samples. A-configuration measurements yields the lowest sensitivity to position errors, whereas B-configuration measurements yields the highest sensitivity to position errors for $R_t/R_b = 10$.

Similar plots are presented in Fig. 2.8 and Fig. 2.9 for R_t/R_b -ratios of 1 and 0.1, respectively. Comparing the three plots illustrates the how the geometrical coefficients for measurements on MTJs, for all values of s/λ , will approach those of their counterparts for single sheet samples in the extreme case of $R_t/R_b \rightarrow 0$, which is in line with our previous observations (see section 2.2).

With R_A , R_t and R_b being unknown variables it is not possible to correctly estimate electrode position errors based on measurements of R_A , R_B and R_C .

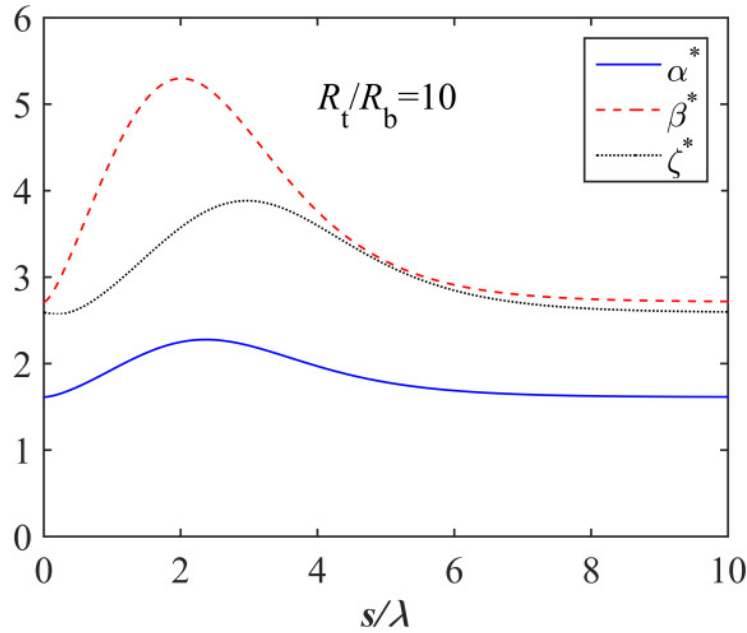


Fig. 2.7: Geometrical coefficients α^* , β^* and ζ^* plotted for $R_t/R_b = 10$, where $R_t = 10 \Omega/\square$ and $R_b = 1 \Omega/\square$, as a function of electrode spacing (normalized to λ).

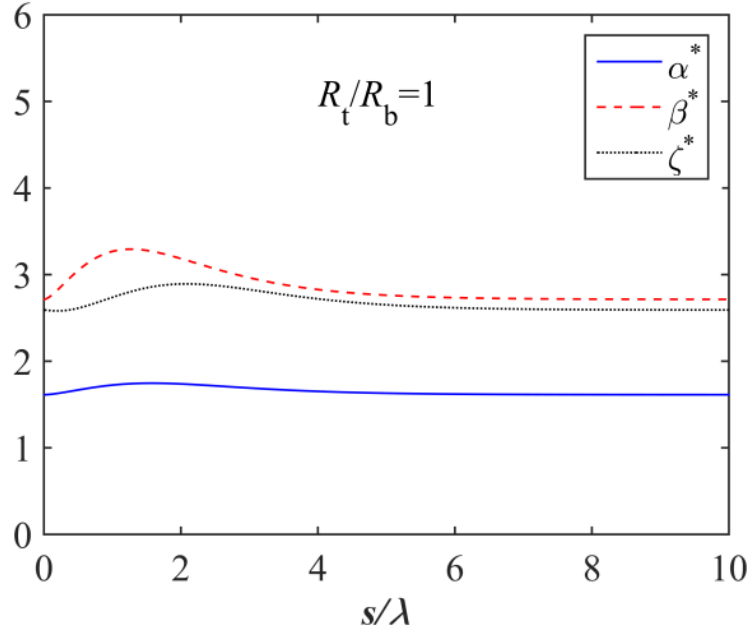


Fig. 2.8: Geometrical coefficients α^* , β^* and ζ^* plotted for $R_t/R_b = 1$, where $R_t = 10 \, \Omega/\square$ and $R_b = 10 \, \Omega/\square$, as a function of electrode spacing (normalized to λ).

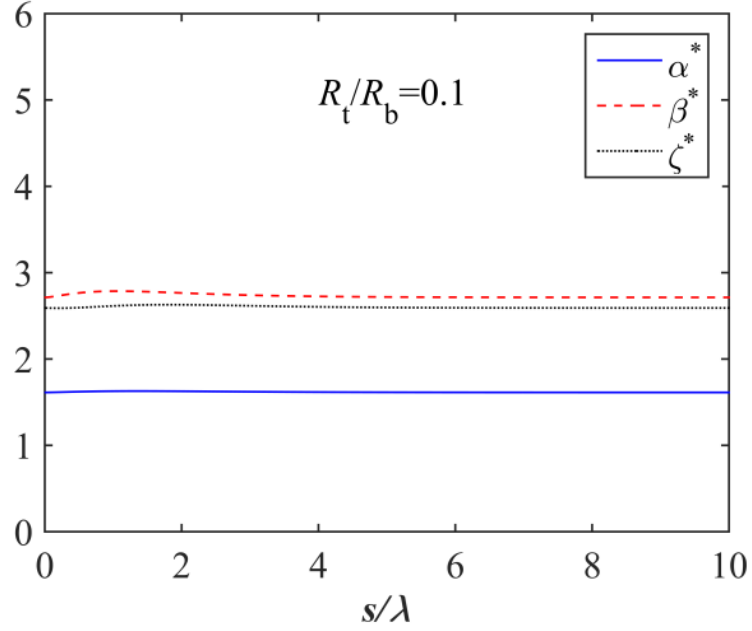


Fig. 2.9: Geometrical coefficients α^* , β^* and ζ^* plotted for $R_t/R_b = 0.1$, where $R_t = 10 \, \Omega/\square$ and $R_b = 100 \, \Omega/\square$, as a function of electrode spacing (normalized to λ).

2.2.2 Position error correction (MTJ)

As pointed out in the previous section concerning four-point resistance measurements on MTJs the standard deviation on R_A , R_B and R_C is dependent not only on the electrode positions but also the three defining properties, R_A , R_t and R_b , of the particular MTJ under test. This added complexity to the resistance dependence means that the position error correction methods described in section 2.1.2 will not hold true for measurements on MTJs i.e. the resulting, position corrected resistance value will not be meaningful in a physical sense. Exceptions to this statement of course include four-point measurements obtained at electrode spacing $s \ll \lambda$ or $s \gg \lambda$ as well as measurements on samples with $R_t/R_b \rightarrow 0$, since MTJs will exhibit single sheet behavior in these cases.

Applying the position correction algorithms (the vdp method or the first order approximation) to four-point measurements on MTJs will, however, yield a so-called pseudo resistance value, R_p , which is less sensitive to electrode position errors as compared to R_A , R_B and R_C . Pseudo resistance values based on first order correction (Eqs. 22-27) are denoted R_p^w , R_p^v and R_p^u for AB, AC and BC correction, respectively. For static, in-line position errors and in-line geometry errors with standard deviation σ_x the relative standard deviation on the position corrected pseudo resistance estimated from first order correction is identical for all dual combinations of R_A , R_B and R_C (due to reciprocity [54]–[56]), that is $\sigma_{R_p^w}^{\text{rel}} = \sigma_{R_p^v}^{\text{rel}} = \sigma_{R_p^u}^{\text{rel}}$, and given by (notation for AB correction is used):

$$\sigma_{R_p^w}^{\text{rel}} = \frac{1}{R_p^w} \sqrt{\sum_{n=1}^4 \left(\frac{\partial R_p^w}{\partial x_n} \sigma_x \right)^2} = \chi \frac{\sigma_x}{\langle s \rangle}, \quad (53)$$

where $\langle s \rangle = (s_1 + s_2 + s_3)/3$ is the mean electrode pitch. For equidistant electrodes ($s_n = s$) the geometrical coefficient χ is given by

$$\chi = \frac{s\sqrt{2}}{\lambda} \frac{\sqrt{\left(K_1\left(\frac{s}{\lambda}\right) - 4K_1\left(\frac{2s}{\lambda}\right) + 3K_1\left(\frac{3s}{\lambda}\right)\right)^2 + \left(2K_1\left(\frac{s}{\lambda}\right) - 4K_1\left(\frac{2s}{\lambda}\right)\right)^2}}{5K_0\left(\frac{s}{\lambda}\right) - 8K_0\left(\frac{2s}{\lambda}\right) + 3K_0\left(\frac{3s}{\lambda}\right) + \frac{R_b}{R_t}(4\ln 4 - 3\ln 3)}. \quad (54)$$

In Fig. 2.10 χ along with α^* , β^* and ζ^* for $R_t/R_b = 10$, where $R_t = 10 \Omega/\square$ and $R_b = 1 \Omega/\square$, are plotted as a function of electrode spacing (normalized to λ). At electrode spacing $s \ll \lambda$ or $s \gg \lambda$, χ approaches zero, which reflects the fact that in this range the MTJ shows single sheet behavior and therefore the position correction algorithm completely eliminates static, in-line errors. In the intermediate range of s/λ we observe that χ remains significantly lower than the coefficient for single configuration measurements, clearly indicating the advantage of the position correction method also for MTJs.

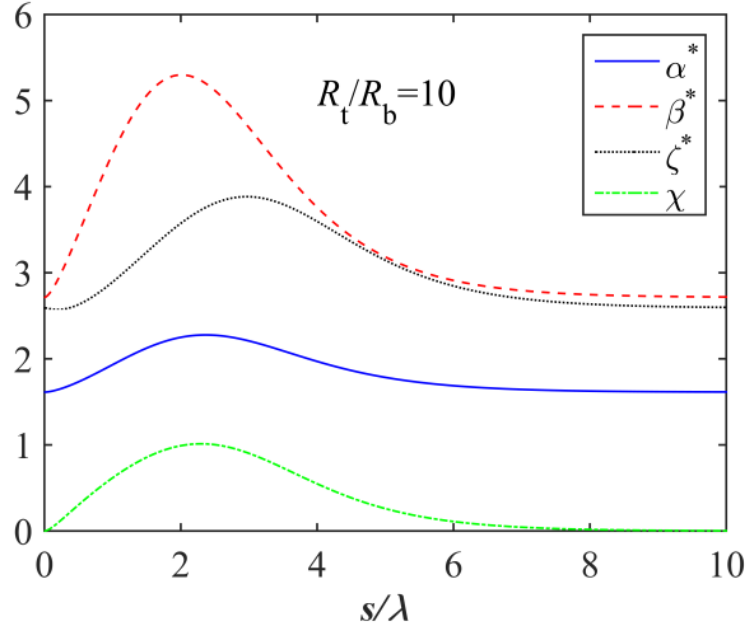


Fig. 2.10: Geometrical coefficients α^* , β^* , ζ^* and χ plotted for $R_t/R_b = 10$, where $R_t = 10 \text{ } \Omega/\square$ and $R_b = 1 \text{ } \Omega/\square$, as a function of electrode spacing (normalized to λ).

In Fig. 2.11 χ is plotted for a range of R_t/R_b -ratios and it is observed that for $R_t/R_b \rightarrow 0$ the sensitivity to position errors will vanish, which is in line with our observations in section 2.2.1.

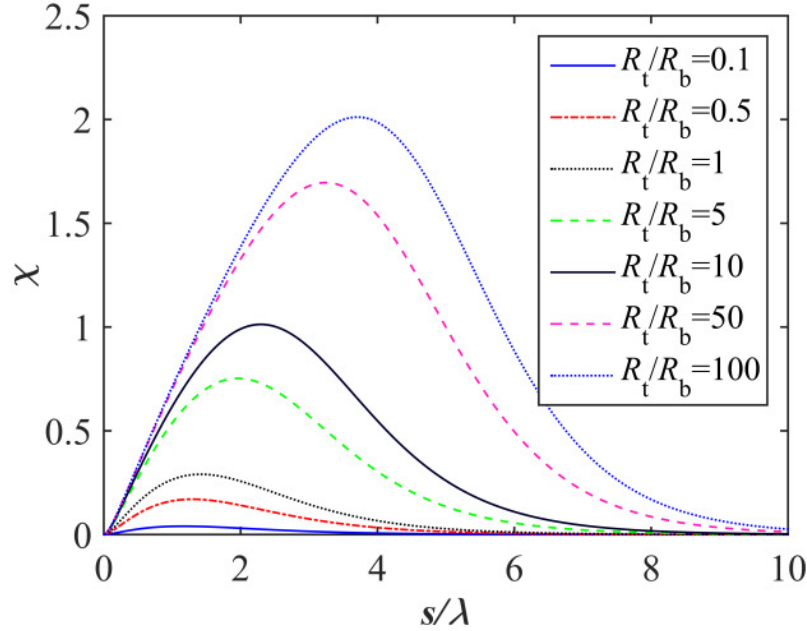


Fig. 2.11: The geometrical coefficient χ plotted as a function of electrode spacing (normalized to λ) for a range of R_t/R_b -ratios.

This section has focused exclusively on static, in-line position errors and in-line geometry errors. Obviously, dynamic in-line errors and all off-line errors will also influence the standard deviation of the position corrected pseudo resistance. The contribution from these errors will not be evaluated analytically. However, a comparative study of the different position correction methods and their sensitivity to static and dynamic in-line and off-line errors is presented in chapter 6.

2.2.3 Tunnel barrier conductance

Usually the electrical conduction across the barrier of an MTJ is considered to happen exclusively by tunneling, as implied by its designation. This is true only for MTJs of good barrier quality and without pinholes [11], [67]–[69]. Therefore, to describe the current transport across non-ideal barriers a more complex model must be applied.

Experimental data [67], [70]–[74] as well as theoretical considerations [11], [67], [70]–[74] suggest that for thicker tunnel barriers the RA_{low} and RA_{high} products both depend exponentially on the thickness of the tunnel barrier with the same exponential factor, while the pre-factors to the exponential depend primarily on the spin polarization of the ferromagnets used. As a result the TMR is hardly affected by changes in the thickness of the tunnel barrier. For thinner barriers this is not true anymore, since pinholes and nanobridges provide an alternative current path to tunneling and may for very thin barriers dominate the transport altogether. This has been modeled as a parallel resistor network [75] such that

$$\frac{1}{RA_{\text{low}}} = (1 - \alpha_\ell) g_{\text{low}} T(d, \Phi_B) + \alpha_\ell g_{\text{leak}} \quad (55)$$

$$\frac{1}{RA_{\text{high}}} = (1 - \alpha_\ell) g_{\text{high}} T(d, \Phi_B) + \alpha_\ell g_{\text{leak}} \quad (56)$$

where $T(d, \Phi_B)$ is the tunneling probability, which primarily depends on the tunnel barrier thickness, d , and barrier height Φ_B . The conductances per area g_{low} and g_{high} are characteristic pre-factors for low and high spin states, respectively, and g_{leak} is the characteristic leak conductance per area due to pinholes and nanobridges. The factor α_ℓ is the area fraction occupied by pinholes and nanobridges, and this area fraction is of course not available for tunneling. As a result, the tunneling magnetoresistance ratio becomes

$$\text{TMR} = \frac{RA_{\text{high}} - RA_{\text{low}}}{RA_{\text{low}}} = \frac{(1 - \alpha_\ell) g_{\text{low}} T(d, \Phi_B) + \alpha_\ell g_{\text{leak}}}{(1 - \alpha_\ell) g_{\text{high}} T(d, \Phi_B) + \alpha_\ell g_{\text{leak}}} - 1. \quad (57)$$

Obviously, for a perfect tunnel barrier, with $\alpha_\ell=0$, $\text{TMR}=g_{\text{low}}/g_{\text{high}}-1$ and is essentially independent on the tunnel barrier thickness to first order, while for a defective barrier, with $\alpha_\ell=1$, $\text{TMR}=0$. The transition between these two extreme cases happens over a very narrow range of barrier thicknesses (a small fraction of a nm) depending on the preparation of the barrier [76] since α_ℓ is extremely thickness dependent. As a result, cut-off values for RA_{low} and RA_{high} exist, below which TMR becomes too small to be useful due to the increase of α_ℓ .

Chapter 3

3 Experimental

This chapter describes the experimental setup used for the work presented in this thesis. Some of the measurement parameters were varied for different experiments and will be specified along with the experimental results presented in the subsequent chapters. Here follows first a detailed description of the M12PP as well as a general introduction to the CIPT measurement equipment in which the micro probe is utilized. After this the standard data treatment routines are introduced and finally sample preparation is presented.

3.1 Micro 12-point probe

Various micro probes with 4 to 12 electrodes are today commercially available and aimed at different applications [50]. The CIPT measurement technique relies on four-point resistance measurements carried out at varying electrode pitch, which is the reason why M12PPs are utilized with this method. By selecting individual subsets of four electrodes (sub-probes), the mean electrode spacing, $\langle s \rangle$, may be varied. For experiments presented in this thesis a conventional M12PP (see Fig. 3.1) with $\langle s \rangle$ in the range from $1.5 \mu\text{m}$ to $8.25 \mu\text{m}$ was used and a total of eight sub-probes were addressed, some of which result in non-equidistant sub-probes (see Tab. 3.1).

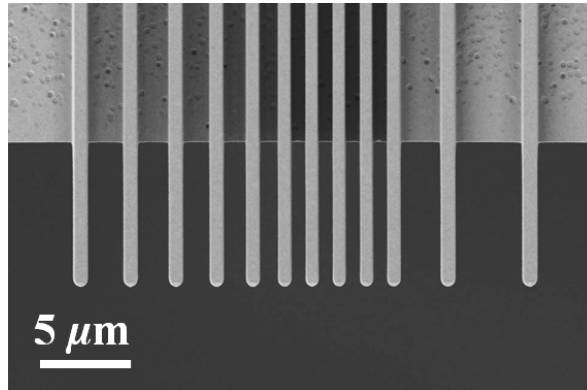


Fig. 3.1: Scanning electron micrograph of a 12-point probe with Au-coated, straight cantilever electrodes. Reproduced from paper II.

s_1	s_2	s_3	$\langle s \rangle$
μm	μm	μm	μm
1.50	1.50	1.50	1.50
2.00	2.25	2.50	2.25
3.00	3.00	3.00	3.00
4.50	4.50	3.75	4.25
4.50	4.50	4.50	4.50
6.00	6.00	5.25	5.75
7.50	7.75	6.75	7.33
9.00	8.25	7.50	8.25

Tab. 3.1: Geometric details of the eight sub-probes formed using the 12-point probe. Distances between neighboring electrodes (s_1 , s_2 , and s_3) and mean probe pitch, $\langle s \rangle$, are listed. Adapted from paper II.

The probe is realized using standard fabrication techniques for Silicon-based micro-electro-mechanical systems (MEMS) [77]. The cantilevers are made of SiO_2 and have nominal dimensions: $0.75 \mu\text{m}$, $10 \mu\text{m}$ and $1 \mu\text{m}$ (width, length and thickness) and the nominal spring constant is 20 N/m [50]. To establish electrical contact to a sample the probe is covered by 100 nm Au deposited on top of 10 nm Ti, which acts as an adhesion layer to the SiO_2 .

3.2 Experimental setup

Regular four-point sheet resistance measurements as well as CIPT measurements presented in this work were carried out using a CAPRES CIPTech M300 [50]. The system incorporates a full multiplexer, which allows any selection of electrodes to be appointed to the in- and out-puts of the measurement electronics, I+, I-, V+ and V-, respectively. To reduce measurement noise a lock-in amplifier is used. The set AC measurement current is supplied between I+ and I-, while the voltage drop over V+ and V- is measured. The tool's standard setting for measurement current is $200 \mu\text{A}$ but up to $2500 \mu\text{A}$ can be supplied. During measurements a stage with two linear motors controls the X-/Y-positioning of the sample with respect to the probe, which is kept stationary in the X-/Y-plane and lowered into contact with the sample by a Z-stage (see Fig. 3.2). The relative precision of the movement of these stages are on the order of $\pm 10 \text{ nm}$ for the X-/Y-stage and $\pm 5 \text{ nm}$ for the Z-stage.

Probe-sample engage is controlled by electrical surface detection [78] (see Fig. 3.3). In this landing routine every second electrode of the probe are connected to form what is basically a two-point configuration with one subset of six electrodes connected to I+ and V+, while the other subset is connected to I- and V-. When probe landing is initiated the two subsets are shorted by a shunt resistor of $5 \text{ M}\Omega$. The voltage drop over the shunt resistor is monitored as the probe is continuously moved towards the sample. A sharp drop in the measured voltage, when any electrodes representing the two individual subsets are connected via the sample, will reveal probe-sample engage. At this point the shunt resistor is disconnected and the probe is moved down further by an overdrive commonly referred to as the engage depth. Typically an engage depth of 500 nm is used to ensure stable mechanical contact for all electrodes.

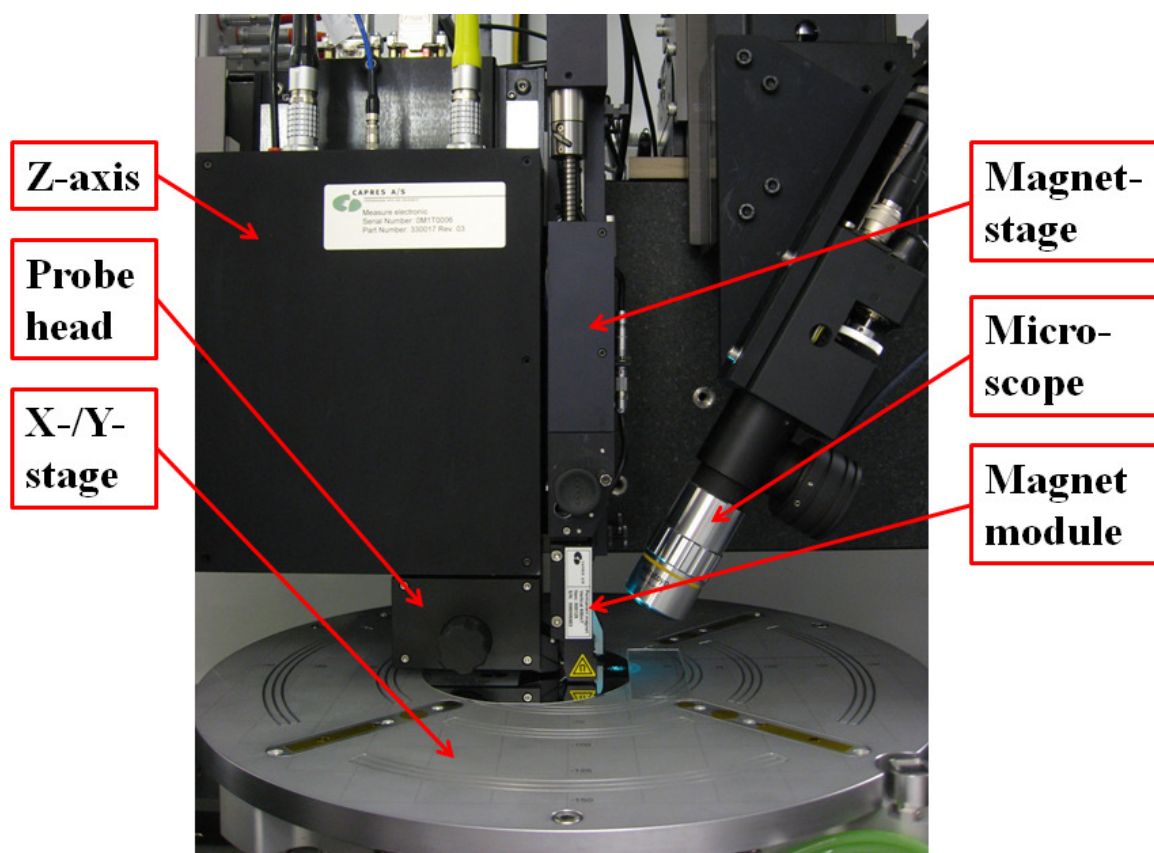


Fig. 3.2: View of central components of the CAPRES CIPTech M300 including a standard magnet setup for vertical field. Image supplied by courtesy of Mette S. Balslev.

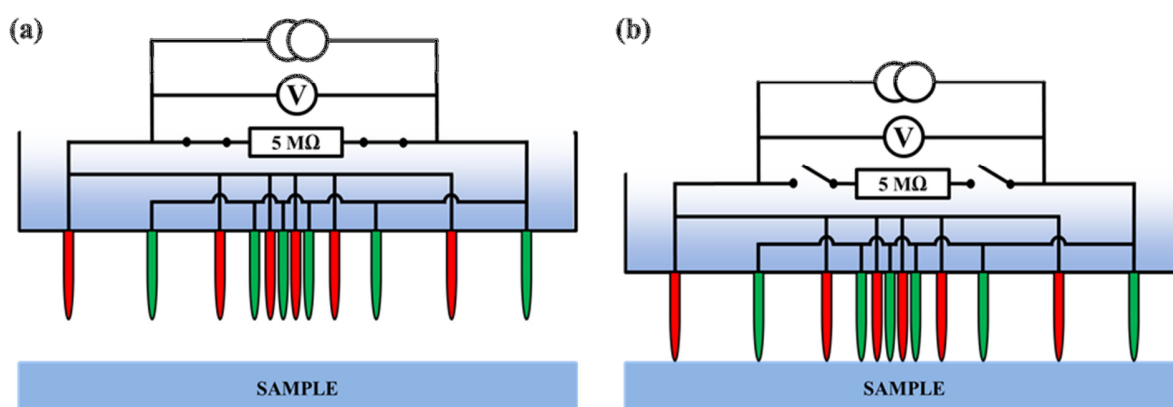


Fig. 3.3: Illustration of the probe-sample engage routine. (a) While moving towards the sample the potential drop over a 5 MΩ shunt resistor is monitored. (b) Upon probe-sample contact the voltage will drop sharply and the shunt resistor is disconnected.

The micro probe is mounted manually in a probe fixture (the so-called probe head) attached to the Z-stage. When mounted the probe is positioned at an angle of 30 degrees with respect to the sample surface (see Fig. 3.4). As a result of frictional wear the electrode material and to some extent also the

tip of the SiO_2 cantilever itself will be deformed during measurements [79]. For this reason, and due to unavoidable variations in the manual positioning of the probe inside the probe head, probes should not be removed from the probe head before it is unfit for further measurements (dead). Re-mounting a used probe will typically lead to reduced probe lifetime.



Fig. 3.4: Probe head with probe mounted. Image supplied by courtesy of Mette S. Balslev.

The magnetic field necessary to set the magnetization of the ferromagnetic layers is supplied by a magnet placed in close proximity of the probe. The magnet setup includes a permanent magnet, which can be rotated with respect to the surrounding pole shoes. Depending on the rotation of the permanent magnet the magnetic flux density between the pole shoes can be adjusted. Separate magnets are available for horizontal and vertical magnetic field, respectively.

The CIPTech M300 is equipped with two fan filter units (FFUs) providing a steady flow of clean air inside the tool enclosure. Measurements reported in this thesis were, however, carried out with the FFUs turned off. This was done in order to rule-out the possible negative influence on the measurement quality caused by vibrations generated by the FFUs.

Standard CIPT measurements with implemented position correction are carried out in sequenced procedure listed below. This procedure is repeated for every individual CIPT measurement.

1. Probe landing
2. Set magnetic field corresponding to parallel or anti-parallel state of the MTJ
3. Measure four-point resistances at varying electrode spacing using the dual configuration method to minimize the influence of electrode position error. For each sub-probe four resistance measurements are recorded using two of the independent four-point configurations, e.g. A-B-A'-B' for AB position correction.
4. Set magnetic field corresponding to parallel or anti-parallel state of the MTJ
5. Measure four-point resistances at varying electrode spacing using the dual configuration method to minimize the influence of electrode position error.
6. Probe disengage

For CIPT measurements without position correction only A-configuration measurements are used [28].

3.3 Data treatment

Four-point measurements on single sheet samples are typically reported as position corrected values obtained from the application of the vdp method or the first order approximation. Four individual, single configuration measurements (e.g. A-B-A'-B') are combined to form three continuous pairs (i.e. A-B, B-A' and A'-B'), which are then used to calculate three, position corrected resistance values, based on which an average value is reported as the final measurement result.

For CIPT measurements a series of four-point resistance measurements is carried out using n different sub-probes of varying electrode spacing (in this work $n = 8$). For each sub-probe the measurement routine is identical to that of measurements on single sheet sample described above and leads to n position corrected R_p values. Even though the physical meaning of R_p is very limited it can serve as a useful input for the data fitting routine designed to extract the MTJ parameters, RA, R_t and R_b , from a series of four-point resistance measurements. In a least-squares fitting routine n theoretical pseudo resistance values, R_p^{mod} , based on the CIPT model and information on the intended electrode distances, are fitted to the experimentally obtained pseudo resistance values, R_p^{exp} , by varying R_t , R_b and RA to lower the value of the sum, S , given by

$$S = \sum_{i=1}^n [R_{p,i}^{\text{exp}} - R_{p,i}^{\text{mod}}(R_t, R_b, \text{RA})]^2. \quad (58)$$

The number of elements in the sum is n , when only one RA value is fitted (see chapter 4) and $2n$ when both RA_{low} and RA_{high} are fitted as is the case for conventional, switching field CIPT measurements [28].

3.4 Samples

MTJ samples to be characterized with the CIPT-method should include a conductive top-layer that does not form an insulating oxide, when exposed to air. This is first and foremost a precaution to avoid probe crash on the sample surface, since the tool relies on electrical surface detection as described above. Another general sample design guideline concerns the sample R_t/R_b -ratio. If R_t is significantly lower than R_b , very little of the current will tunnel through the barrier, since the top electrode effectively shorts out the measurement [48]. This will lower the measurement precision and therefore it is typically recommended by the tool manufacturer to keep the R_t/R_b -ratio above 1 [50]. Finally, to evaluate the sample transfer length (and thus RA), measurements at an electrode pitch on the order of λ are needed [28], [76]. This can be a challenge especially for low-RA samples, where λ is close to the minimum electrode spacing practically achievable. However, this challenge may to some extent be circumvented. Since $\lambda = [\text{RA}/(R_t + R_b)]^{1/2}$ it is possible to increase the transfer length by lowering R_t and/or R_b and thereby allow useful CIPT data to be obtained [48].

The MTJ sample investigated in this work is a 200 mm wafer with a non-patterned MTJ and in-plane magnetization. The MTJ was prepared in a magnetron sputtering process with a subsequent thermal anneal in an applied magnetic field of 1 T, and has the following stack composition: {bottom electrode: Ta (5 nm)/CuN (50 nm)/Ta (3 nm)}/PtMn (16 nm)/Co₇₀Fe₃₀ (2.2 nm)/Ru (0.85 nm)/Co₄₀Fe₄₀B₂₀ (2.5 nm)/MgO (1 nm)/Co₄₀Fe₄₀B₂₀ (2.5 nm)/{top electrode: Ta (5 nm)/CuN (15 nm)/Ru (7 nm)}. This design of the stack ensures that the lower CoFeB layer is pinned while the upper CoFeB layer is free.

Since the value of RA depends on the state of the magnetization (parallel or anti-parallel) it follows that the transfer length of the sample will change accordingly, which can be expressed as $\lambda_{\text{low}} = [RA_{\text{low}}/(R_t + R_b)]^{1/2}$ and $\lambda_{\text{high}} = [RA_{\text{high}}/(R_t + R_b)]^{1/2}$. For this particular sample $RA_{\text{low}} = 8.5 \Omega\mu\text{m}^2$, $RA_{\text{high}} = 23.4 \Omega\mu\text{m}^2$, $R_t = 3.5 \Omega/\square$ and $R_b = 0.6 \Omega/\square$. It follows that the respective transfer lengths for the sample are nominally $\lambda_{\text{low}} = 1.5 \mu\text{m}$ and $\lambda_{\text{high}} = 2.5 \mu\text{m}$. The switching field of the sample can be observed from the hysteresis loop presented in Fig. 3.5.

Due to shadowing effects of the edge exclusion ring in the processing equipment, an area along the perimeter of the sample is left un-metalized and has therefore not been probed in this work.

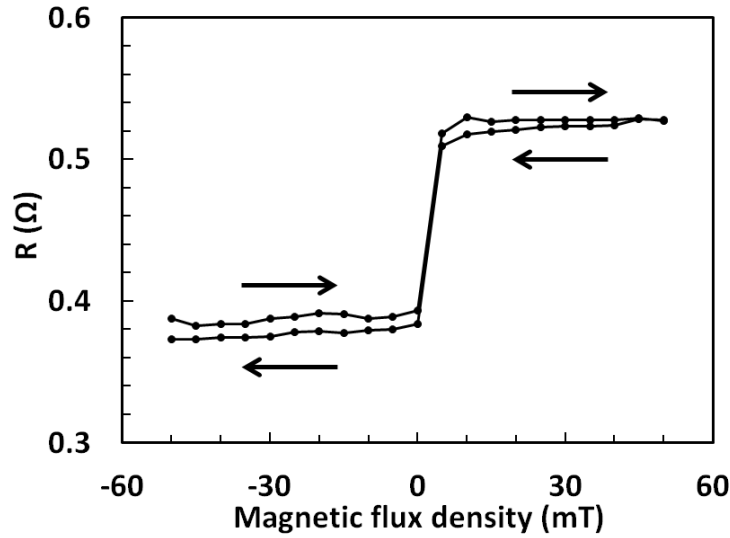


Fig. 3.5: Hysteresis loop of the free layer recorded using a micro four-point probe with a pitch of $1.5 \mu\text{m}$. Arrows indicate the magnetic sweep direction. Reproduced from paper I.

Using the same sputtering equipment another sample was prepared with a layer of 100 nm Ru deposited on top of a 200 nm wafer. This sample, with a nominal sheet resistance of 1.6Ω , has been used for four-point resistance measurements presented in paper II.

Chapter 4

4 Static field CIPT method

The standard (switching field) CIPT method measures both RA and TMR, but the usefulness for uniformity mapping, e.g. for tool optimization, is limited by excessive measurement time (see section 1.3). In this chapter a fast complementary static magnetic field CIPT method focused only on measurement of RA is described together with a conceptual presentation of an alternative magnet design. We compare the static field method to the standard CIPT method and find perfect agreement between the extracted RA values and measurement repeatability while the static field method is several times faster. Finally, we present a detached magnet concept enabled by the proposed static field CIPT method.

This chapter is based on and repeats text and figures from paper I.

4.1 Sample uniformity

To investigate sample uniformity high density area mapping of a quarter of an MTJ wafer (see section 3.4) was carried out using the conventional switching field CIPT measurement method, with an implementation of van der Pauw like AB correction, see Fig. 4.1. 1613 measurements were acquired with a step size of 2 mm and at two separate magnetic flux densities, in this case ± 10 mT, corresponding to anti-parallel and parallel magnetization of the sample (see Fig. 3.5). The measurement current was 200 μ A.

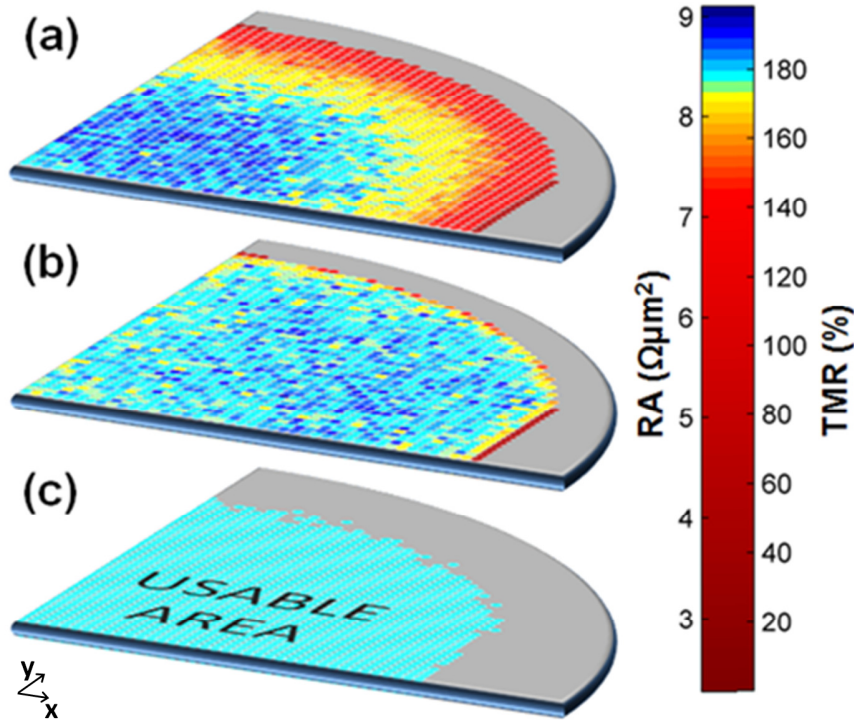


Fig. 4.1: High density map of RA (a) and TMR (b) obtained with 2 mm step size on a quarter of a 200 mm wafer. (c) The usable wafer area vs. edge exclusion zone is based on an acceptance limit of $\pm 10\%$ with respect to the mean value at the center of the wafer.

From the quarter wafer area map we observe a radially asymmetric variation in the MTJ-defining parameters TMR and RA. To highlight this asymmetry, we performed two cross-wafer line scans (1 mm step size) presented in Fig. 4.2. We only depict RA_{high} since RA_{low} showed equivalent behavior. Whereas the parameters TMR and RA appear radially symmetric along the X-axis, a clear gradual change in RA is observed along the Y-axis. It is reasonable to assume that the asymmetry is related to the fact that the target dimension along the Y-axis is smaller than the wafer size while the target dimension along the X-axis is much larger than the wafer size. As a result good uniformity can be expected along the X-axis while on the y-axis the uniformity is very poor without movement, and even with linear movement of the sample along the y-axis with respect to the static target, which is the case for this study, the uniformity is inferior to that along the x-axis. Such process variability is most detailed observed by full wafer mapping of sample homogeneity, but with the conventional CIPT method this can be very time consuming as the measurement time per point is ~ 60 s.

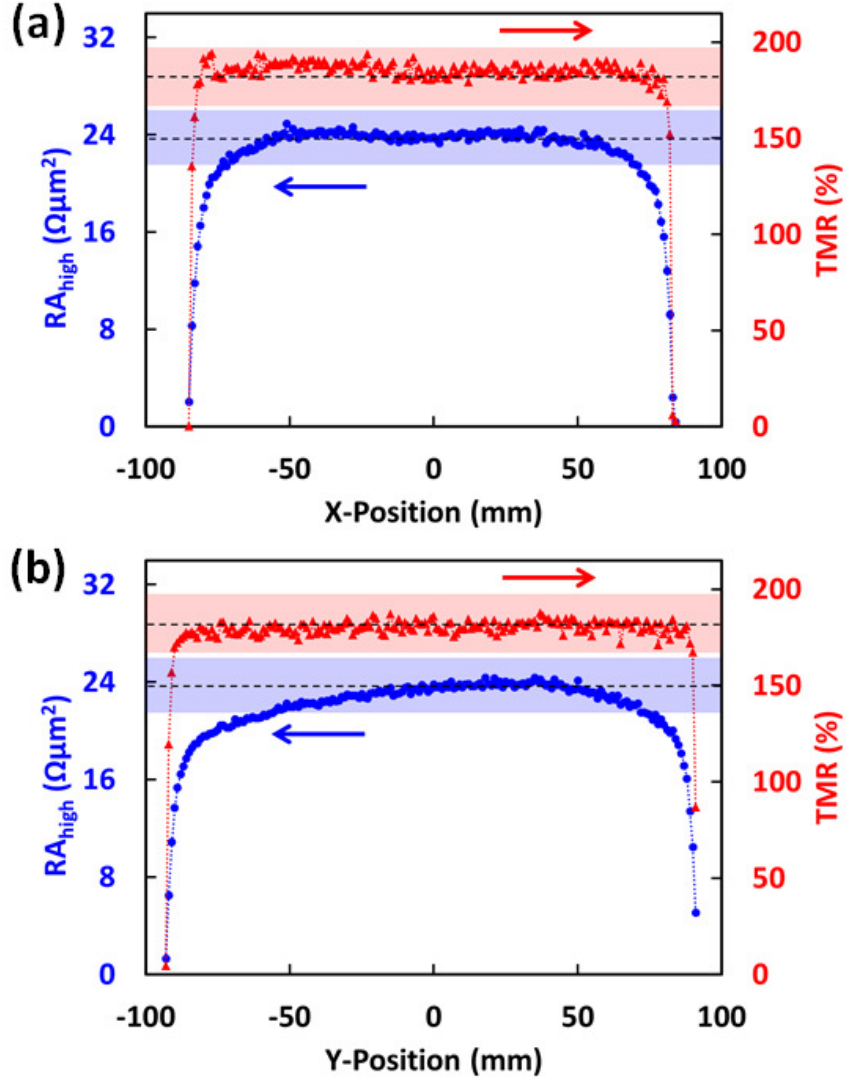


Fig. 4.2: Line scan measurements of RA_{high} and $TMR = (RA_{\text{high}} - RA_{\text{low}}) / RA_{\text{low}}$ with a step size of 1 mm along the X-axis (a) and Y-axis (b) across a 200 mm wafer. The colored regions mark a $\pm 10\%$ band with respect to the mean values indicated by the dashed lines. While RA and TMR appear radially symmetric along the X-axis (a), an asymmetric slope in RA is clearly observed along the Y-axis (b). Reproduced from paper I.

From Fig. 4.1 and Fig. 4.2 it is evident that the relative variation of RA is the dominant factor when estimating the usable area of the wafer, here defined by a $\pm 10\%$ acceptance band centered on the mean value of the central $20 \times 20 \text{ mm}^2$ area of the sample. Whereas TMR appears constant with an abrupt change in close proximity of the edge of the processed area, we observe that RA begins to decrease significantly at an approximate distance of 50 mm from the wafer center. This is in good agreement with the theory for conduction across tunnel barriers discussed in section 2.2.3. For MTJs of good barrier quality and without pinholes the TMR is hardly affected by changes in RA, which is directly related to the barrier thickness. However, as the thickness of the barrier is lowered, pinholes and nanobridges provide an alternative current path to tunneling, which is the reason for the abrupt drop of TMR observed. Near the edge of the processed area, the barrier is defective and the area fraction

available for leakage, α_ℓ (see Eqs. 55-57), is close to 1. This is in line with our observations from Fig. 4.3 showing TMR as a function of RA as extracted from a conventional switching field CIPT wafer mapping.

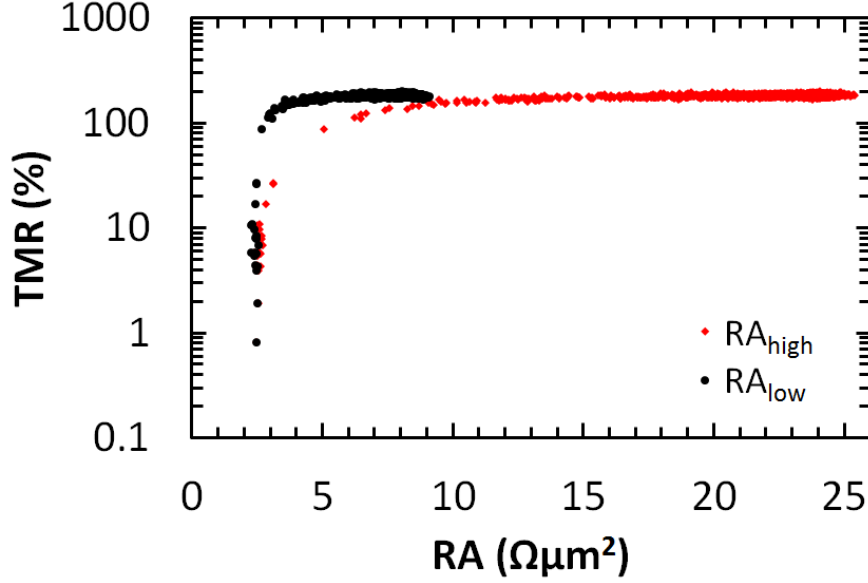


Fig. 4.3: TMR vs. RA extracted from a wafer mapping using the conventional switching field CIPT measurement practice. Reproduced from paper I.

The results in Fig. 4.3 suggest that variations in RA_{high} are most easily evaluated due to the larger relative change compared with RA_{low} . Also, evaluating the transfer length requires measurements using electrode pitches in a range on the order of λ [28], [76]. For typical MTJ's intended for MRAM, λ is close to the minimum electrode pitch practically achievable, and accurate four-point measurements become increasingly challenging for reduced electrode pitch. Thus, it may be an advantage to measure only in the anti-parallel magnetization state, as RA_{high} yields the most easily accessible and most relevant sample parameter in the shortest measurement time possible. On the other hand the option of simply applying a strong magnetic field and thereby ascertain that the layers are in a well-defined, parallel state is a unique advantage for measurements in the parallel state. Similarly, but more time consuming, first applying a strong magnetic field in one direction to saturate the sample and subsequently measuring in a weaker, static magnetic field of opposite orientation could lead to a more precise characterization of the anti-parallel state. In general we shall refer to this selective and less comprehensive measurement method as the static field CIPT method. Note that mapping of RA could be supplemented by a few switching field CIPT measurements, e.g. near the wafer centre, to establish TMR.

In Fig. 4.4 we present high resolution wafer maps obtained with the static field CIPT method for both RA_{low} and RA_{high} . The two maps are presented for comparison only, since the necessary information for tool optimization can be extracted from a single one of them as argued above. Each map contains 6510 measurement positions distributed with a step size of 2 mm. The asymmetric behavior of RA seen in Fig. 4.2 (b) is also observable from both maps and the usable area based on an acceptance limit of $\pm 10\%$ with respect to the mean value at the center of the wafer is also consistent. For the particular combination of sample properties and range of electrode pitches in question, there is no significant

advantage from measuring RA_{high} as opposed to RA_{low} . However, we do observe a higher density of outliers in the usable area determined by RA_{low} , which might be attributed to measurement precision.

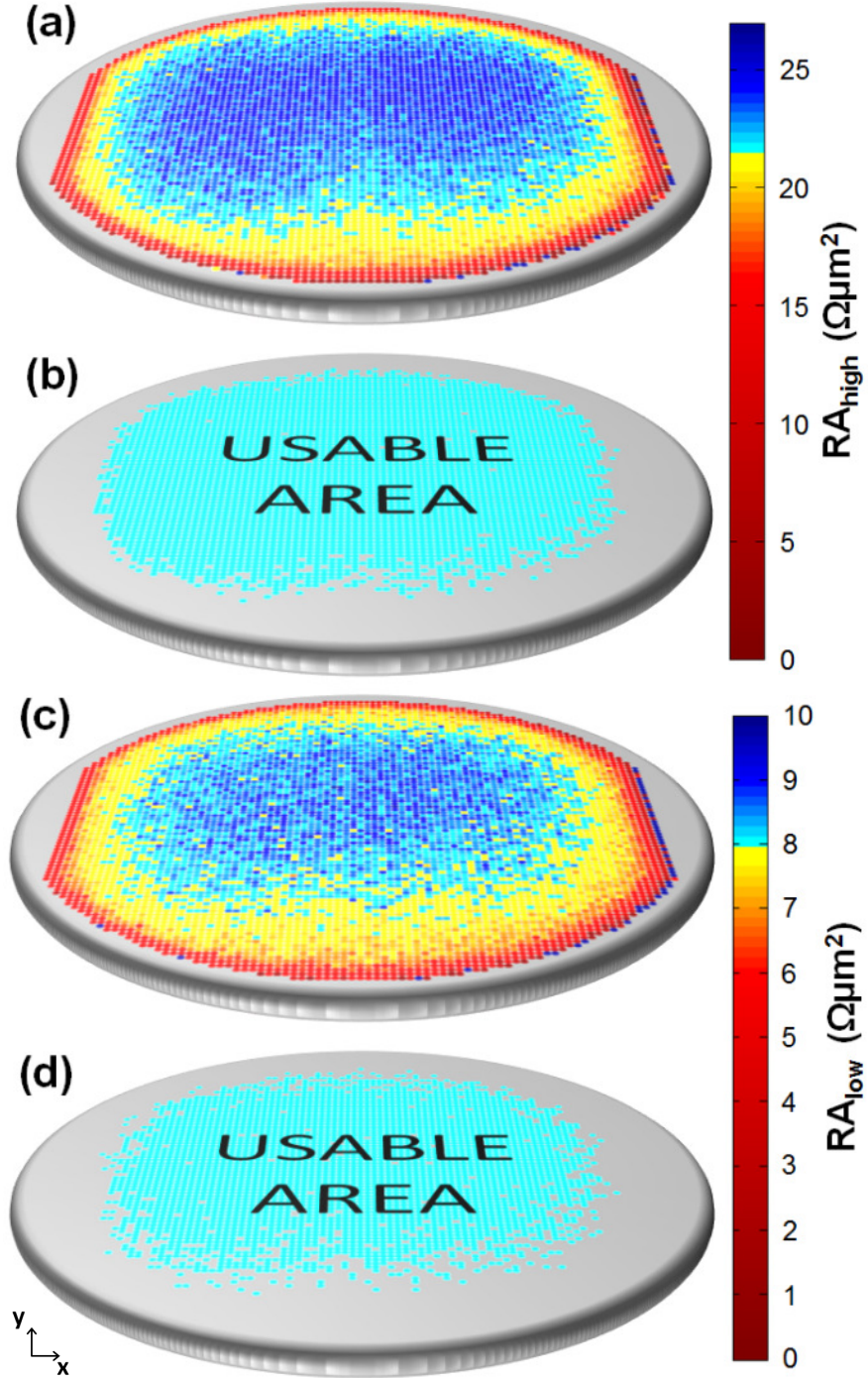


Fig. 4.4: High density maps of RA_{high} (a) and RA_{low} (c) on the full 200 mm wafer obtained with 2 mm step size totaling 6510 measurement points per map. (b and d) The usable wafer area vs. edge exclusion zone based on an acceptance limit of $\pm 10\%$ with respect to the mean value at the center of the wafer for RA_{high} and RA_{low} respectively. Reproduced from paper I.

4.2 Switching field CIPT vs. static field CIPT

While uniformity mapping is possible with conventional CIPT measurements on a full wafer, the task turns out to be impractical due to the resulting measurement time. The overall time spent per measurement point can be split into 3 contributing factors:

$$t_{\text{tot}} = t_{\text{meas}} + t_{\text{mov}} + t_{\text{mag}}, \quad (59)$$

where t_{meas} is the time spent sampling data, t_{mov} is the time spent on stage movement and t_{mag} is the time spent on adjustments of the magnetic field.

In a timed comparison of the two methods, a square grid of 10x10 points with a step size of 100 μm in a homogeneous region of the sample was measured using a current of 200 μA at a frequency of 24.11 Hz and an integration time of 83 ms. The static field method was found to be more than 5 times faster than the conventional CIPT method. Fig. 4.5 compares the time consumption of the two methods in their regular implementation and predicts how they would relate in other scenarios where one or more of the contributing factors are negligible while the other factors remain unchanged. In the regular implementation $t_{\text{meas}} = 5.6$ s and 2.8 s for CIPT and static field methods respectively, t_{mov} , which applies to both methods, is 8.9 s and t_{mag} , which applies only to the conventional CIPT method, is 46.1 s. The time reduction observed for the regular implementation of the methods is mainly due to the lack of magnet adjustments in the static field method. However, as is seen from Fig. 4.5, changes to other factors can greatly influence the ratio of time spent with the different method implementations.

Thus, when we utilize the proposed static field CIPT method and measure only RA_{low} or RA_{high} , we can drastically reduce the time spent per point, which in turn allows us to map the entire wafer within a reasonable timespan.

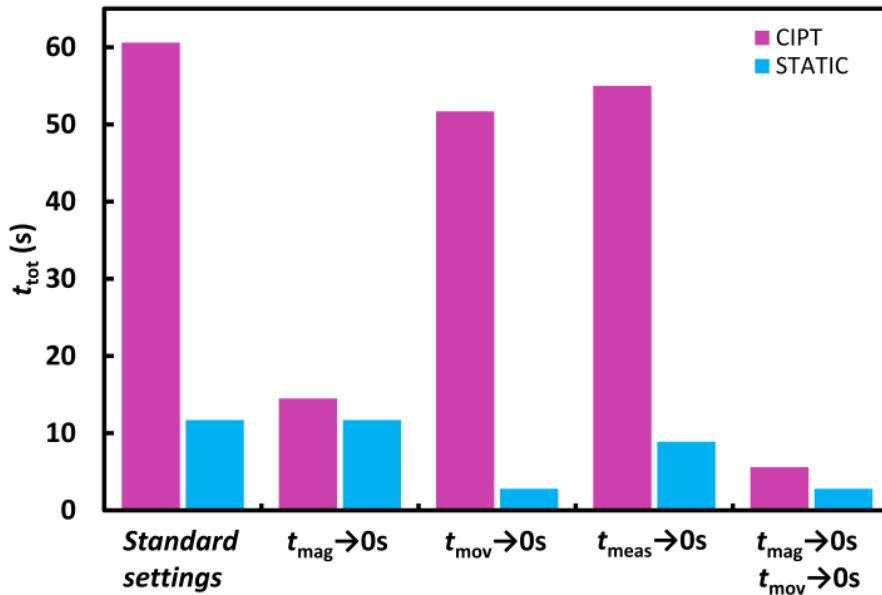


Fig. 4.5: Time spent per point, t_{tot} , for conventional CIPT and static field method respectively are presented for the regular implementation of the methods as well as 4 scenarios for which one or more contributing factors are negligible while the other factors remain unchanged. Reproduced from paper I.

To allow for a comparison of measurement quality for the two different methods, three individual, high density line scans each containing 100 measurement points were carried out using a step size of only 2 μm . This was done in order to reduce the influence of local sample variations; otherwise the same measurement settings as mentioned above were used. One series of traditional switching field CIPT measurements as well as two series of static field CIPT measurements in an applied magnetic field of respectively +10 mT and -10 mT were performed. A comparison of the measurement results are summarized in Tab. 4.1, and the two methods are found to be in good agreement.

		CIPT	STATIC	
B	(mT)	± 10	-10	+10
RA_{low}	($\Omega\mu\text{m}^2$)	8.5	8.6	
$\sigma(RA_{\text{low}})$	(%)	2.3	2.2	
RA_{high}	($\Omega\mu\text{m}^2$)	23.4		23.6
$\sigma(RA_{\text{high}})$	(%)	1.6		2.0

Tab. 4.1: Mean value and relative standard deviation of RA_{low} and RA_{high} based on 3 line scans: One series of traditional switching field CIPT measurements (CIPT) and two series of static field CIPT measurements (STATIC). Each scan contains 100 measurement points distributed with a step size of 2 μm . Reproduced from paper I.

4.3 Detached magnet concept

With the proposed static field CIPT method ground has been laid to rethink the magnet setup of the CIPT measurement tool. With the conventional CIPT method the magnetic field is switched for every measurement, which demands a magnet setup positioned at the actual measurement location. Additionally, the general desire for large dynamic range with respect to obtainable magnetic field, while at the same time maintaining field homogeneity in the measurement spot, has led to magnet setups being placed in close proximity of both probe and sample during measurement (see Fig. 3.2). The complexity of such systems is generally high, and the fact that space available for the magnet setup is limited, since room is needed for probe, sample and optics, only adds to the complexity. Finally, the complexity can be expected to increase even further in a future, fully automated CIPTech tool, requiring automatic probe change, which is a concept known from the commercially available CAPRES A300 μRSP [50].

Taking the static field CIPT method a step further could include the implementation of a detached magnet setup and measuring the sample without an applied magnetic field. To remove the magnet from the measurement area entirely would drastically reduce the complexity of the measurement system and pave the way for new magnet setups with superior dynamic range and field homogeneity. One such magnet setup would be the “letterbox”-type (see Fig. 4.6), which is especially suited for providing vertical magnetic field. In the concept drawing of Fig. 4.6 the magnet setup (green) is shown together with an automated wafer handler, which can move the sample through the narrow gap of the letterbox magnet. The limiting factor with respect to the gap size is the thickness of the wafer handler and the wafer itself. With this being the only design restriction, it is clear that magnets can be created with which very high magnetic fields can be reached e.g. by placing two permanent magnets (or electromagnets) of opposite, vertical magnetization on either side (over and below) the narrow gap (see

Fig. 4.6 (b)). By moving the sample through the letterbox magnet the entire wafer will be exposed to a homogeneous magnetic field and can subsequently be moved to the x-/y-stage for electrical characterization.

Other concepts suited for providing horizontal magnetic field can be designed.

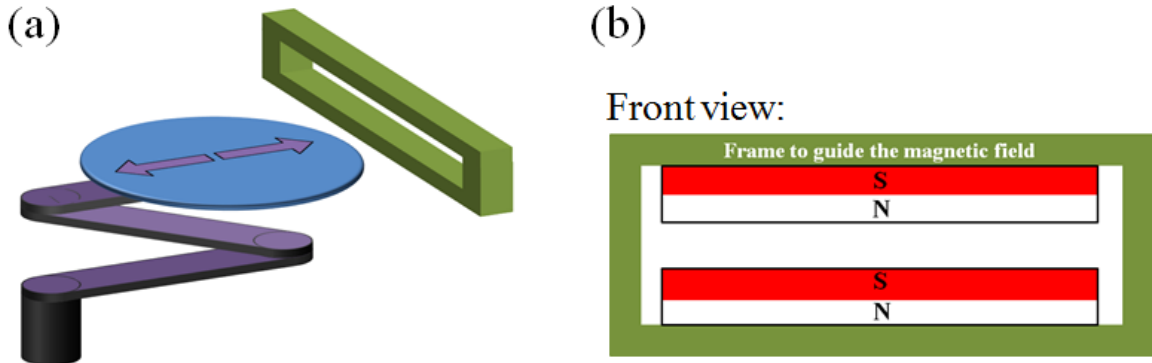


Fig. 4.6: Concept drawing. (a) An automated wafer handler (wafer robot) and a detached magnet setup (green) of the “letterbox”-type. (b) Front view of the magnet.

Of course a detached magnet setup would also include some disadvantages as compared to the conventional magnet setup. First of all, the setup would not be suited for characterizing the hysteresis loop of a sample. Secondly, some MTJs would not be characterized without the presence of an applied magnetic field during CIPT measurements. However, the concept would be suited MTJs for MRAM application.

4.4 Summary

High density mapping of an un-patterned MTJ sample reveals variations of RA and TMR, exceeding by far an acceptance limit of $\pm 10\%$. We find the variation of RA to be the most critical process parameter as compared to the variation of TMR. Because of process induced, radial asymmetry in the variations of RA, we argue that high resolution wafer mapping of the entire processed area is necessary for adequate process optimization and tool qualification. Since the CIPT method is a serial characterization technique, the time associated with mapping an entire wafer is directly proportional to the measurement time per point and resolution. Thus, to enable high resolution mapping, we have demonstrated a static field CIPT method, which allows us to reduce the measurement time by a factor of 5, by measuring only RA thus excluding TMR. This enhancement is obtained purely by acquiring only half of the data needed for the conventional switching field CIPT measurement and particularly by avoiding magnetic field switching. In a homogeneous region of the investigated sample, we observe that the two methods measure essentially the same RA values. By offering the choice of characterizing either RA_{low} or RA_{high} the static field CIPT method has an added advantage over the conventional switching field CIPT method, which relies on the characterization of both RA values. This allows for an improved matching of the range of available electrode pitches and sample transfer lengths λ_{low} or λ_{high} , which may effectively increases the dynamic range of any given 12-point probe.

Without the requirement for switching magnetic fields during measurements the static field CIPT method has inspired the concept of detached magnet setups for future CIPTech tools. While lowering

the complexity of the measurement system a detached magnet setup, e.g. the proposed letterbox magnet, could provide superior dynamic range and field homogeneity as compared to current state of the art solutions.

Chapter 5

5 Characterization of position errors and electrical noise

It is a declared goal of this project to improve the precision of CIPT measurements on MTJs (see section 1.3). In relation to achieve this goal, it is useful to gain some insight into the nature of electrode position errors, which are known to be a limiting factor with respect to measurement precision. However, electrode positions errors are best evaluated based on measurements on single sheet samples. This is due to the fact that only for single sheet samples will the vdp method truly correct for positional errors, and thus allow us to correctly estimate the size of said errors. In this chapter we therefore characterize the electrode position errors in measurements on a Ru thin film sample (see section 3.4) using the M12PP described in section 3.1, which is the same probe type being used for CIPT measurements.

The standard deviation of the static electrode position error is shown to be on the order of 5 nm, which significantly affects the result of single configuration measurements. Position error corrected dual configuration measurements, however, are shown to eliminate the effect of position errors to a level limited either by electrical measurement noise or dynamic position errors. The probe contact points remain almost static on the surface during the measurements (measured on an atomic scale) with a standard deviation of the dynamic position errors of 3 Å. Furthermore it is demonstrated how to experimentally distinguish between different sources of measurement errors, e.g. electrical measurement noise, probe geometry error as well as static and dynamic electrode position errors. New measurement systems and probe designs may be evaluated and benchmarked against each other using the same strategy, which is the topic of section 5.3.

This chapter is based on and repeats text and figures from paper II.

5.1 Experimental

Measurements were performed using a current of either 200 or 2000 μA at 24.11 Hz and an integration time of 83 ms. For each sub-probe the following sequence of measurement configurations was run during each probe-sample engage: A, B, A' and B'. For studies of the dynamic in-line position error the standard deviations on $\Delta R_A = R_A - R_{A'}$ and $\Delta R_B = R_B - R_{B'}$ were used since variations in ΔR are largely unaffected by static position errors and probe geometry errors. Possible offsets between measurements in A- and A'- and/or B- and B'-configurations will not affect the relative standard deviation of the results.

The eight sub-probe geometries and corresponding geometric pre-factors α , β and γ_w , used for AB position error correction (vdp method and first order approximation), are summarized in Tab. 5.1.

s_1	s_2	s_3	$\langle s \rangle$	α	β	γ
μm	μm	μm	μm			
1.50	1.50	1.50	1.50	1.61	2.71	0.75
2.00	2.25	2.50	2.25	1.62	2.71	0.75
3.00	3.00	3.00	3.00	1.61	2.71	0.75
4.50	4.50	3.75	4.25	1.56	2.44	0.77
4.50	4.50	4.50	4.50	1.61	2.71	0.75
6.00	6.00	5.25	5.75	1.57	2.50	0.77
7.50	7.75	6.75	7.33	1.55	2.45	0.77
9.00	8.25	7.50	8.25	1.62	2.71	0.75

Tab. 5.1: Geometric details of the eight sub-probes formed using the 12-point probe. Distances between neighboring electrodes (s_1 , s_2 , and s_3), mean probe pitch, $\langle s \rangle$, and geometric pre-factors (α , β , and γ) are listed. Reproduced from paper II.

5.2 Results and discussion

Measurements were carried out as a rectangular area scan of 10 by 10 points distributed with a step size of $100\ \mu\text{m}$ in a homogeneous area of the sample. The scan was repeated in the same area to compare measurements at $200\ \mu\text{A}$ and $2000\ \mu\text{A}$, respectively. Fig. 5.1 summarizes the results of the measurements at $2000\ \mu\text{A}$; here the sheet resistances, R_s , with respective errors are shown as a function of the mean probe pitch. Sheet resistances extracted directly from A or B measurements using Eqs. 2 or 3 are shown along with position error corrected sheet resistances calculated using the same data. Position error correction is carried out using the vdp method (see Eq. 16) as well as the first order approximation (see Eq. 22). From Fig. 5.1 it is clear that both error correction schemes result in almost identical extracted sheet resistances and a low standard deviation, while sheet resistances extracted directly from A or B measurements deviate significantly from the position corrected mean and have a much larger standard deviation. Measurements at $200\ \mu\text{A}$ are not shown but give essentially the same results.

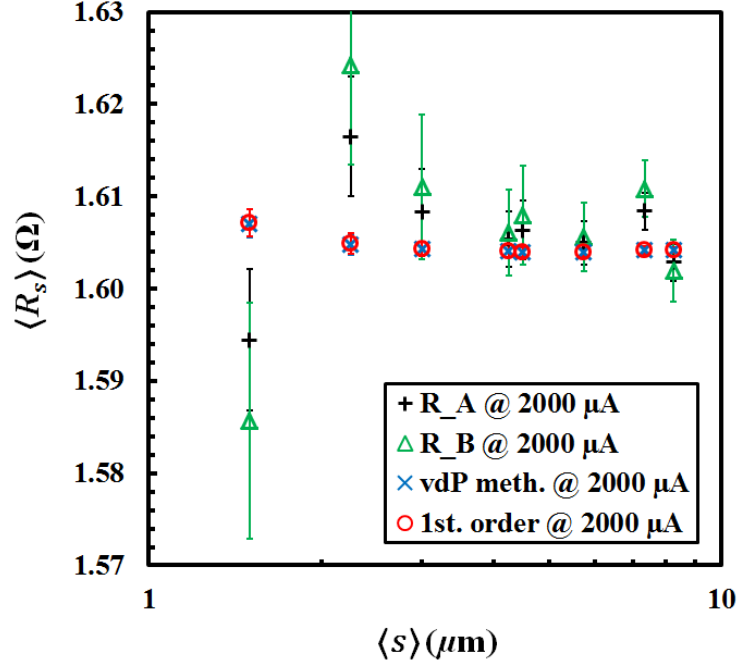


Fig. 5.1: The mean sheet resistance for A- and B-configuration measurements as well as position corrected values based on the van der Pauw (vdp) method and the first order approximation as a function of the mean electrode pitch $\langle s \rangle$. Measurements were obtained with an applied current of 2000 μA . Error-bars indicate the standard deviation. Reproduced from paper II.

For the static position error analysis, the relative standard deviations of the measured resistances are plotted in Fig. 5.2. As predicted by Eqs. 13-14, we observe a higher relative standard deviation for measurements in the B-configuration as compared to that of measurements in the A-configuration. We observe that the standard deviations decrease approximately inversely with the mean electrode pitch, which indicates that positional errors constitute the dominant source of error in this experiment. Changing the current by an order of magnitude does not influence the standard deviation significantly. Applying the expressions of Eqs. 7-8 to the measurement data in Fig. 5.2 allows the static in-line position error of the electrodes to be estimated. From Fig. 5.3 we observe that the standard deviations of static in-line position errors are in the range from 4.5 nm to 7.2 nm and without any clear correlation to neither the applied current nor the mean pitch. The values are significantly lower than what has previously been reported (20 nm) in similar experiments [51]. We find a remarkable agreement between the in-line position errors extracted from A- and B-configuration measurements, respectively. This supports the validity of Eqs. 7-8.

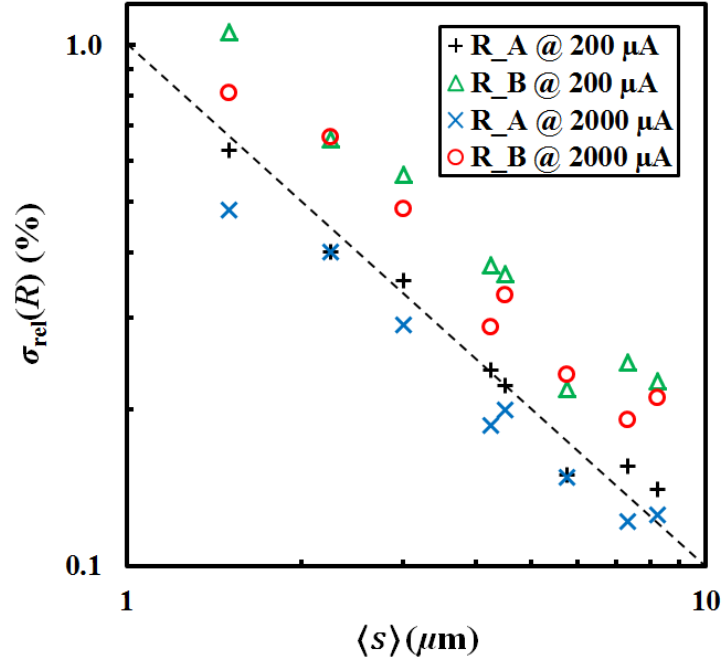


Fig. 5.2: The relative standard deviation of A- and B-configuration measurements at applied currents of 200 μA and 2000 μA as a function of the mean electrode pitch $\langle s \rangle$. A trend line with a slope of -1 decade/decade is added. Reproduced from paper II.

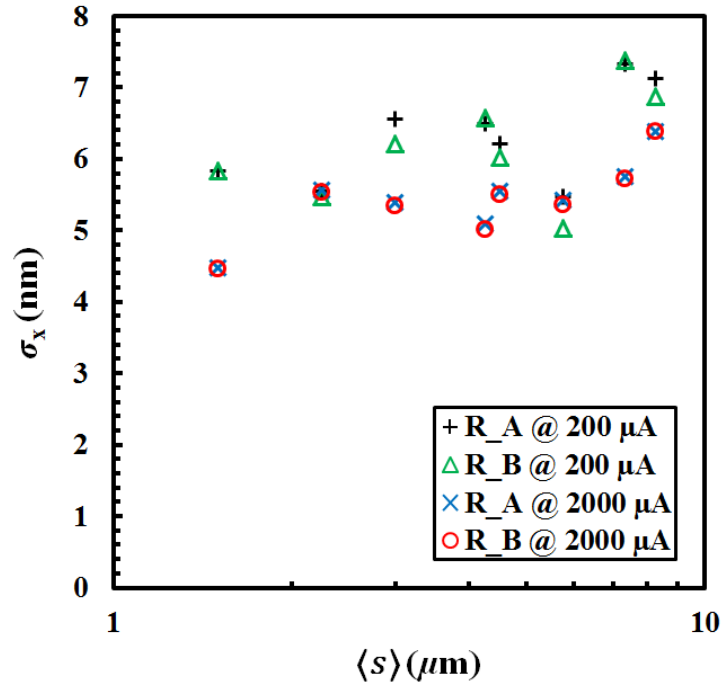


Fig. 5.3: The standard deviation of the in-line electrode positions for A- and B-configurations respectively at applied currents of 200 μA and 2000 μA as a function of mean electrode pitch $\langle s \rangle$. Reproduced from paper II.

Fig. 5.4 shows a plot of the relative standard deviation of ΔR for A- and B-configuration measurements, respectively. The standard deviations at $200\ \mu\text{A}$ are independent of the mean electrode pitch and differ from those at $2000\ \mu\text{A}$ that are approximately inversely proportional to the electrode pitch. The data at $2000\ \mu\text{A}$ are consistent with dynamic position errors with a standard deviation of $\sim 3\ \text{\AA}$, while the data at $200\ \mu\text{A}$ are consistent with electrical measurement noise with a standard deviation of $\sim 65\ \text{nV}$. The electrical measurement noise hardly affects the precision of the measurements at the higher current level. Again, the relative magnitudes of the standard deviations in A- and B-configuration measurements are in agreement with theory.

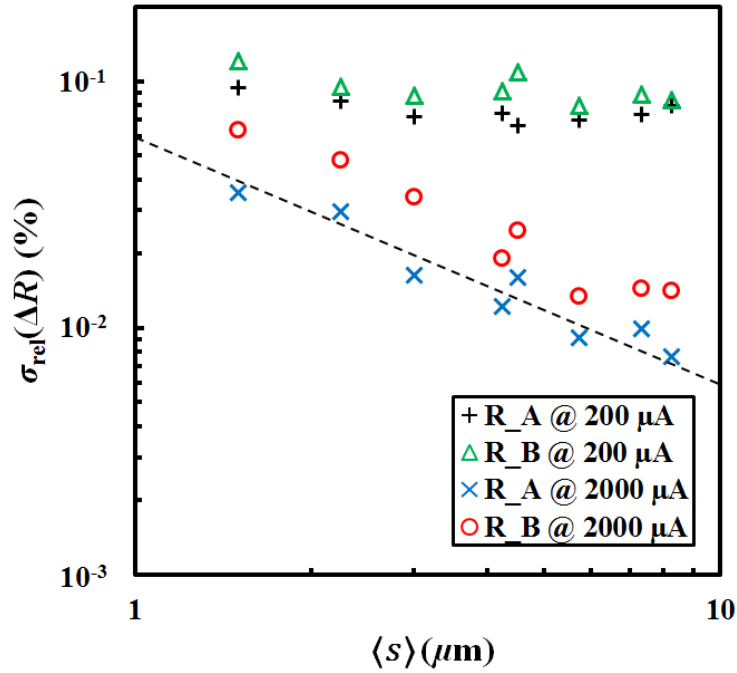


Fig. 5.4: The relative standard deviation of ΔR for A- and B-configuration measurements, respectively, at applied currents of $200\ \mu\text{A}$ and $2000\ \mu\text{A}$ as a function of mean electrode pitch $\langle s \rangle$. A trend line with a slope of -1 decade/decade is added. Reproduced from paper II.

To the extent that positional errors are indeed static throughout the measurement sequence for each subset of four electrodes and entirely located along the line of contact points they can be compensated for using the position correction algorithms, Eqs. 16 and 19. Here the two methods are compared by applying them to the measurements presented in Fig. 5.1 - Fig. 5.4. The results are shown in Fig. 5.5 and represent statistics on the position corrected sheet resistance results of the first A-B pair for each subset of four electrodes; the other possible A-B pairs give almost identical results.

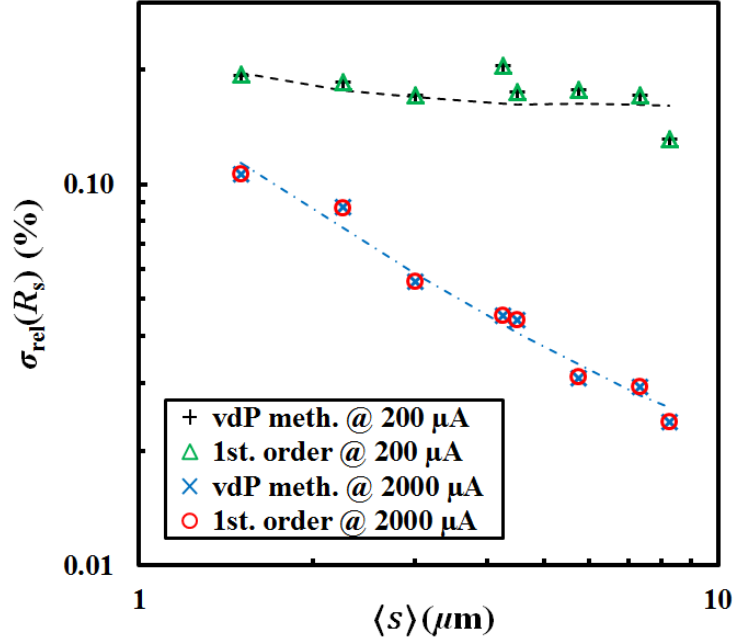


Fig. 5.5: The relative standard deviation of the position corrected sheet resistance as a function of the mean electrode pitch $\langle s \rangle$. Position corrections based on the van der Pauw (vdp) method and the first order approximation were used. The curves represent Monte Carlo simulations mimicking the σ_x measurement conditions (parameters: $\sigma_x = 5$ nm, $\sigma_x^{\text{dyn}} = 0.3$ nm and $V_n = 65$ nV). Reproduced from paper II.

It is easily recognized that the two position correction algorithms perform equally well. For the measurements at $200 \mu\text{A}$ there is almost no pitch related trend, which implies that for this dataset (after position correction is applied) electrical noise is the dominant source of residual error. When the current is increased to $2000 \mu\text{A}$, the position corrected data yields a significantly lower relative standard deviation and there is a clear trend of decreasing standard deviation for increasing pitch, which means that position errors are still dominant. These errors cannot be corrected for using the position correction algorithms and must therefore be a combination of the following factors: static off-line errors, dynamic off-line errors or dynamic in-line errors, which cannot be corrected by the algorithms. The curves in Fig. 5.5 are results of Monte Carlo simulations using static position errors with a standard deviation of 5 nm, dynamic position errors with a standard deviation of 3 Å and an electrical measurement noise with a standard deviation of 65 nV. Both position corrected measurements at $200 \mu\text{A}$ and $2000 \mu\text{A}$ are consistent with these three error sources found from the single configuration analysis.

To investigate possible ageing effects on the probe position errors, a micro-probe was engaged at 5000 measurement locations distributed in a small homogeneous area of the wafer. Using a current of $2000 \mu\text{A}$ measurements with eight sub-probes were carried out in a sequence containing four electrode configurations, A, B, A' and B', at each measurement position. Evaluating data sub-sets of 100 consecutive measurements the individual static in-line position error for each sub-probe and electrode configuration, $\sigma_x^{\text{sub,A}}$ and $\sigma_x^{\text{sub,B}}$, was found. Fig. 5.6 shows mean-, maximum- and minimum-value of σ_x evaluated across all sub-probes and electrode configurations. The average static in-line position error, $\langle \sigma_x^{\text{all}} \rangle$, was found to be 5.1 nm with minimum position error $\sigma_{x,\text{min}}^{\text{all}} = 3.9$ nm and maximum

position error $\sigma_{x,\max}^{\text{all}} = 7.5$ nm. A slight decrease in position error is seen with increasing measurement age of the probe.

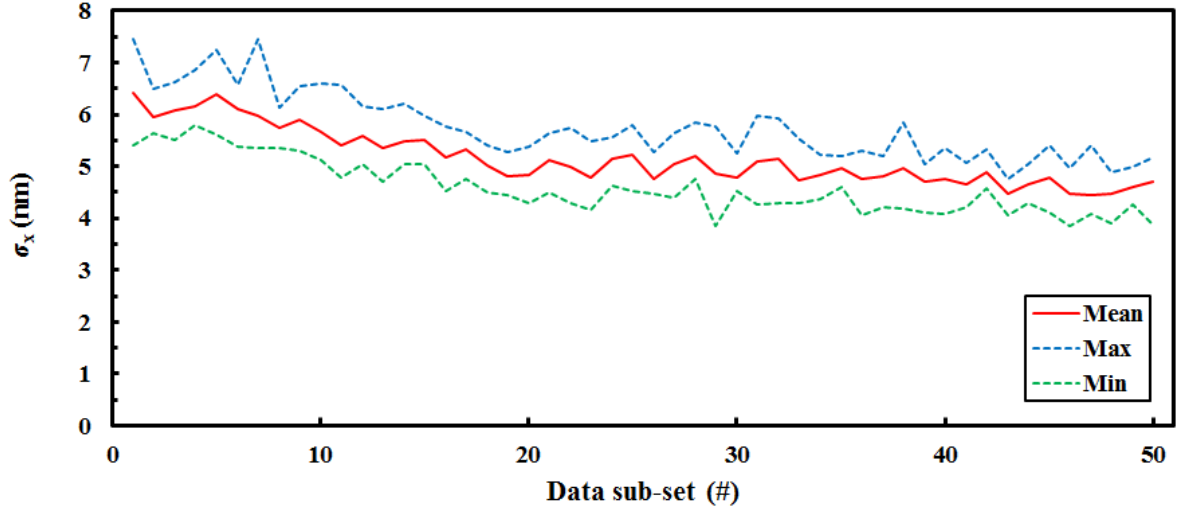


Fig. 5.6: Static in-line position error evaluated across 50 data sub-sets containing 100 unique and consecutive measurements in an area scan totaling 5000 points. For each sub-set of data σ_x is evaluated individually for each sub-probe and electrode configuration and we show mean-, maximum- and minimum-value of σ_x evaluated across all sub-probes and electrode configurations. Reproduced from paper II.

Fig. 5.7 shows the relative standard deviation of ΔR for A-configuration measurements evaluated across the 50 data sub-sets. No clear aging trend is observed.

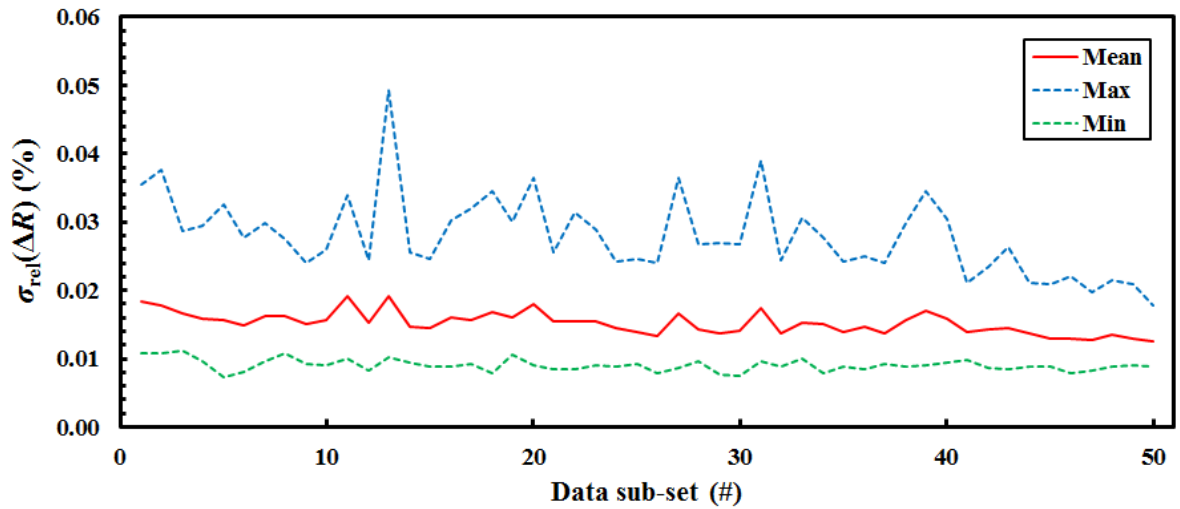


Fig. 5.7: The relative standard deviation of ΔR for A-configuration measurements evaluated across 50 data sub-sets containing 100 unique and consecutive measurements in an area scan totaling 5000 points. For each sub-set of data $\sigma_{\text{rel}}(\Delta R)$ is evaluated individually for each sub-probe and we show mean-, maximum- and minimum-value of $\sigma_{\text{rel}}(\Delta R)$ evaluated across all sub-probes. Reproduced from paper II.

5.3 Evaluation of alternative probe design

During measurements for the study presented above the tool's fan-filters were turned off. However, in a production environment the FFUs of the tool will be running to keep a clean environment, which will result in an increased vibration level inside the tool. Other production related sources of vibrations includes pumps incorporated in other tools or service facilities of the fab itself. To meet the challenge of a vibration intense environment alternative probe designs are being developed and can be compared and benchmarked against each other using the characterization strategy presented above.

Here we present in partial a preliminary, comparative study of the two probe designs. An experimental 12-point probe incorporating ?-shaped ("question mark"-shaped), SiO₂ cantilever electrodes (see Fig. 5.8) was compared with the straight cantilever probe used above. This probe has mean probe pitches in the range from 1.5 μm to 18.5 μm , three of which being obtained using sub-probes exactly matching those of the conventional 12-point probe ($\langle s \rangle = 1.5 \mu\text{m}$, 3 μm and 4.5 μm).

Measurements were performed while running the fan-filter of the tool at different speeds (airflows): 0.49 m/s (low vibration level), 0.65 m/s (medium vibration level) and 0.72 m/s (high vibration level). Area scan arrays of 10x10 points with a step size of 100 μm were measured. The results presented in Fig. 5.9 covers data obtained at 3 nominally, identical sub-probes ($\langle s \rangle = 1.5 \mu\text{m}$, 3 μm and 4.5 μm) for the two probe designs. It is clear from the plot that the ?-shaped probe provides a lower relative standard deviation even at low vibration level. As the vibration intensity is increased the ?-shaped probe retains a relative standard deviation of less than 0.1% at a probe pitch of 1.5 μm , which corresponds to the performance of the straight cantilever probe at low vibration level. At high vibration level the straight cantilever probe returns a relative standard deviation of 0.22%.

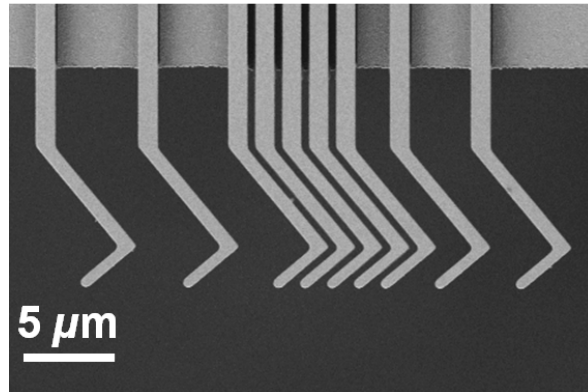


Fig. 5.8: Section of a scanning electron micrograph of an experimental 12-point probe with Au-coated, ?-shaped cantilever electrodes.

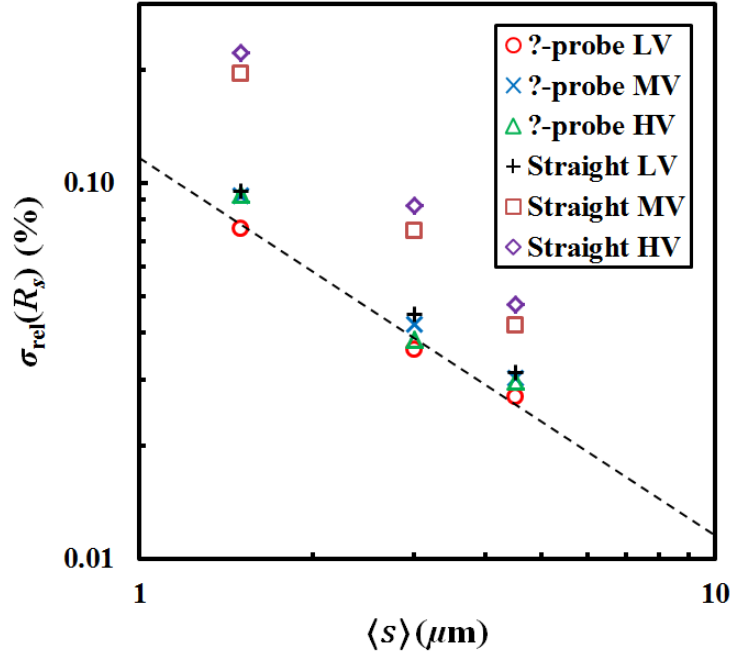


Fig. 5.9: The relative standard deviation of the position corrected sheet resistance obtained using two different probe designs, straight cantilever and ?-shape cantilever probes, at three different vibration levels (low LV, medium MV and high HV). A trend line with a slope of -1 decade/decade is added.

5.4 Summary

We have experimentally shown that the dominant sources of error in single configuration micro four-point probe sheet resistance measurements are in-line probe geometry errors and in-line static position errors. These errors were shown to be eliminated very effectively using dual-configuration measurements and position error correction algorithms. At the error level observed in this study both position error correction algorithms – van der Pauw and the first order approximation by D.C. Worledge – are equally effective, this will not be the case at large relative position errors where the van der Pauw method is the better choice.

The standard deviation of the static in-line position error for measurements with Au coated electrodes on Ru thin film samples was found to be in the range from 3.9 nm to 7.5 nm. The standard deviation of the dynamic in-line position error was shown to be small ~ 3 Å and only detectable in measurements with high measurement current. At lower measurement currents the electrical measurement noise was the dominant error source. No significant ageing effect on position errors (except for a very slight reduction in position error with measurement age) was observed for a probe in the course of 5000 measurements. Finally we have demonstrated how new probe designs may be evaluated and benchmarked against each other using the same strategy.

Chapter 6

6 Enhanced precision for CIPT measurements

In this chapter focus will be aimed at four-point measurements on MTJ samples and in particular the influence of electrode position errors will be described. In section 2.2.1 and 2.2.2 analytical expressions covering static in-line errors and their reduction based on first order position correction were presented. Here we use Monte Carlo (MC) simulations to unfold the scenario to include static and dynamic, in-line and off-line errors as well as electrical noise and compare the performance of both vdp and first order position correction (here denoted “dcw”) while evaluating all available configuration combinations; AB, AC and BC. We show that for all scenarios vdp correction based on AC-configuration measurements, vdp(AC), outperforms all other correction schemes.

Based on the results presented in the previous chapter on specific position errors for the M12PP used in this project, MC simulations are carried out mimicking the performance of this probe and the available corrections schemes on a range of MTJs. This allows us to evaluate the dynamic range of the probe and we find vdp(AC) correction to provide the largest dynamic range for the probe.

Actual four-point resistance measurements recorded on an MTJ sample are compared to simulated results indicating that electrode position errors on this sample are roughly one order of magnitude larger as compared our findings reported in chapter 5.

To further enhance the precision of CIPT measurements we propose the use of added sub-probes with nominally identical electrode distances. We use theoretical calculations to prove the existence of an optimal, overlapping pin combination for two sub-probes.

Finally, a new equidistant probe design for high precision CIPT measurements is presented.

6.1 Experimental

The presented four-point resistance measurements were performed using a current of $2000\ \mu\text{A}$ at 24.11 Hz and an integration time of 83 ms. The probe itself is described in section 3.1 and for each sub-probe the following sequence of measurement configurations was run during each probe-sample engage: A, B, C, A', B' and C'. This measurement sequence was used to allow for comparison of position correction based on AB-, AC- and BC-configurations.

6.2 Results and discussion

Since the results presented in this section include several figures, subsections have been added to create a better overview and in rare cases a figure is shown prior to its formal introduction in the text.

6.2.1 Static position errors

MC simulations were carried out to determine the influence of static in-line errors, $\sigma_x/s = 1\%$, on the measured four-point resistance. Fig. 6.1 shows the relative standard deviation of single configuration and position corrected four-point resistances as a function of equidistant electrode spacing, s , (normalized to λ) for an MTJ sample with $R_t/R_b = 10$. Since we consider only static errors, the relation $R_c = R_A - R_B$ holds true also for MTJs [54]–[56]. Thus the position corrections based on the vdp-method and the first order approximation (dcw) are independent of the specific combination of configuration (AB, AC or BC). The plotted results are in excellent agreement with the theoretical predictions presented in Fig. 2.10 and it is noted that the vdp method results in a lower relative standard deviation as compared to the first order correction. As the R_t/R_b -ratio of the sample is lowered so is the influence of static in-line errors on the position corrected results, which is evident from Fig. 6.2 ($R_t/R_b = 1$) and Fig. 6.3 ($R_t/R_b = 0.1$). This is also in line with theory (see section 2.2.2) predicting single sheet behavior for MTJs for $R_t/R_b \rightarrow 0$ and at electrode spacing $s \ll \lambda$ or $s \gg \lambda$, and therefore the position correction algorithms completely eliminates static, in-line errors in these regimes.

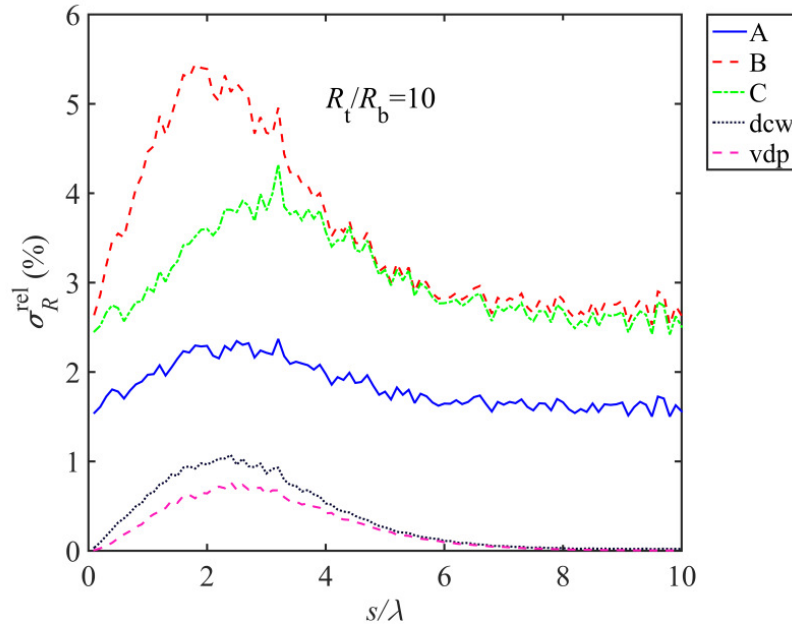


Fig. 6.1: The relative standard deviation of single configuration and position corrected four-point resistances as a function of equidistant electrode spacing, s , (normalized to λ) for an MTJ sample with $R_t/R_b = 10$. Position corrections based on the vdp-method (vdp) and the first order approximation (dcw) were used. The presented data is based on Monte Carlo simulations (parameters: $\sigma_x/s = 1\%$, 500 iterations).

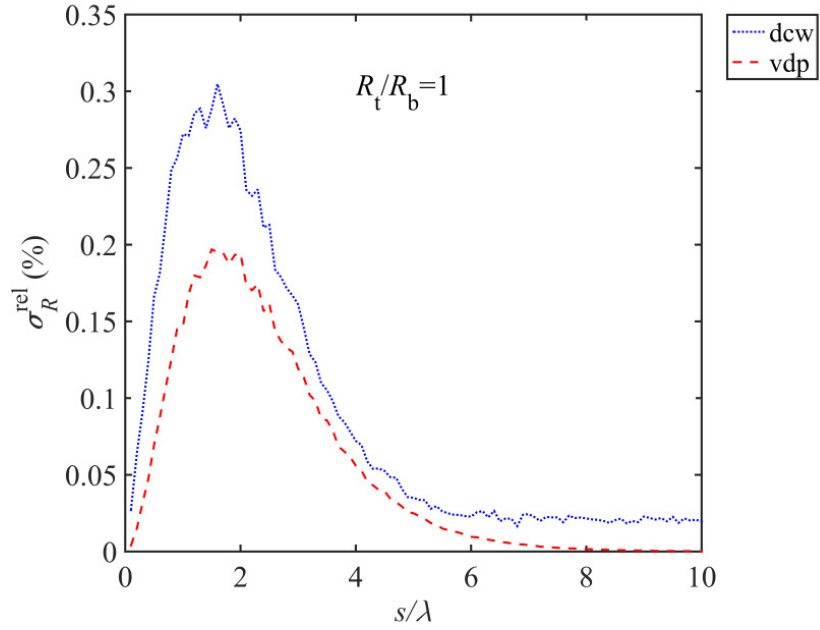


Fig. 6.2: The relative standard deviation of position corrected four-point resistances as a function of equidistant electrode spacing, s , (normalized to λ) for an MTJ sample with $R_t/R_b = 1$. Position corrections based on the vdp-method (vdp) and the first order approximation (dcw) were used. The presented data is based on Monte Carlo simulations (parameters: $\sigma_x/s = 1\%$, 500 iterations).

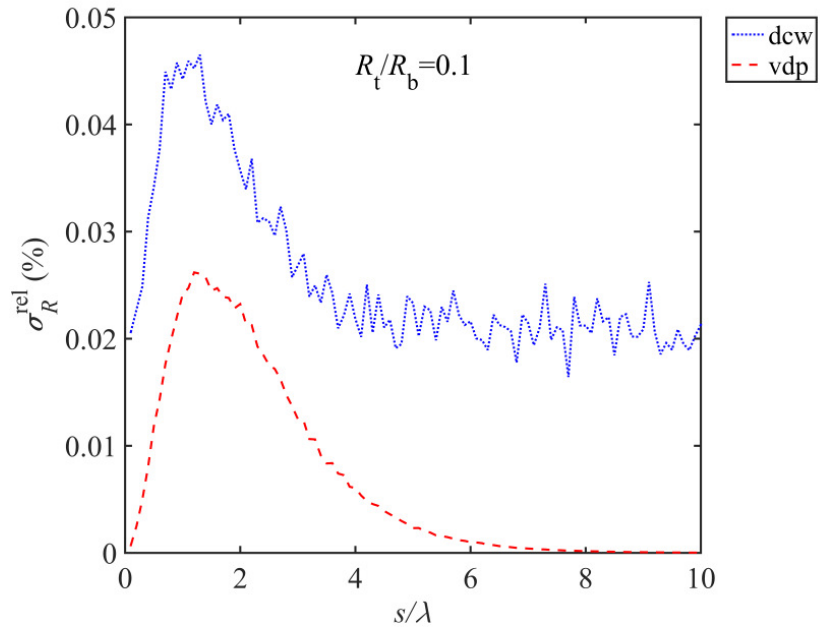


Fig. 6.3: The relative standard deviation of position corrected four-point resistances as a function of equidistant electrode spacing, s , (normalized to λ) for an MTJ sample with $R_t/R_b = 0.1$. Position corrections based on the vdp-method (vdp) and the first order approximation (dcw) were used. The presented data is based on Monte Carlo simulations (parameters: $\sigma_x/s = 1\%$, 500 iterations).

The position correction strategies do not correct for static off-line errors. The results of MC simulations for, $\sigma_y / s = 1\%$, are presented in Fig. 6.4 and for all s/λ the lowest relative standard deviation is obtain for single A-configuration measurements. However, on the absolute scale the influence of off-line errors are limited and for realistic scenarios where $\sigma_x \approx \sigma_y$ the influence of σ_x will overshadow that of the off-line error.

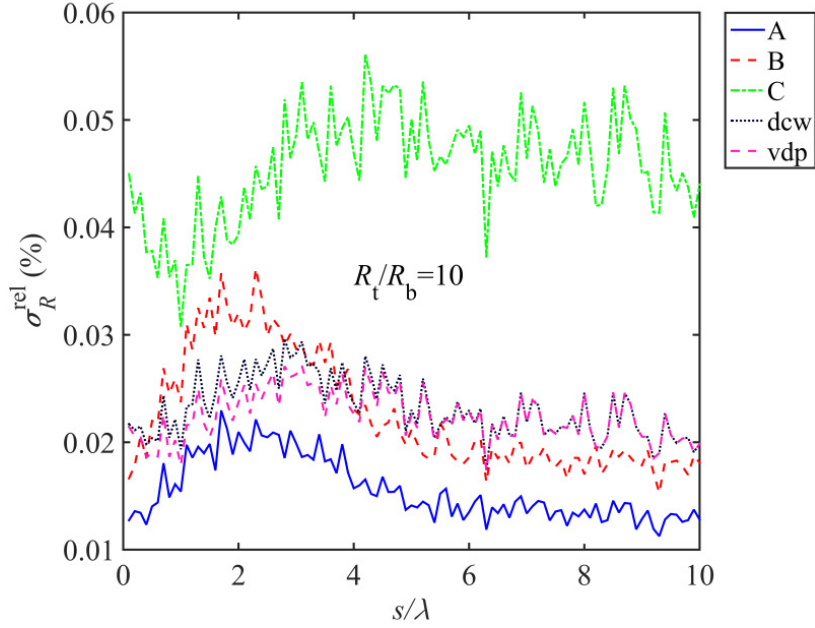


Fig. 6.4: The relative standard deviation of single configuration and position corrected four-point resistances as a function of equidistant electrode spacing, s , (normalized to λ) for an MTJ sample with $R_t/R_b = 10$. Position corrections based on the vdp-method (vdp) and the first order approximation (dcw) were used. The presented data is based on Monte Carlo simulations (parameters: $\sigma_y / s = 1\%$, 500 iterations).

6.2.2 Dynamic position errors

Since R_A , R_B and R_C are not measured simultaneously the relation, $R_C = R_A - R_B$, no longer holds true in the presence of dynamic errors, and theory predicts different response to dynamic in-line errors for AB, AC and BC correction, respectively (see Eqs. 28-30). The influence of dynamic in-line errors, $\sigma_x^{\text{dyn}} / s = 1\%$, has been simulated for three different R_t/R_b -ratios and the results are plotted in Fig. 6.5 ($R_t/R_b = 10$), Fig. 6.6 ($R_t/R_b = 1$) and Fig. 6.7 ($R_t/R_b = 0.1$). Comparing the three plots we immediately recognize the single sheet behavior of MTJs for $R_t/R_b \rightarrow 0$ and at electrode spacing $s \ll \lambda$ or $s \gg \lambda$. In these “single sheet”-regimes the sensitivity to position errors matches the theoretical predictions for single sheet samples (see Eqs. 28-30). For the full range of s/λ AC correction yields the lowest relative standard deviation, and at an intermediate range around $s \approx \lambda$, the vdp(AC) method performs slightly better than the corresponding first order correction, dcw(AC). Single A-configuration measurements result in lower relative standard deviation as compared to both AB and BC correction. In particular AB correction always yields larger relative standard deviation than any other position correction scheme or

single configuration measurements. At intermediate range around $s \approx \lambda$ the gap between vdp(AB) and single B-configuration measurements is closing for $R_t/R_b = 10$, but measurements using vdp(AB) and dcw(AB) correction remain at a significantly higher relative standard deviation than any other measurement scheme.

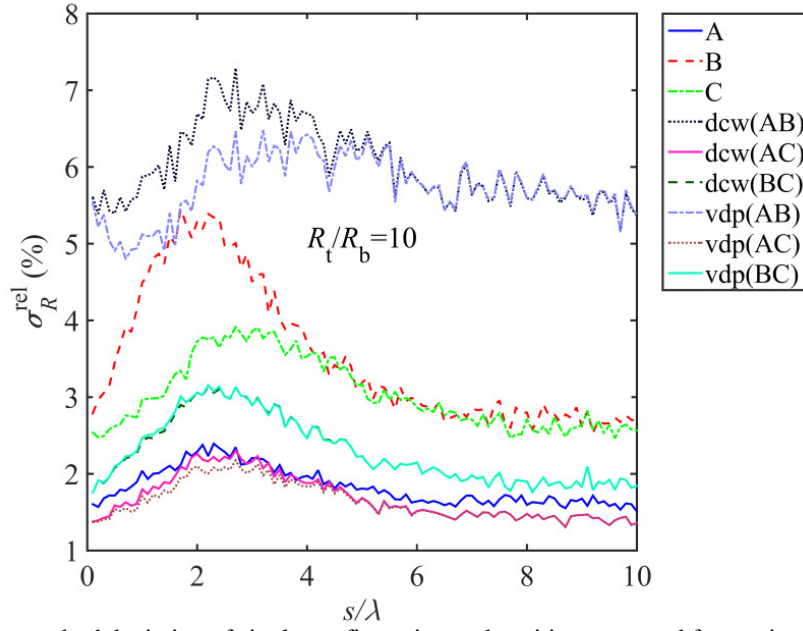


Fig. 6.5: The relative standard deviation of single configuration and position corrected four-point resistances as a function of equidistant electrode spacing, s , (normalized to λ) for an MTJ sample with $R_t/R_b = 10$. Position corrections based on the vdp-method (vdp) and the first order approximation (dcw) were used. The presented data is based on Monte Carlo simulations (parameters: $\sigma_x^{\text{dyn}} / s = 1\%$, 500 iterations).

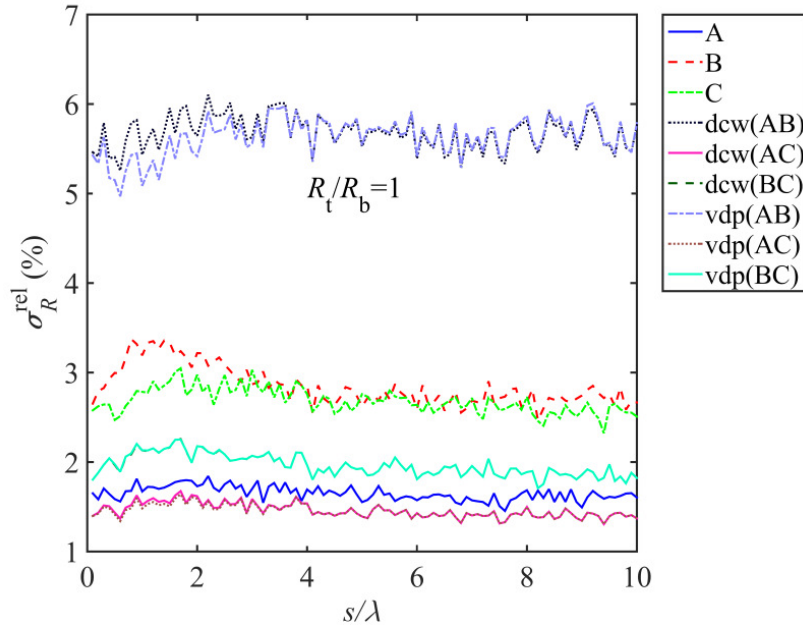


Fig. 6.6: The relative standard deviation of single configuration and position corrected four-point resistances as a function of equidistant electrode spacing, s , (normalized to λ) for an MTJ sample with $R_t/R_b = 1$. Position corrections based on the vdp-method (vdp) and the first order approximation (dcw) were used. The presented data is based on Monte Carlo simulations (parameters: $\sigma_x^{\text{dyn}} / s = 1\%$, 500 iterations).

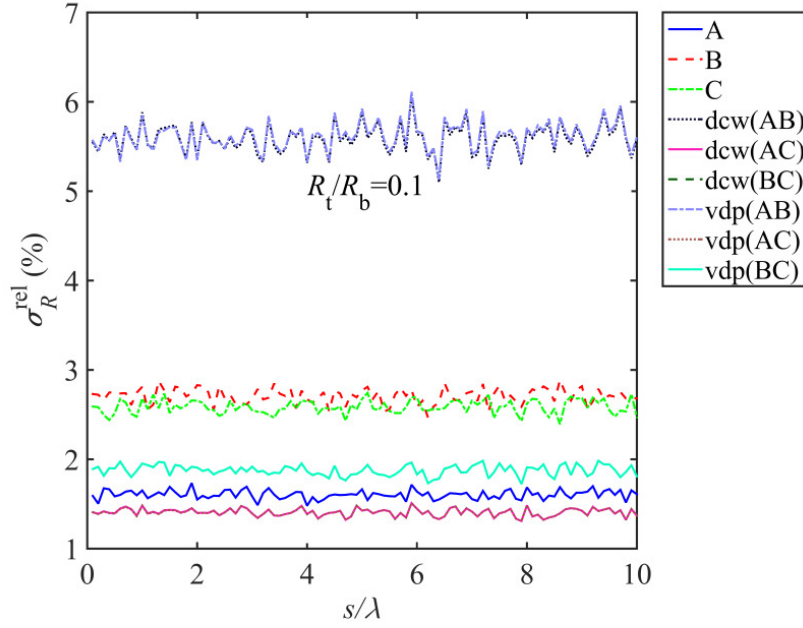


Fig. 6.7: The relative standard deviation of single configuration and position corrected four-point resistances as a function of equidistant electrode spacing, s , (normalized to λ) for an MTJ sample with $R_t/R_b = 0.1$. Position corrections based on the vdp-method (vdp) and the first order approximation (dcw) were used. The presented data is based on Monte Carlo simulations (parameters: $\sigma_x^{\text{dyn}} / s = 1\%$, 500 iterations).

Simulations of dynamic off-line errors are presented in Fig. 6.8 and the results are almost identical to what was observed for static off-line errors (see Fig. 6.4) with the one main difference being the significant response to dynamic errors exhibited by AB correction. However, the influence of dynamic off-line errors is still negligible as compared to that of in-line errors (static and dynamic).

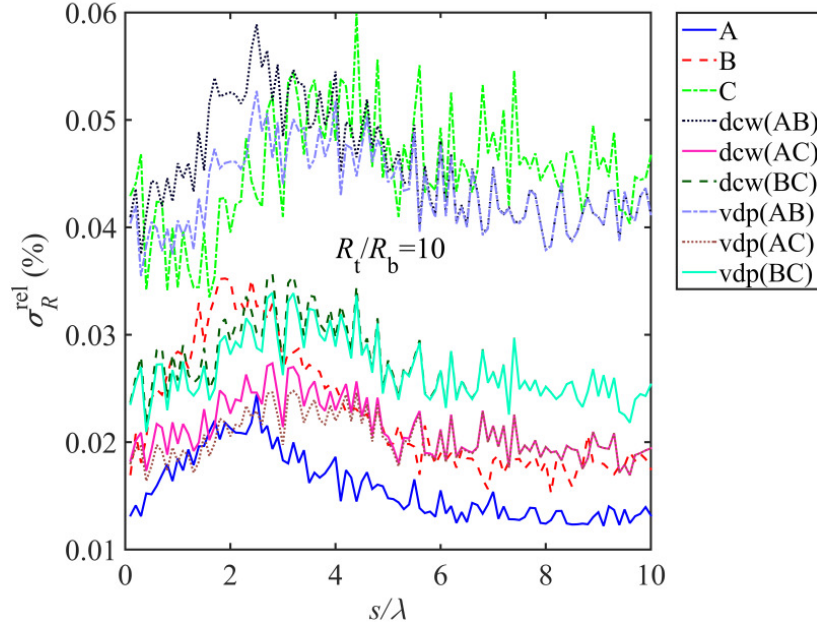


Fig. 6.8: The relative standard deviation of single configuration and position corrected four-point resistances as a function of equidistant electrode spacing, s , (normalized to λ) for an MTJ sample with $R_t/R_b = 10$. Position corrections based on the vdp-method (vdp) and the first order approximation (dcw) were used. The presented data is based on Monte Carlo simulations (parameters: $\sigma_y^{\text{dyn}} / s = 1\%$, 500 iterations).

6.2.3 Electrical noise

In the MTJ “single sheet”-regimes the sensitivity to electrical noise (see Fig. 6.9) is found to match the theoretical predictions for single sheet samples (see Eqs. 34-36). The electrical noise is assumed to be identical for all measurement configurations and is set to 0.01% with respect to R_A (note that the standard deviation for R_A remains constant at 0.01%). As was the case for off-line errors (static and dynamic) single A-configuration measurements yields the lowest relative standard deviation as a function of electrical noise. Comparing the different correction schemes also leads to the same conclusion as was found in the studies presented above, namely that AC correction and in particular vdp(AC) correction yields the lowest relative standard deviation.

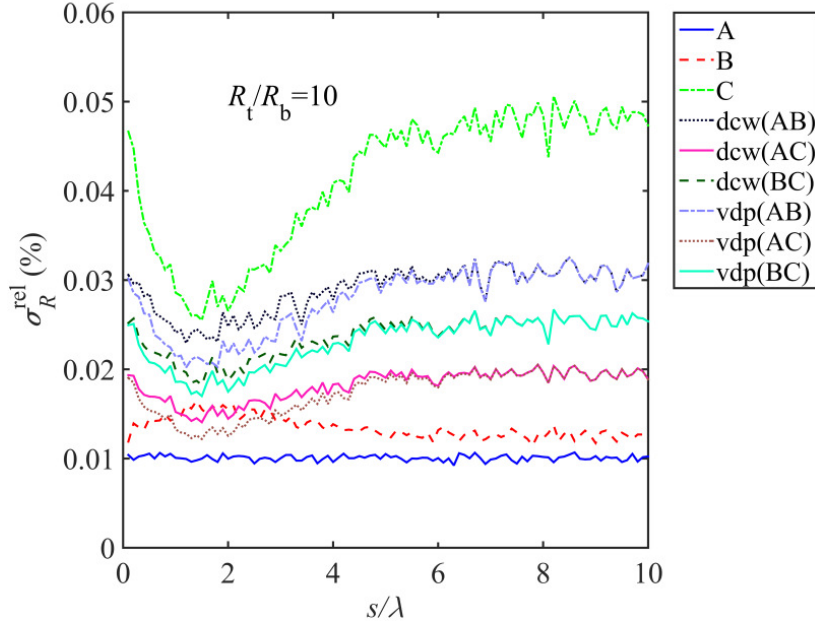


Fig. 6.9: The relative standard deviation of single configuration and position corrected four-point resistances as a function of equidistant electrode spacing, s , (normalized to λ) for an MTJ sample with $R_t/R_b = 10$. Position corrections based on the vdp-method (vdp) and the first order approximation (dcw) were used. The presented data is based on Monte Carlo simulations (parameters: E-noise = 0.01% (based on R_A), 500 iterations).

6.2.4 Combined errors

In the previous sections the three main categories of errors influencing the precision of four-point resistance measurements have been analyzed separately. In Fig. 6.10 the results of simulations combining static position errors, $\sigma_{x,y}/s = 1\%$, dynamic position errors, $\sigma_{x,y}^{\text{dyn}}/s = 0.1\%$, and electrical noise, 0.01% (based on R_A), are presented. With this combination of errors all position correction schemes yield relative standard deviations that are at least a factor of two lower than the best performing single configuration strategy, which is the A-configuration measurement. The vdp(AC) correction is consistently delivering the lowest relative standard deviation, which is also true when evaluating the results presented in Fig. 6.11. Here simulations were carried out for $\sigma_{x,y}/s = \sigma_{x,y}^{\text{dyn}}/s = 1\%$ and electrical noise, 0.01% (based on R_A). The increase of dynamic errors renders AB-correction useless compared to AC- and BC-correction and is surpassed in relative standard deviation only by single B-configuration measurements (for s in the range from λ to 3λ).

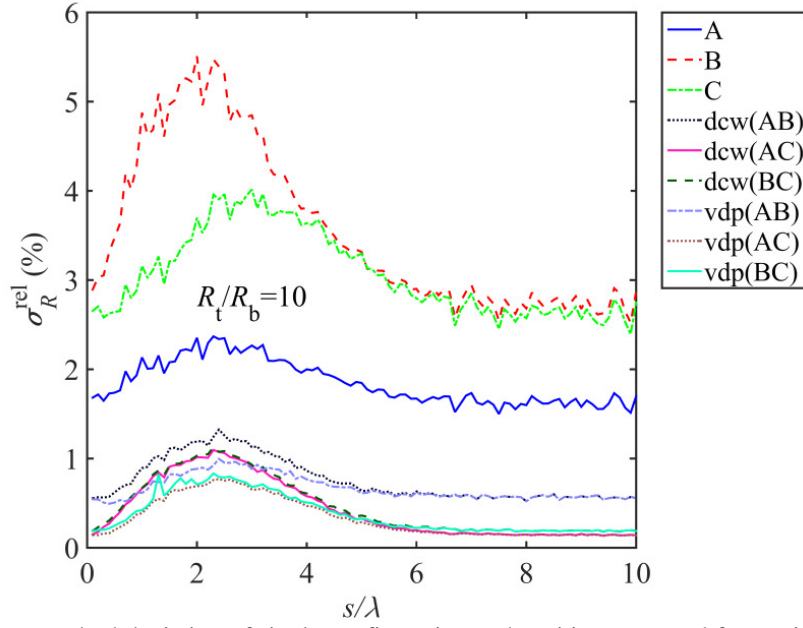


Fig. 6.10: The relative standard deviation of single configuration and position corrected four-point resistances as a function of equidistant electrode spacing, s , (normalized to λ) for an MTJ sample with $R_t/R_b = 10$. Position corrections based on the vdp-method (vdp) and the first order approximation (dcw) were used. The presented data is based on Monte Carlo simulations (parameters: $\sigma_{x,y} / s = 1\%$, $\sigma_{x,y}^{\text{dyn}} / s = 0.1\%$, E-noise = 0.01% (based on R_A), 500 iterations).

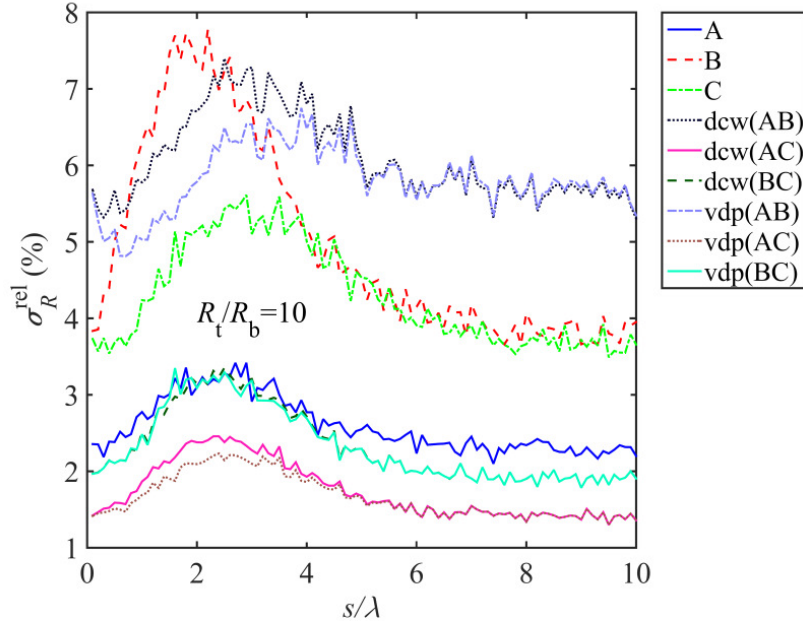


Fig. 6.11: The relative standard deviation of single configuration and position corrected four-point resistances as a function of equidistant electrode spacing, s , (normalized to λ) for an MTJ sample with $R_t/R_b = 10$. Position corrections based on the vdp-method (vdp) and the first order approximation (dcw) were used. The presented data is based on Monte Carlo simulations (parameters: $\sigma_{x,y}/s = 1\%$, $\sigma_{x,y}^{\text{dyn}}/s = 1\%$, E-noise = 0.01% (based on R_A), 500 iterations).

6.2.5 Increased dynamic range

In this section the dynamic range of the M12PP used in this project (see section 3.1) is evaluated through series of MC simulations mimicking full static field CIPT measurements (see section 3.3) on MTJs with a variation of λ and R_t/R_b -ratios. Throughout the study the sum of R_t and R_b is kept constant at $R_t + R_b = 10 \text{ } \Omega/\square$. The simulations also include position errors according to the findings presented in chapter 5; $\sigma_{x,y} = 5 \text{ nm}$ and $\sigma_{x,y}^{\text{dyn}} = 0.3 \text{ nm}$ as well as electrical noise of 1% (based on R_A). Based on these simulations we will be able to determine which position correction scheme provides the broadest dynamic range for the probe.

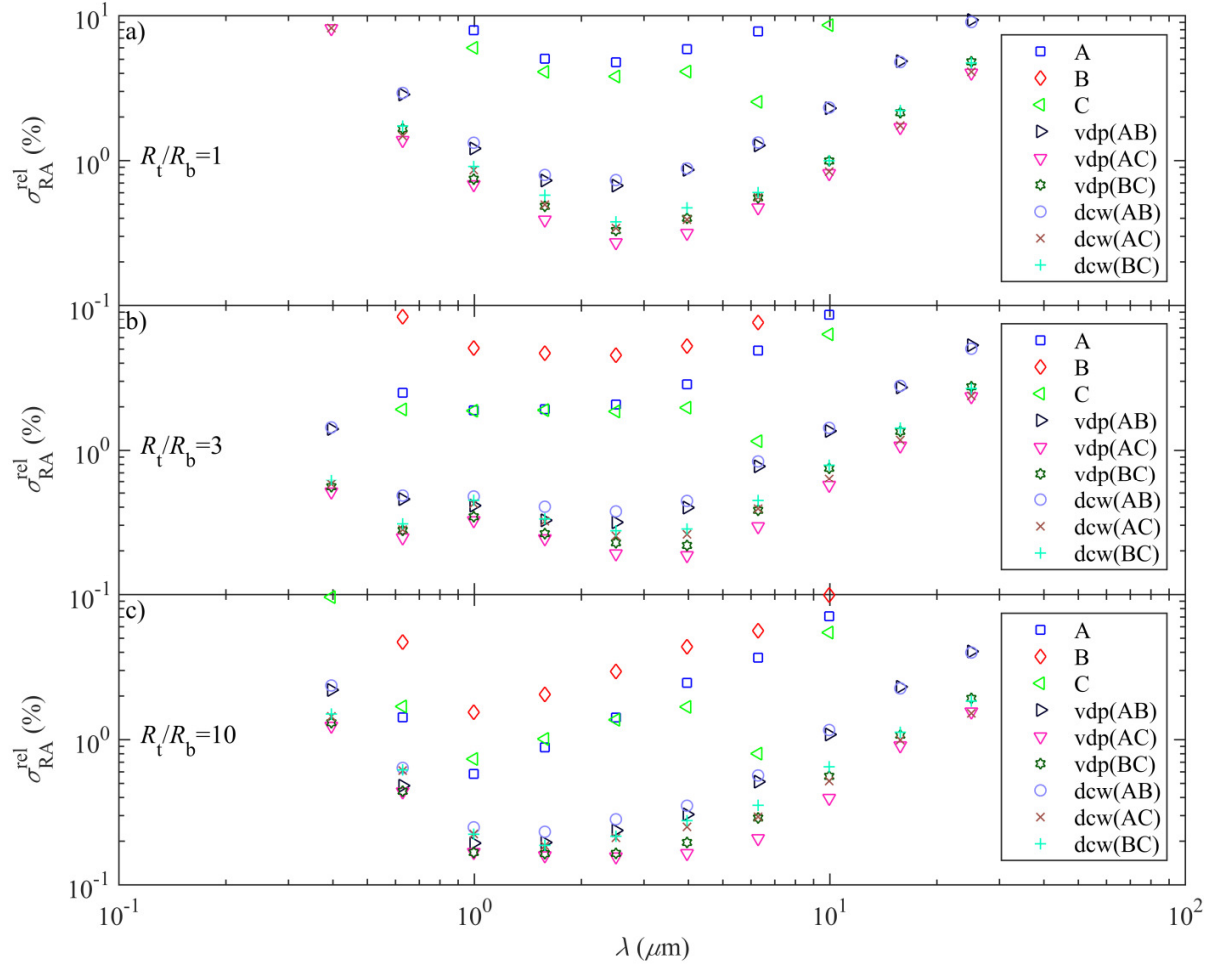


Fig. 6.12: The relative standard deviation of RA as a function of λ for an MTJ sample with $R_t/R_b = 1$ (a), $R_t/R_b = 3$ (b) and $R_t/R_b = 10$ (c). RA is extracted from CIPT-model-fits to series of single configuration and position corrected four-point resistances. Position corrections based on the vdp-method (vdp) and the first order approximation (dcw) were used. The presented data is based on Monte Carlo simulations mimicking the measurement conditions for one specific M12PP-design (parameters: $\sigma_{x,y} = 5$ nm, $\sigma_{x,y}^{\text{dyn}} = 0.3$ nm, E-noise = 0.01% (based on R_A), 100 iterations).

In Fig. 6.12 the relative standard deviation of the fitted RA, $\sigma_{\text{RA}}^{\text{rel}}$, is plotted as a function of λ for various CIPT measurement strategies including vdp and first order position correction. R_t/R_b is varied in three steps: $R_t/R_b = 1$ (see (a)), $R_t/R_b = 3$ (see (b)) and $R_t/R_b = 10$ (see (c)).

Similar plots are presented for the other fitting parameters; R_t (see Fig. 6.13) and R_b (see Fig. 6.14).

For RA the broadest dynamic range with respect to λ is observed for vdp(AC) correction and $R_t/R_b = 3$. In this range the relative standard deviation RA is roughly one order of magnitude lower for vdp(AC) correction as compared to single A-configuration measurements. In general the data series plotted in Fig. 6.12 (a) and Fig. 6.12 (b) forms parabolas, whereas the position corrected results for $R_t/R_b = 3$ seem to rise more slowly for $\lambda \rightarrow 0$. Focusing on the lower values of λ , which pose the greatest technical challenge, one might speculate that a slightly different R_t/R_b -ratio could turn out to be even more optimal than $R_t/R_b = 3$ for the estimation of RA at low λ .

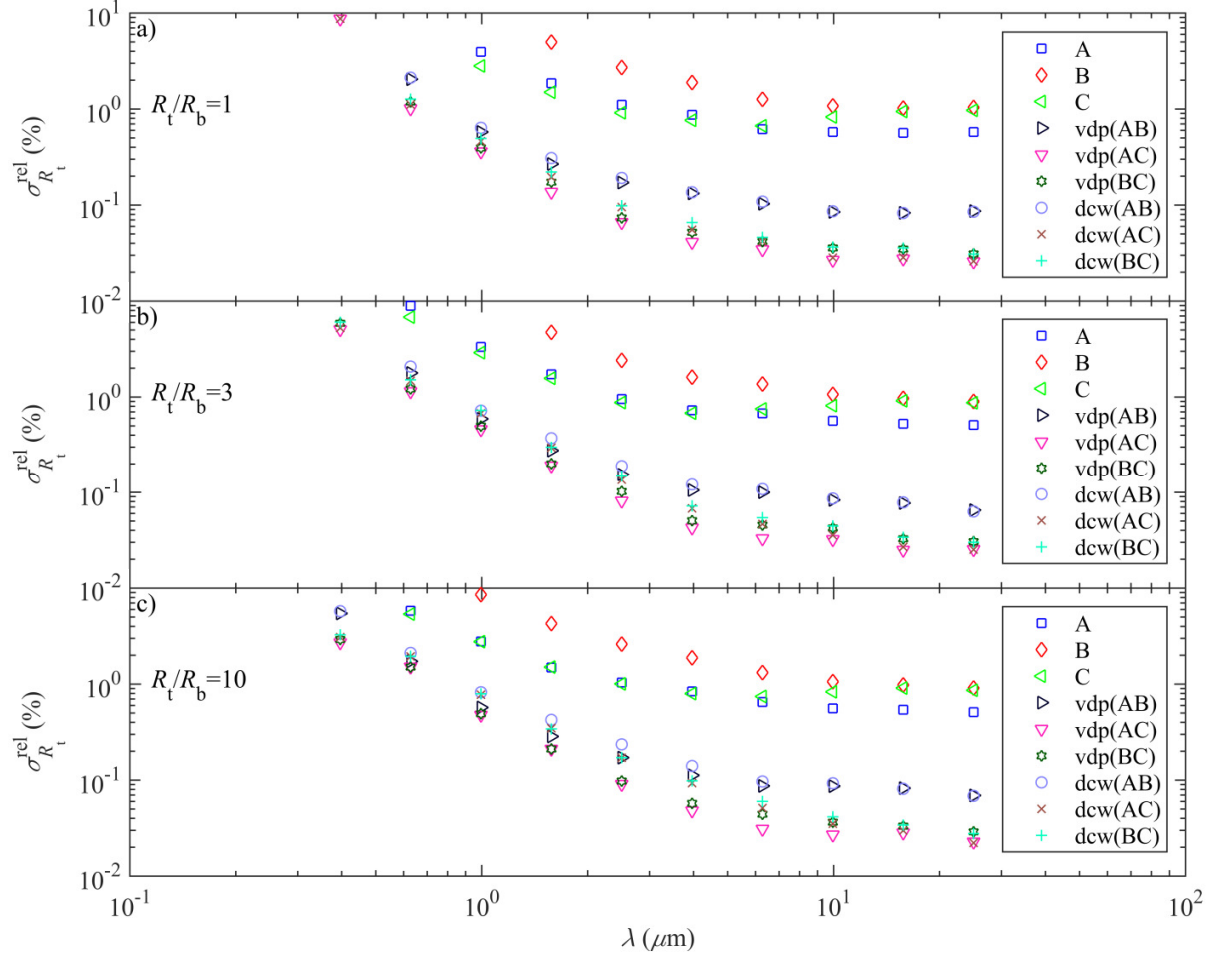


Fig. 6.13: The relative standard deviation of R_t as a function of λ for an MTJ sample with $R_t/R_b = 1$ (a), $R_t/R_b = 3$ (b) and $R_t/R_b = 10$ (c). R_t is extracted from CIPT-model-fits to series of single configuration and position corrected four-point resistances. Position corrections based on the vdp-method (vdp) and the first order approximation (dcw) were used. The presented data is based on Monte Carlo simulations mimicking the measurement conditions for one specific M12PP-design (parameters: $\sigma_{x,y} = 5$ nm, $\sigma_{x,y}^{\text{dyn}} = 0.3$ nm, E-noise = 0.01% (based on R_A), 100 iterations).

For R_t no clear trend is observed with respect to the R_t/R_b -ratio. In general the relative standard deviation is increasing for $\lambda \rightarrow 0$, which is in good agreement with the trend observed in Fig. 2.4, namely that $s \ll \lambda$ essentially R_t is measured. As λ is decreased the less information on R_t is picked up by the probe (minimum pitch of the applied probe in this case is fixed at $1.5 \mu\text{m}$). In the optimal range, $\lambda \geq 10 \mu\text{m}$ the relative standard deviation on R_t is 20 times lower for vdp(AC) correction as compared to single A-configuration measurements.

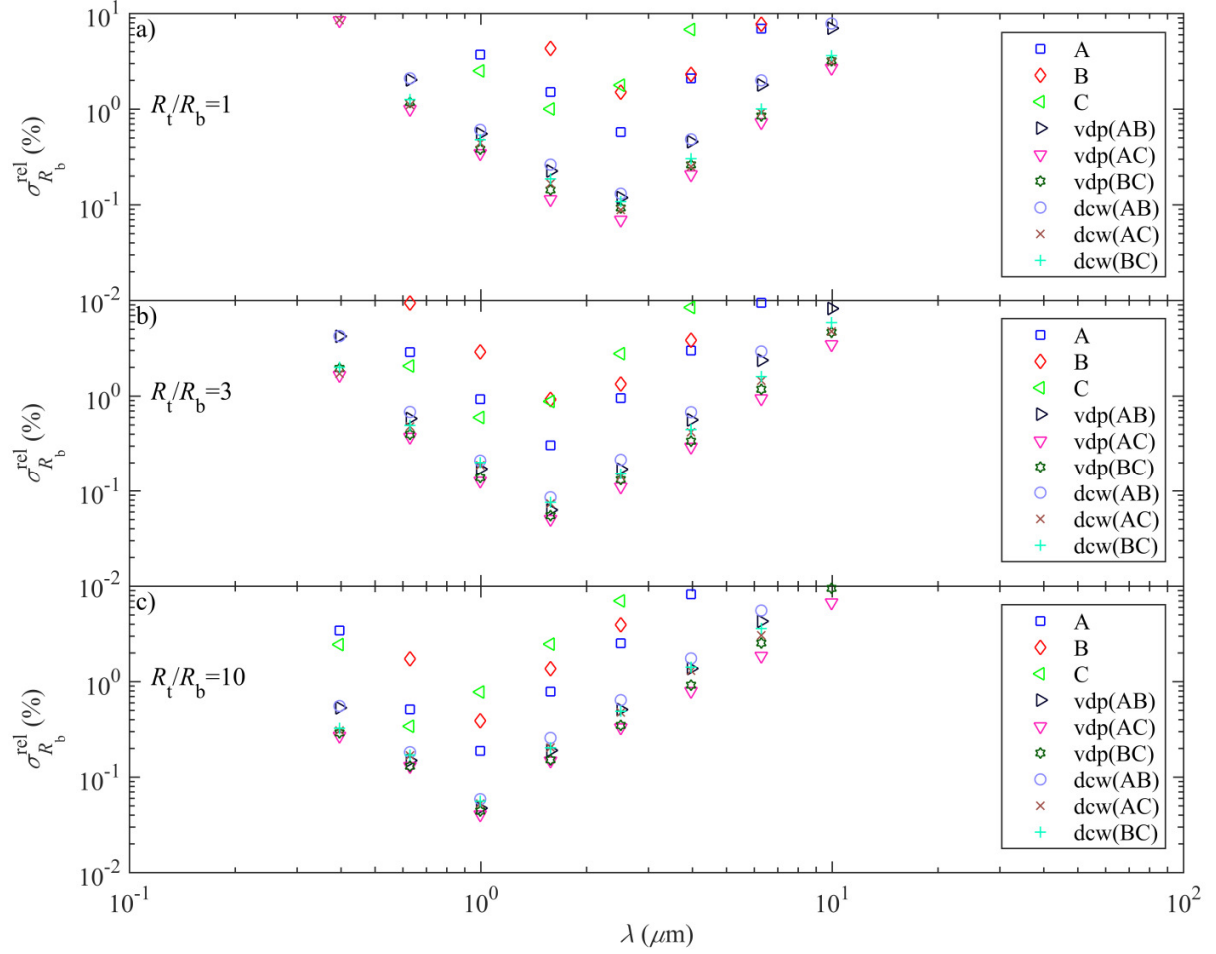


Fig. 6.14: The relative standard deviation of R_b as a function of λ for an MTJ sample with $R_t/R_b = 1$ (a), $R_t/R_b = 3$ (b) and $R_t/R_b = 10$ (c). R_b is extracted from CIPT-model-fits to series of single configuration and position corrected four-point resistances. Position corrections based on the vdp-method (vdp) and the first order approximation (dcw) were used. The presented data is based on Monte Carlo simulations mimicking the measurement conditions for one specific M12PP-design (parameters: $\sigma_{x,y} = 5$ nm, $\sigma_{x,y}^{\text{dyn}} = 0.3$ nm, E-noise = 0.01% (based on R_A), 100 iterations).

For R_b the data points form a distinct arrow-shape “pointing” to an optimum value with respect to λ . The optimum value changes slightly from $\lambda \approx 2.3$ μm for $R_t/R_b = 1$, to $\lambda \approx 1.6$ μm for $R_t/R_b = 3$ and $\lambda \approx 1$ μm for $R_t/R_b = 10$. This characteristic behavior is observed because R_b cannot be probed individually at any electrode pitch, which is in contrast to the case of R_t . For $s \gg \lambda$ the parallel resistance of R_t and R_b is measured but in order to obtain a good precision on the estimated the value of R_b one also needs a fairly precise estimate for R_A and R_t . The lowest relative standard deviation on R_b is obtained for $R_t/R_b = 10$ and with the application of vdp(AC) correction. For this scenario the relative standard deviation is approximately 5 times lower for vdp(AC) correction as compared to single A-configuration measurements.

6.2.6 Measurements and position errors

In this section MC simulations are compared to actual four-point resistance measurements recorded on the MTJ sample described in section 3.4. Simulations are carried out using MTJ parameters for this particular sample and position errors according to the findings presented in chapter 5. The results of these simulations are plotted in Fig. 6.15. The relative standard deviation on the measured four-point resistance is plotted as a function of pitch (for equidistant probe) and is observed for the vdp(AC) correction to range from a value of $\sim 0.1\%$, for $s = 1.5 \mu\text{m}$, to 0.02% , for $s = 8.3 \mu\text{m}$.

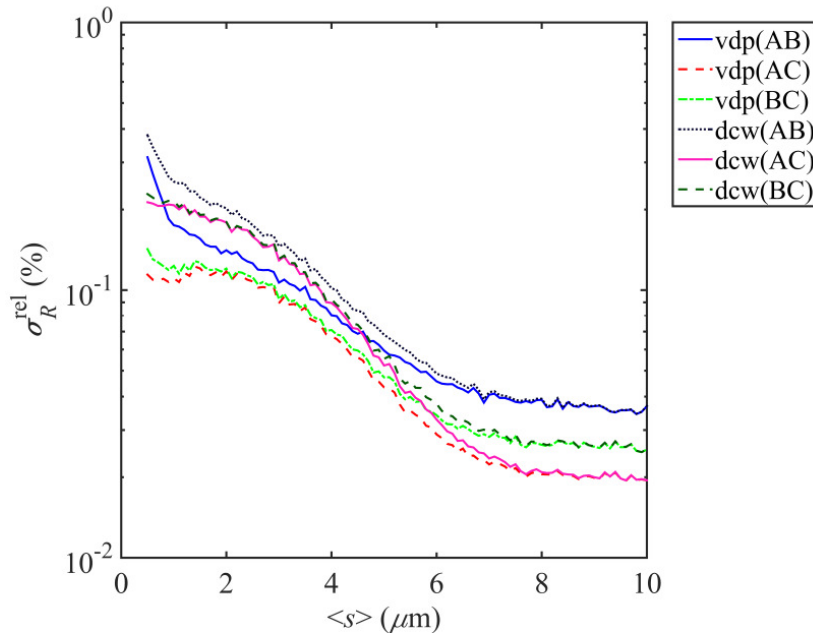


Fig. 6.15: The relative standard deviation of position corrected four-point resistances as a function of equidistant electrode spacing, $\langle s \rangle = s$, for a specific MTJ sample (parameters: $RA_{\text{low}} = 8.5 \Omega\mu\text{m}^2$, $R_t = 3.5 \Omega/\square$, $R_b = 0.6 \Omega/\square$ and $\lambda_{\text{low}} = 1.5 \mu\text{m}$). Position corrections based on the vdp-method (vdp) and the first order approximation (dcw) were used. The presented data is based on Monte Carlo simulations (parameters: $\sigma_{x,y} = 5 \text{ nm}$, $\sigma_{x,y}^{\text{dyn}} = 0.3 \text{ nm}$, E-noise = 0.01% (based on R_A), 1000 iterations).

Experimental four-point resistance measurements were performed in a homogeneous area of the sample, in square grid of 10 by 10 measurement points distributed with a step size of $100 \mu\text{m}$. Other measurement parameters are listed in section 6.1. The measurement results obtained at 8 different mean probe pitches, corresponding to the standard sup-probe selection for this probe (see section 3.1), are presented in Fig. 6.16. It is clearly observed from the plot, that the relative standard deviation on the measured resistance for vdp(AC) correction, which provides the lowest relative standard deviation, is roughly an order of magnitude higher than predicted by the simulations.

By repeated simulations (see Fig. 6.17) the position errors (static and dynamic) matching the experimental results were found to be one order of magnitude larger than the position errors reported in paper II.

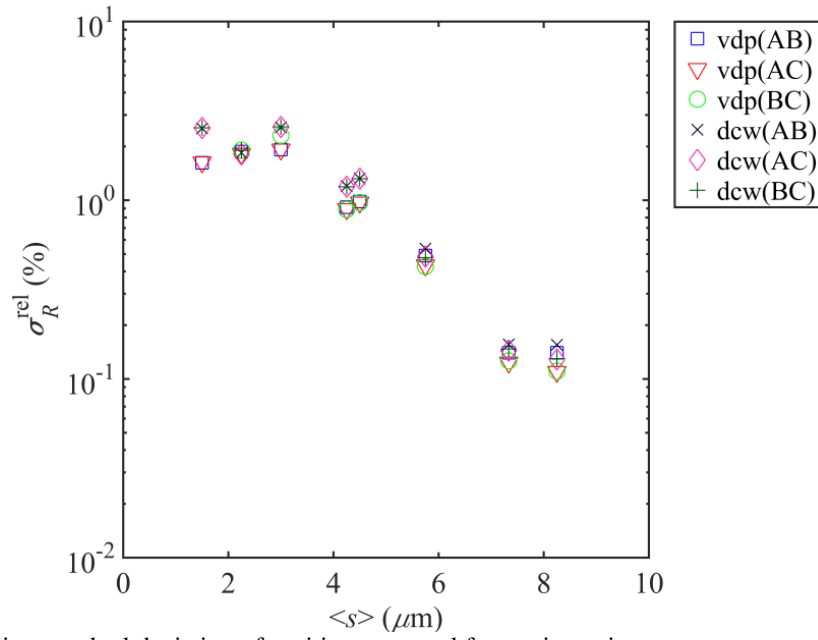


Fig. 6.16: The relative standard deviation of position corrected four-point resistance measurements as a function of average electrode spacing, $\langle s \rangle$, for a specific MTJ sample (parameters: $RA_{\text{low}} = 8.5 \, \Omega\mu\text{m}^2$, $R_t = 3.5 \, \Omega/\square$, $R_b = 0.6 \, \Omega/\square$ and $\lambda_{\text{low}} = 1.5 \, \mu\text{m}$). Position corrections based on the vdp-method (vdp) and the first order approximation (dcw) were used. The presented data are based on 100 measurements carried out using one specific M12PP-design.

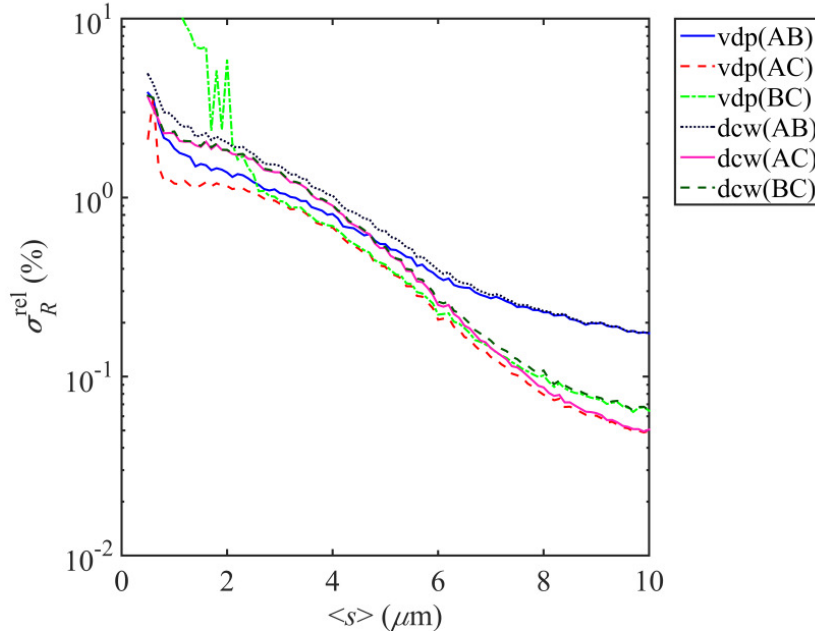


Fig. 6.17: The relative standard deviation of position corrected four-point resistances as a function of equidistant electrode spacing, $\langle s \rangle = s$, for a specific MTJ sample (parameters: $RA_{\text{low}} = 8.5 \, \Omega \mu\text{m}^2$, $R_t = 3.5 \, \Omega/\square$, $R_b = 0.6 \, \Omega/\square$ and $\lambda_{\text{low}} = 1.5 \, \mu\text{m}$). Position corrections based on the vdp-method (vdp) and the first order approximation (dcw) were used. The presented data is based on Monte Carlo simulations (parameters: $\sigma_{x,y} = 50 \, \text{nm}$, $\sigma_{x,y}^{\text{dyn}} = 3 \, \text{nm}$, E-noise = 0.01% (based on R_A), 1000 iterations). NOTE: The random variations for single C-configuration measurements observed at $\langle s \rangle = 2 \, \mu\text{m}$ is confirmed to be an unintended artefact of the MC simulations.

A conclusion has not been made with respect to what could cause this dramatic difference in position errors. Preliminary AFM experiments suggest that the single sheet sample has a higher surface flatness on the scale of the probe contact area (100-300 nm in diameter), as compared to that of the MTJ sample. This could lead to a more discretized probe sample contact for measurements on the MTJ, where only one or a few highly localized contacts (physical and electrical) are established within the potential contact area of the probe. This may serve as a plausible explanation for our observations. However, further investigations are needed before a conclusion can be made.

6.2.7 Enhanced measurement precision

A simple yet effective way to reduce a normal distributed error from an experiment is to simply repeat the experiment. In this way one can expect to lower the standard deviation of the average result by a factor of $1/\sqrt{n}$, where n , is the number of experiments. In the case of electrode position errors (and electrical noise) we do assume a normal distribution, and we therefore propose to include more sub-probes of nominally identical electrode spacing in the experiment by changing the probe design (see section 6.3).

Since additional measurements will increase the overall measurement time and also require changes to the probe design, we will here consider a minimum solution where only one additional sub-probe (= one extra position corrected measurement) is included. Fig. 6.18 illustrates that in practice such a

solution could be realized by adding just one more electrode to a probe design with four equidistant electrodes. Based on the notation in Fig. 6.18 we shall name this option “5 pins” and it allows the following combination of sub-probes: [1,2,3,4] and [2,3,4,5]. Adding another electrode enables a new combination (“6 pins”) and so on:

- 4 pins: [1,2,3,4] (included as reference)
- 5 pins: [1,2,3,4] and [2,3,4,5]
- 6 pins: [1,2,3,4] and [3,4,5,6]
- 7 pins: [1,2,3,4] and [4,5,6,7]
- 8 pins: [1,2,3,4] and [5,6,7,8]

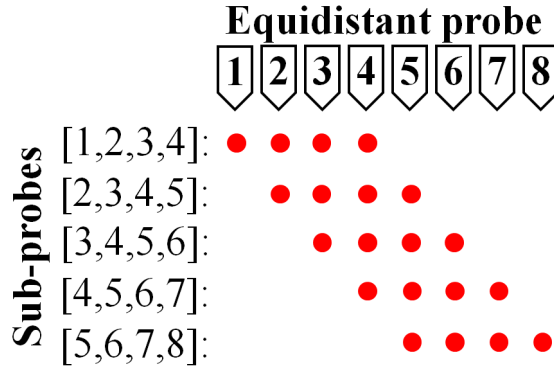


Fig. 6.18: Illustration of the 5 different, equidistant sub-probes of minimum pitch, obtainable from a probe with 8 equidistant electrodes.

We will now evaluate if any particular combination of two sub-probes is favorable when it comes to reduction of electrode position errors. Here the problem is treated analytically and considering solely static in-line errors with standard deviation σ_x . The relative standard deviation on the average of the two position corrected pseudo resistance values, $\sigma_{R_{p,ave}}^{rel}$, estimated based on first order correction, is identical for all dual combinations of R_A , R_B and R_C due to reciprocity [54]–[56]. With the notation for AB correction the average, position corrected pseudo resistance is given by

$$R_{p,ave}^w = \sum_{N=1}^n \frac{R_{p,N}^w}{n} = \frac{R_{p,1}^w + R_{p,2}^w}{2}, \quad (60)$$

and the relative standard deviation follows

$$\sigma_{R_{p,ave}^w}^{rel} = \frac{\sigma_x}{R_{p,ave}^w} \sqrt{\sum_{N=1}^n \left(\frac{\partial R_{p,ave}^w}{\partial x_N} \right)^2} = \chi \frac{\sigma_x}{\langle s \rangle}, \quad (61)$$

where the geometrical coefficient χ can be expressed for each of the options stated above.

4 pins, [1,2,3,4] (included as reference):

$$\chi_{4p} = \frac{s\sqrt{2}}{\lambda} \frac{\sqrt{\left(K_1\left(\frac{s}{\lambda}\right) - 4K_1\left(\frac{2s}{\lambda}\right) + 3K_1\left(\frac{3s}{\lambda}\right)\right)^2 + \left(2K_1\left(\frac{s}{\lambda}\right) - 4K_1\left(\frac{2s}{\lambda}\right)\right)^2}}{5K_0\left(\frac{s}{\lambda}\right) - 8K_0\left(\frac{2s}{\lambda}\right) + 3K_0\left(\frac{3s}{\lambda}\right) + \frac{R_b}{R_t}(4\ln 4 - 3\ln 3)}. \quad (62)$$

5 pins, [1,2,3,4] and [2,3,4,5]:

$$\chi_{5p} = \frac{\frac{1}{\sqrt{2}} \frac{s}{\lambda} \sqrt{\left(\frac{1}{4} K_1\left(\frac{s}{\lambda}\right) - K_1\left(\frac{2s}{\lambda}\right) + \frac{3}{4} K_1\left(\frac{3s}{\lambda}\right)\right)^2 + \left(\frac{3}{4} K_1\left(\frac{s}{\lambda}\right) - 2K_1\left(\frac{2s}{\lambda}\right) + \frac{3}{4} K_1\left(\frac{3s}{\lambda}\right)\right)^2}}{\left(\frac{5}{4} K_0\left(\frac{s}{\lambda}\right) - 2K_0\left(\frac{2s}{\lambda}\right) + \frac{3}{4} K_0\left(\frac{3s}{\lambda}\right)\right) + \frac{R_b}{R_t} (\ln(4) - \frac{3}{4} \ln(3))}. \quad (63)$$

6 pins, [1,2,3,4] and [2,3,4,5]:

$$\chi_{6p} = \frac{\frac{1}{\sqrt{2}} \frac{s}{\lambda} \sqrt{\left(\frac{1}{4} K_1\left(\frac{s}{\lambda}\right) - K_1\left(\frac{2s}{\lambda}\right) + \frac{3}{4} K_1\left(\frac{3s}{\lambda}\right)\right)^2 + \left(\frac{1}{2} K_1\left(\frac{s}{\lambda}\right) - K_1\left(\frac{2s}{\lambda}\right)\right)^2 + \left(\frac{1}{4} K_1\left(\frac{s}{\lambda}\right) - \frac{3}{4} K_1\left(\frac{3s}{\lambda}\right)\right)^2}}{\frac{5}{4} K_0\left(\frac{s}{\lambda}\right) - 2K_0\left(\frac{2s}{\lambda}\right) + \frac{3}{4} K_0\left(\frac{3s}{\lambda}\right) + \frac{R_b}{R_t} (\ln 4 - \frac{3}{4} \ln 3)}. \quad (64)$$

7 pins, [1,2,3,4] and [2,3,4,5]:

$$\chi_{7p} = \frac{\frac{1}{\sqrt{2}} \frac{s}{\lambda} \sqrt{\left(\frac{1}{4} K_1\left(\frac{s}{\lambda}\right) - K_1\left(\frac{2s}{\lambda}\right) + \frac{3}{4} K_1\left(\frac{3s}{\lambda}\right)\right)^2 + 2\left(\frac{1}{2} K_1\left(\frac{s}{\lambda}\right) - K_1\left(\frac{2s}{\lambda}\right)\right)^2}}{\frac{5}{4} K_0\left(\frac{s}{\lambda}\right) - 2K_0\left(\frac{2s}{\lambda}\right) + \frac{3}{4} K_0\left(\frac{3s}{\lambda}\right) + \frac{R_b}{R_t} (\ln(4) - \frac{3}{4} \ln(3))}. \quad (65)$$

8 pins, [1,2,3,4] and [2,3,4,5]:

$$\chi_{8p} = \frac{s}{\lambda} \frac{\sqrt{\left(K_1\left(\frac{s}{\lambda}\right) - 4K_1\left(\frac{2s}{\lambda}\right) + 3K_1\left(\frac{3s}{\lambda}\right)\right)^2 + \left(2K_1\left(\frac{s}{\lambda}\right) - 4K_1\left(\frac{2s}{\lambda}\right)\right)^2}}{5K_0\left(\frac{s}{\lambda}\right) - 8K_0\left(\frac{2s}{\lambda}\right) + 3K_0\left(\frac{3s}{\lambda}\right) + \frac{R_b}{R_t} (4 \ln 4 - 3 \ln 3)}. \quad (66)$$

The different options are compared in Fig. 6.19 and the 6 pins option is found to yield the lowest relative standard deviation for almost the entire range of s/λ .

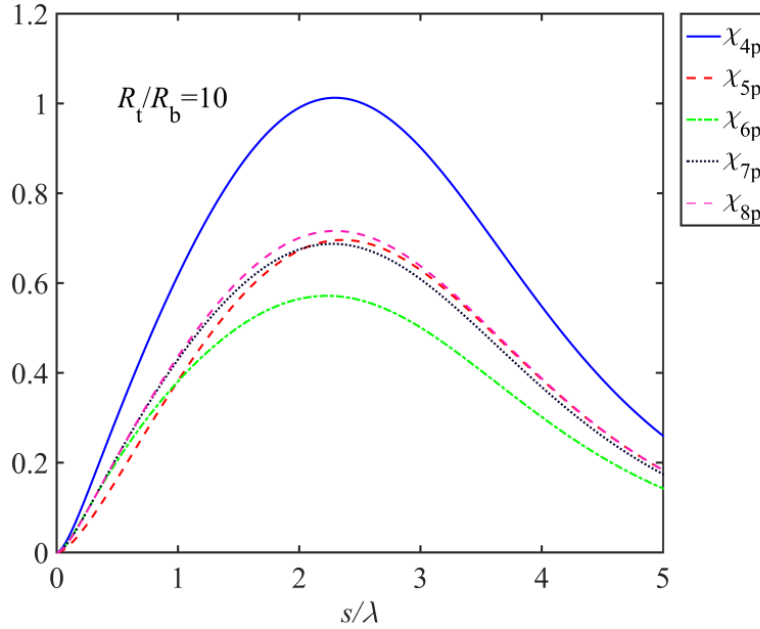


Fig. 6.19: Geometrical coefficients χ_{4p} , χ_{5p} , χ_{6p} , χ_{7p} and χ_{8p} plotted for $R_t/R_b = 10$, where $R_t = 10 \Omega/\square$ and $R_b = 1 \Omega/\square$, as a function of equidistant electrode spacing (normalized to λ).

6.3 Equidistant probe design

Based on a more brute force approach we propose a probe design entirely occupied by equidistant electrodes. This allows for the highest number of sub-probes with minimum pitch, for which electrode positional errors are typically most influential.

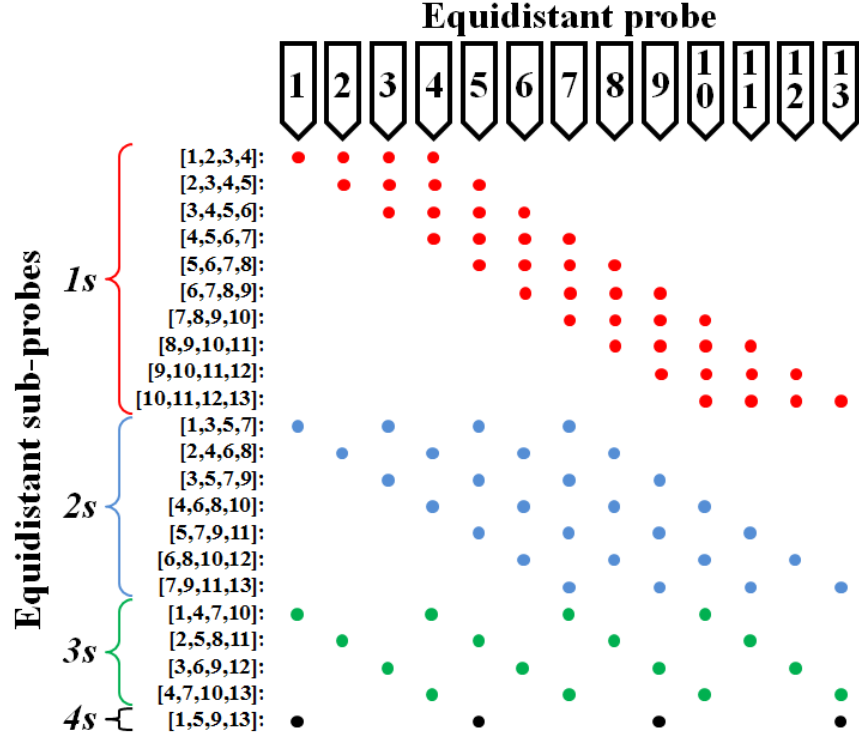


Fig. 6.20: Illustration of the different, equidistant sub-probes of pitch $1s$ (10 sub-probes), $2s$ (7 sub-probes), $3s$ (4 sub-probes) and $4s$ (1 sub-probe), obtainable from a probe with 13 equidistant electrodes.

Fig. 6.20 illustrates an example of such a probe with a total of 13 electrodes. Note that the 13th electrode contributes by enabling a sub-probe with a pitch of $4s$.

With an addition of two pins, the abovementioned probe design (see Fig. 6.20) may include a single sub-probe of pitch $12s$. Even though only one such sub-probe would be available it may still add considerably to the measurement precision and dynamic range. First of all the sensitivity to electrode position errors would be very reduced at $12s$ and in addition one could, depending on the sample λ , assume single sheet behavior in this regime, which, justified by the assumption that at $12s$ $R_p = R$, would allow accurate estimation of the parallel resistance of R_t and R_b solely on the basis of measurements at $12s$. Knowing the true parallel resistance would allow us to fix the value of R_b (or R_t) and leave us with only two variables to fit.

6.4 Summary

In this work we applied MC simulations to study the influence of electrical noise as well as static and dynamic, in-line and off-line electrode position errors on four-point resistance measurements on MTJs. The irrefutable result of this study points to the vdp(AC) correction scheme as being the most effective method to lower the relative standard deviation on the measured resistance. In line with this we find that vdp(AC) correction also provides the broadest dynamic range for the M12PP used in this project. Actual measurements obtained on an MTJ sample confirms that vdp(AC) correction provides the lowest relative standard deviation. However, we find that the electrode position errors on this sample are roughly one order of magnitude larger as compared to the position errors reported for measurements on a single sheet sample (see chapter 5). Further investigations are needed to establish the cause of this.

As a means to further enhance the measurement precision we propose the addition of more sub-probes of nominally identical electrode spacing and show that for one added sub-probe the 6 pins option (two sub-probes sharing two pins) yields the most significant reduction of electrode positional errors. Finally, a radical probe design entirely occupied by equidistant electrodes is proposed.

Chapter 7

7 Outlook

So far this thesis has focused on measurements on infinite films, which has been a prerequisite for CIPT measurements since the introduction of this metrology. Now, we will look at MTJ metrology for discontinued samples, which becomes relevant when the industry moves to large scale production of MTJ-based devices.

This chapter presents selected highlights from ongoing work on CIPT measurements on small test pads and direct characterization of magnetic tunnel junction devices using microscopic multi-point probes. Section 7.1 is based on and repeats text and figures from papers III, IV and V.

7.1 CIPT measurements on small test pads

Measurements on test pads is used for inline production monitoring throughout the semiconductor industry as it proves to be a cost effective alternative to otherwise expensive, dedicated monitor wafers. Small test pads can be conveniently placed in scribe lines areas and as such do not take up any of the wafer real estate area available for products. However, in order to lower production costs per chip, wafer scribe lines are continuously downscaled and thus the size of test pads also decreases. This underlines the need for MTJ metrology that will work even on small test areas where the assumption of an infinite sheet does not hold true.

Here we investigate how CIPT measurements will be affected when performed on test pads with insulating boundaries (see Fig. 7.1), and modify the original CIPT model by the method of images to derive a new model which is valid for rectangular samples.

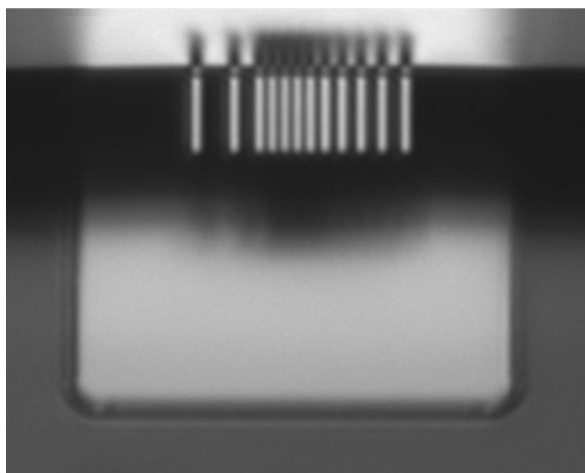


Fig. 7.1: Picture of a micro 12-point probe positioned over a square test pad of $w = 50 \mu\text{m}$. Reproduced from paper III.

The original CIPT model is no longer valid when performing measurements near an insulating boundary, since the current density normal to the boundary must be zero. In order to fulfil this boundary condition the method of images is applied. This method was recently used in studies of four-point measurements near insulating line defects in single sheet graphene (see paper IV and paper V) and involves placing additional current sources and drains at the mirror-positions obtained by mirroring the current sources and drains in the boundary lines as shown in Fig. 7.2. Mirror images of the additional current sources and drains are also needed, which result in a double infinite sum (see paper III). Fig. 7.2 shows a sketch of a rectangular sample with dimensions of length, l , and width, w . The insulating boundaries are represented by solid black lines and the two original current source and drain are labeled I_+ and I_- , respectively. The center of the M4PP is positioned at the center of the test pad (x_0, y_0) and only the mirror images closest to the pad are shown.

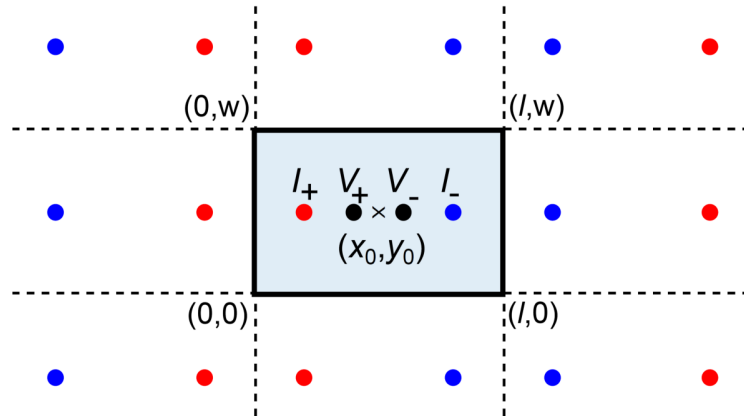


Fig. 7.2: Sketch of a rectangular shaped sample (light blue) of length, l , and width, w , with insulating boundaries (solid black lines). A four-point probe is placed on the sample, with the center of the probe at (x_0, y_0) . The eight closest mirror images of both the current source and drain are also included. Reproduced from paper III.

Applying the modified CIPT model significantly increases the measurement accuracy on small samples. This is seen from Fig. 7.3, which compares the performance of the traditional CIPT model (Inf theory) to that of the modified model for squares (Sq theory). The extracted value of RA_{low} is plotted as a function of probe position along the centerline of a square test pad of $w = 30 \mu\text{m}$. It is clearly observed that while data based on the original CIPT model fluctuate considerably across the pad, the values of RA_{low} extracted with the modified theory remain stable.

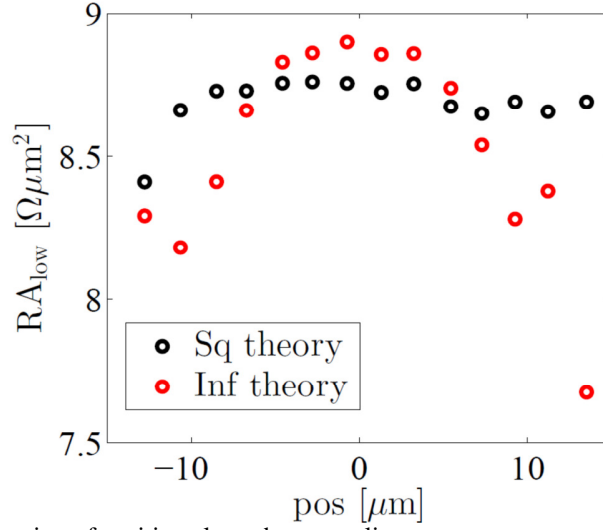


Fig. 7.3: Extracted RA_{low} as a function of position along the center line on a square test pad of $w = 30 \mu m$. Reproduced from paper III.

7.2 Direct characterization of MTJ devices using a microscopic multi-point probe

Following the general industry trend of downscaling in order to increase memory density MRAM cell sizes of down to 20 nm have been reported [80]. The device defining etch process has been pointed out as being one of the main challenges in the fabrication of MRAM and specifically etch induced edge defects have attracted attention as a limiting factor for the performance of the final device [80]–[82]. Characterization of an MTJ at device level has so far required the execution of several process steps in which interconnects and contact pads are defined. Here we present a novel method for direct characterization of single MTJ cells right after the device defining etch and subsequent passivation and chemical-mechanical polishing (CMP) using micro-sized multi-point probes (see Fig. 7.4) in a routine, which is independent of the cell size and therefore is able follow the continued downscaling trend.

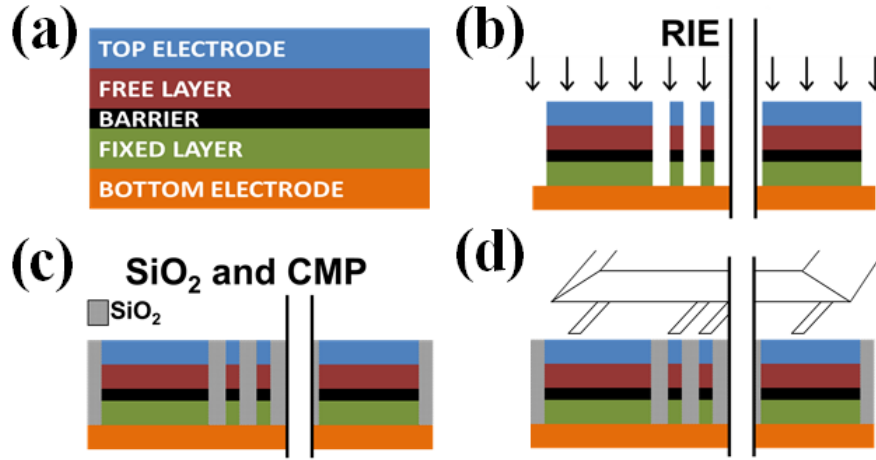


Fig. 7.4: (a) Sample composition. (b) Reactive ion etching of photo resist, hard mask and MTJ stack. The bottom electrode is left un-etched. (c) Cross sectional view of the test structure after passivation with SiO_2 and subsequent CMP. (d) Top electrodes are exposed and may be probed using a micro-sized multi-point probe.

A novel test pattern (see Fig. 7.5) is written using electron beam lithography and subsequently transferred to the MTJ in a reactive ion etch (RIE) leaving the bottom electrode un-etched. The etched structure was passivated by deposition of SiO_2 . Lift-off and planarization with CMP followed to expose the top electrode of the test structure.

The number of cells as well as their size, shape and position in the overall test structure may vary and could for instance be correlated to the dimension of available multi-point probes. The general design of the test structure does not impose an upper/lower limit on the cell size. In this particular case the distribution of cells matches the pin positions of a commercially available 12-point probe (see section 3.1). From Fig. 7.4 and Fig. 7.5 it is clear that the 2 outermost electrodes are intended to contact the two test pads while the remaining electrodes probe the MTJ cells distributed between the two test pads. It is also clear that the precision of alignment between test structure and the probe necessary to ensure contact to at least one MTJ cell is considerably lower if MTJ cells are distributed along a sloped line between the two test pads. Furthermore information on which specific cells have been contacted will provide accurate information on the distance to all other cells included in the test structure. The slope of the line could e.g. be optimized according to the number of available electrodes and their effective contact area. Other schemes for optimizing the probability of contact between an electrode and an MTJ cell may include the option of adding more cells to the structure.

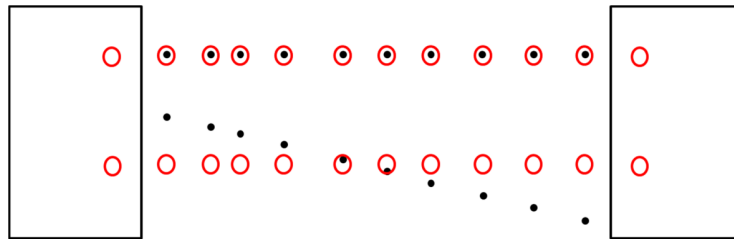


Fig. 7.5: Schematic diagram showing test structure (top view). Two sets of 10 MTJ cells (black dots) are distributed at a pre-defined variation of pitch between two relatively large test pads (squares). Red circles indicate assumed contact area of an M12PP.

Preliminary tests have been carried out on MTJ pillars with a diameter of 600 nm using a CAPRES CIPTech-M300 (see Fig. 7.6). Characterization is handled in a sequential manner: 1) landing, 2) contact check and 3) measurements. Landing is completed once electrical contact has been detected between the two outermost probes touching down on the two test pads. Other means of surface detection includes the use of a probe with one or more strain gauges [53]. Contact check is performed by systematically attempting to pass a small current from one of the outermost electrodes (pin #1 or pin #12) to one of the remaining electrodes (pin #2-11). All successful attempts mark a connection between an electrode and an MTJ cell, for which numerous properties, including the barrier resistance, can then be characterized in various two- and/or three-point measurements.

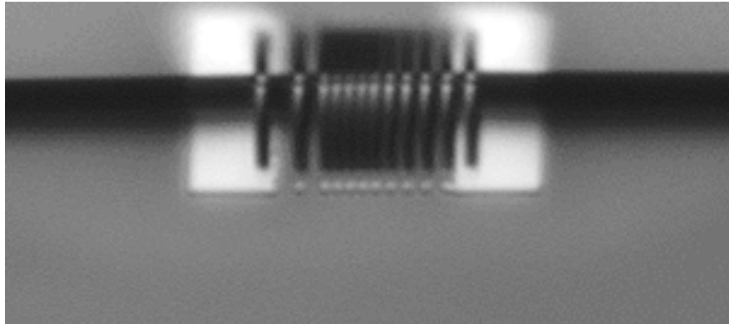


Fig. 7.6: Microscope image showing a 12-point probe landed on a test structure.

Chapter 8

8 Conclusion

The fundamental goal of this project has been to provide cheaper, faster and more precise metrology for MTJs.

This goal has been achieved in part by the demonstration of a static field CIPT method, which allows us to reduce the measurement time by a factor of 5, by measuring only RA thus excluding TMR. This enhancement is obtained purely by acquiring only half of the data needed for the conventional switching field CIPT measurement and particularly by avoiding magnetic field switching. We observe that the new method measures essentially the same RA values as compared to the conventional strategy. By offering the choice of characterizing either RA_{low} or RA_{high} the static field CIPT method has an added advantage over the conventional switching field CIPT method, which relies on the characterization of both RA values. This allows for an improved matching of the range of available electrode pitches and sample transfer lengths λ_{low} or λ_{high} , which may effectively increase the dynamic range of any given 12-point probe.

Without the requirement for switching magnetic fields during measurements the static field CIPT method has inspired the concept of detached magnet setups for future CIPTech tools. While lowering the complexity of the measurement system a detached magnet setup, e.g. a proposed letterbox magnet, could provide superior dynamic range and field homogeneity as compared to current state of the art solutions.

We have carried out an extensive characterization of electrode position errors and experimentally shown that the dominant sources of error in single configuration micro four-point probe sheet resistance measurements are in-line probe geometry errors and in-line static position errors. These errors were shown to be eliminated very effectively using dual-configuration measurements and position error correction algorithms. The standard deviation of the static in-line position error for measurements with Au coated electrodes on Ru thin film samples was found to be in the range from 3.9 nm to 7.5 nm. The standard deviation of the dynamic in-line position error was shown to be small ~ 3 Å and only detectable in measurements with high measurement current. At lower measurement currents the electrical measurement noise was the dominant error source. No significant ageing effect on position errors (except for a very slight reduction in position error with measurement age) was observed for a probe in the course of 5000 measurements. We have demonstrated how new probe designs may be evaluated and benchmarked against each other using the same strategy.

Based on Monte Carlo simulations we have studied the influence of electrical noise as well as static and dynamic, in-line and off-line electrode position errors on four-point resistance measurements on MTJs. This study points out the van der Pauw position correction strategy based on combined measurement in four-point configuration A and C as being the most effective method to lower the relative standard deviation on the measured resistance. In line with this we find that the same method also provides the broadest dynamic range for the M12PP used in this project.

Actual measurements obtained on an MTJ sample confirm that $vdp(AC)$ correction provides the lowest relative standard deviation. However, we find that the electrode position errors on this sample are roughly one order of magnitude larger as compared to the position errors reported for measurements on a single sheet sample (see chapter 5). Further investigations are needed to establish the cause of this. As a means to further enhance the measurement precision we have proposed the addition of more sub-probes of nominally identical electrode spacing and show that for one added sub-probe the 6 pins option (two sub-probes sharing two pins) yields the most significant reduction of electrode positional errors. Finally, a radical probe design entirely occupied by equidistant electrodes is proposed.

Bibliography

- [1] G. E. Moore, “Cramming more components onto integrated circuits,” *Proc. IEEE*, vol. 86, no. 1, pp. 82–85, 1998.
- [2] G. E. Moore, “Cramming More Components onto Integrated Circuits,” *Electronics*, pp. 114–117, Apr-1965.
- [3] M. Kanellos, “Moore says nanoelectronics face tough challenges,” *CNET News*, 09-Mar-2005.
- [4] “Today’s Tiny Transistors,” *Next Wave*, vol. 20, no. 3, 2014.
- [5] L. S., “The end of Moore’s law,” *The Economist*. 19-Apr-2015.
- [6] Rachel Courtland, “Gordon Moore: The Man Whose Name Means Progress, The visionary engineer reflects on 50 years of Moore’s Law,” *IEEE Spectrum*, 2015.
- [7] S. A. Wolf, D. D. Awschalom, R. A. Buhrman, J. M. Daughton, S. von Molnár, M. L. Roukes, A. Y. Chtchelkanova, and D. M. Treger, “Spintronics: a spin-based electronics vision for the future.,” *Science*, vol. 294, no. 5546, pp. 1488–1495, 2001.
- [8] S. Parkin, X. Jiang, C. Kaiser, A. Panchula, K. Roche, and M. Samant, “Magnetically engineered spintronic sensors and memory,” *Proc. IEEE*, vol. 91, no. 5, pp. 661–679, 2003.
- [9] S. S. P. Parkin, “Giant Magneto Resistance in Magnetic Nanostructures,” *Annu. Rev. Mater. Sci.*, vol. 25, pp. 357–388, 1995.
- [10] S. S. P. Parkin, C. Kaiser, A. Panchula, P. M. Rice, B. Hughes, M. Samant, and S.-H. Yang, “Giant tunnelling magnetoresistance at room temperature with MgO (100) tunnel barriers.,” *Nat. Mater.*, vol. 3, no. 12, pp. 862–867, 2004.
- [11] S. Yuasa, T. Nagahama, A. Fukushima, Y. Suzuki, and K. Ando, “Giant room-temperature magnetoresistance in single-crystal Fe/MgO/Fe magnetic tunnel junctions.,” *Nat. Mater.*, vol. 3, no. 12, pp. 868–871, 2004.
- [12] J. Zhu and C. Park, “Magnetic tunnel junctions,” *Mater. Today*, vol. 9, no. 11, pp. 36–45, 2006.
- [13] S. Mao, J. Nowak, D. Song, P. Kolbo, L. Wang, E. Linville, D. Saunders, E. Murdock, and P. Ryan, “Spin tunneling heads above 20 Gb/in²,” *IEEE Trans. Magn.*, vol. 38, no. 1, pp. 78–83, 2002.

- [14] S. Araki, K. Sato, T. Kagami, S. Saruki, T. Uesugi, N. Kasahara, T. Kuwashima, N. Ohta, J. Sun, K. Nagai, S. Li, N. Hachisuka, H. Hatate, T. Kagotani, N. Takahashi, K. Ueda, and M. Matsuzaki, "Fabrication and electric properties of lapped type of TMR heads for ~ 50 Gb/in² and beyond," *IEEE Trans. Magn.*, vol. 38, no. 1, pp. 72–77, 2002.
- [15] T. Kagami, T. Kuwashima, S. Miura, T. Uesugi, K. Barada, N. Ohta, and N. Kasahara, "A Performance Study of Next Generation's TMR Heads Beyond 200 Gb/in²," *IEEE Trans. Magn.*, vol. 42, no. 2, pp. 200–203, 2006.
- [16] M. K. Ho, C. H. Tsang, R. E. J. Fontana, S. S. Parkin, K. J. Carey, T. P. T. Pan, S. MacDonald, P. C. Arnett, and J. O. Moore, "Study of magnetic tunnel junction read sensors," *IEEE Trans. Magn.*, vol. 37, no. 4, pp. 1691–1694, 2001.
- [17] B. N. Engel, N. D. Rizzo, J. Janesky, J. M. Slaughter, R. Dave, M. Deherrera, M. Durlam, and S. Tehrani, "The Science and Technology of Magnetoresistive Tunneling Memory," *IEEE Trans. Nanotechnol.*, vol. 1, no. 1, pp. 32–37, 2002.
- [18] R. W. Dave, G. Steiner, J. M. Slaughter, J. J. Sun, B. Craigo, S. Pietambaram, K. Smith, G. Grynkewich, M. DeHerrera, J. Åkerman, and S. Tehrani, "MgO-based tunnel junction material for high-speed toggle magnetic random access memory," *IEEE Trans. Magn.*, vol. 42, no. 8, pp. 1935–1939, 2006.
- [19] M. DeVoss, "Analysis: Freescale's MRAM ready to fly?," *EE Times*, 21-Jul-2006.
- [20] B. N. Engel, J. Åkerman, B. Butcher, R. W. Dave, M. DeHerrera, M. Durlam, G. Grynkewich, J. Janesky, S. V. Pietambaram, N. D. Rizzo, J. M. Slaughter, K. Smith, J. J. Sun, and S. Tehran, "A 4-Mb toggle MRAM based on a novel bit and switching method," *IEEE Trans. Magn.*, vol. 41, no. 1, pp. 132–136, 2005.
- [21] S. Tehrani, J. Slaughter, and M. Deherrera, "Magnetoresistive random access memory using magnetic tunnel junctions," *Proc. IEEE*, vol. 91, no. 5, pp. 703–714, 2003.
- [22] N. D. Rizzo, D. Houssameddine, J. Janesky, R. Whig, F. B. Mancoff, M. L. Schneider, M. Deherrera, J. J. Sun, K. Nagel, S. Deshpande, H. J. Chia, S. M. Alam, T. Andre, S. Aggarwal, and J. M. Slaughter, "A fully functional 64 Mb DDR3 ST-MRAM built on 90 nm CMOS technology," *IEEE Trans. Magn.*, vol. 49, no. 7, pp. 4441–4446, 2013.
- [23] S. S. P. Parkin, K. P. Roche, M. G. Samant, P. M. Rice, R. B. Beyers, R. E. Scheuerlein, E. J. O'Sullivan, S. L. Brown, J. Bucchigano, D. W. Abraham, Y. Lu, M. Rooks, P. L. Trouilloud, R. A. Wanner, and W. J. Gallagher, "Exchange-biased magnetic tunnel junctions and application to nonvolatile magnetic random access memory (invited)," *J. Appl. Phys.*, vol. 85, no. 8, pp. 5828–5833, 1999.

- [24] J. S. Moodera, L. R. Kinder, T. M. Wong, and R. Meservey, "Large magnetoresistance at room temperature in ferromagnetic thin film tunnel junctions," *Phys. Rev. Lett.*, vol. 74, no. 16, pp. 3273–3276, 1995.
- [25] M. Julliere, "Tunneling between ferromagnetic films," *Phys. Lett. A*, vol. 54, no. 3, pp. 225–226, 1975.
- [26] T. Miyazaki and N. Tezuka, "Spin polarized tunneling in ferromagnet/insulator/ferromagnet junctions," *J. Magn. Magn. Mater.*, vol. 151, no. 3, pp. 403–410, 1995.
- [27] N. Miyazaki, T.; Tezuka, "Giant magnetic tunneling effect in Fe/Al₂O₃/Fe junction," *J. Magn. Magn. Mater.*, vol. 139, pp. L231–L234, 1995.
- [28] D. C. Worledge and P. L. Trouilloud, "Magnetoresistance measurement of unpatterned magnetic tunnel junction wafers by current-in-plane tunneling," *Appl. Phys. Lett.*, vol. 83, no. 1, pp. 84–86, 2003.
- [29] "Graffs Data Recovery." [Online]. Available: <http://www.graffs.co.uk/drive-failure-issues-and-symptoms/>. [Accessed: 20-Apr-2015].
- [30] T. R. McGuire and R. I. Potter, "Anisotropic Magnetoresistance," *IEEE Trans. Magn.*, vol. 11, pp. 1018–1038, 1975.
- [31] C. Chappert, A. Fert, and F. N. Van Dau, "The emergence of spin electronics in data storage," *Nat. Mater.*, vol. 6, no. 11, pp. 813–823, 2007.
- [32] G. Binasch, P. Grünberg, F. Saurenbach, and W. Zinn, "Enhanced magnetoresistance in layered magnetic structures with antiferromagnetic interlayer exchange," *Phys. Rev. B*, vol. 39, no. 7, pp. 4828–4830, 1989.
- [33] J. Baibich, M. N.; Broto, J. M.; Fert, A.; Nguyen Van Dau, F.; Petroff, F.; Eitenne, P.; Creuzet, G.; Friederich, A.; Chazelas, "Giant Magnetoresistance of (001)Fe/(001)Cr Magnetic Superlattices," *Phys. Rev. Lett.*, vol. 61, no. 21, pp. 2472–2475, 1988.
- [34] S. S. P. Parkin, Z. G. Li, and D. J. Smith, "Giant magnetoresistance in antiferromagnetic Co/Cu multilayers," *Appl. Phys. Lett.*, vol. 58, no. 23, pp. 2710–2712, 1991.
- [35] S. S. P. Parkin, "Origin of enhanced magnetoresistance of magnetic multilayers: Spin-dependent scattering from magnetic interface states," *Phys. Rev. Lett.*, vol. 71, no. 10, pp. 1641–1644, 1993.
- [36] S. S. P. Parkin, "Dramatic enhancement of interlayer exchange coupling and giant magnetoresistance in Ni₈₁Fe₁₉/Cu multilayers by addition of thin Co interface layers," *Appl. Phys. Lett.*, vol. 61, no. 11, pp. 1358–1360, 1992.

- [37] D. M. Edwards, J. Mathon, and R. B. Muniz, “A resistor network theory of the giant magnetoresistance in magnetic superlattices,” *IEEE Trans. Magn.*, vol. 27, no. 4, pp. 3548–3552, 1991.
- [38] B. Dieny, V. S. Speriosu, S. S. P. Parkin, B. a. Gurney, D. R. Wilhoit, and D. Mauri, “Giant magnetoresistance in soft ferromagnetic multilayers,” *Phys. Rev. B*, vol. 43, no. 1, pp. 1297–1300, 1991.
- [39] S. Ikeda, J. Hayakawa, Y. Ashizawa, Y. M. Lee, K. Miura, H. Hasegawa, M. Tsunoda, F. Matsukura, and H. Ohno, “Tunnel magnetoresistance of 604% at 300 K by suppression of Ta diffusion in Co Fe B/Mg O/Co Fe B pseudo-spin-valves annealed at high temperature,” *Appl. Phys. Lett.*, vol. 93, no. 8, pp. 110–113, 2008.
- [40] W. H. Butler and A. Gupta, “Magnetic memory: A signal boost is in order,” *Nat. Mater.*, vol. 3, no. 12, pp. 845–847, 2004.
- [41] K. L. Wang, J. G. Alzate, and P. Khalili Amiri, “Low-power non-volatile spintronic memory: STT-RAM and beyond,” *J. Phys. D. Appl. Phys.*, vol. 46, no. 7, p. 074003, 2013.
- [42] B. Jovanovic, R. M. Brum, and L. Torres, “Evaluation of hybrid MRAM / CMOS cells for “normally-off and instant-on” computing,” *Analog Integr. Circ. Sig. Process.*, vol. 81, pp. 607–621, 2014.
- [43] D. D. Awschalom and M. E. Flatté, “Challenges for semiconductor spintronics,” *Nat. Phys.*, vol. 3, no. 3, pp. 153–159, 2007.
- [44] I. L. Dieny, B.; Sousa, R.C. ; Herault, J.; Papusoi, C.; Prenat, G.; Ebels, U.; Houssameddine, D.; Rodmacq, B.; Auffret, S.; Buda-Prejbeanu, L.D.; Cyrille, M.C.; Delaet, B.; Redon, O.; Ducruet, C.; Nozieres, J-P.; Prejbeanu, “Spin-transfer effect and its use in spintronic components,” *Int. J. Nanotechnol.*, vol. 7, no. 4–8, pp. 591–614, 2010.
- [45] I. L. Prejbeanu, S. Bandiera, J. Alvarez-Hérault, R. C. Sousa, B. Dieny, and J.-P. Nozières, “Thermally assisted MRAMs: ultimate scalability and logic functionalities,” *J. Phys. D. Appl. Phys.*, vol. 46, no. 7, p. 74002, 2013.
- [46] L. Berger, “Emission of spin waves by a magnetic multilayer traversed by a current,” *Phys. Rev. B*, vol. 54, no. 13, pp. 9353–9358, 1996.
- [47] J. C. Slonczewski, “Current-driven excitation of magnetic multilayers,” *J. Magn. Magn. Mater.*, vol. 159, no. 1–2, pp. L1–L7, 1996.
- [48] D. W. Abraham, P. L. Trouilloud, and D. C. Worledge, “Rapid-turnaround characterization methods for MRAM development,” *IBM J. Res. Dev.*, vol. 50, no. 1, pp. 55–67, 2006.

- [49] Q. T. Vu, E. Kolawa, L. Halperin, and M. A. Nicolet, "Specific contact resistance extraction from four-point-probe measurements on multilayered film structures," *Solid. State. Electron.*, vol. 34, no. 3, pp. 279–283, 1991.
- [50] "CAPRES A/S." [Online]. Available: www.capres.com.
- [51] P. R. E. Petersen, C. L.; Worledge, D.; Petersen, "Reproducibility of Nano- and Micro-Scale Multi-Point Probe Sheet Resistance Measurements," *Mater. Res. Soc. Symp. Proc.*, vol. 738, pp. 157–162, 2003.
- [52] F. M. Smits, "Measurement of Sheet Resistivities With the 4-Point Probe," *Bell Syst. Tech. J.*, vol. 37, pp. 711–718, 1958.
- [53] D. H. Petersen, O. Hansen, T. M. Hansen, P. Bøggild, R. Lin, D. Kjær, P. F. Nielsen, T. Clarysse, W. Vandervorst, E. Rosseel, N. S. Bennett, and N. E. B. Covern, "Review of electrical characterization of ultra-shallow junctions with micro four-point probes," *J. Vac. Sci. Technol. B Microelectron. Nanom. Struct.*, vol. 28, no. 1, pp. C1C27–33, 2010.
- [54] R. Rymaszewski, "Relationship between the correction factor of the four-point probe value and the selection of potential and current electrodes," *J. Phys. E.*, vol. 2, no. 2, pp. 170–174, 1969.
- [55] L. J. van der Pauw, "A Method of Measureing the Resisitivity and Hall Coefficient on Lamellae of Arbitrary Shape," *Philips Tech. Rev.*, vol. 20, no. 8, pp. 220–224, 1958.
- [56] D. H. Petersen, O. Hansen, R. Lin, and P. F. Nielsen, "Micro-four-point probe Hall effect measurement method," *J. Appl. Phys.*, vol. 104, no. 1, p. 013710, 2008.
- [57] D. H. Petersen, O. Hansen, T. M. Hansen, P. R. E. Petersen, and P. Bøggild, "Static contact micro four-point probes with <11 nm positioning repeatability," *Microelectron. Eng.*, vol. 85, no. 5–6, pp. 1092–1095, 2008.
- [58] L. J. van der Pauw, "A Method of Measuring Specific Resistivity and Hall Effect of Discs of Arbitrary Shape," *Philips Tech. Rev.*, vol. 13, no. 1, pp. 1–9, 1958.
- [59] D. C. Worledge, "Reduction of positional errors in a four-point probe resistance measurement," *Appl. Phys. Lett.*, vol. 84, no. 10, p. 1695, 2004.
- [60] R. J. Pedersen and F. L. Vernon, "Effect of film resistance on low-impedance tunneling measurements," *Appl. Phys. Lett.*, vol. 10, no. 1, pp. 29–31, 1967.
- [61] D. K. Schroder, *Semiconductor Material and Device Characterization*, 3rd ed. New York: John Wiley & Sons, 2006.

- [62] H. Murrmann and D. Widmann, "Current crowding on metal contacts to planer devices," *1969 IEEE Int. Solid-State Circuits Conf. Dig. Tech. Pap.*, vol. XII, pp. 162–163, 1969.
- [63] H. H. Berger, "Contact Resistance on Diffused Resistors," *1969 IEEE Int. Solid-State Circuits Conf. Dig. Tech. Pap.*, vol. XII, pp. 160–161, 1969.
- [64] P. J. Severin, "4-point-probe resistivity measurements on Silicon heterotype epitaxial layers with altered probe order," *Philips Res. Reports*, vol. 26, p. 279, 1971.
- [65] Q. T. Vu, E. Kolawa, and M.-A. Nicolet, "Structural and electrical evolution of the Al/RuO₂ interface upon thermal annealing," *Solid. State. Electron.*, vol. 34, no. 3, pp. 271–278, 1991.
- [66] S. Thorsteinsson, F. Wang, D. H. Petersen, T. M. Hansen, D. Kjær, R. Lin, J. Y. Kim, P. F. Nielsen, and O. Hansen, "Accurate microfour-point probe sheet resistance measurements on small samples," *Rev. Sci. Instrum.*, vol. 80, no. 5, p. 053902, 2009.
- [67] J. MacLaren, X.-G. Zhang, and W. Butler, "Validity of the Julliere model of spin-dependent tunneling," *Phys. Rev. B*, vol. 56, no. 18, pp. 11827–11832, 1997.
- [68] W. Skowroński, T. Stobiecki, J. Wrona, K. Rott, A. Thomas, G. Reiss, and S. Van Dijken, "Interlayer exchange coupling and current induced magnetization switching in magnetic tunnel junctions with MgO wedge barrier," *J. Appl. Phys.*, vol. 107, no. 9, 2010.
- [69] S. Serrano-Guisan, W. Skowronski, J. Wrona, N. Liebing, M. Czapkiewicz, T. Stobiecki, G. Reiss, and H. W. Schumacher, "Inductive determination of the optimum tunnel barrier thickness in magnetic tunneling junction stacks for spin torque memory applications," *J. Appl. Phys.*, vol. 110, no. 2, 2011.
- [70] T. Seki, H. Kubota, A. Fukushima, K. Yakushiji, S. Yuasa, K. Ando, H. Maehara, S. Yamagata, H. Okuyama, and K. Tsunekawa, "Evaluation of barrier uniformity in magnetic tunnel junctions prepared using natural oxidation of thin Mg layers," *J. Appl. Phys.*, vol. 108, no. 12, pp. 1–4, 2010.
- [71] H. Maehara, K. Nishimura, Y. Nagamine, K. Tsunekawa, T. Seki, H. Kubota, A. Fukushima, K. Yakushiji, K. Ando, and S. Yuasa, "Tunnel Magnetoresistance above 170% and Resistance-Area Product of 1 Ω (μm)² Attained by In situ Annealing of Ultra-Thin MgO Tunnel Barrier," *Appl. Phys. Express*, vol. 4, no. 3, pp. 18–21, 2011.
- [72] B. Oliver, Q. He, X. Tang, and J. Nowak, "Dielectric breakdown in magnetic tunnel junctions having an ultrathin barrier," *J. Appl. Phys.*, vol. 91, no. 7, pp. 4348–4352, 2002.
- [73] K. Komagaki, M. Hattori, K. Noma, H. Kanai, K. Kobayashi, Y. Uehara, M. Tsunoda, and M. Takahashi, "Influence of diffused boron into MgO barrier on pinhole creation in

CoFeB/MgO/CoFeB magnetic tunnel junctions,” *IEEE Trans. Magn.*, vol. 45, no. 10, pp. 3453–3456, 2009.

- [74] P. K. George, Y. Wu, R. M. White, E. Murdock, and M. Tondra, “Shot noise in low-resistance magnetic tunnel junctions,” *Appl. Phys. Lett.*, vol. 80, no. 4, pp. 682–684, 2002.
- [75] A. Zaleski, J. Wrona, M. Czapkiewicz, W. Skowroski, J. Kanak, and T. Stobiecki, “The study of conductance in magnetic tunnel junctions with a thin MgO barrier: The effect of Ar pressure on tunnel magnetoresistance and resistance area product,” *J. Appl. Phys.*, vol. 111, no. 3, p. 33903, 2012.
- [76] R. Lin, D. H. Petersen, F. Wang, B. R. Yates, K. S. Jones, O. Hansen, A. Kontos, and P. F. Nielsen, “Junction leakage measurements with micro four-point probes,” *AIP Conf. Proc.*, vol. 1496, no. 2012, pp. 175–178, 2012.
- [77] C. L. Petersen, T. M. Hansen, P. Bøggild, A. Boisen, O. Hansen, T. Hassenkam, and F. Grey, “Scanning microscopic four-point conductivity probes,” *Sensors Actuators, A Phys.*, vol. 96, no. 1, pp. 53–58, 2002.
- [78] C. L. Petersen and P. F. Nielsen, “Electrical feedback detection system for multi-point probes,” US patent 7135876B2, 2006.
- [79] T. Ansbaek, D. H. Petersen, O. Hansen, J. B. Larsen, T. M. Hansen, and P. Bøggild, “Fundamental size limitations of micro four-point probes,” *Microelectron. Eng.*, vol. 86, no. 4–6, pp. 987–990, 2009.
- [80] M. Gajek, J. J. Nowak, J. Z. Sun, P. L. Trouilloud, E. J. O’Sullivan, D. W. Abraham, M. C. Gaidis, G. Hu, S. Brown, Y. Zhu, R. P. Robertazzi, W. J. Gallagher, and D. C. Worledge, “Spin torque switching of 20 nm magnetic tunnel junctions with perpendicular anisotropy,” *Appl. Phys. Lett.*, vol. 100, no. 13, pp. 1–4, 2012.
- [81] K. Kinoshita, H. Utsumi, K. Suemitsu, H. Hada, and T. Sugibayashi, “Etching magnetic tunnel junction with metal etchers,” *Jpn. J. Appl. Phys.*, vol. 49, no. 8 part 2, 2010.
- [82] T. Mukai, B. Jinnai, Y. Fukumoto, N. Ohshima, H. Hada, and S. Samukawa, “Plasma irradiation damages to magnetic tunneling junction devices,” *J. Appl. Phys.*, vol. 102, no. 7, 2007.

List of papers

Paper I

D. Kjaer, O. Hansen, H. H. Henrichsen, J. W. Chenchen, K. Noergaard, P. F. Nielsen and D. H. Petersen

Fast static field CIPT mapping of unpatterned MRAM film stacks

Meas. Sci. Technol., vol. 26, no. 4, p. 045602, 2015

Paper II (accepted for publication)

D. Kjaer, O. Hansen, F. W. Østerberg, H. H. Henrichsen, C. Markvardsen, P. F. Nielsen and D. H. Petersen

Characterization of positional errors and their influence on micro four-point probe measurements on a 100 nm Ru film

Manuscript accepted (14 May 2015) for publication in *Meas. Sci. Technol.*

Paper III (draft)

F. W. Østerberg, D. Kjaer, P. F. Nielsen, O. Hansen and D. H. Petersen

Accuracy of Current-In-Plane Tunneling measurements on test pads for MRAM

Draft (May 2015)

Paper IV

M. R. Lotz, M. Boll, O. Hansen, D. Kjær, P. Bøggild, and D. H. Petersen

Revealing origin of quasi-one dimensional current transport in defect rich two dimensional materials

Appl. Phys. Lett., vol. 105, no. 5, p. 053115, 2014

Paper V

M. Boll, M. R. Lotz, O. Hansen, F. Wang, D. Kjær, P. Bøggild, and D. H. Petersen

Sensitivity analysis explains quasi-one-dimensional current transport in two-dimensional materials

Phys. Rev. B, vol. 90, no. 24, p. 245432, 2014.

Papers not included in this thesis:

Paper A

P. F. Nielsen, D. H. Petersen, R. Lin, A. Jensen, H. H. Henrichsen, L. Gammelgaard, D. Kjaer and O. Hansen

Microprobe Metrology for direct Sheet Resistance and Mobility characterization

Proceedings of the 12th International Workshop on Junction Technology (IWJT), 14-15 May 2012.

DOI: 10.1109/IWJT.2012.6212819

Paper B

H. H. Henrichsen, O. Hansen, D. Kjaer, P. F. Nielsen, F. Wang and D. H. Petersen

Precision of single-engage micro Hall effect measurements

Proceedings of the 14th International Workshop on Junction Technology (IWJT), 18-20 May 2014.

DOI: 10.1109/IWJT.2014.6842029

Paper I

D. Kjaer, O. Hansen, H. H. Henrichsen, J. W. Chenchen, K. Noergaard, P. F. Nielsen and
D. H. Petersen

Fast static field CIPT mapping of unpatterned MRAM film stacks

Meas. Sci. Technol., vol. 26, no. 4, p. 045602, 2015

Fast static field CIPT mapping of unpatterned MRAM film stacks

Daniel Kjaer^{1,2}, Ole Hansen^{2,3}, Henrik Hartmann Henrichsen^{2,1},
Jacob Wang Chenchen^{4,5}, Kristian Noergaard¹, Peter Folmer Nielsen¹ and
Dirch Hjorth Petersen²

¹ CAPRES A/S, Diplomvej 373, DK-2800 Kgs. Lyngby, Denmark

² DTU Nanotech—Department of Micro- and Nanotechnology, Technical University of Denmark, Building 345 East, DK-2800 Kgs. Lyngby, Denmark

³ CINF—Centre for Individual Nanoparticle Functionality, Technical University of Denmark, Building 345 East, DK-2800 Kgs. Lyngby, Denmark

⁴ DSI—Data Storage Institute, A*STAR (Agency for Science, Technology and Research), DSI Building, 5 Engineering Drive 1, Singapore 117608, Singapore

E-mail: dk@capres.com and ole.hansen@nanotech.dtu.dk

Received 13 December 2014, revised 27 January 2015

Accepted for publication 9 February 2015

Published 9 March 2015



Abstract

While investigating uniformity of magnetic tunnel junction (MTJ) stacks we find experimentally and analytically that variation in the resistance area product (RA) is more important to monitor as compared to the tunnel magnetoresistance (TMR), which is less sensitive to MTJ variability. The standard Current In-Plane Tunneling (CIPT) method measures both RA and TMR, but the usefulness for uniformity mapping, e.g. for tool optimization, is limited by excessive measurement time. Thus, we develop and demonstrate a fast complementary static magnetic field method focused only on measurement of RA. We compare the static field method to the standard CIPT method and find perfect agreement between the extracted RA values and measurement repeatability while the static field method is several times faster. The static field CIPT method is demonstrated for 200 mm wafer mapping showing radial as well as asymmetrical variations related to the MTJ deposition conditions.

Keywords: four-point measurement, four-point probe, sheet resistance, magnetoresistance, magnetic tunnel junction (MTJ), current in-plane tunneling (CIPT), magnetic ram (MRAM)

(Some figures may appear in colour only in the online journal)

1. Introduction

The need for suitable metrology is increasing as the industry moves towards volume production of magnetic random access memory (MRAM) and starts focusing on thin film homogeneity and other performance related factors [1–3]. Thus, to identify and maximize the usable area of a wafer is of fundamental importance. This involves characterization of the resistance area product RA (or equivalently the specific contact resistance) in the two spin polarized states from which the tunneling magnetoresistance ratio (TMR) can be calculated.

For several decades, specific contact resistance measurements have been done using a variety of so-called transmission line methods [4–7]. The use of collinear four-point probes for specific contact resistance measurements was pioneered by Severin *et al* [8] in 1971 and extended in 1991 in a hitherto unnoticed paper by Vu *et al* [9] for the specific case of two parallel coupled sheets of finite conductance. They both solved for the electrical potential distribution on the surface of a two-layer structure with a specific contact resistance at the interface, and showed how the transfer length could be extracted from four-point probe configuration switching [8] and variable electrode pitch [9]. Vu *et al* also applied the measurement technique to an Al/RuO₂/Al stack [10]. Essentially

⁵ Presently at GLOBALFOUNDRIES Singapore Pte. Ltd.

the same technique, Current In-Plane Tunneling (CIPT) [11], has in the past decade been the standard method to evaluate the two most critical parameters, RA and TMR, associated with magnetic tunnel junctions of the unpatterned tunnel junction stack.

The CIPT metrology method reduces the turnaround time in tunnel junction development due to the ability of measuring on unpatterned magnetic tunnel junction (MTJ) stacks. However, with a measurement time of 1–2 min per measurement, the technique is commonly used just for research and development of novel MTJ stacks, and not for full wafer analysis with high spatial resolution.

In this work we evaluate the CIPT metrology for optimization and production qualification of deposition tools. We show that the variation of RA is the most critical process parameter as compared to the variation of TMR and propose that MTJ variability is best characterized by uniformity mapping of just RA. This approach reduces the total measurement time by a factor of 5 since such data acquisition can be done in a static magnetic field and thus time-consuming magnetic field switching and excessive data acquisition are avoided.

2. Experiment

MTJs rely on spin polarized electron transport between two ferromagnets across a thin tunnel barrier, which results in a ‘low’ and a ‘high’ state for the resistance-area product of the junction, RA_{low} and RA_{high} , respectively. The contrast between these values is the tunneling magnetoresistance $TMR = (RA_{\text{high}} - RA_{\text{low}})/RA_{\text{low}}$. The top and bottom layers are characterized by their sheet resistances labeled R_t and R_b , respectively.

A microscopic 12-point probe, see figure 1(a), is landed on top of an unpatterned MTJ and a series of four-point measurements at varying electrode pitch is carried out by combining different subsets of four electrodes. The theoretical expression provided by Vu *et al* [9] is then fitted to the measurement data using R_t , R_b and RA as fitting parameters.

Figure 1(b) shows an electrical model describing the current flow in a small sample volume of width dr placed a radial distance, r , away from the current inlet. At some small electrode pitch, s , the current will flow primarily in the top layer, while at some large electrode pitch the barrier resistance will be negligible and the current flow will be limited only by the parallel resistance of the top and bottom layers. The latter is the case for probe pitches $s \gg \lambda$, where $\lambda = [RA/(R_t + R_b)]^{1/2}$ is the transfer length for a given sample [9–11].

The electrostatic potential of the sample surface a distance $\mathbf{r} - \mathbf{r}_0$ away from a single current source is given by [9]:

$$\Phi(\mathbf{r}, \mathbf{r}_0) = \frac{IR_t R_b}{2\pi(R_t + R_b)} \left[\frac{R_t}{R_b} K_0 \left(\frac{|\mathbf{r} - \mathbf{r}_0|}{\lambda} \right) - \ln(|\mathbf{r} - \mathbf{r}_0|) \right],$$

where I is the injected current and K_0 is the modified Bessel function of the second kind of order zero. In a four-point probe setup two current electrodes positioned at \mathbf{r}_+ and \mathbf{r}_- can be considered using the superposition principle to evaluate the potential at position \mathbf{r} . The four-point resistance can be defined

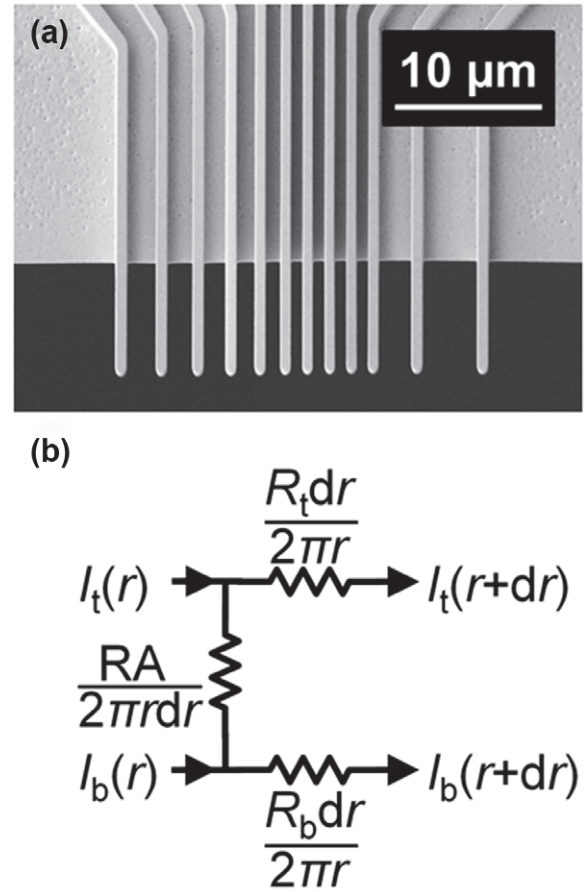


Figure 1. (a) Scanning electron micrograph of a 12-point probe. (b) Electrical model describing the current flow in a small sample volume of width dr placed a radial distance, r , away from the current inlet.

as $R = V/I$, where V is the voltage difference between the two potential electrodes and I is the current passed between the two current electrodes.

The results reported here are based on an implementation of van der Pauw like dual configuration measurements [12], where each subset of four cantilevers measures in both A- and B-configurations (see below). This method is known to give excellent electrode position correction [13]; position correction can also be obtained using a first order correction method as suggested by Worledge *et al* [14]. For a standard four-point probe with electrodes at positions \mathbf{r}_1 , \mathbf{r}_2 , \mathbf{r}_3 and \mathbf{r}_4 the measured potential difference can be evaluated as:

$$V_A = \Phi(\mathbf{r}_2, \mathbf{r}_1) - \Phi(\mathbf{r}_2, \mathbf{r}_4) - \Phi(\mathbf{r}_3, \mathbf{r}_1) + \Phi(\mathbf{r}_3, \mathbf{r}_4),$$

and

$$V_B = \Phi(\mathbf{r}_2, \mathbf{r}_1) - \Phi(\mathbf{r}_2, \mathbf{r}_3) - \Phi(\mathbf{r}_4, \mathbf{r}_1) + \Phi(\mathbf{r}_4, \mathbf{r}_3)$$

for A- and B-configurations, respectively [13].

The investigated sample was a 200 mm wafer with an unpatterned, in-plane (bottom electrode)/PtMn (16 nm)/Co₇₀Fe₃₀ (2.2 nm)/Ru (0.85 nm)/Co₄₀Fe₄₀B₂₀ (2.5 nm)/MgO (1 nm)/Co₄₀Fe₄₀B₂₀ (2.5 nm)/(top electrode) MTJ prepared in a magnetron sputtering process with a subsequent thermal anneal. This design of the stack ensures that the lower CoFeB layer is pinned while the upper CoFeB layer is free. Since the

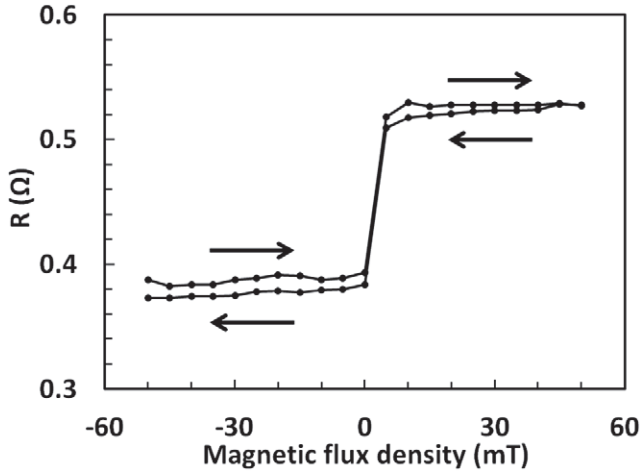


Figure 2. Hysteresis loop of the free layer recorded using a micro four-point probe with a pitch of $1.5\mu\text{m}$. Arrows indicate the magnetic sweep direction.

value of RA depends on the state of the magnetization (parallel or anti-parallel) it follows that the transfer length of the sample will change accordingly, which can be expressed as $\lambda_{\text{low}} = [\text{RA}_{\text{low}}/(R_t + R_b)]^{1/2}$ and $\lambda_{\text{high}} = [\text{RA}_{\text{high}}/(R_t + R_b)]^{1/2}$. The respective transfer lengths for the sample investigated in this work are nominally $\lambda_{\text{low}} = 1.5\mu\text{m}$ and $\lambda_{\text{high}} = 2.5\mu\text{m}$. Due to shadowing effects of the edge exclusion ring in the processing equipment, an area along the perimeter of the sample is left unmetallized and has therefore not been probed in this work.

Measurements were carried out on a semi-automatic CAPRES CIPTECH-M300 using micro 12-point probes with electrode pitches in the range from $1.5\mu\text{m}$ to $8.3\mu\text{m}$. In the conventional switching field CIPT measurement [11], variable pitch four-point probe resistance measurements are acquired at two separate magnetic flux densities, in this case $\pm 10\text{mT}$, corresponding to anti-parallel and parallel magnetization of the two $\text{Co}_{40}\text{Fe}_{40}\text{B}_{20}$ layers separated by the MgO barrier. These magnetic flux densities were chosen based on the measured hysteresis loop in figure 2 measured using a micro four-point probe with $1.5\mu\text{m}$ pitch during a magnetic flux density sweep.

In this work a static field CIPT method is introduced where variable pitch four-point probe resistance is acquired only in a static magnetic flux density of either -10mT or $+10\text{mT}$. From this measurement, either RA_{low} or RA_{high} of the sample can be deduced using only half of the dataset required in the conventional switching field CIPT method.

3. Results and discussion

While investigating MTJ wafer uniformity, we performed two cross-wafer line scans (1 mm step size) presented in figure 3 using the conventional switching field CIPT measurement practice. We only depict RA_{high} since RA_{low} showed equivalent behavior. Whereas the parameters TMR and RA appear radially symmetric along the X-axis, a clear gradual change in RA is observed along the Y-axis. It is reasonable to assume that the asymmetry is related to the fact that the target dimension along the Y-axis is smaller than the wafer size while the target

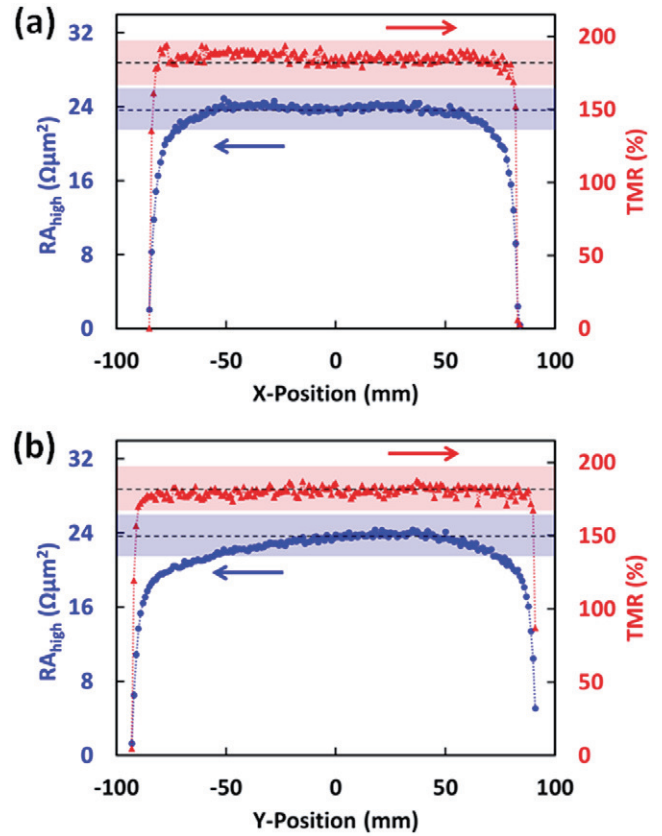


Figure 3. Line scan measurements of RA_{high} and $\text{TMR} = (\text{RA}_{\text{high}} - \text{RA}_{\text{low}})/\text{RA}_{\text{low}}$ with a step size of 1 mm along the X-axis (a) and Y-axis (b) across a 200 mm wafer. The colored regions mark a $\pm 10\%$ band with respect to the mean values indicated by the dashed lines. While RA and TMR appear radially symmetric along the X-axis (a), an asymmetric slope in RA is clearly observed along the Y-axis (b).

dimension along the X-axis is much larger than the wafer size. As a result good uniformity can be expected along the X-axis while on the Y-axis the uniformity is very poor without movement, and even with linear movement of the sample along the Y-axis with respect to the static target, which is the case for this study, the uniformity is inferior to that along the X-axis. Such process variability is observed in most detail by full wafer mapping of sample homogeneity, but with the conventional CIPT method this can be very time consuming.

From figures 3(a) and (b) it is evident that the relative variation of RA is the dominant factor when estimating the usable area of the wafer, here defined by a $\pm 10\%$ acceptance band centered on the mean value of the central $20 \times 20\text{mm}^2$ area of the sample. Whereas TMR appear constant with an abrupt change in close proximity of the edge of the processed area, we observe that RA begins to decrease significantly at an approximate distance of 50 mm from the wafer center. This is in good agreement with previously reported results for MTJs of good barrier quality without pinholes [15–18].

Experimental data [15, 19–23] as well as theoretical considerations [15, 16, 19–23] suggest that for thicker tunnel barriers the RA_{low} and RA_{high} products both depend exponentially on the thickness of the tunnel barrier with the same exponential factor, while the pre-factors to the exponential

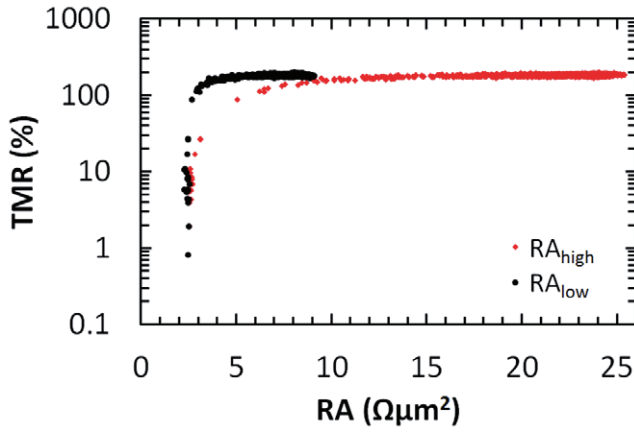


Figure 4. TMR versus RA extracted from a wafer mapping using the conventional switching field CIPT measurement practice.

depend primarily on the spin polarization of the ferromagnets used. As a result the TMR is hardly affected by changes in the thickness of the tunnel barrier. For thinner barriers this is not true anymore, since pinholes and nanobridges provide an alternative current path to tunneling and may for very thin barriers dominate the transport altogether. This has been modeled as a parallel resistor network [24] such that

$$\frac{1}{RA_{low}} = (1 - \alpha_\ell)g_{low}T(d, \Phi_B) + \alpha_\ell g_{leak}$$

$$\frac{1}{RA_{high}} = (1 - \alpha_\ell)g_{high}T(d, \Phi_B) + \alpha_\ell g_{leak}$$

where $T(d, \Phi_B)$ is the tunneling probability, which primarily depends on the tunnel barrier thickness d and barrier height Φ_B . The conductances per area g_{low} and g_{high} are characteristic pre-factors for low and high spin states, respectively, and g_{leak} is the characteristic leak conductance per area due to pinholes and nanobridges. The factor α_ℓ is the area fraction occupied by pinholes and nanobridges, and this area fraction is of course not available for tunneling. As a result, the tunneling magnetoresistance ratio becomes

$$\begin{aligned} TMR &= \frac{RA_{high} - RA_{low}}{RA_{low}} \\ &= \frac{(1 - \alpha_\ell)g_{low}T(d, \Phi_B) + \alpha_\ell g_{leak}}{(1 - \alpha_\ell)g_{high}T(d, \Phi_B) + \alpha_\ell g_{leak}} - 1. \end{aligned}$$

Obviously, for a perfect tunnel barrier, with $\alpha_\ell = 0$, $TMR = g_{low}/g_{high} - 1$ and is essentially independent of the tunnel barrier thickness to first order, while for a defective barrier, with $\alpha_\ell = 1$, $TMR = 0$. The transition between these two extreme cases happens over a very narrow range of barrier thicknesses (a small fraction of 1 nm) depending on the preparation of the barrier [25] since α_ℓ is extremely thickness dependent. As a result, cut-off values for RA_{low} and RA_{high} exist, below which TMR becomes too small to be useful due to the increase of α_ℓ . This is in line with our observations from figure 4 showing TMR as a function of RA as extracted from a conventional switching field CIPT wafer mapping. The results in figure 4 suggest that variations in RA_{high} are most easily evaluated

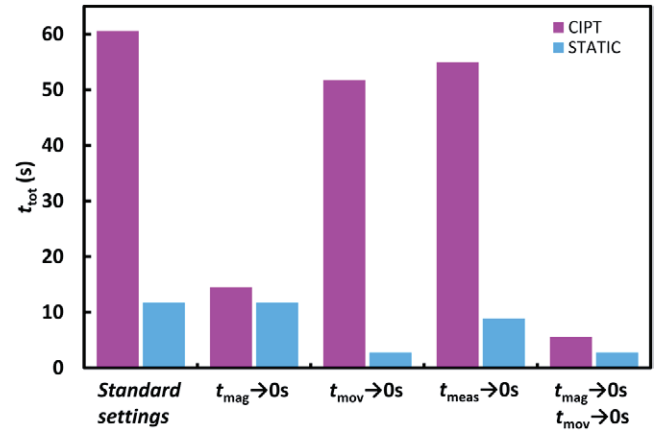


Figure 5. Time spent per point, t_{tot} , for conventional CIPT and static field method respectively are presented for the regular implementation of the methods as well as four scenarios for which one or more contributing factors are negligible while the other factors remain unchanged.

due to the larger relative change compared with RA_{low} . Also, evaluating the transfer length requires measurements using electrode pitches in a range of the order of λ [11, 25]. For typical MTJs intended for MRAM, λ is close to the minimum electrode pitch practically achievable, and accurate four-point measurements becomes increasingly challenging for reduced electrode pitch. Thus, it may be an advantage to measure only in the anti-parallel magnetization state, as RA_{high} yields the most easily accessible and most relevant sample parameter in the shortest measurement time possible. On the other hand the option of simply applying a strong magnetic field and thereby ascertaining that the layers are in a well-defined, parallel state is a unique advantage for measurements in the parallel state. Similarly, but more time consuming, first applying a strong magnetic field in one direction to saturate the sample and subsequently measuring in a weaker, static magnetic field of opposite orientation could lead to a more precise characterization of the anti-parallel state. In general we shall refer to this selective and less comprehensive measurement method as the static field CIPT method.

While uniformity mapping is possible with conventional CIPT measurements on a full wafer, the task turns out to be impractical due to the resulting measurement time. The overall time spent per measurement point can be split into three contributing factors:

$$t_{tot} = t_{meas} + t_{mov} + t_{mag},$$

where t_{meas} is the time spent sampling data, t_{mov} is the time spent on stage movement and t_{mag} is the time spent on adjustments of the magnetic field.

In a timed comparison of the two methods, a square grid of 10×10 points with a step size of $100\mu m$ in a homogeneous region of the sample was measured using a current of $200\mu A$ at a frequency of 25Hz and an integration time of 81ms. The static field method was found to be more than 5 times faster than the conventional CIPT method. Figure 5 compares the time consumption of the two methods in their regular implementation and predicts how they would relate in

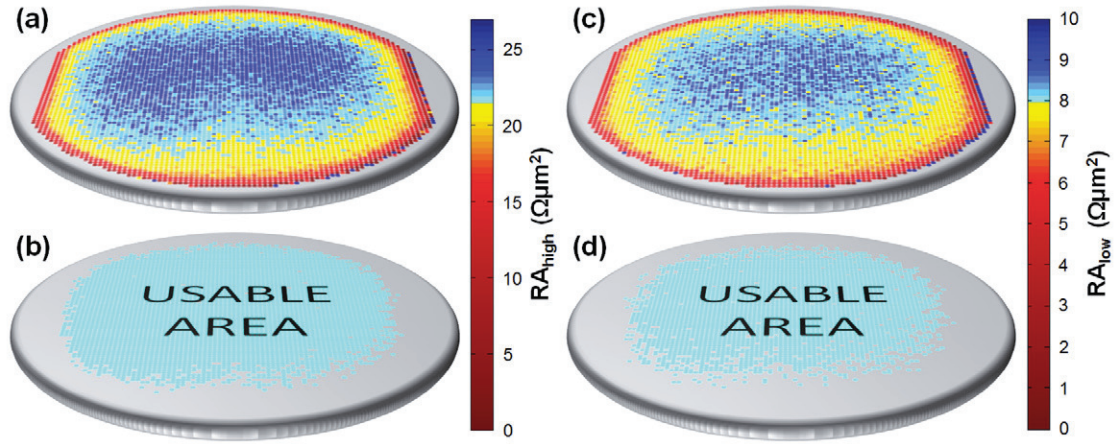


Figure 6. High density maps of RA_{high} (a) and RA_{low} (c) on the full 200mm wafer obtained with 2mm step size totaling 6510 measurement points per map. (b) and (d) The usable wafer area versus edge exclusion zone based on an acceptance limit of $\pm 10\%$ with respect to the mean value at the center of the wafer for RA_{high} and RA_{low} respectively.

Table 1. Mean value and relative standard deviation of RA_{low} and RA_{high} based on three line scans: one series of traditional switching field CIPT measurements (CIPT) and two series of static field CIPT measurements (STATIC).

		CIPT	STATIC	
B	(mT)	± 10	-10	+10
RA_{low}	($\Omega\mu m^2$)	8.5	8.6	
$\sigma(RA_{low})$	(%)	2.3	2.2	
RA_{high}	($\Omega\mu m^2$)	23.4		23.6
$\sigma(RA_{high})$	(%)	1.6		2.0

Note: Each scan contains 100 measurement points distributed with a step size of $2\mu m$.

other scenarios where one or more of the contributing factors are negligible while the other factors remain unchanged. In the regular implementation $t_{meas} = 5.6s$ and $2.8s$ for CIPT and static field methods respectively, t_{mov} , which applies to both methods, is $8.9s$ and t_{mag} , which applies only to the conventional CIPT method, is $46.1s$. The time reduction observed for the regular implementation of the methods is mainly due to the lack of magnet adjustments in the static field method. However, as is seen from figure 5, changes to other factors can greatly influence the ratio of time spent with the different method implementations.

Thus, when we utilize the proposed static field CIPT method and measure only RA_{low} or RA_{high} , we can drastically reduce the time spent per point, which in turn allows us to map the entire wafer within a reasonable timespan. The mapping of RA should of course be supplemented by a few switching field CIPT measurements, e.g. near the wafer centre, to establish TMR. In figure 6 we present high resolution wafer maps obtained with the static field CIPT method for both RA_{low} and RA_{high} . The two maps are presented for comparison only, since the necessary information for tool optimization can be extracted from a single one of them as argued above. Each map contains 6510 measurement positions distributed with a step size of $2mm$. The asymmetric behavior of RA seen in figure 3(b) is also observable from both maps and the usable area based on an acceptance limit of $\pm 10\%$ with respect to the

mean value at the center of the wafer is also consistent. For the particular combination of sample properties and range of electrode pitches in question, there is no significant advantage from measuring RA_{high} as opposed to RA_{low} . However, we do observe a higher density of outliers in the usable area determined by RA_{low} , which might be attributed to measurement precision.

To allow for a comparison of measurement quality for the two different methods, three individual, high density line scans each containing 100 measurement points were carried out using a step size of only $2\mu m$. This was done in order to reduce the influence of local sample variations; otherwise the same measurement settings as mentioned above were used. One series of traditional switching field CIPT measurements as well as two series of static field CIPT measurements in an applied magnetic field of respectively $+10mT$ and $-10mT$ were performed. A comparison of the measurement results is summarized in table 1, and the two methods are found to be in good agreement.

4. Conclusion

High density mapping of an unpatterned MTJ sample reveals variations of RA and TMR, exceeding by far an acceptance limit of $\pm 10\%$. We find the variation of RA to be the most critical process parameter as compared to the variation of TMR. Because of process induced, radial asymmetry in the variations of RA, we argue that high resolution wafer mapping of the entire processed area is necessary for adequate process optimization and tool qualification. Since the CIPT method is a serial characterization technique, the time associated with mapping an entire wafer is directly proportional to the measurement time per point and resolution. Thus, to enable high resolution mapping, we have demonstrated a static field CIPT method, which allows us to reduce the measurement time by a factor of 5, by measuring only RA, thus excluding TMR. This enhancement is obtained purely by acquiring only half of the data needed for the conventional switching field CIPT measurement and particularly by avoiding magnetic

field switching. In a homogeneous region of the investigated sample, we observe that the two methods measure essentially the same RA values. By offering the choice of characterizing either RA_{low} or RA_{high} the static field CIPT method has an added advantage over the conventional switching field CIPT method, which relies on the characterization of both RA values. This allows for an improved matching of the range of available electrode pitches and sample transfer lengths λ_{low} or λ_{high} , which may effectively increase the dynamic range of any given 12-point probe.

Acknowledgments

The authors wish to thank Christian Markvardsen, Lim Sze Ter and Frederik Westergaard Østerberg for fruitful discussions and Lauge Gammelgaard for experimental assistance. The authors are grateful for the financial support of the Danish Ministry of Science, Innovation and Higher Education, the Danish National Research Foundation for funding the Center for Individual Nanoparticle Functionality (DNRF54) and the Danish National Advanced Technology Foundation. This work was supported by the Villum Foundation, project no. VKR023117.

References

- [1] Shi J 2005 *Ultrathin Magnetic Structures IV* (Berlin: Springer) p 188
- [2] Ikeda S, Hayakawa J, Lee Y M, Matsukura F, Ohno Y, Hanyu T and Ohno H 2007 *IEEE Trans. Electron Devices* **54** 991
- [3] Khvalkovskiy A V et al 2013 *J. Phys. D: Appl. Phys.* **46** 074001
- [4] Pedersen R J and Vernon F L 1967 *Appl. Phys. Lett.* **10** 29
- [5] Berger H H 1969 *IEEE Int. Solid-State Circuits Conf. 69: Digest of Technical Papers* (New York: L. Winner) p 160
- [6] Murrmann H and Widmann D 1969 *IEEE Int. Solid-State Circuits Conf. 69: Digest of Technical Papers* (New York: L. Winner) p 162
- [7] Schroder D K 2006 *Semiconductor Material and Device Characterization* (New York: Wiley)
- [8] Severin P J 1971 *Philips Res. Rep.* **26** 279
- [9] Vu Q T, Kolawa E, Halperin L and Nicolet M-A 1991 *Solid-State Electron.* **34** 279
- [10] Vu Q T, Kolawa E and Nicolet M-A 1991 *Solid-State Electron.* **34** 271
- [11] Worledge D C and Trouilloud P L 2003 *Appl. Phys. Lett.* **83** 84
- [12] Rymaszewski R 1969 *J. Phys. E: Sci. Instrum.* **2** 170
- [13] Thorsteinsson S, Wang F, Petersen D H, Hansen T M, Kjaer D, Lin R, Kim J-Y, Nielsen P F and Hansen O 2009 *Rev. Sci. Instrum.* **80** 053902
- [14] Worledge D C 2004 *Appl. Phys. Lett.* **84** 1695–7
- [15] MacLaren J M, Zhang X-G and Butler W H 1997 *Phys. Rev. B* **56** 11827
- [16] Yuasa S, Nagahama T, Fukushima A, Suzuki Y and Ando K 2004 *Nat. Mater.* **3** 868
- [17] Skowronski W, Stobiecki T, Wrona J, Rott K, Thomas A, Reiss G and van Dijken S 2010 *J. Appl. Phys.* **107** 093917
- [18] Serrano-Guisan S, Skowronski W, Wrona J, Leibing N, Czapkiewicz M, Stobiecki T, Reiss G and Schumacher H W 2011 *J. Appl. Phys.* **110** 023906
- [19] Seki T, Kubota H, Fukushima A, Yakushiji K, Yuasa S, Ando K, Maehara H, Yamagata S, Okuyama H and Tsunekawa K 2010 *J. Appl. Phys.* **108** 123915
- [20] Maehara H, Nishimura K, Nagamine Y, Tsunekawa K, Seki T, Kubota H, Fukushima A, Yakushiji K, Ando K and Yuasa S 2011 *Appl. Phys. Express* **4** 033002
- [21] Oliver B, He Q, Tang X and Nowak J 2002 *J. Appl. Phys.* **91** 4348
- [22] Komagaki K, Hattori M, Noma K, Kanai H, Kobayashi K, Uehara Y, Tsunoda M, and Takahashi M 2009 *IEEE Trans. Magn.* **45** 3453
- [23] George P K, Wu Y, White R M, Murdock E and Tondra M 2002 *Appl. Phys. Lett.* **80** 682
- [24] Zaleski A et al 2012 *J. Appl. Phys.* **111** 033903
- [25] Lin R, Petersen D H, Wang F, Yates B R, Jones K S, Hansen O, Kontos A and Nielsen P F 2012 *AIP Conf. Proc.* **1496** 175

Paper II

D. Kjaer, O. Hansen, F. W. Østerberg, H. H. Henriksen, C. Markvardsen, P. F. Nielsen and
D. H. Petersen

Characterization of positional errors and their influence on micro four-point probe measurements on a
100 nm Ru film

Meas. Sci. Technol., vol. 26, no. 9, p. 095005, 2015

Characterization of positional errors and their influence on micro four-point probe measurements on a 100 nm Ru film

Daniel Kjaer^{1,2}, Ole Hansen^{2,3}, Frederik Westergaard Østerberg^{1,2},
Henrik Hartmann Henrichsen¹, Christian Markvardsen¹,
Peter Folmer Nielsen¹ and Dirch Hjorth Petersen²

¹ CAPRES A/S, Diplomvej 373, DK-2800 Kgs. Lyngby, Denmark

² DTU Nanotech—Department of Micro- and Nanotechnology, Technical University of Denmark, Building 345 East, DK-2800 Kgs. Lyngby, Denmark

³ CINF—Centre for Individual Nanoparticle Functionality, Technical University of Denmark, Building 345 East, DK-2800 Kgs. Lyngby, Denmark

E-mail: dk@capres.com and ole.hansen@nanotech.dtu.dk

Received 6 March 2015, revised 8 May 2015

Accepted for publication 14 May 2015

Published 24 July 2015



Abstract

Thin-film sheet resistance measurements at high spatial resolution and on small pads are important and can be realized with micrometer-scale four-point probes. As a result of the small scale the measurements are affected by electrode position errors. We have characterized the electrode position errors in measurements on Ru thin film using an Au-coated 12-point probe. We show that the standard deviation of the static electrode position error is on the order of 5 nm, which significantly affects the results of single configuration measurements. Position-error-corrected dual-configuration measurements, however, are shown to eliminate the effect of position errors to a level limited either by electrical measurement noise or dynamic position errors. We show that the probe contact points remain almost static on the surface during the measurements (measured on an atomic scale) with a standard deviation of the dynamic position errors of 3 Å. We demonstrate how to experimentally distinguish between different sources of measurement errors, e.g. electrical measurement noise, probe geometry error as well as static and dynamic electrode position errors.

Keywords: four-point measurement, four-point probe, sheet resistance, position correction, four-point resistance, microprobe, thin film

(Some figures may appear in colour only in the online journal)

1. Introduction

Electrical characterization of thin films is of crucial importance to obtain and maintain control of fabrication processes in the micro- and nanoelectronics industry. The most important reference metrology has for the past six decades been four-point resistance measurements [1]. As the semiconductor industry continues to increase the substrate size, the cost of dedicated monitor wafers needed for process control also increases. Meanwhile, the thickness of the films is steadily decreasing

and more advanced processing applied, which complicates the nature of process variations to be monitored. This has led to development of metrology based on micrometer-scale four-point probes (M4PP) [2] with high spatial resolution [3] as well as the possibility of performing measurements in micrometer-sized scribe line test pads on product wafers [4], thus eliminating the need of expensive monitor wafers. However, with the micrometer-sized electrode spacing the influence of electrode position errors increases [5], and different schemes have been proposed to compensate for this effect [6, 7].

In this work we characterize position errors for M4PPs, and we evaluate the effectiveness of two position-correction algorithms. New measurement systems and probe designs may be evaluated and benchmarked against each other using the same strategy.

2. Theory

The purpose of a four-point probe measurement on a thin film is usually to determine the sheet resistance, R_S , of the film. The generic measurement is carried out by passing current, I_{ij} , through two point-like electrode contacts, (i, j) , to the sample and measure the voltage, V_{kl} , across two other point-like electrode contacts, (k, l) . For a uniform thin film sample the expected four-point resistance, $R_{kl, ij}$, is [8]

$$R_{kl, ij} = \frac{V_{kl}}{I_{ij}} = \frac{R_S}{2\pi} \ln \frac{|\mathbf{r}_l - \mathbf{r}_i| |\mathbf{r}_k - \mathbf{r}_j|}{|\mathbf{r}_k - \mathbf{r}_i| |\mathbf{r}_l - \mathbf{r}_j|}, \quad (1)$$

where \mathbf{r}_n is the in-plane position vector for the contacts and $n, m \in [i, j, k, l]$. It follows that the sheet resistance can be calculated from a measured value of $R_{kl, ij}$ by solving equation (1) for R_S if the four inter-electrode distances, $|\mathbf{r}_n - \mathbf{r}_m|$, are known accurately. In most practical implementations the electrodes are arranged on a single line, a collinear probe, as illustrated in figure 1, where the intended distances between neighboring contact points are s_1 , s_2 and s_3 .

Four-point probe measurements with the collinear probe can be arranged in several configurations, usually denoted A, B, and C and their inverted versions A', B', and C' [9] (see figure 1). Of the resistances R_A , R_B and R_C , measured in configurations A, B and C, only two are independent since $R_C = R_A - R_B$ [6]. Equivalent dependence applies to resistances measured in the inverted configurations and in the absence of a magnetic field, $R_A = R_A$, $R_{B'} = R_B$ and $R_{C'} = R_C$, due to reciprocity [10, 11]. For the collinear four-point probe the expected measured resistances according to equation (1) are

$$R_A = \frac{R_S}{2\pi} \ln \frac{|\mathbf{r}_3 - \mathbf{r}_1| |\mathbf{r}_2 - \mathbf{r}_4|}{|\mathbf{r}_2 - \mathbf{r}_1| |\mathbf{r}_3 - \mathbf{r}_4|} = \frac{R_S}{2\pi} \ln \frac{s_1 + s_2}{s_1} \frac{s_2 + s_3}{s_3} \quad (2)$$

$$R_B = \frac{R_S}{2\pi} \ln \frac{|\mathbf{r}_4 - \mathbf{r}_1| |\mathbf{r}_2 - \mathbf{r}_3|}{|\mathbf{r}_2 - \mathbf{r}_1| |\mathbf{r}_4 - \mathbf{r}_3|} = \frac{R_S}{2\pi} \ln \frac{s_1 + s_2 + s_3}{s_1} \frac{s_2}{s_3}. \quad (3)$$

When the electrode spacings, s_1 , s_2 , and s_3 , become small, the actual spacings may differ significantly from their nominal value such that e.g. $|\mathbf{r}_2 - \mathbf{r}_1| \neq s_1$ and then resistances calculated from equations (2) and (3) will be inaccurate due to the electrode spacing error; this is what we define as general position errors. These position errors arise for a number of

different physical reasons and may have both in-line and off-line components:

Probe geometry errors. The real probe may be fabricated with different electrode spacings than intended.

Static position errors. Each probe-sample engage may result in slightly different contact spacing, e.g. induced by plastic deformation of the electrode tips.

Dynamic position errors. While the probe is engaged on the sample, the contact points may move slightly on the sample surface, e.g. due to vibrations.

As a result of these errors the position, \mathbf{r}_n , of electrode $n \in [1, 2, 3, 4]$ may be displaced from the ideal position, $\mathbf{r}_{n0} = (x_{n0}, 0)$, according to

$$\begin{aligned} \mathbf{r}_n &= (x_{n0} + \Delta x_{n0} + \Delta x_n + \delta x_n, \Delta y_{n0} + \Delta y_n + \delta y_n) \\ &= (x_{n0} + \Delta_{nx}, \Delta_{ny}), \end{aligned} \quad (4)$$

where the ideal y-position is taken as $y_0 = 0$ without loss of generality; Δx_{n0} and Δy_{n0} are probe geometry errors and Δx_n and Δy_n are static position errors, while δx_n and δy_n are dynamic position errors; finally Δ_{nx} and Δ_{ny} are total in-line and off-line errors, respectively. As a result the probe spacing, $|\mathbf{r}_2 - \mathbf{r}_1|$, becomes

$$\begin{aligned} |\mathbf{r}_2 - \mathbf{r}_1| &= \sqrt{(s_1 + \Delta_{2x} - \Delta_{1x})^2 + (\Delta_{2y} - \Delta_{1y})^2} \\ &= s_1 \sqrt{\left(1 + \frac{\Delta_{2x} - \Delta_{1x}}{s_1}\right)^2 + \left(\frac{\Delta_{2y} - \Delta_{1y}}{s_1}\right)^2} \\ &\approx s_1 \left(1 + \frac{\Delta_{2x} - \Delta_{1x}}{s_1} + \frac{1}{2} \left(\frac{\Delta_{2y} - \Delta_{1y}}{s_1}\right)^2\right), \end{aligned} \quad (5)$$

and similar expressions are valid for the other probe spacings involved in the measurements. It follows that in-line position errors affect four-point probe measurements to first order, while the effects of off-line position errors are of second order. Thus, off-line position errors may be neglected for small electrode position errors relative to the electrode spacing.

When the electrical measurement noise on the extracted four-point resistance is smaller than contributions from geometrically induced errors, we may evaluate the extent of these geometrical errors. We assume that all electrodes suffer from normally distributed static in-line position errors with standard deviation σ_x and dynamic in-line position errors with standard deviation σ_x^{dyn} . With these assumptions it has been shown [12] that the relative standard deviations, $\sigma_{R_A}^{\text{rel}}$ and $\sigma_{R_B}^{\text{rel}}$, on R_A and R_B , respectively, are

$$\sigma_{R_A}^{\text{rel}} = \alpha \frac{\sigma_x}{\langle s \rangle} \quad \text{and} \quad \sigma_{R_B}^{\text{rel}} = \beta \frac{\sigma_x}{\langle s \rangle}, \quad (6)$$

where $\langle s \rangle = (s_1 + s_2 + s_3)/3$ is the mean electrode pitch. The geometrical coefficients, α and β , can be shown to be

$$\alpha = \frac{\frac{s_3 + s_2 + s_1}{3} \sqrt{\left(\frac{1}{s_1} - \frac{1}{s_2 + s_1}\right)^2 + \left(\frac{1}{s_1} + \frac{1}{s_2 + s_3}\right)^2 + \left(\frac{1}{s_2 + s_1} + \frac{1}{s_3}\right)^2 + \left(\frac{1}{s_3 + s_2} - \frac{1}{s_3}\right)^2}}{\ln\left(\frac{s_2 + s_1}{s_1} \frac{s_2 + s_3}{s_3}\right)}, \quad (7)$$

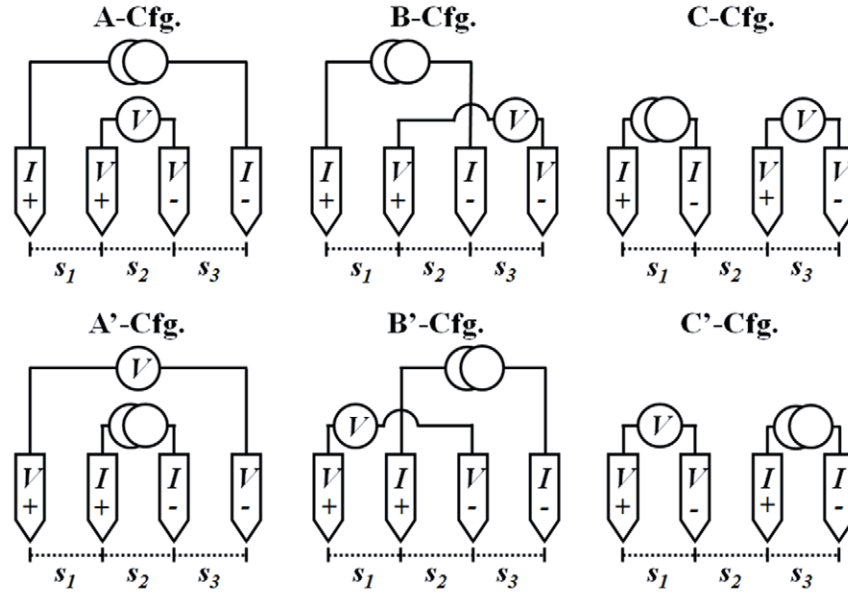


Figure 1. Collinear four-point probes and the independent configurations A, B, and C, as well as their inverted (dual) versions, A', B', and C'. The distances between neighboring electrodes are denoted s_1 , s_2 and s_3 .

and

$$\beta = \frac{\frac{s_3 + s_2 + s_1}{3} \sqrt{\left(\frac{1}{s_1} - \frac{1}{s_3 + s_2 + s_1}\right)^2 + \left(\frac{1}{s_1} + \frac{1}{s_2}\right)^2 + \left(\frac{1}{s_2} + \frac{1}{s_3}\right)^2 + \left(\frac{1}{s_3 + s_2 + s_1} - \frac{1}{s_3}\right)^2}}{\ln\left(\frac{s_1 + s_2 + s_3}{s_1 s_3}\right)}. \quad (8)$$

In the case of equidistant electrodes ($s_n = s$) the geometrical coefficients become particularly simple:

$$\sigma_{R_A}^{\text{rel}} = \frac{\sqrt{5}}{\ln 4} \frac{\sigma_x}{s} \cong 1.61 \times \frac{\sigma_x}{s}, \quad (9a)$$

$$\sigma_{R_B}^{\text{rel}} = \frac{4\sqrt{5}}{3 \ln 3} \frac{\sigma_x}{s} \cong 2.71 \times \frac{\sigma_x}{s}. \quad (9b)$$

With these equations, static position errors are evaluated from repeated measurements of R_A and R_B , where the probe is retracted from the sample and re-engaged between each recorded four-point measurement. Similarly, we can evaluate the dynamic in-line position errors from the variations of R_A or R_B during probe-sample engage. This gives similar expressions, i.e. $\sigma_{R_A}^{\text{rel, dyn}} = \alpha \sigma_x^{\text{dyn}} / \langle s \rangle$ and $\sigma_{R_B}^{\text{rel, dyn}} = \beta \sigma_x^{\text{dyn}} / \langle s \rangle$.

Rymaszewski has suggested a position correction algorithm [6] which eliminates the influence of in-line position errors for four-point measurements obtained using collinear electrodes. Based on the work by van der Pauw [13], he showed that the sheet resistance, R_S , must be related to R_A and R_B as follows:

$$\exp \frac{2\pi R_A}{R_S} - \exp \frac{2\pi R_B}{R_S} = 1. \quad (10)$$

From this expression (without geometric parameters), the sheet resistance can be calculated accurately if the measured resistances are only affected by in-line static position errors and in-line geometry errors. We shall denote this position correction scheme the van der Pauw (vdP) method. However, this

correction scheme will not correct for off-line position errors, and it will not correct for dynamic in-line position errors since R_A and R_B are not measured simultaneously. This can be understood by substituting equation (1) in equation (10) to get the geometry requirement, which must be fulfilled in order for equation (10) to be correct:

$$\left(\frac{|\mathbf{r}_3 - \mathbf{r}_1|}{|\mathbf{r}_2 - \mathbf{r}_1|} \frac{|\mathbf{r}_2 - \mathbf{r}_4|}{|\mathbf{r}_3 - \mathbf{r}_4|} \right)_A - \left(\frac{|\mathbf{r}_4 - \mathbf{r}_1|}{|\mathbf{r}_2 - \mathbf{r}_1|} \frac{|\mathbf{r}_2 - \mathbf{r}_3|}{|\mathbf{r}_4 - \mathbf{r}_3|} \right)_B = 1, \quad (11)$$

where subscripts indicate geometry during the respective measurements. The geometry requirement is trivially fulfilled under static conditions if the electrode-sample contacts are in-line. Any off-line component in the geometry will violate this condition, as will any dynamic in-line electrode displacement, and thus this scheme cannot correct such errors.

The position correction algorithm [7] proposed by Worledge uses a linear combination of R_A and R_B , i.e. $R_A - \gamma R_B$ where γ is a geometric prefactor introduced to reduce the influence of position errors. With this method the sheet resistance is calculated from

$$R_S = \frac{2\pi(R_A - \gamma R_B)}{\ln\left(\frac{s_1 + s_2}{s_1} \frac{s_2 + s_3}{s_3}\right) - \gamma \ln\left(\frac{s_1 + s_2 + s_3}{s_1} \frac{s_2}{s_3}\right)}, \quad (12)$$

with the geometric prefactor defined as

$$\gamma = \frac{(s_1 + s_2 + s_3) s_2}{(s_1 + s_2)(s_2 + s_3)}. \quad (13)$$

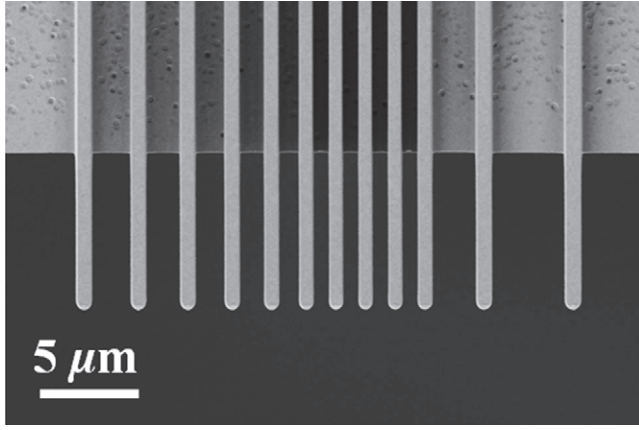


Figure 2. Scanning electron micrograph of a 12-point probe with Au-coated, straight cantilever electrodes.

Table 1. Geometric details of the eight subprobes formed using the 12-point probe. Distances between neighboring electrodes (s_1 , s_2 and s_3), mean probe pitch, $\langle s \rangle$, and geometric prefactors (α , β and γ) are listed.

s_1 (μm)	s_2 (μm)	s_3 (μm)	$\langle s \rangle$ (μm)	α	β	γ
1.50	1.50	1.50	1.50	1.61	2.71	0.75
2.00	2.25	2.50	2.25	1.62	2.71	0.75
3.00	3.00	3.00	3.00	1.61	2.71	0.75
4.50	4.50	3.75	4.25	1.56	2.44	0.77
4.50	4.50	4.50	4.50	1.61	2.71	0.75
6.00	6.00	5.25	5.75	1.57	2.50	0.77
7.50	7.75	6.75	7.33	1.55	2.45	0.77
9.00	8.25	7.50	8.25	1.62	2.71	0.75

Since this method is essentially a first-order approximation to the vdP method it is expected to correct the same errors, but only if they are sufficiently small that higher-order terms can be ignored.

Dynamic position errors are expected to affect the position-corrected sheet resistance according to

$$\sigma_{R_s}^{\text{rel}} = \frac{\sqrt{\alpha^2 + \left(\gamma \frac{R_B}{R_A} \beta\right)^2}}{1 - \gamma \frac{R_B}{R_A}} \frac{\sigma_x^{\text{dyn}}}{\langle s \rangle} \cong 5.61 \frac{\sigma_x^{\text{dyn}}}{\langle s \rangle}, \quad (14)$$

resulting from a first-order calculation valid for both correction schemes; the numerical value is valid for the equidistant probe.

3. Experimental

In order to characterize position errors and test the position-correction algorithms described above, a series of M4PP sheet resistance measurements were performed using a CAPRES MicroRSP-M300 [14]. The tool incorporates a multiplexer, which allows for four-point measurements at different electrode spacing when a multi-point probe is used. Figure 2 shows a conventional 12-point probe with Au-coated straight cantilever electrodes arranged with an irregular pitch distribution, which allows a variety of subprobes (individual subsets of four electrodes) with mean pitches, s , in the range from 1.5

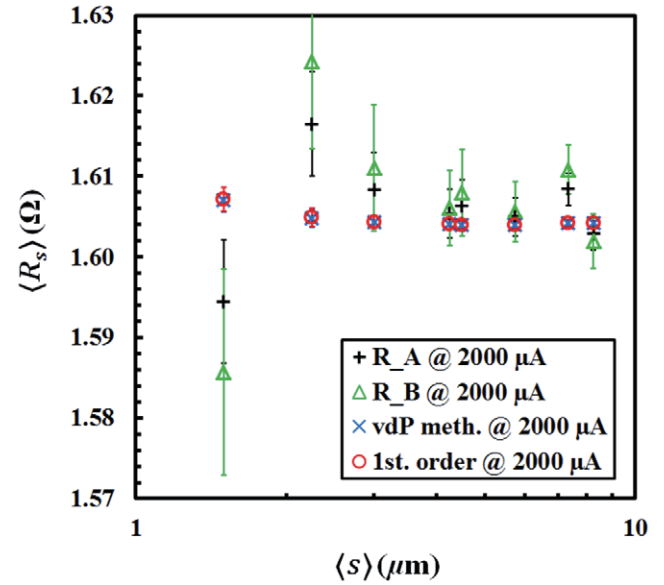


Figure 3. Mean sheet resistances for A- and B-configuration measurements as well as position-corrected values based on the van der Pauw (vdP) method and the first-order approximation as a function of the mean electrode pitch $\langle s \rangle$. Measurements were obtained with an applied current of 2000 μA . Error bars indicate the standard deviation.

to 8.25 μm to be obtained (see table 1). The cantilevers are made of SiO_2 and have nominal dimensions 0.75, 10 and 1 μm (width, length, and thickness). During measurements all cantilevers simultaneously contact the sample at an angle of 30°. A total of eight subprobes were used, some of which have non-equidistant electrode spacing. The eight subprobe geometries and geometric prefactors α , β and γ are summarized in table 1.

The sample measured in this study was a 200 mm silicon wafer with a sputter-deposited 100 nm Ru layer. Measurements were performed with a lock-in technique using a fixed current of either 200 or 2000 μA at 24.11 Hz and an integration time of 83 ms. The tool's fan-filter units were turned off in order to reduce the vibration level. For each subprobe the following sequence of measurement configurations was run during each probe-sample engage: A, B, A', and B'. For studies of the dynamic in-line position error the standard deviation on $\Delta R_A = R_A - R_{A'}$ and $\Delta R_B = R_B - R_{B'}$ were used since variations in ΔR are largely unaffected by static position errors and probe geometry errors. Possible offsets between measurements in A- and A'- and/or B- and B'-configurations will not affect the relative standard deviation of the results.

4. Results and discussion

Measurements were carried out as a rectangular area scan of 10 by 10 points distributed with a step size of 100 μm in a homogeneous area of the sample. The scan was repeated in the same area to compare measurements at 200 μA and 2000 μA , respectively. Figure 3 summarizes the results of the measurements at 2000 μA ; here the sheet resistances, R_s , with respective errors are shown as a function of the mean probe pitch. Sheet resistances extracted directly from A or B

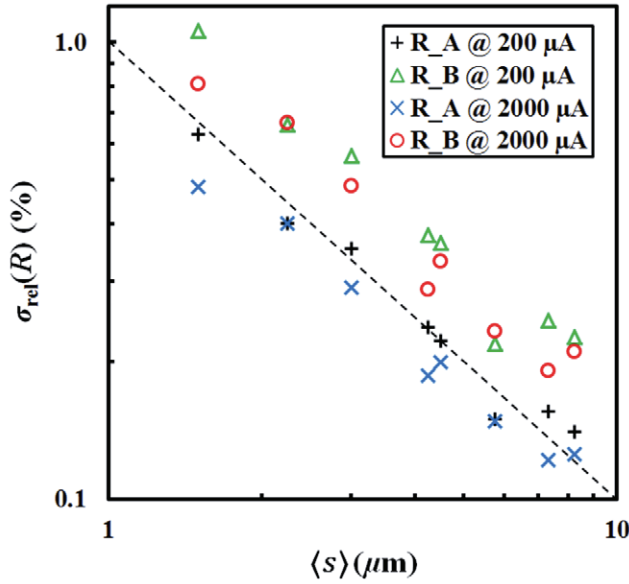


Figure 4. The relative standard deviations of A- and B-configuration measurements at applied currents of 200 and 2000 μ A as a function of the mean electrode pitch $\langle s \rangle$. A trend line with a slope of -1 decade/decade is added.

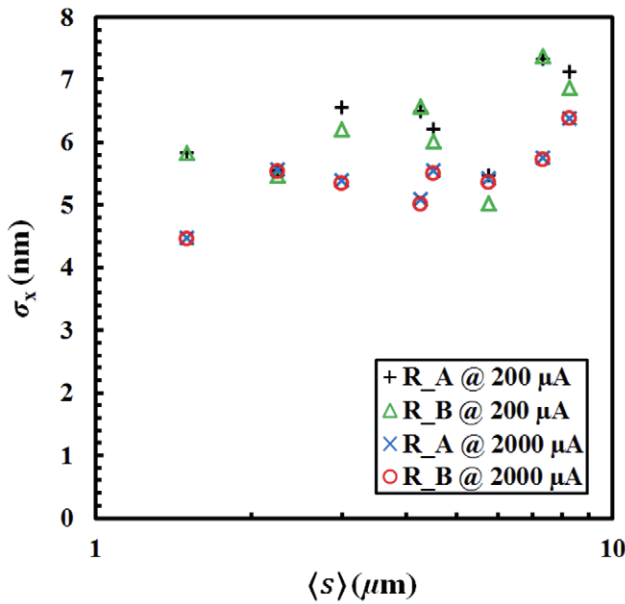


Figure 5. The standard deviation of the in-line electrode positions for A- and B-configurations respectively at applied currents of 200 and 2000 μ A as a function of mean electrode pitch $\langle s \rangle$.

measurements using equation (2) or (3) are shown along with position error corrected sheet resistances calculated using the same data. From figure 3 it is clear that both error correction schemes result in almost identical extracted sheet resistances and a low standard deviation, while sheet resistances extracted directly from A or B measurements deviates significantly from the position corrected mean and have a much larger standard deviation. Measurements at 200 μ A are not shown but give essentially the same results.

For the static position error analysis, the relative standard deviations of the measured resistances are plotted in figure 4.

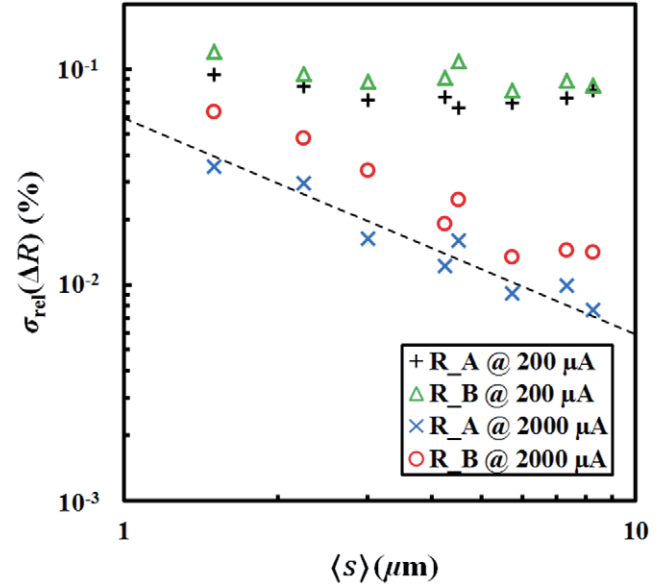


Figure 6. The relative standard deviation of ΔR for A- and B-configuration measurements, respectively, at applied currents of 200 and 2000 μ A as a function of mean electrode pitch $\langle s \rangle$. A trend line with a slope of -1 decade/decade is added.

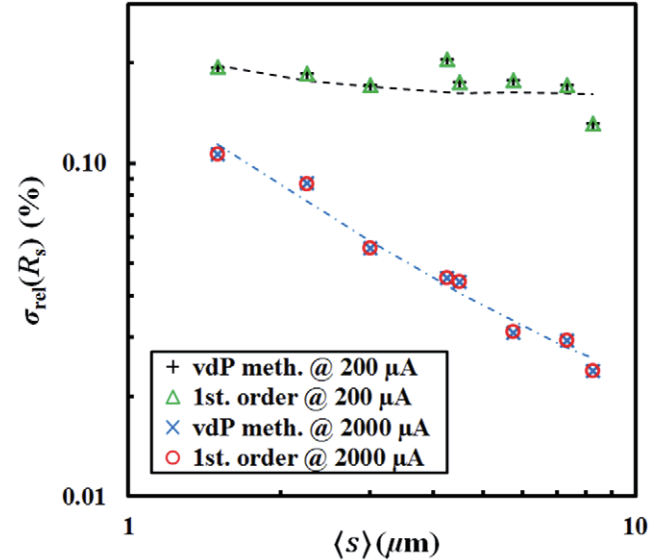


Figure 7. The relative standard deviation of the position corrected sheet resistance as a function of the mean electrode pitch $\langle s \rangle$. Position corrections based on the vdP method and the first-order approximation were used. The curves represent Monte Carlo simulations mimicking the measurement conditions (parameters: $\sigma_x = 5$ nm, $\sigma_x^{\text{dyn}} = 0.3$ nm and $V_n = 65$ nV).

As predicted, we observe a higher relative standard deviation for measurements in the B-configuration as compared to that of measurements in the A-configuration. We observe that the standard deviations decreases approximately inversely with the mean electrode pitch, which indicates that positional errors constitute the dominant source of error in this experiment. Changing the current by an order of magnitude does not influence the standard deviation significantly.

Applying the expressions of equations (6) to the measurement data in figure 4 allows the static in-line position error of

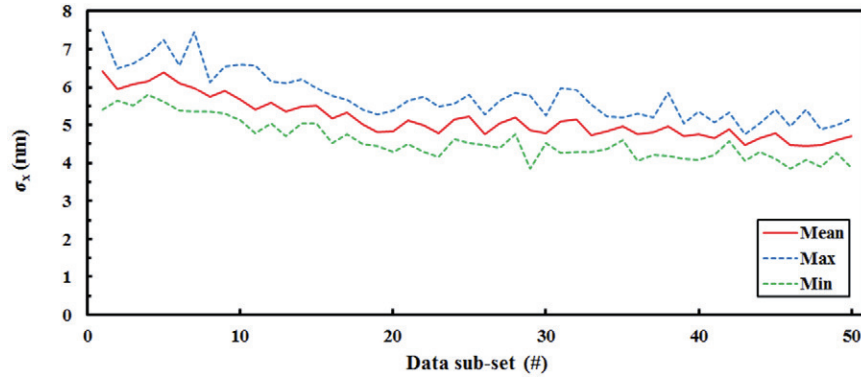


Figure 8. Static in-line position error evaluated across 50 data subsets containing 100 unique and consecutive measurements in an area scan totaling 5000 points. For each subset of data σ_x is evaluated individually for each subprobe and electrode configuration and we show mean, maximum, and minimum values of σ_x evaluated across all subprobes and electrode configurations.

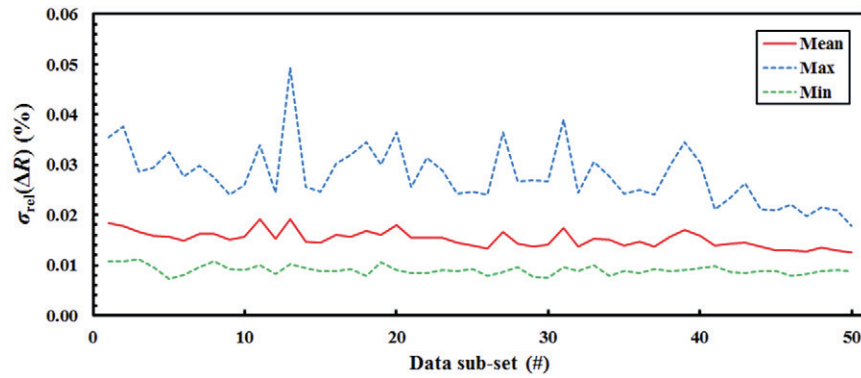


Figure 9. The relative standard deviation of ΔR for A-configuration measurements evaluated across 50 data subsets containing 100 unique and consecutive measurements in an area scan totaling 5000 points. For each subset of data $\sigma_{rel}(\Delta R)$ is evaluated individually for each subprobe and we show mean, maximum, and minimum value of $\sigma_{rel}(\Delta R)$ evaluated across all subprobes.

the electrodes to be estimated. From figure 5 we observe that the standard deviations of static in-line position errors are in the range from 4.5 to 7.2 nm and without any clear correlation to neither the applied current nor the mean pitch. The values are significantly lower than what has previously been reported (20 nm) in similar experiments [5]. We find a remarkable agreement between the in-line position errors extracted from A- and B-configuration measurements, respectively. This supports the validity of equations (6)–(9).

Figure 6 shows a plot of the relative standard deviation of ΔR for A- and B-configuration measurements, respectively. The standard deviations at 200 μA are independent on the mean electrode pitch and differ from those at 2000 μA that are approximately inversely proportional to the electrode pitch. The data at 2000 μA are consistent with dynamic position errors with a standard deviation of $\sim 3 \text{ \AA}$, while the data at 200 μA are consistent with electrical measurement noise with a standard deviation of $\sim 65 \text{ nV}$. The electrical measurement noise hardly affects the precision of the measurements at the higher current level. Again, the relative magnitudes of the standard deviations in A- and B-configuration measurements are in agreement with theory.

To the extent that positional errors are indeed static throughout the measurement sequence for each subset of four electrodes and entirely located along the line of contact points they can be compensated for using the position correction

algorithms, equations (10) and (12). Here we compare the two methods by applying them to the measurements presented in figures 3–6. The results are shown in figure 7 and represent statistics on the position corrected sheet resistance results of the first A–B pair for each subset of four electrodes; the other possible A–B pairs give almost identical results.

It is easily recognized that the two position correction algorithms perform equally well. For the measurements at 200 μA there is almost no pitch related trend, which implies that for this dataset (after position correction is applied) electrical noise is the dominant source of residual error. When the current is increased to 2000 μA , the position corrected data yields a significantly lower relative standard deviation and there is a clear trend of decreasing standard deviation for increasing pitch, which means that position errors are still dominant. These errors cannot be corrected for using the position correction algorithms and must therefore be a combination of the following factors: static off-line errors, dynamic off-line errors or dynamic in-line errors, which cannot be corrected by the algorithms. The curves in figure 7 are results of Monte Carlo simulations using static position errors with a standard deviation of 5 nm, dynamic position errors, with a standard deviation of 3 \AA and an electrical measurement noise with a standard deviation of 65 nV. Both position corrected measurements at 200 and 2000 μA are consistent with these three error sources found from the single configuration analysis.

To investigate possible aging effects on the probe position errors, a microprobe was engaged at 5000 measurement locations distributed in a small homogeneous area of the wafer. Using a current of $2000\mu\text{A}$ measurements with eight subprobes were carried out in a sequence containing four electrode configurations, A, B, A' and B', at each measurement position. Evaluating data subsets of 100 consecutive measurements the individual static in-line position error for each subprobe and electrode configuration, $\sigma_x^{\text{sub,A}}$ and $\sigma_x^{\text{sub,B}}$, was found. Figure 8 shows mean, maximum, and minimum values of σ_x evaluated across all subprobes and electrode configurations. The average static in-line position error, σ_x^{all} , was found to be 5.1 nm with minimum position error $\sigma_{x,\text{min}}^{\text{all}} = 3.9$ nm and maximum position error $\sigma_{x,\text{max}}^{\text{all}} = 7.5$ nm. A slight decrease in position error is seen with increasing measurement age of the probe.

Figure 9 shows the relative standard deviation of ΔR for A-configuration measurements evaluated across the 50 data subsets. No clear aging trend is observed.

5. Conclusion

We have experimentally shown that the dominant sources of error in single configuration micro four-point probe sheet resistance measurements are in-line probe geometry errors and in-line static position errors. These errors were shown to be eliminated very effectively using dual-configuration measurements and position error correction algorithms. At the error level observed in this study both position error correction algorithms—vdP and the first-order approximation by Worledge—are equally effective, this will not be the case at large relative position errors where the vdP method is the better choice.

The standard deviation of the static in-line position error for measurements with Au-coated electrodes on Ru thin film samples was found to be in the range from 3.9 nm to 7.5 nm. The standard deviation of the dynamic inline position error was shown to be small $\sim 3\text{ \AA}$ and only detectable in measurements with high measurement current. At lower measurement currents the electrical measurement noise was the dominant error source. No significant aging effect on position errors (except for a very slight reduction in position error with measurement age) was observed for a probe in the course of 5000 measurements.

Acknowledgments

The authors wish to thank Lauge Gammelgaard and Lior Shiv for their experimental assistance and fruitful discussions

concerning probe fabrication. The authors are grateful for the financial support of the Danish Ministry of Science, Innovation and Higher Education, the Danish National Research Foundation for funding the Center for Individual Nanoparticle Functionality (DNRF54), and Innovation Fund Denmark. This work was supported by Villum Foundation, project no. VKR023117.

References

- [1] Schroder D K 2006 *Semiconductor Material and Device Characterization* 3rd edn (Hoboken, NJ: Wiley)
- [2] Petersen C L, Hansen T M, Bøggild P, Boisen A, Hansen O, Hassenkam T and Grey F 2002 Scanning microscopic four-point conductivity probes *Sensors Actuators A* **96** 53–8
- [3] Petersen D H, Lin R, Hansen T M, Rosseel E, Vandervorst W, Markvardsen C, Kjær D and Nielsen P F 2008 Comparative study of size dependent four-point probe sheet resistance measurement on laser annealed ultra-shallow junctions *J. Vac. Sci. Technol. B* **26** 362
- [4] Thorsteinsson S, Wang F, Petersen D H, Hansen T M, Kjær D, Lin R, Kim J-Y, Nielsen P F and Hansen O 2009 Accurate microfour-point probe sheet resistance measurements on small samples *Rev. Sci. Instrum.* **80** 053902
- [5] Petersen C L, Worledge D and Petersen P R E 2003 Reproducibility of nano- and micro-scale multi-point probe sheet resistance measurements *Mater. Res. Soc. Symp. Proc.* **738** 157–62
- [6] Rymaszewski R 1969 Relationship between the correction factor of the four-point probe value and the selection of potential and current electrodes *J. Phys. E: Sci. Instrum.* **2** 170–4
- [7] Worledge D C 2004 Reduction of positional errors in a four-point probe resistance measurement *Appl. Phys. Lett.* **84** 1695–7
- [8] Smits F M 1958 Measurement of sheet resistivities with the 4-point probe *Bell Syst. Tech. J.* **37** 711–18
- [9] Petersen D H et al 2010 Review of electrical characterization of ultra-shallow junctions with micro four-point probes *J. Vac. Sci. Technol. B* **28** C1C27–33
- [10] van der Pauw L J 1958 A method of measuring the resistivity and Hall coefficient on lamellae of arbitrary shape *Philips Tech. Rev.* **20** 220
- [11] Petersen D H, Hansen O, Lin R and Nielsen P F 2008 Micro four-point probe Hall effect measurement method *J. Appl. Phys.* **104** 013710
- [12] Petersen D H, Hansen O, Hansen T M, Petersen P R E and Bøggild P 2008 Static contact micro four-point probes with <11 nm positioning repeatability *Microelectron. Eng.* **85** 1092–5
- [13] van der Pauw L J 1958 A method of measuring specific resistivity and Hall effect of discs of arbitrary shape *Philips Tech. Rev.* **13** 1–9
- [14] CAPRES A/S www.capres.com

Paper III

F. W. Østerberg, D. Kjaer, P. F. Nielsen, O. Hansen and D. H. Petersen
Accuracy of Current-In-Plane Tunneling measurements on test pads for MRAM
Draft as submitted to Journal of Applied Physics, July 3rd 2015

Characterization of magnetic tunnel junction test pads

Frederik Westergaard Østerberg,^{1, a)} Daniel Kjær,^{1, 2} Peter Folmer Nielsen,² Ole Hansen,^{1, 3} and Dirch Hjorth Petersen^{1, b)}

¹⁾DTU Nanotech - Department of Micro- and Nanotechnology, Technical University of Denmark, Building 345 East, DK-2800 Kongens Lyngby, Denmark

²⁾CAPRES A/S, Scion-DTU, Building 373, DK-2800 Kgs. Lyngby, Denmark

³⁾CINF - Centre for Individual Nanoparticle Functionality, Technical University of Denmark, Building 345 East, DK-2800 Kongens Lyngby, Denmark

(Dated: 3 July 2015)

We show experimentally as well as theoretically that *patterned* magnetic tunnel junctions can be characterized using the current-in-plane tunneling (CIPT) method, and the key parameters, the resistance area product (RA) and the tunnel magnetoresistance (TMR), can be determined. The CIPT method relies on four-point probe measurements performed with a range of different probe pitches and was originally developed for infinite samples. Using the method of images we derive a modified CIPT model, which compensates for the insulating boundaries of a finite rectangular sample geometry. We measure on square tunnel junction pads with varying sizes and analyze the measured data using both the original and the modified CIPT model. Thus we determine in which sample size range the modified CIPT model is needed to ensure validity of the extracted sample parameters, RA and TMR. In addition, measurements as a function of position on a square tunnel junction pad are used to investigate the sensitivity of the measurement results to probe misalignment.

Keywords: Magnetic tunnel junctions, Characterization, Four-point-probes, Test pads

I. INTRODUCTION

Since their discovery by Jullière¹ magnetic tunnel junctions (MTJ) have attracted considerable interest due to the multitude of applications as sensors,² read heads in hard disc drives³⁻⁷ and in particular their use in magnetoresistive random-access memory (MRAM).^{4, 8-10} MRAM has the potential to become the preferred memory technology of the future, due to the outstanding technical performance, such as high speed, high density, non-volatility, reliability, and very low power consumption.^{4, 9, 11}

Traditional a MTJ consists of two ferromagnetic layers separated by a thin tunnel barrier layer; often one ferromagnetic layer is pinned while the other is "free", i.e. has a much lower switching magnetic field. As a result the MTJ can assume two states, where the magnetization of the ferromagnetic layers are either parallel or anti-parallel, corresponding to low or high tunnel resistance; often characterized by the corresponding resistance-area products RA_{low} and RA_{high} ,¹² respectively. The contrast between RA_{low} and RA_{high} is the tunnel magnetoresistance (TMR), i.e. $TMR = (RA_{\text{high}} - RA_{\text{low}}) / RA_{\text{low}}$, which is of particular importance for MRAM applications. These key parameters can either be measured on final devices or on complete films prior to device fabrication using the current-in-plane tunneling (CIPT) method.¹² A distinct advantage of the CIPT method is that TMR and $RA \equiv RA_{\text{low}}$ can be determined without performing lithography, etching and inter-connections to

the top and bottom electrodes of the MTJ, and thereby information about TMR and RA can be obtained at an earlier stage than that of the final device. On the other hand, one of the disadvantages of the current CIPT method is that it requires an "infinite" sample, which means it is not possible to monitor whether the processes following the deposition of the MTJ stack influence the TMR and RA values.

CIPT measurements on actual device wafers have to be performed on test pads, that potentially can be placed in scribe lines to save area. Here, we investigate how the insulating boundaries of patterned square test pads affect CIPT measurements when compared to measurements on a full film. The original theory for the CIPT method was derived assuming *infinite* samples. Here, we use the method of images^{13, 14} to derive a modified model which is valid for *finite* samples of rectangular shape.

II. THEORY

CIPT measurements can be performed using a collinear multi-point probe, where four-point sub-probes are used for individual measurements. Four-point probe measurements may be done in several different configurations, and here configurations A and B are of interest. In configuration A the two outer pins are used as current source and drain while the two inner pins used for measuring the voltage drop as sketched in Fig. 1. For configuration B the roles of pins 3 and 4 are interchanged compared to configuration A as shown in Fig. 1.

Worledge *et al.*¹² models the MTJ film as two infinite, thin conducting sheets of sheet resistances R_t (top) and R_b (bottom) with a connecting interface specific contact resistance RA. The potential Φ at the point \mathbf{r} from a

^{a)}Electronic mail: Frederik.Osterberg@nanotech.dtu.dk

^{b)}Electronic mail: Dirch.Petersen@nanotech.dtu.dk

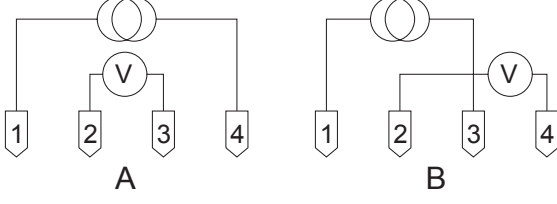


FIG. 1. The probe configurations A and B used for CIPT measurements.

single current source I_0 placed at \mathbf{r}_0 on an infinite MTJ film can be written as

$$\Phi(\mathbf{r}, \mathbf{r}_0) = \frac{I_0 R_{\parallel}}{2\pi} \left\{ \frac{R_t}{R_b} K_0 \left(\frac{|\mathbf{r} - \mathbf{r}_0|}{\lambda} \right) - \ln \left(\frac{|\mathbf{r} - \mathbf{r}_0|}{\lambda} \right) \right\}, \quad (1)$$

where K_0 is the modified Bessel function of the second kind of order 0, and R_{\parallel} is the sheet resistance of the two sheets in parallel

$$R_{\parallel} = \frac{R_t R_b}{R_t + R_b}, \quad (2)$$

while λ is the transfer length, a characteristic sample length scale, obtained from

$$\lambda = \sqrt{\frac{RA}{R_t + R_b}}. \quad (3)$$

In Eq. 1 the logarithmic term is reminiscent of the expression for a single sheet, while the Bessel term is the correction needed due to the finite specific contact resistance between the sheets.

For a four-point probe on an infinite sample with the current source I_0 placed at \mathbf{r}_i and drain at \mathbf{r}_j and the voltage probes at \mathbf{r}_k and \mathbf{r}_l the four-point resistance can be calculated from Eq. 1 using super-position

$$R = \frac{\Phi(\mathbf{r}_k, \mathbf{r}_i) - \Phi(\mathbf{r}_l, \mathbf{r}_i) - \Phi(\mathbf{r}_k, \mathbf{r}_j) + \Phi(\mathbf{r}_l, \mathbf{r}_j)}{I_0}. \quad (4)$$

If the four probe pins are equally spaced with the pin spacing s the expected resistances for CIPT measurements on an infinite sample in probe configurations A and B are

$$R_{A_{\text{inf}}} = \frac{R_{\parallel}}{2\pi} \left\{ \frac{R_t}{R_b} \left[2K_0 \left(\frac{s}{\lambda} \right) - 2K_0 \left(\frac{2s}{\lambda} \right) \right] + \ln(4) \right\}, \quad (5)$$

$$R_{B_{\text{inf}}} = \frac{R_{\parallel}}{2\pi} \left\{ \frac{R_t}{R_b} \left[K_0 \left(\frac{s}{\lambda} \right) - K_0 \left(\frac{3s}{\lambda} \right) \right] + \ln(3) \right\}, \quad (6)$$

respectively.

However, in real measurements the probe pins will not land exactly where expected, each electrode will have some position error as described by Kjaer *et al.*¹⁵ For single sheet micro four-point probe sheet resistance measurements it has previously¹⁵ been shown that van der Pauw's method^{16,17} effectively reduces the effect of pin

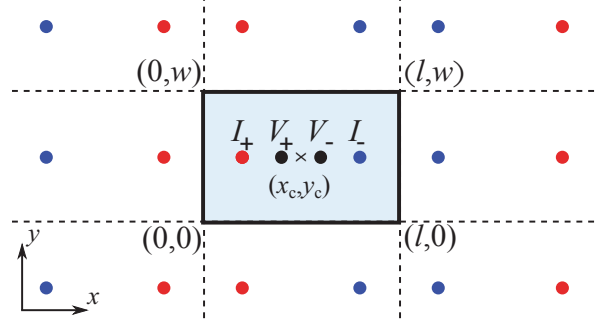


FIG. 2. Sketch of a rectangular shaped sample of length l and width w (light blue) with insulating boundaries (solid black lines). A four-point probe is placed on the sample, with the center of the probe at (x_c, y_c) . The eight closest mirror images of both the current source and drain are also shown.

position errors. In van der Pauw's method a pseudo sheet resistance R_P is defined by the equation

$$\exp \frac{2\pi R_A}{R_P} - \exp \frac{2\pi R_B}{R_P} = 1. \quad (7)$$

In the case of a single infinite sheet R_P is identical to the sheet resistance; on a MTJ R_P does not have a direct physical interpretation, but it proves useful anyway and is less affected by pin position errors than both R_A and R_B even though perfect error cancellation cannot be expected.

A. Rectangular Samples

For measurements in vicinity of an insulating boundary the theory derived for an infinite sample is no longer valid, since the current density normal to the boundary must be zero. In order to fulfil this boundary condition the method of images is applied.^{13,14} In practice this means that additional current sources and drains are placed at the positions obtained by mirroring the current sources and drains in the lines defining the boundaries as shown in Fig. 2. Mirror images of the additional current sources and drains are also needed.

Figure 2 shows a sketch of a rectangular sample with dimensions of length l and width w , the insulating boundaries are represented by solid black lines. The original current source and drain are labelled I_+ and I_- , respectively. The center of the four-point probe is marked by an \times and is positioned at (x_c, y_c) . For practical reasons only the mirror images closest to the pad are shown.

The potential for a rectangle, $0 \leq y \leq w$, $0 \leq x \leq l$, with insulating boundaries at $y = 0$, $y = w$, $x = 0$ and $x = l$ can be written as a double infinite sum, since the images of the source or drain are positioned at $\pm \mathbf{r}_0 + 2(n\mathbf{w} + m\mathbf{l})$ and $\pm \bar{\mathbf{r}}_0 + 2(n\mathbf{w} + m\mathbf{l})$. Here n and m are summation integers and the vectors are defined as $\mathbf{w} = w\mathbf{e}_y$ and $\mathbf{l} = l\mathbf{e}_x$; the vector $\mathbf{r}_0 = (x_0, y_0)$ is the position of the source or drain, while $\bar{\mathbf{r}}_0 = (x_0, -y_0)$. As

a result the potential becomes

$$\Phi(\mathbf{r}, \mathbf{r}_0) = I_0 \frac{R_{\parallel}}{2\pi} \sum_{n=-\infty}^{\infty} \sum_{m=-\infty}^{\infty} \left\{ \frac{R_t}{R_b} \left[K_0 \left(\frac{|\mathbf{r} - \mathbf{r}_0 - 2(n\mathbf{w} + m\mathbf{l})|}{\lambda} \right) + K_0 \left(\frac{|\mathbf{r} - \bar{\mathbf{r}}_0 - 2(n\mathbf{w} + m\mathbf{l})|}{\lambda} \right) + K_0 \left(\frac{|\mathbf{r} + \mathbf{r}_0 - 2(n\mathbf{w} + m\mathbf{l})|}{\lambda} \right) + K_0 \left(\frac{|\mathbf{r} + \bar{\mathbf{r}}_0 - 2(n\mathbf{w} + m\mathbf{l})|}{\lambda} \right) \right] - \ln \left(\frac{|\mathbf{r} - \mathbf{r}_0 - 2(n\mathbf{w} + m\mathbf{l})|}{\lambda} \right) - \ln \left(\frac{|\mathbf{r} - \bar{\mathbf{r}}_0 - 2(n\mathbf{w} + m\mathbf{l})|}{\lambda} \right) - \ln \left(\frac{|\mathbf{r} + \mathbf{r}_0 - 2(n\mathbf{w} + m\mathbf{l})|}{\lambda} \right) - \ln \left(\frac{|\mathbf{r} + \bar{\mathbf{r}}_0 - 2(n\mathbf{w} + m\mathbf{l})|}{\lambda} \right) \right\}. \quad (8)$$

By inserting Eq. 8 into Eq. 4 the four-point resistances for a rectangular sample with pin configuration A ($R_{A,\text{rect}}$) and pin configuration B ($R_{B,\text{rect}}$) can be calculated. These values can be inserted into Eq. 7 to obtain the pseudo sheet resistance for a rectangular sample ($R_{P,\text{rect}}$).

B. Resistances on square pads and infinite samples

The impact of insulating boundaries on the resistances R_A , R_B and R_P can be illustrated by the relative deviation, $(R_{\text{sq}} - R_{\text{inf}})/R_{\text{inf}}$, between resistances calculated for a square sample (R_{sq}) and those of an infinite sample (R_{inf}) with otherwise identical parameters. In Fig. 3 the relative deviations for R_A , R_B and R_P are shown as a function of the normalized width (w/s) of the square. The sample parameters used in the calculation were $R_{\parallel} = 1 \, \Omega$, $R_t/R_b = 1$ and $\lambda = 1 \, \mu\text{m}$, while the probe pitch was $s = \lambda$. Any reasonable change of sample parameters will only cause minor changes to the curves in Fig. 3, thus the general trends remain the same as do the orders of magnitude.

Figure 3 shows that the resistances on the square sample are always larger than those on the infinite sample for a probe placed at the centre of a pad with the electrodes parallel to two of the boundaries. The relative deviation of the resistances are seen to decrease rapidly with increasing size of the square, approximately according to $(w/s)^{-2}$. Importantly, the relative deviation of R_P is approximately an order of magnitude smaller than those of R_A and R_B ; this clearly demonstrates how useful it is to calculate R_P . It appears that in order for R_P to deviate less than 1% the pad should be at least 8 probe pitches wide and to deviate less than 0.1% the width must be at least 20 probe pitches. Note, this behavior of four-point probe MTJ measurements differs from similar measurements on a single sheet, where measurements performed on a mirror symmetry line of a small sample (such as a square) results in R_P exactly identical to that of an infinite sheet.¹⁸

III. EXPERIMENTAL

The measured sample was a 200 mm silicon wafer with a patterned, in-plane (bottom electrode)/PtMn

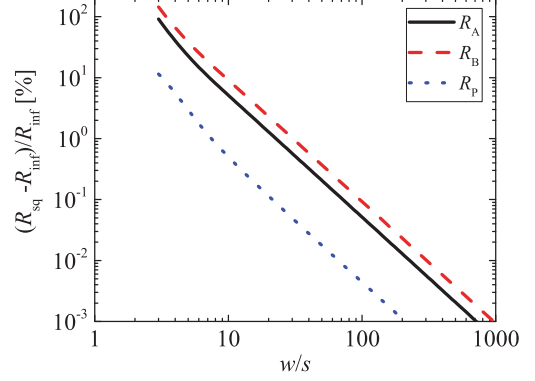


FIG. 3. The relative deviation $(R_{\text{sq}} - R_{\text{inf}})/R_{\text{inf}}$ between calculated four-point resistances for square samples (R_{sq}) compared to calculated resistances for an infinite sample (R_{inf}) as function of normalized square size w/s . Deviations for R_A , R_B and R_P are shown. The resistances for the squares were calculated assuming a four-point probe placed at the centre of the pad and parallel to an edge of the pad.

(16 nm)/Co₇₀Fe₃₀ (2.2 nm)/Ru (0.85 nm)/Co₄₀Fe₄₀B₂₀ (2.5 nm)/MgO (1 nm)/Co₄₀Fe₄₀B₂₀ (2.5 nm)/(top electrode) MTJ prepared using magnetron sputtering processes with a subsequent thermal anneal. The bottom electrode comprised Ta (5 nm)/CuN (50 nm)/Ta₂N (30 nm)/Ta (5 nm), while the top electrode comprised Ta (5 nm)/Ru (80 nm). The stack was designed to pin the magnetization of the lower CoFeB layer while the magnetization of the upper CoFeB layer is free. In the parallel spin polarized state the nominal transfer length of the sample is $\lambda_{\text{low}} = 1.9 \, \mu\text{m}$ while anti-parallel spin polarization results in $\lambda_{\text{high}} = 3.2 \, \mu\text{m}$. Square patterns of nominal widths $w = 30, 35, 40, 50, 60, 80, 100, 150, 250, 500, 1000$, and $2500 \, \mu\text{m}$ were defined on the MTJ wafer using photolithography and ion beam etching.

Measurements were done on a semi-automatic CAPRES CIPTECH-M200 using a micro 12-point probe as shown in Fig. 4. For each measurement a sub-probe with only 4 electrodes was used. This allows for measurements with different probe pitches without replacement or re-engagement of the probe between measurements. In a measurement series eight different sub-probes were used. Only some of the eight sub-probes are equidistant, thus the average probe pitch $\langle s \rangle$ is reported in each case; the average probe pitch of the eight sub-probes varies from $\langle s \rangle = 1.5 \, \mu\text{m}$ to $\langle s \rangle = 8.3 \, \mu\text{m}$. Details of the probe design can be found in Ref. 15. Non-equidistant probes are accounted for in the theoretical models, and thus this fact will not affect the results.

Two series of CIPT measurements were performed with the eight sub-probes: a series with an applied magnetic flux density ($B_x = -15 \, \text{mT}$) which results in the low resistance parallel spin state corresponding to $R_{A,\text{low}}$, and a second series with an applied magnetic flux density

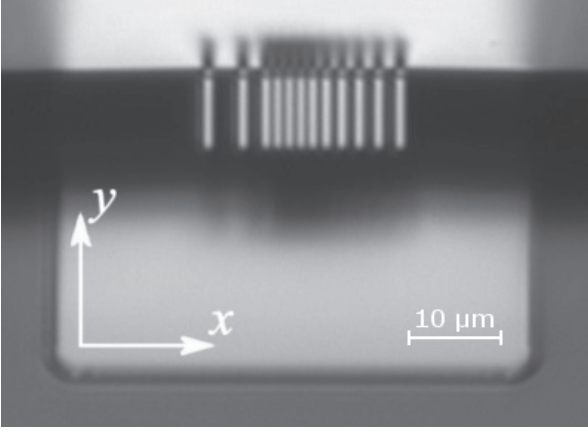


FIG. 4. Picture of a micro 12-point probe positioned over a $w = 50 \mu\text{m}$ pad.

($B_x = 15 \text{ mT}$) which results in the high resistance anti-parallel spin state corresponding to RA_{high} . For each sub-probe and field direction both A and B configuration measurements were done. From the R_A and R_B pairs, 16 R_P values were calculated and used for least square fitting of the CIPT models for both infinite samples and rectangular samples, respectively. From the fits the model parameters (e.g. R_t , R_b , RA_{low} , RA_{high}) were extracted.

CIPT measurements were performed on square pads with 12 different widths ranging from $30 \mu\text{m}$ to 2.5 mm with the probe positioned at the centre of the pads and the line of the probe parallel to an edge of the pads. Four different pads of each size were measured and two measurements were performed on each pad, i.e. 8 measurements were performed for each of the 12 different sized squares. Since R_t and R_b does not depend on RA they are assumed to be independent on the magnetic field direction. This leaves R_t , R_b , RA_{low} and RA_{high} as the four free fitting parameters assuming that the 12-point probe is placed exactly at the centre of the pads and that the dimensions of the pads are accurately known.

CIPT measurement were also performed as function of y -position on a $30 \mu\text{m}$ square pad (again with the line of the probe parallel to an edge of the pad). When the model was fitted to these measurements R_t , R_b , RA_{low} , RA_{high} , x_c and y_c were used as free fitting parameters. Thus, only the dimension of the pad was assumed known.

IV. RESULTS AND DISCUSSION

A. Measurements on various square pads

In Fig. 5 the measured pseudo sheet resistances for the eight sub-probes are plotted as function of average probe pitch for measurements on the pads with widths of $30 \mu\text{m}$, $50 \mu\text{m}$ and 2.5 mm . As expected the measured R_P increases with decreasing probe pitch, while

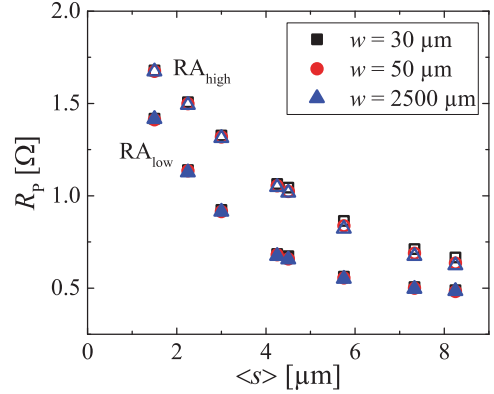


FIG. 5. Measured pseudo sheet resistances R_P as function of average probe pitch for squares with widths of 30 , 50 and $2500 \mu\text{m}$. Closed symbols signify measurements with $B_x = -15 \text{ mT}$ (RA_{low}), while open symbols signify measurements with $B_x = 15 \text{ mT}$ (RA_{high}).

the measured resistances are largely independent on the pad size, and only resistances measured with large pitch on the small samples deviate a few percent from that on the large pad; this is in agreement with Fig. 3. Figure 5 also represents an example of the data to which the two theoretical CIPT models are fitted.

By fitting CIPT models for an infinite sample and a square sample to the measured R_P data the electrical parameters (R_t , R_b , RA_{low} and RA_{high}) of the stack are extracted as function of sample size. In Figs. 6 - 7 R_t , R_b , RA_{low} and RA_{high} are plotted as function of samples size. The values extracted from both of the CIPT models are plotted for each parameter. The error bars correspond to one standard deviation. The horizontal dashed lines represent the mean values obtained from measurements on the 2.5 mm pad. The solid lines in Figs. 6 - 7 show the expected behavior of extracted parameters using the infinite sample CIPT model on synthetic R_P data. The synthetic data were calculated R_P values for square samples as a function of square size using the experimental sample parameters extracted from the 2.5 mm sample.

The parameter values extracted from the two models essentially coincide for samples larger than $100 \mu\text{m}$. For samples smaller than $100 \mu\text{m}$ the values obtained from the model for an infinite sample starts to deviate from the level obtained for large samples. These trends are in good agreement with the theoretical deviations plotted in Fig. 3. Since the largest probe pitch used is $8.3 \mu\text{m}$ w/s will become less than 12 for samples smaller than $100 \mu\text{m}$, which leads to an overestimation of R_P by approximately 0.5% . As the sample size is decreased this overestimation along with the overestimation of the resistances for the other sub-probes will increase. Thus, the extracted parameter results become increasingly different from parameters from measurements on a large pad.

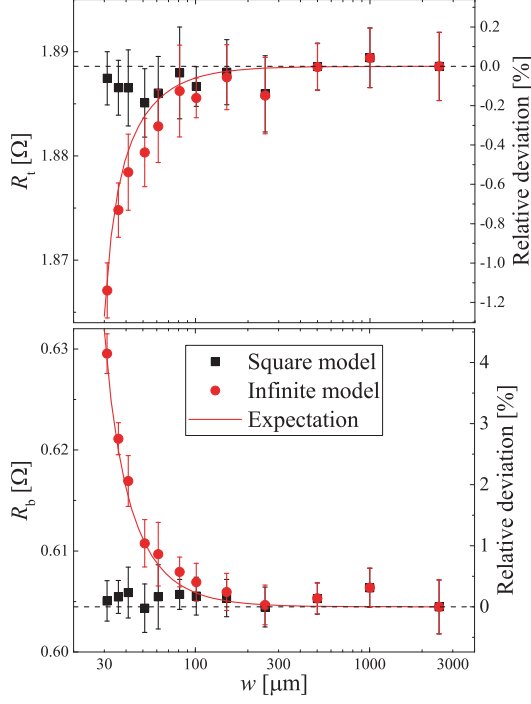


FIG. 6. Extracted values of R_t and R_b as function of sample width. Both the infinite sample CIPT model and the square sample CIPT model were fitted to the measurements.

From Fig. 6 it is seen that the values of R_t and R_b obtained using the model for a square sample are independent of sample size. The values of RA_{low} and RA_{high} (Fig. 7) changes slightly as function of sample size. These small changes are believed to be due to sample variation across the wafer. Note, the resistance area product is known to depend exponentially on the tunnel barrier thickness,¹⁹ and thus the observed variation in resistance area product may be caused by deep sub-nanometer variations in tunnel barrier thickness. In contrast, the infinite sample CIPT model results in extracted parameters that deviate significantly when large and small samples are compared, in agreement with the expectation (full lines).

B. Sensitivity to probe position on a small pad

Figure 8 shows RA_{low} and RA_{high} extracted from CIPT measurements on a $30\text{ }\mu\text{m}$ by $30\text{ }\mu\text{m}$ square pad as function of probe position when the probe was scanned parallel to an edge of the pad. From the plots it is seen that RA_{low} and RA_{high} can be extracted within $\pm 1\%$ as long as the probe is more than $5\text{ }\mu\text{m}$ from the sample boundary if the square sample CIPT model is used. Use of the infinite sample CIPT model leads to larger discrepancies; if the probe is near the centre of the pad RA is overestimated systematically and close to the boundary

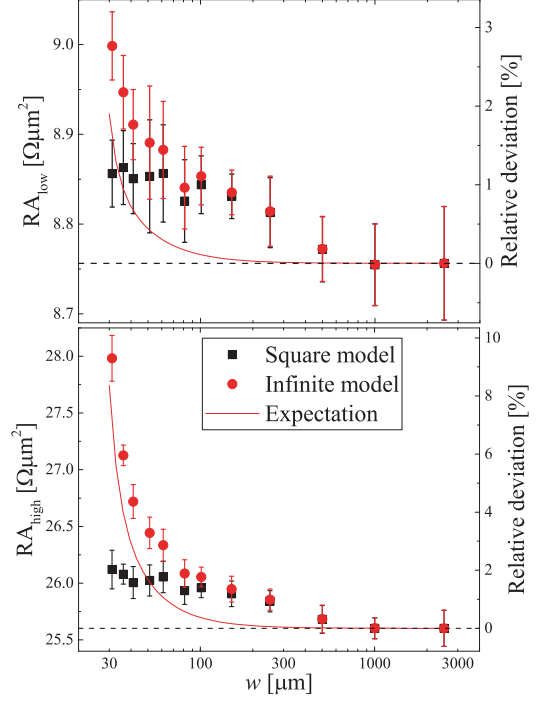


FIG. 7. Extracted values of RA_{low} and RA_{high} as function of sample width. Both the infinite sample CIPT model and the square sample CIPT model were fitted to the measurements.

the error becomes very large.

V. CONCLUSION

We have shown that CIPT measurement can indeed be performed on small MTJ square pads and that meaningful, accurate sample parameters can be extracted from the measurements. For this stack and probe design we found that as long as the square is $100\text{ }\mu\text{m}$ wide and measurements are performed at the center of the pad, it does not matter whether the sample is treated as a rectangle or an infinite sample. However, for samples smaller than $100\text{ }\mu\text{m}$ wide the new model for a rectangular sample should be used to obtain reliable results. We have demonstrated successful CIPT measurements on square samples as small as $30\text{ }\mu\text{m} \times 30\text{ }\mu\text{m}$. Measurements on a $30\text{ }\mu\text{m} \times 30\text{ }\mu\text{m}$ pad show that RA can be measured within $\pm 1\%$ as long as the probe lands more than $5\text{ }\mu\text{m}$ from the boundary parallel to the probe pins; in practice this means that even on such a small pad the sensitivity to probe misalignment is small. The results are very promising and may lead to application of CIPT measurements at later stages in MTJ fabrication as well as on pads in scribe lines on fabrication wafers.

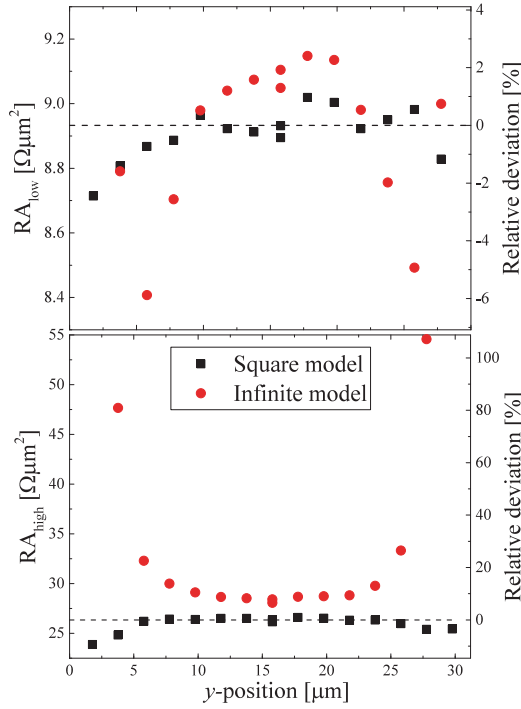


FIG. 8. Extracted values of RA_{low} (top) and RA_{high} (bottom) as function of y -position on a $30\ \mu\text{m}$ pad.

ACKNOWLEDGMENTS

This work was financially supported by Innovation Fund Denmark. CINF is funded by the Danish National Research Foundation (DNRF54). This work was supported by Villum Foundation, project no. VKR023117.

- ¹M. Julliere, Phys. Lett. A **54**, 225 (1975).
- ²R. Ferreira, P. Wisniowski, P. P. Freitas, J. Langer, B. Ocker, and W. Maass, J. Appl. Phys. **99**, 08 (2006).
- ³S. Mao, J. Nowak, D. Song, P. Kolbo, L. Wang, E. Linville, D. Saunders, E. Murdock, and P. Ryan, IEEE Trans. Magn. **38**, 78 (2002).
- ⁴J.-G. J. Zhu and C. Park, Mater. Today **9**, 36 (2006).
- ⁵T. Kagami, T. Kuwashima, S. Miura, T. Uesugi, K. Barada, N. Ohta, N. Kasahara, K. Sato, T. Kanaya, H. Kiyono, *et al.*, IEEE Trans. Magn. **42**, 93 (2006).
- ⁶S. Araki, K. Sato, T. Kagami, S. Saruki, T. Uesugi, N. Kasahara, T. Kuwashima, N. Ohta, J. Sun, K. Nagai, *et al.*, IEEE Trans. Magn. **38**, 72 (2002).
- ⁷M. K. Ho, C. H. Tsang, R. E. Fontana Jr, S. S. Parkin, K. J. Carey, T. Pan, S. MacDonald, P. C. Arnett, and J. O. Moore, IEEE Trans. Magn. **37**, 1691 (2001).
- ⁸R. W. Dave, G. Steiner, J. Slaughter, J. Sun, B. Craig, S. Pietambaram, K. Smith, G. Grynkeiwich, M. DeHerrera, J. Akerman, *et al.*, IEEE Trans. Magn. **42**, 1935 (2006).
- ⁹B. N. Engel, N. D. Rizzo, J. Janesky, J. M. Slaughter, R. Dave, M. DeHerrera, M. Durlam, and S. Tehrani, IEEE Trans. Nanotechnol. **1**, 32 (2002).
- ¹⁰N. Rizzo, D. Houssameddine, J. Janesky, R. Whig, F. Mancoff, M. Schneider, M. DeHerrera, J. Sun, K. Nagel, S. Deshpande, *et al.*, IEEE Trans. Magn. **49**, 4441 (2013).
- ¹¹S. Parkin, K. Roche, M. Samant, P. Rice, R. Beyers, R. Scheuerlein, E. Osullivan, S. Brown, J. Bucchigano, D. Abraham, *et al.*, J. Appl. Phys. **85**, 5828 (1999).
- ¹²D. C. Worledge and P. L. Trouilloud, Appl. Phys. Lett. **83**, 84 (2003).
- ¹³S. Ramo, J. R. Whinnery, and T. Van Duzer, *Fields and Waves in Communication Electronics* (Wiley, New York, 1984).
- ¹⁴D. H. Petersen, O. Hansen, R. Lin, and P. F. Nielsen, J. Appl. Phys. **104**, 013710 (2008).
- ¹⁵D. Kjaer, O. Hansen, F. Østerberg, H. Henriksen, C. Markvardsen, P. Nielsen, and D. Petersen, Meas. Sci. Technol., accepted (2015).
- ¹⁶L. J. Van der Pauw, Philips Tech. Rev. **20**, 220 (1958).
- ¹⁷L. J. Van der Pauw, Philips Res. Rep **13**, 1 (1958).
- ¹⁸S. Thorsteinsson, F. Wang, D. H. Petersen, T. M. Hansen, D. Kjaer, R. Lin, J.-Y. Kim, P. F. Nielsen, and O. Hansen, Rev. Sci. Instrum. **80**, 053902 (2009).
- ¹⁹S. Yuasa, T. Nagahama, A. Fukushima, Y. Suzuki, and K. Ando, Nat. Mater. **3**, 868 (2004).

Paper IV

M. R. Lotz, M. Boll, O. Hansen, D. Kjær, P. Bøggild, and D. H. Petersen

Revealing origin of quasi-one dimensional current transport in defect rich two dimensional materials
Appl. Phys. Lett., vol. 105, no. 5, p. 053115, 2014

Revealing origin of quasi-one dimensional current transport in defect rich two dimensional materials

Mikkel R. Lotz,^{1,a)} Mads Boll,^{1,a)} Ole Hansen,^{2,3} Daniel Kjær,^{2,4} Peter Bøggild,¹ and Dirch H. Petersen^{1,b)}

¹Center for Nanostructured Graphene (CNG), Department of Micro- and Nanotechnology, Technical University of Denmark, DTU Nanotech Building 345 East, DK-2800 Kgs. Lyngby, Denmark

²Department of Micro- and Nanotechnology, Technical University of Denmark, DTU Nanotech Building 345 East, DK-2800 Kgs. Lyngby, Denmark

³Danish National Research Foundation's Center for Individual Nanoparticle Functionality (CINF), Technical University of Denmark, DK-2800 Kgs. Lyngby, Denmark

⁴CAPRES A/S, Scion-DTU, Building 373, DK-2800 Kgs. Lyngby, Denmark

(Received 27 June 2014; accepted 28 July 2014; published online 8 August 2014)

The presence of defects in graphene have for a long time been recognized as a bottleneck for its utilization in electronic and mechanical devices. We recently showed that micro four-point probes may be used to evaluate if a graphene film is truly 2D or if defects in proximity of the probe will lead to a non-uniform current flow characteristic of lower dimensionality. In this work, simulations based on a finite element method together with a Monte Carlo approach are used to establish the transition from 2D to quasi-1D current transport, when applying a micro four-point probe to measure on 2D conductors with an increasing amount of line-shaped defects. Clear 2D and 1D signatures are observed at low and high defect densities, respectively, and current density plots reveal the presence of current channels or branches in defect configurations yielding 1D current transport. A strong correlation is found between the density filling factor and the simulation yield, the fraction of cases with 1D transport and the mean sheet conductance. The upper transition limit is shown to agree with the percolation threshold for sticks. Finally, the conductance of a square sample evaluated with macroscopic edge contacts is compared to the micro four-point probe conductance measurements and we find that the micro four-point probe tends to measure a slightly higher conductance in samples containing defects. © 2014 AIP Publishing LLC. [<http://dx.doi.org/10.1063/1.4892652>]

Since the first demonstrations of single and few-layer graphene devices,^{1,2} and later growth of large continuous graphene films by chemical vapor deposition (CVD), the issue of defects has been a central research topic.^{3–6} The reason for this is that defects have been recognized as a bottleneck for electronic⁶ and mechanical⁷ applications, as well as for fundamental research. Defects in small pieces of exfoliated single crystal 2D materials can today be avoided almost entirely,^{8,9} but it remains an issue for large area graphene grown by CVD, which is the dominant method for high quality graphene production. In the broadest sense, defects may refer to anything from lattice imperfections, substitutional atoms, vacancies, physis- or chemisorbed adatoms, as well as extended defects such as grain boundaries,^{3,10} cracks,¹¹ and folds,¹² and finally regions with different doping and contaminants, such as electron-hole puddles.¹³ Such defects may be created during growth due to non-optimal growth conditions, differences in thermal expansion coefficients of substrate and graphene, multiple nucleation points for the CVD growth process, or in the transfer process of graphene onto a target substrate. Techniques such as Raman spectroscopy¹⁴ and field effect measurements are widely used means of assessing the quality of graphene, but neither of these gives clear information on the electrical continuity of the graphene films. Electrical continuity is important to include when

characterizing 2D materials, since the sheet conductance may vary according to the transport regime relevant at different characteristic length scales. At a transport length shorter than the mean free path of the charge carriers, the transport is ballistic and sheet conductance undefined, whereas we can define an intrinsic sheet conductance for a transport length longer than the mean free path. For a 2D material, a mesoscopic transport regime can be defined for a length scale corresponding to the length of extended defects and for much larger length scales a macroscopic sheet conductance. A class of devices where conductance is unlikely to represent the intrinsic sheet conductance is highly nanostructured graphene, such as nanoribbon arrays¹⁵ and nanomesh/antidot lattices.¹⁶ Recent theoretical work shows a quite inhomogeneous current flow in disordered antidot lattices.¹⁷ In previous work,¹⁸ we demonstrated that a quasi-1D current transport can exist in the mesoscopic regime as measured with a micro four-point probe (M4PP). This can be used to evaluate if a graphene film is 2D or not in the near proximity of the probe. This was done simply by inspecting the ratio R_A/R_B between the measured resistances in two different configurations, A and B, and comparing this ratio to the theoretically predicted value for a homogeneous infinite 2D conductor, $\ln(4)/\ln(3) = 1.262$. It was shown that a $4 \times 6 \text{ mm}^2$ CVD graphene film had the largest deviations from this 2D criterion near regions with visible defects.

In this work, we use a combined finite element method (FEM) and Monte Carlo approach to study the effect of an

^{a)}M. R. Lotz and M. Boll contributed equally to this work.

^{b)}Electronic mail: dirch.petersen@nanotech.dtu.dk.

extended defect network on the current flow in a 2D conductor. We demonstrate that the M4PP measurement on a 2D conductor with increasing number of defects exhibit the expected transition from 2D to inhomogeneous current flow, but also in a large number of cases the transition to a 1D current flow, though often with quite complex current paths. The simulations qualitatively explain the statistical distribution of the R_A/R_B values,¹⁸ with the collapse of the current flow to 1D channels being directly responsible for the large fraction of experimental R_A/R_B values exactly equal to 1.

Using Comsol Multiphysics 4.4, we simulated an applied current in an M4PP setup and examined the resulting electrostatic potential across a two dimensional conductor. In the A-configuration, the current is applied from pin 1 to pin 4 (the pin numbers are as shown in Figure 1). In the B-configuration, the current is applied from pin 1 to pin 3. The two remaining pins measure the resulting potential drop in each case, and from the potential difference we can calculate the resistances R_A and R_B in the A- and B-configuration, respectively. The graphene sample was modelled as a two dimensional square with insulating boundaries and a side length of $10s$, where s is the probe pitch. The four probe pins were introduced as points placed on a straight line in the center of the square along the x-direction. Defects were introduced as straight line geometries of length ℓ and set as electrically insulating. To achieve a specific defect density, ρ , a regular grid of defects was constructed. At each grid point, a line defect was placed, each with random orientation and random displacements in x- and y-directions; the displacement amplitudes were at most half the grid spacing. Using this defect grid approach, forces the local defect density to equal the global defect density, as we avoid major defect clusters or voids and thus reducing the uncertainty of the effective defect density locally. An initial coarse free triangular mesh was used followed by adaptive mesh refinement to make a fine mesh only where it is strictly needed. Two mesh refinement steps were found to be enough for the solution to be within a relative error of less than 1% of the fully converged solution. Using a finer initial mesh, or more than two mesh refinement steps, dramatically increases the simulation time, especially for short defects at high densities.

To investigate the change in electrical behaviour of a 2D conductor subjected to extended defects as measured with an M4PP, simulations with stepwise increasing defect

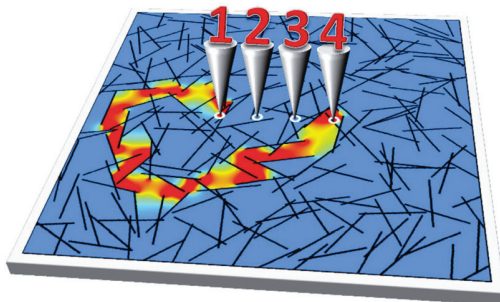


FIG. 1. An M4PP in the A-configuration measuring on a square sample yielding 1D transport. The surface map shows the resulting current density. In this configuration, the pins 1 and 4 are used as current/ground while the two remaining pins measure the electrostatic potential difference. The square sample is $10 \times 10s^2$, where s is the probe pitch.

density and fixed defect length equal to one probe pitch, $\ell = 1s$, were carried out with 1000 simulations per density step. The result is plotted as a 3D histogram of resistance ratios for each density step in Figure 2. The histograms show a distinct 2D peak at low defect density with $R_A/R_B \approx 1.2$ corresponding to the simulated defect free square sample $10 \times 10s^2$. The 2D peak quickly broadens and disappears as the density increases and the conductor is no longer strictly 2D. At intermediate densities, there are no major features or peaks in the plot, which is a characteristic of inhomogeneous current transport. A distinctive 1D peak occurs at high defect densities of around $\rho > 3s^{-2}$, which is very sharply focussed around $R_A/R_B = 1$. At the highest simulated defect density of $\rho = 5.76s^{-2}$, the peak count is significantly lowered since current flow from source to drain is completely obstructed in the majority of simulations, thus making measurements impossible. It can also be seen that for these extreme cases the defect overlap is so significant that if a measurement succeeds, then the current will most likely follow a 1D current path, which is why only $R_A/R_B = 1$ values are observed. The characteristic distribution peaks representing 1D and 2D transports and broadening of the 2D peak are very similar to the distribution peaks found experimentally in Ref. 18. Figure 3 shows an example of the electrostatic potential and the resulting current density, for an M4PP measurement with $\ell = 1.5s$, in a typical case of 1D current transport. Examining the simulated electrostatic potential shown in Figure 3(a), reveals large regions of uniform potential abruptly changing to neighbouring regions, suggesting the transport between them is confined to narrow gaps. The electrodes $\{1, 2\}$ and $\{3, 4\}$ are partially isolated from each other through a relatively high resistance path and pairwise connected through paths of negligible resistance. Consequently, identical resistances can be observed for the A- and B-configuration, which is a prerequisite for 1D transport. Two equivalent but less likely situations can occur with electrodes $\{1, 3\}$ and $\{2, 4\}$ or $\{2, 3\}$ and $\{1, 4\}$ pairwise short circuited. This would result in resistance ratios of infinite and zero, respectively, something which is rarely observed experimentally and in

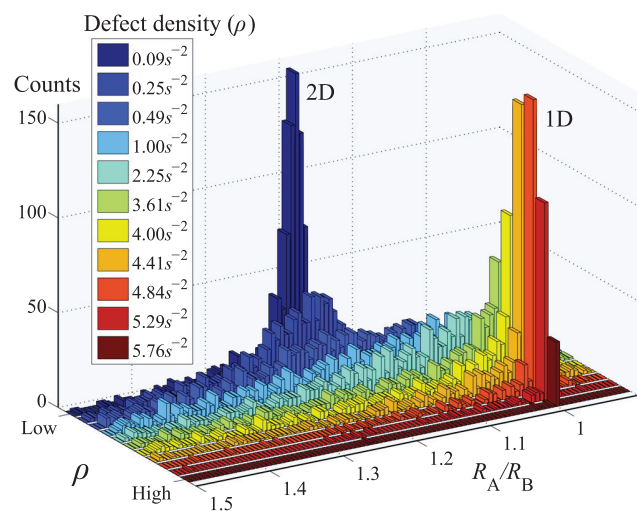


FIG. 2. Histograms of the simulated resistance ratio, R_A/R_B , as a function of defect density, ρ , with a defect length of one probe pitch, $\ell = 1s$. Each histogram contains the collected results from 1000 simulations.

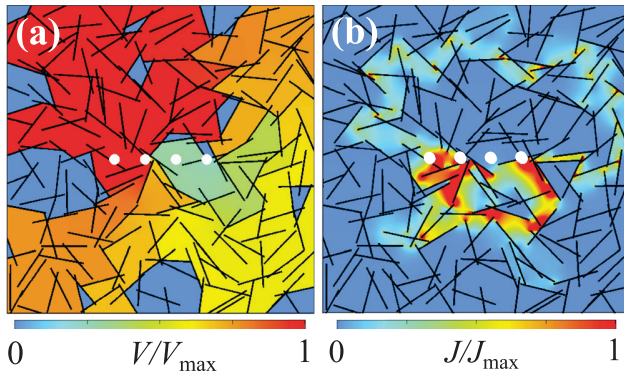


FIG. 3. Simulation of a four-point probe measurement in presence of randomly distributed extended defects with length $1.5s$ and defect density of $2s^{-2}$. The four white dots represent the point-contact positions of the four probe pins. (a) The normalized electrostatic potential and (b) the normalized current density.

simulations. The current density map shown in Figure 3(b) reveals that 1D transport also occur through a branched channel and not only through a single channel as in Figure 1.

A study of how defect length influences the measurement was also carried out with defect lengths ranging between $\ell = 0.5s$ and $\ell = 3s$. Here, data were collected from 100 simulations for each defect length and density together with the data from the 1000 simulations for $\ell = 1s$. Figure 4(a) shows the simulation yield, that is, the number of successful simulated measurements relative to the number of simulation attempts. Figure 4(b) shows the fraction of successful measurements yielding $R_A/R_B = 1 \pm 10^{-4}$ and Figure 4(c) shows the average measured sheet conductance, G_s , evaluated using the modified van der Pauw expression;¹⁹ $\exp(2\pi R_A G_s) - \exp(2\pi R_B G_s) = 1$ and normalized to the intrinsic sheet conductance, G_0 . Figure 4(d) shows G_s for $\ell = 1s$ found both from M4PP simulations and from simulations of a square sample setup. In all four graphs, the data are plotted as a function of the filling factor, $\rho\ell^2$.

With respects to yield there are two main situations in which a simulation output is missing, causing a reduction as seen in Figure 4(a). One situation is when the current source is isolated from the current drain in which case no numerical solution can be found. The other situation is when one of the voltage measuring pins is isolated resulting in a floating potential. Measurements of negative resistances also occur in experiments and are usually not included in the results. These situations occur more often when a significant overlap of the defects is possible, thus the overall yield is expected to decrease when the density of defects becomes large. This overlapping behaviour is well described in percolation theory, more specifically by the percolation threshold of widthless sticks on a 2D surface. Li and Zhang²⁰ found the percolation threshold value was determined to be $\rho_c\ell^2 = 5.637$, where ρ_c is the critical stick density. Below this value, long-range connection of the sticks cease to exist, while at values above the threshold, clusters can form, some of which are comparable in size to the system. This threshold value is indicated in Figure 4 by the vertical dashed line. The yield clearly drops before reaching the threshold value as even short-ranged clusters can isolate a pin but the yield, however, does converge towards zero near the threshold

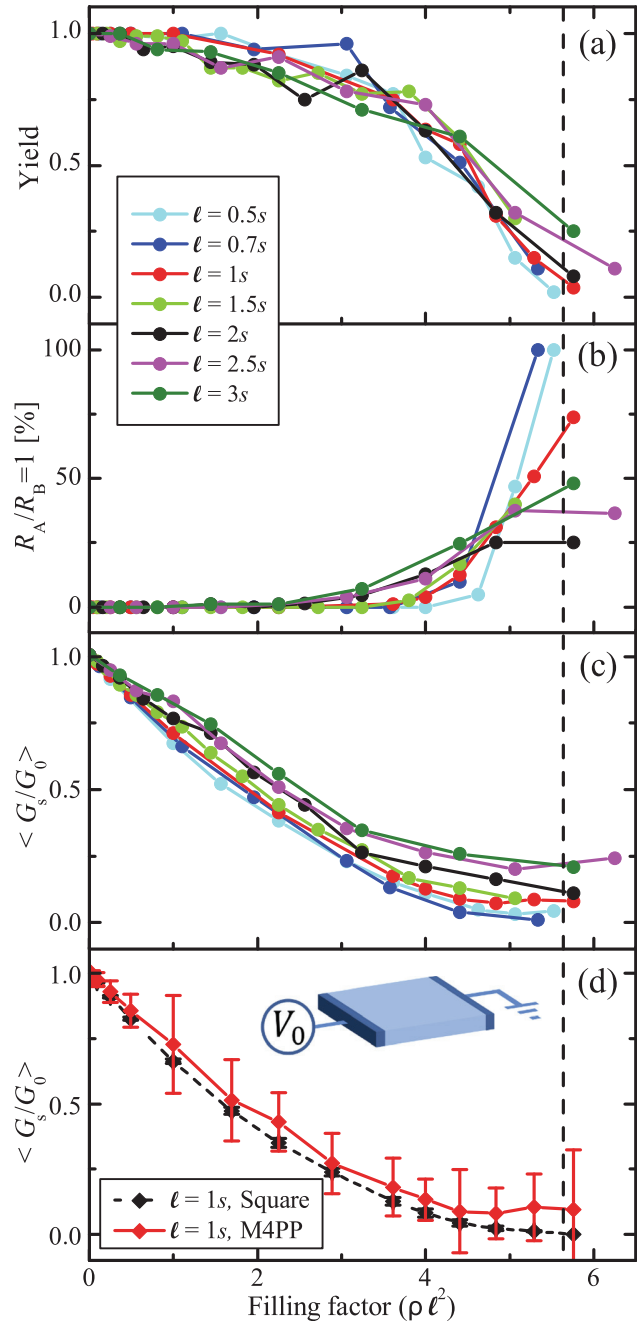


FIG. 4. Simulation results as a function of filling factor for all the investigated defect lengths. Every point indicates a defect density that was simulated 100 times except for $\ell = 1s$, where the 1000 simulations were reused. (a) The overall yield of the simulations. (b) The fraction of simulation attempts that yields a resistance ratio of 1 ± 10^{-4} . For example, for $\ell = 0.5s$ at $\rho\ell^2 = 5.5$, which corresponds to a defect density of $22s^{-2}$, only two simulations did not crash, both exhibiting 1D transport and thus a count of one hundred percent. (c) The average sheet conductance. (d) The sheet conductance for M4PP simulations compared to the sheet conductance of the square sample, both averaged over 100 simulations. The inset illustrates the setup used to find the square sample conductance, with $V_0 = 1$ V. The dashed line across all sub-figures indicates the percolation threshold for sticks on a 2D surface.

value, suggesting that the system behaves as percolation theory predicts.

In common for all defect lengths investigated is the display of 1D transport in proximity to the percolation threshold. This is clearly seen in Figure 4(b) as well as in Figure 2.

Especially, the data for $\ell = 0.5s$ and $\ell = 0.7s$, with all of the successful measurements yielding $R_A/R_B = 1$, have similarities to the results shown in Figure 2, where the simulated measurement yields $R_A/R_B = 1$ or fails at high defect densities.

In Figure 4(c), all simulations yielding zero sheet conductance are effectively neglected, thus only successful simulations contribute to the mean sheet conductance. When the filling factor is increased, the mean sheet conductance decreases. This is expected since adding more defects obstructs the current transport, resulting in increased resistance and lowered sheet conductance. We also notice that when the 1D current transport cases starts to appear, at $\rho\ell^2 > 4$ the conductance is severely lowered. This fits well with the observation in Ref. 18 that 1D transport only occurs in highly damaged areas. Another observation is that at the same filling factor, long defects tend to cause higher mean sheet conductances compared to short defects. This can be explained by considering the limits of the defect lengths at a certain filling factor. If, for instance, the length of defects goes towards infinity, the density ρ would go towards zero, and the sheet conductance would go toward 1 as the M4PP would effectively probe the defect free region between defects. If, however, the defects are infinitesimally short, the density ρ would approach infinity, resulting in a completely insulating sample, with a conductance converging towards zero.

In Figure 4(d), we compare the M4PP simulated sheet conductance to the conductance of the entire sample, where a potential $V_0 = 1$ V is applied on one side of the sample and ground on the opposite side as shown in the inset. Both simulations were carried out on the same 100 defect configuration samples and it is clear that there is a good agreement between the two simulation setups. The large standard deviations on the M4PP conductances are due to a few cases where the defects are placed in such a particular way that the conductance becomes much higher than the average. The square setup generally gives a slightly lower conductance than the M4PP setup. This is attributed to the difference in area probed and related to the defect density/length versus electrode pitch. A similar trend is observed in Figure 4(c) for different defect lengths.

In summary, we have shown through a series of FEM simulations, used in a Monte Carlo fashion, the transition from 2D to quasi-1D current transport when measuring with an M4PP in conductors with low and high defect density, respectively. The collected data showed a striking resemblance in their R_A/R_B distributions to those found experimentally in Ref. 18, revealing a very sharp distribution of measurements around $R_A/R_B = 1$ at defect densities around $\rho = 4.84s^{-2}$ and a more broad distribution around $R_A/R_B = 1.2$ at defect densities below $\rho = 0.09s^{-2}$. Current density plots of selected 1D transport cases featured single channel or branch like current transport across the sample. We have also shown a strong correlation between the filling factor and the simulation yield, the number of 1D transport cases and the mean sheet conductance. This showed that systems, despite having very different defect lengths, behaved in very much the same manner when examined at relatively high defect density with respects to their size. The upper limit of

the range within which successful measurements were achieved, was observed between $\rho\ell^2 = 5.5$ and 6.3 (depending on ℓ), which was reaffirmed by the percolation threshold for widthless sticks stating that this should occur at $\rho_c\ell^2 = 5.637$. It was also shown here that 1D current transport only occur in proximity of the percolation threshold for sticks at which point they would make up a significant fraction of the total number of successful measurements. Finally, the calculated mean sheet conductance showed that the measured conductance was indeed severely reduced in the filling factor range where most cases of 1D transport were observed, which again is very much similar to the conclusion drawn in Ref. 18. Additionally, it was found that the average conductance measured with an M4PP was slightly higher than the conductance of the entire sample in general, but agreed within the standard deviations of the M4PP results.

The Danish National Research Foundation has funded both Center for Individual Nanoparticle Functionality (CINF) (DNRF54) and Center for Nanostructured Graphene (CNG) (DNRF58). This work was supported by Villum Foundation, Project No. VKR023117. We thank Alberto Cagliani, Jonas D. Buron, and Mikkel Settnes for fruitful discussions on current transport in nanomesh, CVD graphene, and graphene with nanoscale defects, respectively.

- ¹K. S. Novoselov, A. K. Geim, S. V. Morozov, D. Jiang, Y. Zhang, S. V. Dubonos, I. V. Grigorieva, and A. A. Firsov, *Science* **306**, 666 (2004).
- ²Y. Zhang, Y.-W. Tan, H. L. Stormer, and P. Kim, *Nature* **438**, 201 (2005).
- ³A. W. Tsen, L. Brown, M. P. Levendoff, F. Ghahari, P. Y. Huang, R. W. Havener, C. S. Ruiz-Vargas, D. A. Muller, P. Kim, and J. Park, *Science* **336**, 1143 (2012).
- ⁴Q. Yu, L. A. Jauregui, W. Wu, R. Colby, J. Tian, Z. Su, H. Cao, Z. Liu, D. Pandey, D. Wei, T. F. Chung, P. Peng, N. P. Guisinger, E. A. Stach, J. Bao, S.-S. Pei, and Y. P. Chen, *Nat. Mater.* **10**, 443 (2011).
- ⁵I. N. Kholmanov, C. W. Magnuson, A. E. Aliev, H. Li, B. Zhang, J. W. Suk, L. L. Zhang, E. Peng, S. H. Mousavi, A. B. Khanikaev, R. Piner, G. Shvets, and R. S. Ruoff, *Nano Lett.* **12**, 5679 (2012).
- ⁶P. M. Ajayan and B. I. Yakobson, *Nat. Mater.* **10**, 415 (2011).
- ⁷P. Zhang, L. Ma, F. Fan, Z. Zeng, C. Peng, P. E. Loya, Z. Liu, Y. Gong, J. Zhang, X. Zhang, P. M. Ajayan, T. Zhu, and J. Lou, *Nat. Commun.* **5**, 3782 (2014).
- ⁸K. Bolotin, K. Sikes, Z. Jiang, M. Klima, G. Fudenberg, J. Hone, P. Kim, and H. Stormer, *Solid State Commun.* **146**, 351 (2008).
- ⁹C. R. Dean, A. F. Young, I. Meric, C. Lee, L. Wang, S. Sorgenfrei, K. Watanabe, T. Taniguchi, P. Kim, K. L. Shepard, and J. Hone, *Nat. Nanotechnol.* **5**, 722 (2010).
- ¹⁰F. Banhart, J. Kotakoski, and A. V. Krashenninnikov, *ACS Nano* **5**, 26 (2011).
- ¹¹S. Chen, Q. Li, Q. Zhang, Y. Qu, H. Ji, R. S. Ruoff, and W. Cai, *Nanotechnology* **23**, 365701 (2012).
- ¹²W. Zhu, T. Low, V. Perebeinos, A. A. Bol, Y. Zhu, H. Yan, J. Tersoff, and P. Avouris, *Nano Lett.* **12**, 3431 (2012).
- ¹³J. Martin, N. Akerman, G. Ulbricht, T. Lohmann, J. H. Smet, K. von Klitzing, and A. Yacoby, *Nat. Phys.* **4**, 144 (2008).
- ¹⁴A. C. Ferrari and D. M. Basko, *Nat. Nanotechnol.* **8**, 235 (2013).
- ¹⁵X. Li, X. Wang, L. Zhang, S. Lee, and H. Dai, *Science* **319**, 1229 (2008).
- ¹⁶T. G. Pedersen, C. Flindt, J. Pedersen, N. A. Mortensen, A.-P. Jauho, and K. Pedersen, *Phys. Rev. Lett.* **100**, 136804 (2008).
- ¹⁷S. R. Power and A.-P. Jauho, "Electronic transport in disordered graphene antidot lattice devices," *Phys. Rev. B* (submitted); e-print [arXiv:1407.0311](https://arxiv.org/abs/1407.0311).
- ¹⁸J. D. Buron, D. H. Petersen, P. Bøggild, D. G. Cooke, M. Hilke, J. Sun, E. Whiteway, P. F. Nielsen, O. Hansen, A. Yurgens, and P. U. Jepsen, *Nano Lett.* **12**, 5074 (2012).
- ¹⁹R. Rymaszewski, *J. Phys. E: Sci. Instrum.* **2**, 170 (1969).
- ²⁰J. Li and S.-L. Zhang, *Phys. Rev. E* **80**, 040104(R) (2009).

Paper V

M. Boll, M. R. Lotz, O. Hansen, F. Wang, D. Kjær, P. Bøggild, and D. H. Petersen

Sensitivity analysis explains quasi-one-dimensional current transport in two-dimensional materials

Phys. Rev. B, vol. 90, no. 24, p. 245432, 2014.

Sensitivity analysis explains quasi-one-dimensional current transport in two-dimensional materials

Mads Boll,^{1,*} Mikkel R. Lotz,^{1,*} Ole Hansen,^{2,3} Fei Wang,⁴ Daniel Kjær,^{2,5} Peter Bøggild,¹ and Dirch H. Petersen^{1,†}

¹*Center for Nanostructured Graphene (CNG), Department of Micro- and Nanotechnology, Technical University of Denmark, DTU Nanotech Building 345 East, DK-2800 Kgs. Lyngby, Denmark*

²*Department of Micro- and Nanotechnology, Technical University of Denmark, DTU Nanotech Building 345 East, DK-2800 Kgs. Lyngby, Denmark*

³*Danish National Research Foundation's Center for Individual Nanoparticle Functionality (CINF), Technical University of Denmark, DK-2800, Kgs. Lyngby, Denmark*

⁴*Department of Electronic and Electrical Engineering, South University of Science and Technology of China, Shenzhen, China*

⁵*CAPRES A/S, Scion-DTU, Building 373, DK-2800 Kgs. Lyngby, Denmark*

(Received 3 October 2014; revised manuscript received 6 December 2014; published 29 December 2014)

We demonstrate that the quasi-one-dimensional (1D) current transport, experimentally observed in graphene as measured by a collinear four-point probe in two electrode configurations A and B, can be interpreted using the sensitivity functions of the two electrode configurations (configurations A and B represents different pairs of electrodes chosen for current sources and potential measurements). The measured sheet resistance in a four-point probe measurement is averaged over an area determined by the sensitivity function. For a two-dimensional conductor, the sensitivity functions for electrode configurations A and B are different. But when the current is forced to flow through a percolation network, e.g., graphene with high density of extended defects, the two sensitivity functions become identical. This is equivalent to a four-point measurement on a line resistor, hence quasi-1D transport. The sensitivity analysis presents a formal definition of quasi-1D current transport, which was recently observed experimentally in chemical-vapor-deposition graphene. Our numerical model for calculating sensitivity is verified by comparing the model to analytical calculations based on conformal mapping of a single extended defect.

DOI: [10.1103/PhysRevB.90.245432](https://doi.org/10.1103/PhysRevB.90.245432)

PACS number(s): 02.60.Cb, 72.80.Vp, 73.23.—b

I. INTRODUCTION

The analysis and control of defects are ongoing topics for graphene films produced via chemical vapor deposition (CVD), which is the preferred method for producing cheap, high-quality graphene suited for large-scale integration. In graphene, such defects can be anything from lattice imperfections (grain boundaries) [1–3], physi- or chemisorbed adatoms, cracks [4], folds [5], areas with contamination, holes due to imperfect transfer from growth substrate, and surface corrugations responsible for various scattering effects reducing the carrier mobility and causing unintended variations in the current flow [6,7].

In a recent study we experimentally observed quasi-one-dimensional (1D) current transport in large area CVD graphene by micro-four-point-probe (M4PP) measurements [7]. We demonstrated how this could be qualitatively reproduced in a two-dimensional (2D) material with randomly distributed insulating line defects near the percolation threshold characterized by the filling factor $\rho\ell^2$, where ρ was the defect density and ℓ the defect length [8]. This was done by inspecting the ratio of the two four-point resistances, R_A/R_B , measured by the electrode configurations shown in Fig. 1. For a material with uniform intrinsic transport properties, the resistance ratio solely depends on the sample geometry including electrode positions and takes on an ideal value of $\ln(4)/\ln(3) = 1.262$ for a homogeneous 2D conductor, i.e., without any form of defects [7,9]. This was verified experimentally in a concurrent study

for graphene without a high density of extended defects [9]. The notion of 1D-like transport or quasi-1D current transport represents the situation when the resistance ratio approaches 1, i.e., the expected result for a 1D conductor or wire measurement [7,8]. For measurements on an inhomogeneous material, the sensitivity (or weighting function) of four-point resistance to small perturbations in the local transport properties has been studied both numerically [10–13] and analytically [14]. Similar studies have been conducted for finite point-like perturbations to include nonlinear effects on the sensitivity [15,16], but the situation is different for highly nonuniform materials with extended insulating defects.

In this paper we present a numerical model of current flow in M4PP measurements in an initially 2D conducting sheet subjected to a large number of insulating line defects of random orientation. We show how the numerical model can be verified for simple situations, involving a single extended defect, using an analytical expression obtained via conformal mapping. The results are analyzed by mapping and comparing the sensitivity of measurements in different probe configurations. Through this technique, it is shown that the frequently occurring 1D signature is a result of the different probe configurations measuring the exact same area on the sample, due to defects confining the current. The approach can be expanded to a general framework for analyzing the sensitivity of other types of defects on electrical measurements.

II. ANALYTICAL MODEL

In a four-point probe measurement, a current I is passed through the sample, using two of the four electrodes, while the resulting potential drop over the remaining two electrodes

*These authors contributed equally to this work.

†dirch.petersen@nanotech.dtu.dk

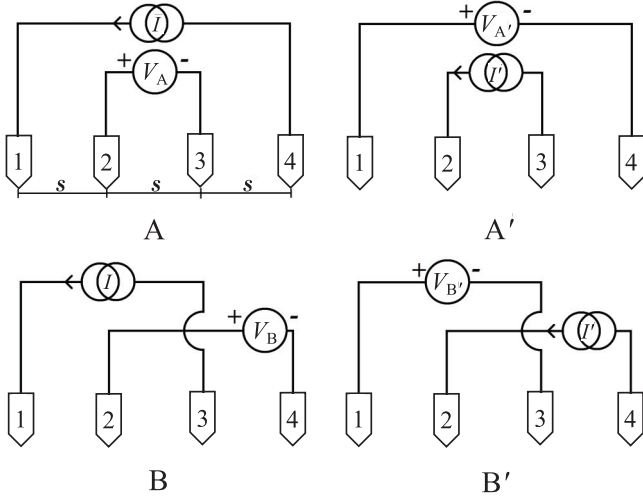


FIG. 1. Schematic of four different probe configurations (A, B, A' and B'). The probe pins are numbered 1 to 4 and are evenly spaced by a probe pitch s .

is measured. The measured resistance is determined by the ratio of measured voltage to applied current. The four-point resistances R_A , R_B , $R_{A'}$, and $R_{B'}$ are measured with the pin configurations (A, B, A', and B') defined in Fig. 1. Due to reciprocity, $R_A = R_{A'}$ and $R_B = R_{B'}$ in the absence of a magnetic field. To analytically model an M4PP measurement on a sample with a line defect, we turn to conformal mapping. Here a linear defect of finite length is mapped onto an infinite border, running along the x axis. Thus the problem is reduced to that of a semi-infinite sheet, for which the electrostatic potential can be calculated for any probe position in the upper half-plane. In the mapping process, the probe pin coordinates are treated as complex numbers, $w = u + iv$ in real space and $z = x + iy$ in the conformal image plane, here $i = \sqrt{-1}$ is the imaginary unit. In the case of a short defect with length ℓ , and its center at the origin of the coordinate system, the transformation of the pin coordinates from the w plane to the z plane and back is given by $z = i\sqrt{\frac{w-\ell/2}{w+\ell/2}}$ and $w = \frac{\ell}{2} \frac{1-z^2}{1+z^2}$, respectively. An example of this mapping procedure for three different M4PP pin positions around a defect is shown in Fig. 2.

The electrostatic potential $\Phi(\mathbf{r}, \mathbf{r}_+, \mathbf{r}_-)$ at position \mathbf{r} with two point current sources $\pm I$, at the positions \mathbf{r}_+ and \mathbf{r}_- in the upper half-plane of the semi-infinite sheet, is found as a solution to the Laplace equation for an infinite sheet

$$\Phi(\mathbf{r}, \mathbf{r}_+, \mathbf{r}_-) = \frac{IR_0}{2\pi} \left(\ln \frac{|\mathbf{r} - \mathbf{r}_+|}{|\mathbf{r} - \mathbf{r}_-|} + \ln \frac{|\mathbf{r} - \bar{\mathbf{r}}_-|}{|\mathbf{r} - \bar{\mathbf{r}}_+|} \right), \quad (1)$$

where $\bar{\mathbf{r}}_{\pm} = (\bar{x}_{\pm}, \bar{y}_{\pm}) = (x_{\pm}, -y_{\pm})$ are the positions of image current sources in the lower half-plane and R_0 is the sheet resistance. This image technique ensures that the current density \mathbf{J}_s across the boundary between two half-planes is zero, $\mathbf{J}_s \cdot \mathbf{n} = 0$, where \mathbf{n} is the unit vector normal to the boundary, which is the correct boundary condition for the semi-infinite system. A detailed derivation of this potential is presented in Ref. [17]. The resistances are found using Ohm's law, for instance, $R_A = [\Phi(\mathbf{r}_2, \mathbf{r}_1, \mathbf{r}_4) - \Phi(\mathbf{r}_3, \mathbf{r}_1, \mathbf{r}_4)]/I$.

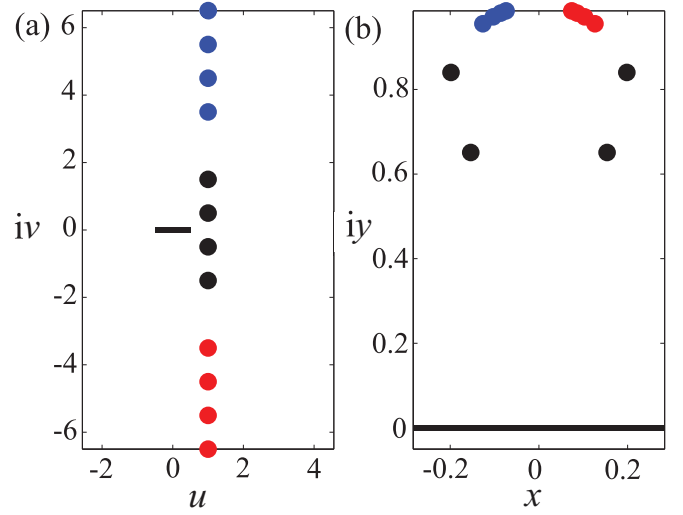


FIG. 2. (Color online) An example of conformal mapping. (a) The probe positions around an insulating line defect, which is indicated by the black line. (b) The corresponding upper half-plane solution where the x axis is an infinite border. The situation on the right can be solved analytically as opposed to the left.

III. NUMERICAL MODEL

With more than one defect there is no simple analytical solution to the electrostatic problem. To calculate the effect of a large number of randomly positioned defects, we must turn to the finite element method (FEM). The numerical simulations were performed using COMSOL Multiphysics 4.4 with LiveLink for Matlab. The sample was modeled as a two-dimensional square-shaped area and the four probe pins were introduced as points placed on a straight line in the center of the square along the x direction and separated by the probe pitch s . One pin was modeled as a current source δ function and one as a current drain δ function, and the two remaining pins were used to monitor the electrostatic potential difference resulting from the current flow. Using point source currents in the calculations is a good approximation when considering the length scale of the probe pitch, which is in micrometers, compared to the physical contact size of ~ 10 nm. Defects were introduced as straight insulating lines, as were the boundaries of the sample, so that in both cases $\mathbf{J}_s \cdot \mathbf{n} = 0$. Adaptive mesh refinement was used on an initial extra-coarse mesh with a maximum of two mesh refinement steps. With these mesh settings the result was within 1% of the fully converged solution even for the highest defect densities.

For numerical simulations, a side length of $10s$ was chosen to reduce computational time for systems with a large number of defects. Due to the proximity of the sample edges, the resistance ratio of the down-scaled system, without added defects, has the value 1.20. To achieve a given defect density, the corresponding amount of defect center coordinates were homogeneously distributed in a square grid, across the sample. Each defect center was then given a random offset in the x and y directions and the offset amplitudes were at most half the distance between two grid points. In addition, each defect was given a random orientation.

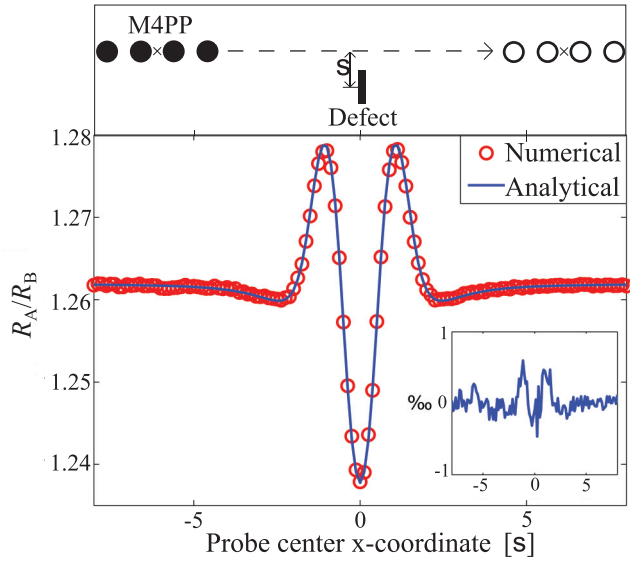


FIG. 3. (Color online) Analytically and numerically calculated resistance ratios for a probe scanned past a single line defect of length s , as indicated by the sketch in the top inset. The lower right inset shows the relative difference between the two models.

The validity of the FEM model was verified by setting up calculations where a probe was scanned past single defects in various configurations relative to the probe axis and scan direction. In all cases the calculated probe response was compared to the analytical result from conformal mapping. An example is shown in Fig. 3, where the top inset shows the probe-defect configuration. The probe was aligned and scanned along the x direction, while the defect of length s was aligned along the y direction and displaced the distance s in the y direction from the probe scan axis. The resulting resistance ratios from numerical and analytical calculations are compared in Fig. 3. To numerically reproduce the resistance ratio of the defect-free semi-infinite sheet, $R_A/R_B = 1.262$, we found that the sample side length had to be at least $450s$. For this reason, the sample used in the numerical model for this verification was $450s \times 450s$. The difference between the numerical and the analytical result was below 0.1%, as shown in the lower right inset in Fig. 3, which is evidence of an excellent agreement between the FEM model and the analytical result and thus serves to verify the FEM model.

IV. SENSITIVITY ANALYSIS

In this work it is essential to visualize and clarify the transition from 2D to 1D-like transport. The signature of 1D transport appears when resistances measured in two different pin configurations, A and B, become equal. For measurements in two different pin configurations the resulting sheet current densities must differ even when the measured resistances are identical; thus the sheet current densities alone do not clearly reveal the transport dimensionality. See Supplemental Material for sheet current densities of 1D-like transport [18]. The sensitivity as explained below will, however, clearly illustrate the dimensionality of the transport.

The sensitivity of an M4PP measurement is a very useful concept that reveals detailed insight into which part of a sample contributes to the measured transfer resistance R_T . Here we use a dimensionless sensitivity S_T defined [13] as $S_T = s^2 \delta R_T / (\delta R_0 \delta \Omega)$, where δR_0 is a small local deviation in sheet resistance R_0 within the incremental area $\delta \Omega$, and δR_T is the resulting change in measured transfer resistance. In the Appendix we show that the sensitivities of A and B configuration measurements are

$$S_A = s^2 \frac{\mathbf{J}_A \cdot \mathbf{J}_{A'}}{I I'} \quad \text{and} \quad S_B = s^2 \frac{\mathbf{J}_B \cdot \mathbf{J}_{B'}}{I I'}, \quad (2)$$

respectively [13]. Here \mathbf{J}_A , $\mathbf{J}_{A'}$, \mathbf{J}_B , and $\mathbf{J}_{B'}$ are the local sheet current densities in the respective measurement configurations, while I and I' are the total measurement currents used in the measurements. Multiplication by the probe pitch squared renders the sensitivity dimensionless and eases comparison of absolute sensitivity values for different samples. Specifically, the sensitivities in a defective sample can be calculated to reveal details of how defects alter the measurements. By using the definition of the sensitivity we have for the resistance difference $R_A - R_B = \int_{\Omega} R_0 (S_A - S_B) d\Omega / s^2$, and clearly in cases of identical sensitivities the resistances become identical.

V. 1D MEASUREMENTS

In recent work we found that the numerical model qualitatively reproduces both the 2D and 1D current transport behaviors [8], which were earlier found experimentally [7]. To investigate the cause of the two dominant measurement signatures we consider two representative cases and use sensitivity analysis on their simulated sheet current densities. Sensitivity plots of S_A and S_B and their difference $S_A - S_B$ for the two typical simulations are shown in Fig. 4, where the white dots indicate the probe pins and the black lines are insulating defects. Figures 4(a)–4(c) (left column) are for a system containing a defect density of $1s^{-2}$ with $R_A/R_B = 1.205$, corresponding to that of a sample with the current limited only by the finite area sample boundary, and thus the figures exhibit 2D-like current transport characteristics. For comparison, the three inset images show the respective sensitivities for pure 2D current transport.

Figures 4(d)–4(f) (right column) are for a system containing a defect density of $4.84s^{-2}$ and $R_A/R_B = 1$, corresponding to 1D-like current transport characteristics. Here a larger fraction of the sheet area is characterized by having a higher value of sensitivity than in the left column. This can be explained by the large number of defects obstructing the path of least resistance, which forces the current on a longer route.

In the 2D-like case (left column) the difference in sensitivity between the two configurations is clearly visible in Fig. 4(c). This explains why different resistances are measured in the two configurations, yielding $R_A/R_B = 1.205$. For the 1D-like case (right column) the difference in sensitivity is mapped in Fig. 4(f). The largest values found here are on the order of 10^{-3} and thus very small compared to the 2D-like case. This shows that the areas that contribute to the measured resistances are essentially identical, and therefore identical resistances were measured, and $R_A/R_B = 1$ results. In this

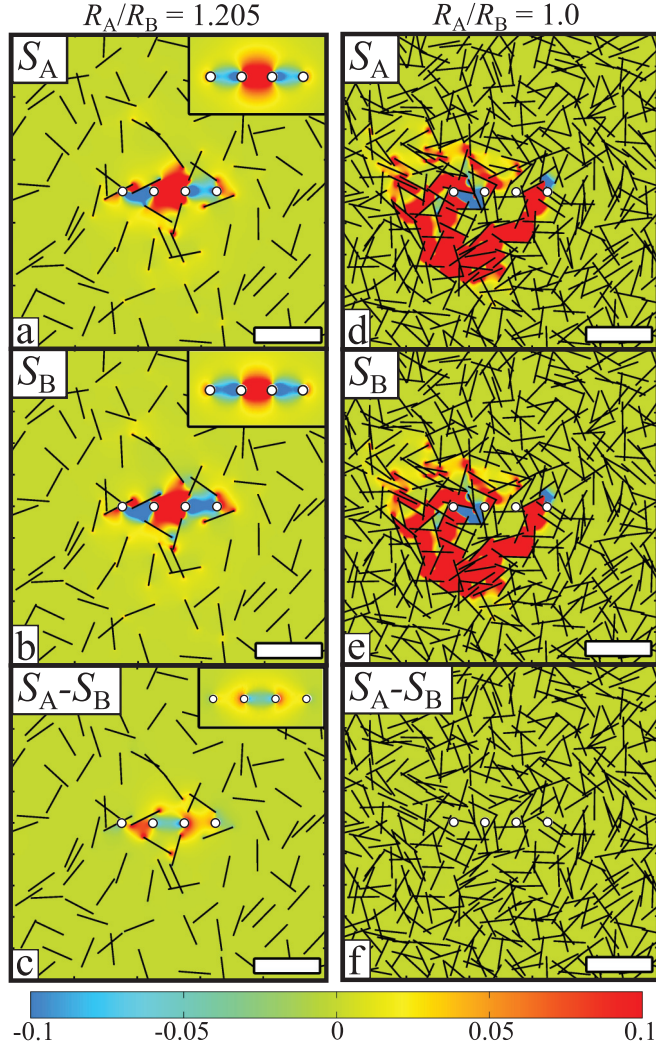


FIG. 4. (Color online) Sensitivity maps for typical 2D and 1D signature measurements where the four white dots represent the probe pin positions, and the black lines are insulating line defects. (a) and (b) are the A and B configuration sensitivity maps for a 2D signature case. (c) is the difference between the values S_A and S_B from (a) and (b). The inset images are the corresponding sensitivity maps for the zero-defect case. (d) and (e) are the A and B configuration sensitivity maps for the 1D signature case. (f) is the difference between the values S_A and S_B from (d) and (e), and is on the order of 10^{-3} , which is very small compared to (c). The scale bar is $2s$ (s is the probe pitch).

case $R_A - R_B = \int_{\Omega} R_0 (S_A - S_B) d\Omega / s^2 = 0$ and thus identical resistances are measured.

VI. CONCLUSION

We have shown that sensitivity analysis of M4PP measurements on 2D materials with extended defects gives considerable insight into the macroscopic transport properties of the materials. In particular we have shown that the sensitivities S_A and S_B in the two M4PP configurations A and B change dramatically when the defect density is increased. At low defect densities, S_A and S_B differ significantly and are localized to an area in the vicinity of the probe pins. As a result the

measured resistances R_A and R_B differ, which is characteristic of 2D transport; the resistance ratio R_A/R_B then becomes $\ln 4 / \ln 3$ for an infinite sample. In contrast, at high defect densities S_A and S_B become essentially identical and localized to a low dimensional path between the probe pins. As a result, the measured resistances R_A and R_B become identical (exactly the same part of the sample is measured), with the ratio $R_A/R_B = 1.0$, a clear 1D signature. This analysis explains the similar behavior observed experimentally on defective graphene in Ref. [7]. The sensitivities were calculated using a FEM model, which was verified by comparison to an analytical calculation for the single-defect case, which we solved exactly by use of conformal mapping.

ACKNOWLEDGMENTS

Center for Individual Nanoparticle Functionality (CINF, DNRF54) and Center for Nanostructured Graphene (CNG, DNRF58) are funded by the Danish National Research Foundation. This work was supported by the Villum Foundation, Project No. VKR023117.

APPENDIX

For the derivation of the sensitivities, Eq. (2), we use an approach similar to that of Paul and Cornils [12]. We now consider a 2D region Ω with an insulating boundary ω (shown in Fig. 5) such that the sheet current density $\mathbf{J}_s \cdot \mathbf{n} = 0$ on ω , except at four electrodes (like the four pins in an M4PP) where a current I_i may flow out of the electrode $i \in [1, 2, 3, 4]$ with the potential V_i . The sheet current densities are considered divergence free, which means that we can write

$$\nabla \cdot (\Phi \tilde{\mathbf{J}}_s) = \nabla \Phi \cdot \tilde{\mathbf{J}}_s + \Phi \nabla \cdot \tilde{\mathbf{J}}_s = \nabla \Phi \cdot \tilde{\mathbf{J}}_s = -\mathbf{E} \cdot \tilde{\mathbf{J}}_s, \quad (\text{A1})$$

where Φ is the potential in region Ω , $\mathbf{E} = -\nabla \Phi$ the electric field, and $\tilde{\mathbf{J}}_s$ is the sheet current density in another region $\tilde{\Omega}$. Taking an integral over the region Ω , and applying Stokes theorem, we get the following identity:

$$\int_{\Omega} \nabla \cdot (\Phi \tilde{\mathbf{J}}_s) d\Omega = \int_{\omega} \Phi \tilde{\mathbf{J}}_s \cdot \mathbf{n} d\omega = - \int_{\Omega} \mathbf{E} \cdot \tilde{\mathbf{J}}_s d\Omega. \quad (\text{A2})$$

The boundary integral is easily evaluated since the boundary conditions make the integral vanish except at the electrodes,

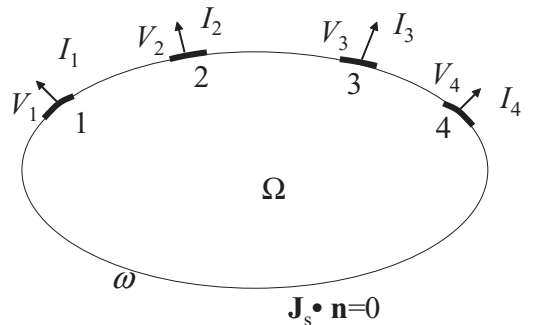


FIG. 5. Illustration of a 2D region Ω with insulating boundary except for four perfect contacts, Nos. 1–4.

and thus a sum results:

$$\int_{\omega} \Phi \tilde{\mathbf{J}}_s \cdot \mathbf{n} d\omega = \sum_{i=1}^4 V_i \tilde{I}_i. \quad (\text{A3})$$

If we now consider the two regions identical but corresponding to reciprocal configurations, e.g., A and A', only two terms remain in the sum, and from Eqs. (A2) and (A3) we find the relation

$$V_k \tilde{I}_k + V_\ell \tilde{I}_\ell = -(V_k - V_\ell) \tilde{I}_{k\ell} = - \int_{\Omega} \mathbf{E} \cdot \tilde{\mathbf{J}}_s d\Omega, \quad (\text{A4})$$

where $i, j, k, \ell \in [1, 2, 3, 4]$ and $i \neq j \neq k \neq \ell$. From this result the transfer resistance $R_T = (V_k - V_\ell) / I_{ij}$ becomes

$$R_T = \frac{V_k - V_\ell}{I_{ij}} = \frac{1}{I_{ij} \tilde{I}_{k\ell}} \int_{\Omega} \mathbf{E} \cdot \tilde{\mathbf{J}}_s d\Omega. \quad (\text{A5})$$

At zero magnetic field the electric field and sheet current density are related as $\mathbf{E} = R_0 \mathbf{J}_s$, where R_0 is the sheet resistance, and thus a general expression for the transfer resistance as a function of the current densities in the two configurations becomes

$$R_T = \tilde{R}_T = \frac{1}{I\tilde{I}} \int_{\Omega} R_0 \mathbf{J}_s \cdot \tilde{\mathbf{J}}_s d\Omega. \quad (\text{A6})$$

Now we can define sensitivity as the change in transfer resistance relative to a change in local direct sheet resistance (δR_0) in a small region $\delta\Omega$ as

$$S = s^2 \frac{\delta R_T}{\delta R_0 \delta\Omega} = s^2 \frac{\mathbf{J}_s \cdot \tilde{\mathbf{J}}_s}{I\tilde{I}}, \quad (\text{A7})$$

where the sensitivity has been made dimensionless by multiplication of s^2 . This result was also given in Ref. [13] without proof.

-
- [1] F. Banhart, J. Kotakoski, and A. V. Krashenninnikov, *ACS Nano* **5**, 26 (2011).
 - [2] A. W. Tsen, L. Brown, M. P. Levendoff, F. Ghahari, P. Y. Huang, R. W. Havener, C. S. Ruiz-Vargas, D. A. Muller, P. Kim, and J. Park, *Science* **336**, 1143 (2012).
 - [3] P. Y. Huang, C. S. Ruiz-Vargas, A. M. van der Zande, W. S. Whitney, M. P. Levendoff, J. W. Kevek, S. Garg, J. S. Alden, C. J. Hustedt, Y. Zhu, J. Park, P. L. McEuen, and D. A. Muller, *Nature* **469**, 389 (2011).
 - [4] S. Chen, Q. Li, Q. Zhang, Y. Qu, H. Ji, R. S. Ruoff, and W. Cai, *Nanotechnology* **23**, 365701 (2012).
 - [5] W. Zhu, T. Low, V. Perebeinos, A. A. Bol, Y. Zhu, H. Yan, J. Tersoff, and P. Avouris, *Nano Lett.* **12**, 3431 (2012).
 - [6] J.-H. Chen, C. Jang, S. Xiao, M. Ishigami, and M. S. Fuhrer, *Nat. Nanotechnol.* **3**, 206 (2008).
 - [7] J. C. D. Buron, D. H. Petersen, P. Bøggild, D. G. Cooke, M. Hilke, J. Sun, E. Whiteway, P. F. Nielsen, O. Hansen, A. Yurgens, and P. U. Jepsen, *Nano Lett.* **12**, 5074 (2012).
 - [8] M. R. Lotz, M. Boll, O. Hansen, D. Kjær, P. Bøggild, and D. H. Petersen, *Appl. Phys. Lett.* **105**, 053115 (2014).
 - [9] J. D. Buron, F. Pizzocchero, B. S. Jessen, T. J. Booth, P. F. Nielsen, O. Hansen, M. Hilke, E. Whiteway, P. U. Jepsen, P. Bøggild, and D. H. Petersen, *Nano Lett.* **14**, 6348 (2014).
 - [10] D. W. Koon and C. J. Knickerbocker, *Rev. Sci. Instrum.* **63**, 207 (1992).
 - [11] D. H. Petersen, R. Lin, T. M. Hansen, E. Rosseel, W. Vander-vorst, C. Markvardsen, D. Kjær, and P. F. Nielsen, *J. Vacuum Sci. Technol. B* **26**, 362 (2008).
 - [12] O. Paul and M. Cornils, *Appl. Phys. Lett.* **95**, 232112 (2009).
 - [13] F. Wang, D. H. Petersen, T. M. Hansen, T. R. Henriksen, P. Bøggild, and O. Hansen, *J. Vac. Sci. Technol. B* **28**, C1C34 (2010).
 - [14] D. Koon, F. Wang, D. Petersen, and O. Hansen, *J. Appl. Phys.* **114**, 163710 (2013).
 - [15] D. W. Koon, *Rev. Sci. Instrum.* **77**, 094703 (2006).
 - [16] D. W. Koon, F. Wang, D. H. Petersen, and O. Hansen, *J. Appl. Phys.* **116**, 133706 (2014).
 - [17] D. H. Petersen, O. Hansen, R. Lin, and P. F. Nielsen, *J. Appl. Phys.* **104**, 013710 (2008).
 - [18] See Supplemental Material at <http://link.aps.org/supplemental/10.1103/PhysRevB.90.245432> for a comparison of sheet current densities and sensitivity of 1D-like transport.



Copyright: Daniel Kjær
All rights reserved

Published by:
DTU Nanotech
Department of Micro- and Nanotechnology
Technical University of Denmark
Ørstedes Plads, building 345B
DK-2800 Kgs. Lyngby